UNIVERSITAT POLITÈCNICA DE VALÈNCIA

# DEVELOPMENT OF NOVEL BIOMIMETIC ELECTROACTIVE ENVIRONMENTS WITH BIOACTIVE MOLECULES FOR MUSCULOSKELETAL REGENERATION

Doctoral Thesis

Doctoral Programme in Biotechnology

Universitat Politècnica de València

Centre for Biomaterials and Tissue Engineering

**José Luís Aparicio Collado**

Supervised by:

Prof. Roser Sabater i Serra

Prof. José Molina Mateo

May 2023

*A toda mi familia*

*En especial a ti, Vicente*

# Acknowledgements

Si hace unos años me hubieran contado que hoy estaría escribiendo estas líneas, no me lo hubiera podido creer. Si a finales de 2019, con el máster terminado y una total inseguridad laboral me hubieran dicho que podía comenzar una carrera investigadora en la misma universidad en la que me formé, hubiera pensado que me estaban tomando el pelo. Y si mi hubieran contado que la oferta de trabajo a la que me inscribí, aquella que ofrecía un contrato de 2 años como técnico superior en el CBIT (a la que valoré ni tan siquiera presentarme por varios motivos), terminaría desembocando en esta Tesis Doctoral, me hubiera vuelto totalmente demente. A todo eso hay que añadirle una pandemia mundial desencadenada tan solo un mes después del inicio de mi contrato y que me ha acompañado hasta prácticamente el final de la tesis. En definitiva, entre toda una mezcla de incertidumbre e inexperiencia se inició un contrato que en principio no pretendía ser una tesis, pero que, por varios motivos, sí lo fue y terminó siendo una de las mejores decisiones de mi vida.

Y he de decir que en un principio no parecía serlo. Con un perfil mucho más enfocado a la biología molecular y la neurociencia, el área de la ingeniería tisular y los biomateriales era totalmente nueva para mí. Sin embargo, con el tiempo, fui cogiendo cariño a los polímeros, a las nanopartículas conductoras y a la diferenciación muscular. Con sus momentos buenos y no tan buenos, he disfrutado al máximo el proceso de aprendizaje y experimentación, pero lo que verdaderamente me llevó a ser feliz con mi trabajo fueron las personas que me acompañaron durante los casi 3 años que he pasado aquí.

**Roser** y **José**, gracias por considerar mi perfil desde la primera entrevista y ofrecerme al poco tiempo la posibilidad de realizar la tesis doctoral bajo vuestra dirección. Gracias por vuestra claridad, amabilidad y respeto en todo momento. El camino ha sido mucho más fácil con vosotros. Os deseo lo mejor en lo personal y lo profesional. Ahora entiendo la importancia del sentirse cómodo y confiar en tus supervisores, así como sentir que ellos confían en ti y verdaderamente valoran tu trabajo. Roser, especialmente gracias a ti por el trato tan cercano que has tenido todo este tiempo conmigo. He sentido que realmente has contado conmigo para todo. Además, nos lo hemos pasado pipa con el “proyectito” de Biotatool y hemos aprendido y trabajado un montón.

No me quiero olvidar de **Ángel** y **Ana**, dos ejemplos de dedicación a la ciencia desde la honestidad, conocimiento y trabajo duro. Gracias por permitirme colaborar con vosotros y obtener tan buenos resultados en tan poco tiempo.

A toda la gente del CBIT que ha estado durante los años que he pasado allí. Infinitas gracias por toda la ayuda que me habéis prestado en todo momento. Empezando por los/as más veteranos/as, gracias a la omnipresente e imprescindible Laura Teruel, a Andrés, Ximo, Luís, Cristina y José Luís. Especialmente a Pachi, gracias por tus consejos, tu sinceridad y tu intención de ayudarme en todo momento. Pasando a los de “mi quinta”, gracias, Dra. Sandra Clara, por tu amabilidad, sabiduría y compañerismo. Sin duda alguna, tienes todo lo necesario para tener una carrera brillante en la ciencia. Mil gracias también a Sara, Inma, Sandra, Raquel, Paco, Irene y Sofía. Especial mención a mis alumnas favoritas, **Natalia** y **Qiqi**, mal del todo no nos lo hemos pasado con tantas pruebas sin sentido y frascos en agitación. También a **Alejandra**, mi

compañera colombiana de aventuras desde el día 0, que desafortunadamente no pudo disfrutar al máximo su estancia aquí debido a la crisis sanitaria.

No podría olvidarme de **Amparo**. Una gran persona luchadora y trabajadora que desde el primer momento he sentido como una segunda madre, mi madre del CBIT. Gracias por acompañarme y cuidarme tanto durante estos años, sin duda eres un ejemplo para todos.

Gracias a mi verdadera **familia** del CBIT. Estela, Julio, Dra. María Guillot y Ana. Han sido tantos los momentos que hemos pasado juntos que me sería imposible agradecéroslos todos. No creo que exista una mejor compañía para trabajar (y para lo que no es trabajar…) que la vuestra. Las comidas de extranjis en la trastienda del CBIT, la noche del Famós, el camping de Viver, el frío de Pamplona, los días de montaña, las cenas en los pisitos, alguna noche loca… Gracias por hacerme sentir como en casa siempre que estoy con vosotros. Estemos donde estemos, lo nuestro es para siempre.

**Estela**, gracias por tu energía y felicidad inagotables desde el primer día que te conocí. Vales muchísimo y tienes todas las cualidades para llegar donde te propongas en la ciencia, eres capaz de todo. Espero poder vivirlo junto a ti. Eso sí, las señales de tráfico deben quedarse en su sitio. Gracias por cerrar tu bolso a mis enciclopedias.

**Julio**, desde el principio hemos sido inseparables. Ya eres como un hermano y te deseo todo lo mejor. Espero que nunca te alejes de mi lado, ni que dejes de enviarme vídeos de animales trambólicos. El siguiente en ser doctor eres tú, amigo. Eso sí, los cuadros de Mr. Wonderful también deben quedarse en su sitio. Los cabezazos siguen estando permitidos.

**María**, siempre has sido un ejemplo para mi, tanto en lo profesional como en lo personal. Vales muchísimo y me siento muy afortunado de tenerte cerca. Eres alegría pura y contagias a quienes te rodean. Muchísimas gracias especialmente por toda la ayuda en estos últimos meses. Que los ratopines sean el comienzo de tu nueva vida.

**Ana**, no tengo ninguna duda de que sin ti nada de esto hubiera sido posible. Eres lo mejor que alguien pueda aspirar a tener a su lado. Una persona que vive por y para los demás, sin escasear en esfuerzos a la hora de ayudar, entender y querer. Te admiro muchísimo, eres única y nunca podré llegar a agradecerte todo lo que haces por mí. Me has hecho crecer como persona y entender la vida de otra manera. El CBIT fue solo el principio de todo lo que nos queda por vivir. Conmigo siempre tendrás un hombro donde apoyarte. Eres hogar, alegría y, sobre todo, amor. No quiero nada si no es contigo. Regálame siempre un minutito más. Te quiero.

Gracias también a mis amigo/as de la UPV del grado en Biotecnología, con quienes di los primeros pasos en el mundo de la ciencia. A ***los más mejores***, por todos los momentos vividos dentro y fuera de la universidad. Y los que nos quedan. Especialmente a "**La Escoria**". Charly, Vendrell, Pablete y Rubén. Literalmente, me sobran las palabras. He tenido que borrar algunas míticas frases conmemorativas por exaltación pública, lo siento. Os quiero, familia.

A mis amigos/as de siempre, de **Losa**. Gracias por todos los momentos juntos, que sin duda me han ayudado a evadirme en las etapas más duras de la tesis. Estabais y estaréis siempre, hay cosas que nunca cambian. En especial a ti, **Dani**. Por determinadas circunstancias el destino nos unió y quiso que fuéramos como hermanos,

siempre me tendrás para lo que necesites. También al C.F. Losa del Obispo; humildes, toscos y la verdad que bastante malos, pero siempre un grupo unido que me ha regalado momentos muy bonitos. El fútbol de antes, el del barro en una noche de enero, es mejor. Qué bonito es ser pequeño.

Por último, gracias a mi familia. Todo en la vida os lo debo a vosotros. Sois lo más importante que tengo y no me cabe duda de que siempre estaremos juntos. Gracias por ser un verdadero hogar y estar siempre para todo. **Mamá**, eres la mejor persona que conozco. Eres sencillez, honestidad, compromiso y, sobre todo, amor y dedicación a tus seres queridos. Espero algún día poder cuidar a mis hijos/as de la misma forma que nos has cuidado tú. Eres mi modelo a seguir en todo. Gracias por tu comprensión, empatía y ayuda en los momentos buenos y en los malos. Sin ti nada de lo que soy en la vida sería posible. **Papá**, gracias por tu constante preocupación, amor y orgullo por tus hijos. Eres un ejemplo de que, en el amor, a veces, sobran las palabras. **Iaia**, gracias por todo lo que me cuidas. Espero poder seguir disfrutando de ti el máximo tiempo posible, ojalá fueras eterna. Tus empanadillas son mundialmente conocidas por la mayoría de gente mencionada en estas líneas. **Héctor** y **Lorena**, infinitas gracias por vuestro apoyo, amor y consejos. Siempre seréis un ejemplo en todo y estoy seguro de que nos quedan muchísimas cosas por vivir de la mano de la nueva reina de la casa, **Carla**. Por último, **Vicente**. Ojalá estuvieras aquí con nosotros, son tantas las cosas que te tendríamos que contar…Gracias por haberme permitido crecer junto a ti y regalarme tantos y tantos momentos inolvidables. Mataría por poder ver un último partido de fútbol contigo en el sofá. Tu recuerdo será siempre imborrable, esto y todo en mi vida va por ti.

Os quiero muchísimo. A todos.

Por último, gracias a la financiación del Ministerio de Ciencia e Innovación, a la Agencia Estatal de Investigación y a los fondos FEDER por la financiación del proyecto RTI2018-097862-B-C21 que ha permitido llevar a cabo esta tesis doctoral.

¡Gracias!

# INDEX

# List of figures

## *Introduction*

## Chapter 1

(24 h of culture). (**c**) Representative actin stained cells from PHBV/PVA E, PHBV/PVA E2 and PHBV/PVA E10 after 24 h culture.

## *Chapter 2*

**Figure 1.** (**a**) Scheme with the steps followed to prepare the semi-IPN and the nanohybrid hydrogels. (**b**) High-resolution field-emission scanning electron microscopy (HRFSEM) images of the cross-section (left column) and surface (right column) in freeze-dried samples. The image at the bottom shows pristine rGO nanosheets dispersed previously in water. (**c**) Representative Atomic Force microscopy (AFM) images (height, vertical deflection, and phase) of the semi-IPN SA/PCL-E and nanohybrid hydrogels with 0.5 and 2% of rGO.

**Figure 2.** (**a**) Fourier transform infrared (FTIR) spectroscopy spectra in the region 4000-300 $cm^{-1}$: SA/PCL blend, semi-IPN SA/PCL (SA/PCL-E) and nanohybrid composites with 0.5 and 2% of rGO nanosheets. Neat PCL and SA, crosslinked SA (SA-E) have been included as a reference. (**b**) Schematic diagram of the structure of nanohybrid hydrogels.

**Figure 3.** (**a**) Swelling degree in equilibrium. (**b**) Water contact angle of semi-IPN SA/PCL-E and nanohybrid hydrogels with 0.5 and 2% of rGO. Crosslinked SA (SA E) and PCL have been included as references. Graphs show mean ± standard deviation. (*) and (***) indicate significant differences ($p<0.05$ and $p<0.001$, respectively).

**Figure 4.** (**a**) DSC thermograms at a rate of 20 °C/min. Normalized heat flow on heating of SA/PCL blend, semi-IPN SA/PCL (SA/PCL-E) and nanohybrid composites with 0.5 and 2% of rGO nanosheets. Thermogravimetry results (TGA): (**b**) SA/PCL blend, semi-IPN SA/PCL (SA/PCL-E) and (**c**) derivative. (**d**) Nanohybrid hydrogels with 0.5 and 2% of rGO and ™ derivative. SA/PCL-E has been also included in (d) and ™ to facilitate comparison. Neat SA and PCL and crosslinked SA (SA-E) have been included as a reference in DSC and TGA results. (**f**) Dynamic mechanical analysis. Storage modulus (*E'*) and loss modulus (*E''*) in the interval 35 to 39 ºC were performed on samples immersed in water. (**g**) Electrical conductivity of semi-IPN SA/PCL (SA/PCL-E) and nanohybrid composites with 0.5% and 2% of rGO nanosheets at different frequencies (20, 50 and 100 kHz). The graph shows mean ± standard deviation. (*), (**) and (***) indicate significant differences ($p<0.05$, $p<.01$ and $p<0.001$, respectively).

**Figure 5.** Cytotoxicity results and cell adhesion. (**a**) MTT cytotoxicity results represented cell viability after 24, 48 and 72 h incubation with extracts from semi-IPN and nanohybrid hydrogels with 0.5% and 2% of rGO nanosheets. Positive control: latex extract, negative control: growth medium. (**b**) Average cell adhesion area for each condition from actin staining after 24 h of culture. (**c**) Representative immunofluorescence images of cells attached to the different hydrogels (actin staining) after 24 h of culture. SA-E was considered as a reference. Graphs show mean ± standard deviation. (*), (**) and (***) indicate significant differences ($p<0.05$, $p<0.01$ and $p<0.001$, respectively).

**Figure 6.** Results of myoblast differentiation. (**a**) Immunofluorescence images of differentiated myoblasts (sarcomeric α-actinin staining) after 6 days of culture in differentiation medium (DMEM+1% P/S+1%ITS). (**b**) Myotube density is represented as the number of myotubes/$cm^2$. (**c**) Average myotubes area. (**d**) The ratio between the areas of differentiated myotubes/area of total sarcomeric α-actinin positive cells. (**e**)

Mean diameter of myotubes after analysis of 80 random myotubes per hydrogel. SA-E was considered as a reference. Graphs show mean ± standard deviation. (*), (**) and (***) indicate significant differences (p<0.05, p<0.01 and p<0.001, respectively).

## *Chapter 3*

## *Future perspectives*

# List of tables

## *Chapter 1*



## *Chapter 2*



## *Chapter 3*

# Glossary

| | |
|---|---|
| **ΔHf** | Enthalpy of fusion (sample) |
| **AFM** | Atomic force microscopy |
| **Ag** | Silver |
| **AP** | Action potentials |
| **Au** | Gold |
| **B** | Boron |
| **$Ca^{2+}$** | Calcium |
| **$CaCl_2$** | Calcium chloride |
| **CBNs** | Carbon-based nanomaterials |
| **CCL-18** | Chemokine CC ligand 18 |
| **CCR2** | Chemokine receptor 2 |
| **CK-MM** | Creatine kinase isoform CK3 |
| **$Cl^-$** | Chloride |
| **CNMs** | Carbon nanomaterials |
| **CNTs** | Carbon nanotubes |
| ***$C_p$*** | Specific heat capacity |
| **CPs** | Conductive polymers |
| **Cu** | Cupper |
| **CX3CR1** | Fractalkine receptor |
| **DAMPs** | Damage associated molecular patterns |
| ***$dc_p/dT$*** | Temperature derivative |
| **DHPR** | Dihydropyridine receptors |
| **DMEM** | Dulbeco's Modified Eagle's Medium |
| **DMTA** | Dynamic mechanical thermal analysis |
| **DN** | Double networks |
| **DNA** | Desoxyribonucleic acid |
| **DPBS** | Dulbecco's phosphate-buffered saline |
| **DSC** | Differential scanning calorimetry |
| **DTG** | Derivative of the weight loss |
| **E'** | Storage modulus |
| **E''** | Loss modulus |

| | |
|---|---|
| **ECC** | Excitation-contraction coupling |
| **ECM** | Extracellular matrix |
| **ENO3** | Enolase 3 |
| **FAPs** | Fibro adipogenic progenitors |
| **FBS** | Fetal bovine serum |
| **FDA** | USFood and drug administration |
| **Fe** | Iron |
| **FGF-2** | Fibroblast growth factor 2 |
| **FGF2R** | Fibroblast growth factor 2 receptor |
| **FTIR** | Fourier-transformed infrared spectroscopy |
| **G** | Graphene |
| **GA** | Glutaraldehyde |
| **GBMs** | Graphene-based materials |
| **GO** | Graphene oxide |
| **GQDs** | Graphene quantum dots |
| **HGF** | Hepatocyte growth factor |
| **HMGB1** | High mobility group box 1 |
| **HR-FESEM** | High-resolution field emission scanning electron miscroscopy |
| **HS** | Horse serum |
| **hSMPCs** | Human skeletal muscle progenitor cells |
| **IFN- γ** | Interferon γ |
| **IGF-1** | Insulin growth factor 1 |
| **IGFR1** | Insulin growth factor receptor 1 |
| **IL-1** | Interleukin 1 |
| **IL-1 α** | Interleukin 1α |
| **IL-10** | Interleukin 10 |
| **IL-12** | Interleukin 12 |
| **IL-13** | Interleukin 13 |
| **IL-1ß** | Interleukin 1ß |
| **IL-6** | Interleukin 6 |
| **IL-8** | Interleukin 8 |
| **IPNs** | Interpenetrating polymer networks |
| **iPSCs** | Induced pluripotent stem cells |
| **IRS1** | Insulin receptor substrate 1 |

| | |
|---|---|
| **$K^+$** | Potassium |
| **Ly6C** | Lymphocyte antigen 6 complex locus |
| **MABs** | Mesoangioblasts |
| **MCK** | Muscle creatin kinase |
| **MHC** | Myosin heavy chain |
| **MPs** | Mesenchymal progenitors |
| **MRF-4** | Myogenic regulatory factor 4 |
| **mROS** | Reactive oxygen species |
| **MSCs** | Mesenchymal stem cells |
| **MTE** | Muscle tissue engineering |
| **MTS** | (3-[4,5, dimethylthiazol-2-yl]-5-[3-carboxymethoxy-phenyl]-2-[4-sulfophenyl]-2H-tetrazolium, inner salt) |
| **MTT** | (3-[4, 5-dimethylthiazol-2-yl]-2, 5 diphenyl tetrazolium bromide) |
| **Myf-5** | Myogenic factor 5 |
| **Myo-D** | Myoblast determination protein |
| **Myo-G** | Myogenin |
| **$Na^+$** | Sodium |
| **NaBC1** | Boron receptor |
| **nAChR** | Nicotinic acetylcholine receptors |
| **NGF** | Nerve growth factor |
| **NMJ** | Neuromuscular junction |
| **NMP** | 1-metil-2-pyrrolidone |
| **OD** | Optical density |
| **P/S** | Penicillin/Streptomycin |
| **PANI** | Polyaniline |
| **Pax 7** | Paired box transcription factor 7 |
| **PCL** | Polycaprolactone |
| **PEG** | Polyethylene glycol |
| **PHAs** | hydroxybutyrate |
| **PHB** | Poly (hydroxybutyrate) |
| **PHBV** | Poly (3-hydroxybutyrate-co-3-hydroxyvalerate) |
| **PI3K** | Phosphoinositide 3′-kinase |
| **PLGA** | Polyglycolic acid |
| **PLA** | Polylactic acid |
| **PP** | Polypropylene |

| | |
|---|---|
| **PPy** | Polypyrrole |
| **PT** | Polytiophene |
| **PVA** | Poly (vinyl alcohol) |
| **rGO** | Reduced graphene oxide |
| **RNA** | Ribonucleic acid |
| $R_S$ | Electrical sheet resistance |
| **RT-qPCR** | Real time quantitative polymerase chain reaction |
| **RyR** | Ryanodine receptors |
| **SA** | Sodium alginate |
| **Semi-IPNs** | Semi-interpenetrating polymer networks |
| **SR** | Sarcoplasmic reticulum |
| **T-tubes** | Trabecular tubes |
| $T_d$**-50%** | 50% weight loss decomposition temperature |
| **TE** | Tissue engineering |
| **TEM** | Transmission electron microscopy |
| $T_g$ | Glass transition temperature |
| **TGA** | Thermogravimetric analysis |
| **TGF-ß** | Transforming growth factor ß |
| **THF** | Tetrahydrofuran |
| $T_m$ | Melting temperature |
| **TNF-α** | Tumour necrosis factor alpha |
| **VEGF** | Vascular endothelial growth factor |
| **VML** | Volumetric muscle loss |
| **WCA** | Water contact angle |
| **Xc** | Degree of crystallinity |
| **Zn** | Zinc |
| **Zip7** | Zinc influx transporter |
| $Zn^{2+}$ | Extracellular inorganic zinc ions |
| $ZnCl_2$ | Zinc chloride |
| $\sigma$ | Electrical conductivity |

# Abstract

The musculoskeletal system can self-regenerate in a limited way. Major tissue losses cannot be regenerated, resulting in necrosis and functional impairment. Traditional treatments based on implants or transplants have not proven to be completely successful, with multiple side effects such as immunogenicity or rejections. Therefore, it is very important to develop new alternatives to treat muscle degeneration. Tissue engineering combines biomaterials, cells and bioactive agents to develop biological and biocompatible constructs where cells find an *in vivo* likely environment to grow, proliferate and differentiate into muscle tissue and restore its functionality.

Conductive biomaterials are of particular interest in electrosensitive tissues such as the musculoskeletal system. Conductive polymers (polypyrrole, polyaniline, etc.), carbon materials (graphene, reduced graphene oxide, etc.) and metal nanomaterials have proved to enhance cell differentiation, even without external electrical stimulation. Moreover, different bioactive molecules such as growth factors (FGF-2, IGF-1, etc.) or inorganic “therapeutic” ions (zinc, magnesium, etc.) are alternatives to enhance cell differentiation into different tissues.

Therefore, the combination of conductive biomaterials and bioactive molecules to enhance muscle regeneration represents an exciting opportunity in muscle tissue engineering. This thesis project aims to develop and characterize novel electroactive biomaterials with different compositions, structures and properties and evaluate their potential to treat musculoskeletal regeneration, as well as its combination with inorganic ions looking forward to discovering new conductive biomaterial-therapeutic ions synergies in terms of muscle differentiation.

# Resumen

El sistema musculoesquelético tiene una capacidad de regeneración limitada. Las pérdidas importantes de tejido no se pueden regenerar, lo que provoca necrosis y deterioro funcional. Los tratamientos tradicionales basados en implantes o trasplantes no han demostrado ser del todo exitosos, con múltiples efectos secundarios como inmunogenicidad o rechazos. Por ello, es muy importante desarrollar nuevas alternativas para tratar la degeneración muscular. La ingeniería tisular combina biomateriales, células y agentes bioactivos para desarrollar constructos biológicos biocompatibles donde las células encuentran un entorno que imita sus condiciones *in vivo* para crecer, proliferar y diferenciarse en tejido muscular y restaurar su funcionalidad.

Los biomateriales conductores son de particular interés en tejidos electro-sensibles como es el caso del sistema musculoesquelético. Se ha demostrado que los polímeros conductores (polipirrol, polianilina, etc.), los materiales de carbono (grafeno, óxido de grafeno reducido, etc.) y los nanomateriales metálicos mejoran la diferenciación muscular, incluso sin estimulación eléctrica externa. Además, diferentes moléculas bioactivas como factores de crecimiento (FGF-2, IGF-1, etc.) o iones inorgánicos “terapéuticos” (zinc, magnesio, etc.) son alternativas para potenciar la diferenciación celular en diferentes tejidos.

Por lo tanto, la combinación de biomateriales conductores y moléculas bioactivas para mejorar la regeneración muscular representa una gran oportunidad en la ingeniería de tejidos musculares. El objetivo de este proyecto de tesis es desarrollar y caracterizar nuevos biomateriales electroactivos con diferentes composiciones, estructuras y propiedades y evaluar su potencial para tratar la regeneración musculoesquelética, así como la combinación de estos biomateriales electroactivos con iones inorgánicos buscando descubrir nuevas sinergias biomateriales conductores-iones terapéuticos en términos de diferenciación muscular.

# Resum

El sistema musculoesquelètic té una capacitat de regeneració limitada. Les pèrdues importants de teixit no es poden regenerar, cosa que provoca necrosi i deteriorament de la funcionalitat. Els tractaments tradicionals basats en implants o trasplantaments no han demostrat ser del tot exitosos, amb múltiples efectes secundaris com ara immunogenicitat o rebutjos. Per això, és molt important desenvolupar noves alternatives per tractar la degeneració muscular. L'enginyeria tissular combina biomaterials, cèl·lules i agents bioactius per desenvolupar constructes biològics biocompatibles on les cèl·lules troben un entorn que imita les seves condicions *in vivo* per créixer, proliferar i diferenciar-se en teixit muscular i restaurar-ne la funcionalitat.

Els biomaterials conductors són de particular interès en teixits electrosensibles com és el cas del sistema musculoesquelètic. S'ha demostrat que els polímers conductors (polipirrol, polianilina, etc.), els materials de carboni (grafè, òxid de grafè reduït, etc.) i els nanomaterials metàl·lics milloren la diferenciació muscular, fins i tot sense estimulació elèctrica externa. A més, diferents molècules bioactives com a factors de creixement (FGF-2, IGF-1, etc.) o ions inorgànics "terapèutics" (zinc, magnesi, etc.) són alternatives per potenciar la diferenciació cel·lular en diferents teixits.

Per tant, la combinació de biomaterials conductors i molècules bioactives per millorar la regeneració muscular representa una gran oportunitat a l'enginyeria de teixits musculars. L'objectiu d'aquest projecte de tesi és desenvolupar i caracteritzar nous biomaterials electroactius amb diferents composicions, estructures i propietats i avaluar-ne el potencial per tractar la regeneració musculoesquelètica, així com la combinació d'aquests biomaterials electroactius amb ions inorgànics buscant descobrir noves sinergies biomaterials conductors-ions terapèutics en termes de diferenciació muscular.

# Introduction

## 1. The muscular system

The muscular system comprises about 40-50% of the total adult body mass and it is responsible for generating voluntary movements, structural support, locomotion and internal organic activity (Mukund & Subramaniam, 2020; Qazi et al., 2015). It is a complex and highly organized tissue comprising different cell types, and it is divided into two different main groups: smooth and striated muscle. Smooth muscle is found in different internal hollow organs and in the vascular system of the body, where it produces mechanical and organized contraction-relaxation movements to control fluids' direction and organs' size and shape (Frismantiene et al., 2018). Striated muscle is divided into cardiac and skeletal muscle. Cardiac muscle is composed of non-voluntary contractile cells with intermediate energy requirements, while skeletal muscle tissue, located in the bone-muscle junction, is responsible for voluntary movement and locomotion with high energy needs (Frismantiene et al., 2018; Mukund & Subramaniam, 2020; Qazi et al., 2015).

### 1.1. The skeletal muscle: structure and organization

Skeletal muscle is a highly vascularized and innervated tissue, which controls body posture, voluntary movement and locomotion. The functional units of this hierarchically organized tissue are called **myofibres**, derived from matured multinucleated and elongated myotubes formed after the undifferentiated myoblasts fusion (Qazi et al., 2015). Myofibres consist of multinucleated cells presenting groups of myofibrils, specific intracellular contractile organelles which contain repetitive units called sarcomeres, composed of actin and myosin filaments (Frontera & Ochala, 2015).

The extracellular matrix (ECM) in the skeletal muscle is essential to control muscle force transmission from the neuromuscular junction and control homeostasis. It provides structural support and enables cell adhesion, migration, proliferation and myogenic differentiation (Y. xiao Liu et al., 2019; W. Zhang et al., 2021).

Three layers of connective tissue surrounding the muscle system compose the ECM of the skeletal muscle. Each myofibre is covered by the **endomysium** (basal lamina), mainly composed of type IV collagen, laminin and fibronectin. The integrity of this outer layer is crucial for the regeneration of damaged fibres (W. Zhang et al., 2021). **Perimysium**, rich in fibronectin, dermatan sulphate and different types of collagen (I, III, V and VI) wraps together groups of myofibres in muscle fascicles, which are finally bundled together along with blood vessels and nerves by the **epimysium**, composed mainly by type IV collagen, fibronectin, and laminin (Frismantiene et al., 2018; Frontera & Ochala, 2015). Figure 1 represents the structural organization of the skeletal muscle.

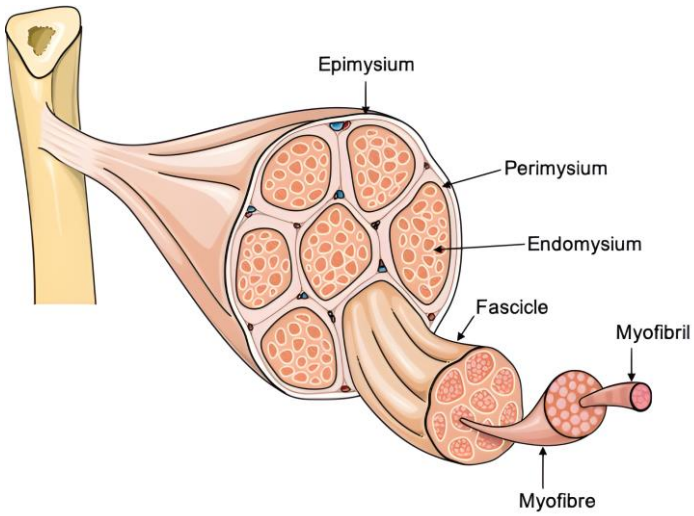


**Figure 1**. Schematic representation of the skeletal muscle structural organization. *Image adapted from Smart Servier Medical Art*.

## 1.2. Cell populations in the adult skeletal muscle

**Myofibres** are known as the functional units of muscle. They are multinucleated cells with up to 100-200 nuclei per cell formed after undifferentiated myoblast fuse into myotubes and their subsequent maturation. These cells present an elongated shape surrounded by the cytoplasmic membrane called sarcolemma. Inside its cytoplasm (sarcoplasm), myofibres contain the specific contractile units known as myofibrils (about 2500 per myofibre). They are organized in parallel and occupy about 85% of the sarcoplasm, thus displacing other cell organelles to the periphery. Each myofibril contains repetitive units called **sarcomeres** (8000 per myofibril) composed of thick myosin and thin actin filaments in combination with structural and regulatory proteins which are responsible of muscle contraction (Frontera & Ochala, 2015). The structure and mechanism of sarcomeres in muscle contraction will be discussed later.

In addition to myofibres, there are some other cell types present in an adult muscle playing different roles. **Satellite cells** are the main population of stem cells present in the skeletal muscle, beneath the basal lamina. They are *paired box transcription factor 7* (Pax7+) positive cells which will remain in a quiescent state only activated after receiving injury or growth signals and will act as muscle precursor stem cells to produce muscle growth and regeneration (Scharner & Zammit, 2011).

Nevertheless, numerous research efforts have elucidated that there are other cell populations with myogenic potential that also play a key role in muscle development. That is the case of a stem cells niche located in the interstitium (space between myofibres and outside their basal lamina) called **PIC cells**, which express Pw1/Peg3 gene, also active in satellite cells, regulating mitochondrial activity, embryonic muscle fibre number and adult satellite cell metabolism (Correra et al., 2018; F. S. Tedesco et al., 2017.). There are other kinds of interstitial progenitor cells expressing CD133 glycoprotein (**CD133$^+$ cells**), which coexist in both the interstitium and under the basal lamina, with a proven contribution to myotubes formation and improved skeletal muscle regeneration (Meng et al., 2014; F. S. Tedesco et al., 2017.; Ten Broek et al., 2010).

In addition, other cells stimulate myogenic differentiation producing different pro-differentiation signals. They are known as **mesenchymal progenitors (MPs)**, interstitial

cells that can differentiate into fibro-adipogenic (FAP), osteogenic and/or chondrogenic lineages. Since they do not fuse with existing myofibres, there is no direct intervention in muscle growth or repair, but it has been shown that MPs produce biochemical signals such as Wnt1, Wnt3A, IGF1 or IL-6 that enhance myogenic activity and regulate muscle homeostasis (Joe et al., 2010; F. S. Tedesco et al., 2017.). They do also regulate the type VI collagen production, present in the endomysium and in the satellite cell niche (F. S. Tedesco et al., 2017.; Urciuolo et al., 2013).

The vascular system provides muscles with specific nutrients to regulate homeostasis and growth. **Pericytes** are contractile cells surrounding endothelial vascular cells that regulate blood vessel homeostasis, permeability and growth (F. S. Tedesco et al., 2017.). Since blood vessels in the skeletal muscle are found to be nearly located with myofibres, it has been shown that some subpopulations of pericytes (expressing CD146) present some myogenic capacity (lower than myoblasts) to regenerate muscle fibres and satellite cells (Sacchetti et al., 2016; Scharner & Zammit, 2011). **Mesoangioblasts** (MABs) are cells derived from adult muscle pericytes with myogenic potential which are considered as the activated form of pericytes in terms of muscle regeneration. They are self-renewable, and can also travel from the interstitium to the basal lamina, helping to keep the satellite cells pool (Rotini et al., 2018; Scharner & Zammit, 2011).

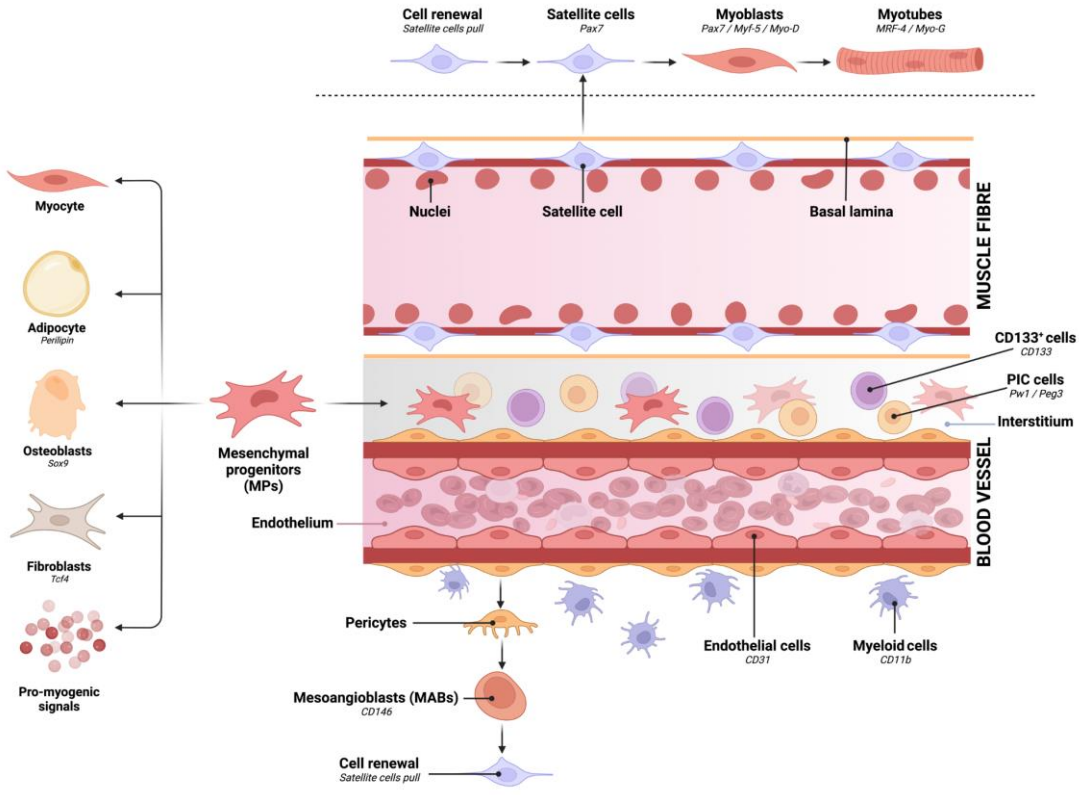


**Figure 2**. Illustration of the different cell populations present in adult skeletal muscle (satellite cells, pericytes, mesoangioblasts, mesenchymal progenitors, PICs, CD133$^{+}$) represented along with their main contributions to muscle regeneration. Vasculature and typical blood cells are also included. The main specific markers of each cell populations are remarked. *Image adapted from (F. S. Tedesco et al., 2017.), created with BioRender.*

## 2. Muscle contraction: structural basis

The contractile activity of the skeletal muscle relies on the activity of myofibrils, specifically on the sarcomeric subunits inside them. The basic structure of a single **sarcomere** is composed of parallelly aligned **thin actin filaments** intertwined with parallel groups of **thick myosin filaments** located in the central part of the sarcomere. The structure is maintained by transversal Z proteins (**Z disc**) and M proteins (**M line**) which support the interaction between thick and thin filaments together with other structural proteins such as nebulin and titin (Figure 2) (Hopkins, 2006).

Furthermore, actin filaments are associated with other regulatory proteins, which regulate the actin-myosin interaction by the **cross-bridge binding sites**: troponin complex and tropomyosin. The **troponin** complex is formed by three subunits: inhibitory (I), calcium-binding site (C), and tropomyosin binding (T). When the muscle is relaxed, **tropomyosin** is blocking the cross-bridge binding sites on actin, but when calcium ($Ca^{2+}$) levels are high enough and ATP is present, calcium binds troponin C and produces a displacement of tropomyosin. This structural change allows actin and myosin to interact through the cross-bridge binding sites and slide along each other producing sarcomeres shortening and muscle contraction (Frontera & Ochala, 2015; Hopkins, 2006).

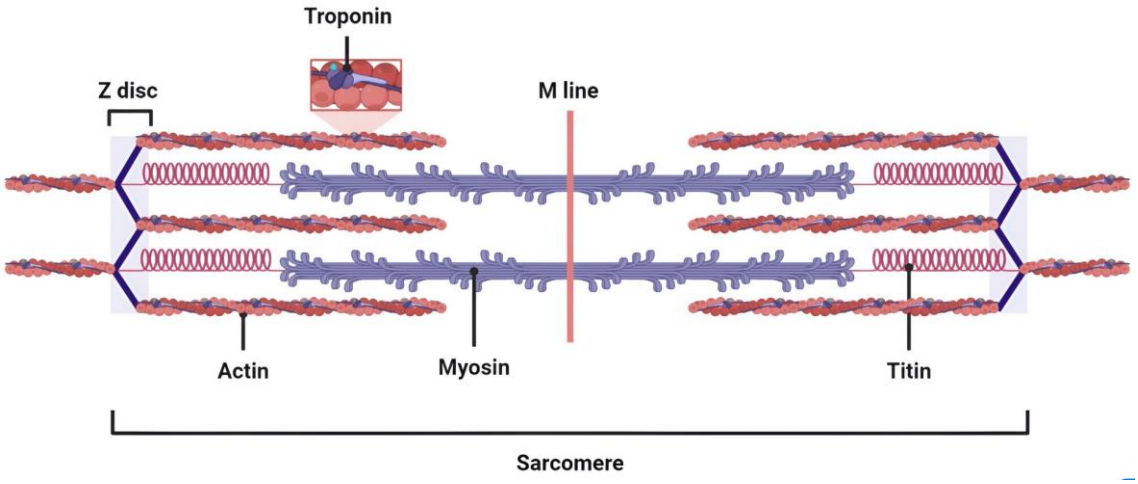


**Figure 3**. Schematic representation of the sarcomere, showing the actin and myosin filaments along with their main regulatory and structural proteins. *Image adapted from BioRender*.

### 2.1. Excitation-contraction coupling

The skeletal muscle presents electrically sensitive cell membranes (sarcolemma) that will start the contractile process in response to electrical signals travelling from the motoneurons. These signals from motoneurons contact with muscle fibres at the **neuromuscular junction** (NMJ), also called motor endplate, producing **action potentials** (AP) that will propagate along the fibre to finally produce muscle contraction. This process is traditionally called **excitation-contraction coupling** (ECC) (Hernández-Ochoa & Schneider, 2018).

Briefly, APs are based on a membrane depolarization-repolarization cycle of the muscle fibres by altering the voltage-dependent ionic channels. As in nerve cells, APs depend on the membrane permeability to sodium ($Na^+$) and potassium ($K^+$) ions by the transmembrane $Na^+$ and $K^+$ channels, as was discovered by Hodking and Huxley almost 70 years ago (Hodking & Huxley, 1952). In resting conditions, $Na^+$ is more abundant in

the extracellular space and $K^+$ predominates in the cytoplasm. The transmembrane potential of the sarcolemma in basal conditions relies on about -84 mV comparing the cytoplasm with the exterior of the fibres. When motoneurons transmit electric impulses and secrete acetylcholine and other neurotransmitters into the synaptic space of the NMJ, voltage-dependent $Na^+$ channels are activated, and $Na^+$ is transported inside the cytoplasm, producing a depolarization of the transmembrane potential from -84 mV to +25 mV. This voltage change instantly activates the $K^+$ channels that produce the release of $K^+$ outwards the cells and repolarizes the membrane potential. Chloride ions ($Cl^-$) do also help to restore the membrane potential at -84 mV again (Jurkat-Rott & Lehmann-Horn, 2004).

APs are propagated both longitudinally along the fibre and radially through the **trabecular tubules** (T-tubes), sarcolemma invaginations that allow the fast transmission of electrical information from the cell membrane to the sarcoplasmic reticulum (SR) by the multiple T-tubes/SR junctions (Calderón et al., 2014; Huxley, 1969). Voltage changes induce a conformational change of dihydropyridine receptors (DHPR) located in the T-tubules. These transformations produce a still unclear structural change in the ryanodine receptors (RyR) of the SR, transmembrane ionic channels with a homotetramer structure that regulates **calcium** ($Ca^{2+}$) influx between the SR and the cytoplasm, and also modulates DHPR structure (Calderón et al., 2014; Rebbeck et al., 2014), covering the majority of space between T-tubules and SR (Dulhunty et al., 2018). When activated, RyR channels release $Ca^{2+}$ ions from the SR to the cytoplasm, where they interact with troponin C and inactivate the modulatory inhibition imposed on actin-myosin filaments interaction by tropomyosin and troponin I. Then, thin actin filaments are enabled to glide over the thick myosin filaments and produce muscle contraction (Kuo & Ehrlich, 2015; Rebbeck et al., 2014).

## 3. Muscle regeneration

Skeletal muscle regeneration comprises a complex process which starts after skeletal tissue suffers a mechanical trauma or other pathogenic conditions such as stress, ischemia, myotoxic agents or inherited neuromuscular disorders (W. Yang & Hu, 2018). This injury derives on myofibre necrosis and is the starting point of muscle regeneration, an organized process on which different cell types try to recover the damaged tissue. It comprises a first inflammatory phase commanded by the immune system to remove the necrotic cells, followed by a second anti-inflammatory phase of muscle regeneration, remodelling and functional recovery.

### 3.1. Tissue necrosis

As mentioned above, several events can produce muscle degeneration, being mechanical traumas the most common ones. The homeostatic equilibrium in the affected zone is disrupted: the functionality of myofibres is impaired, with alterations in the permeability of the sarcolemma and basal lamina, leading to disorders in the ion flux (especially calcium ions) that causes functional loss of different cell organelles and ECM structure alterations. There are different markers of muscle damage, being a specific creatine kinase isoform **CK3** (CK-MM) the most common one. This globular protein is related to the control of muscle energy and homeostasis and is released outside the myofibres after the sarcolemma losses its integrity (Forcina et al., 2020).

Muscle degeneration produces an inflammatory response triggered by the intracellular content released to the extracellular space after permeability disruption, which acts as signalling molecules called ***damage-associated molecular patterns*** (DAMPs). There are plenty of DAMPs released from extracellular proteins (biglycan, tenascin C) or intracellular compartments, such as nuclear high mobility group box 1 (HMGB1), histones and both DNA/RNA, cytosolic F-actin or heat-shock proteins, mitochondrial formyl peptide, and reactive oxygen species (mROS) (Roh & Sohn, 2018).

These DAMPs are recognized by the immune system, and therefore the inflammatory response to tissue damage is initiated (Forcina et al., 2020; Le Moal et al., 2018).

## 3.2. Inflammatory phase: response to injury

The **complement system** is composed by different plasmatic proteins which work together to produce inflammatory responses to infection and/or injury. These proteins are the first ones activated in the early muscle injury (**first wave**) becoming the first innate immunity line; when activated, neutrophils and macrophages infiltrate into the damaged zone. **Mast cells**, granular hematopoietic cells present in the skeletal muscle do also activate and start degranulating into different proinflammatory factors, such as tumour necrosis factor-alpha (TNF-α), interleukin 1 (IL-1), interferon γ (IFN- γ) or histamine, to recruit more neutrophils and mast cells that infiltrate the damaged zone and promote inflammation (Forcina et al., 2020; W. Yang & Hu, 2018). Activated **neutrophils** generate different enzymes and oxidative factors that remove the myofibrillar debris and clear the affected zone. Within this process, neutrophils also generate different pro-inflammatory cytokines (IL-1, IL-6 and IL-8) that stimulate the homing of monocytes and macrophages (Forcina et al., 2020; Tidball, 2005).

**Macrophages** are a heterogeneous cell population derived from circulating blood monocytes, divided into proinflammatory M1 macrophages and anti-inflammatory M2 macrophages M2 (Kratofil et al., 2017). **M1 macrophages** are produced by monocytes expressing high levels of lymphocyte antigen 6 complex loci (Ly6C) and chemokine receptor 2 (CCR2). They are activated after two days of injury in a **second wave** of immune infiltration, generating free radical activity that induces apoptosis of the damaged cells and expression of inflammatory molecules (IL-1ß, IL-6, IL-12, TNF-α) (Forcina et al., 2020; Orekhov et al., 2019). These cytokines produce the migration of satellite cells that will start proliferating and differentiating in the next days. Moreover, M1 macrophages call up T cells to the damaged zone after three days, especially **CD4+ and CD8+** T cells. These cells keep expressing inflammatory molecules (IL-1, IL-6, IL-13, IFN- γ, etc) and keep the debris clearance of the damaged zone. However, at the same time, a combination of four cytokines (IL1α, IL-13, IFN- γ and TNF-α) also promotes muscle stem cell proliferation and differentiation (Fu et al., 2015).

Once the necrotic tissue is removed and muscle stem cells are finally recruited (approximately 3-4 days after injury), the inflammatory response ends. M1 macrophages levels decrease, and monocytes with lower expression levels of Ly6C and CCR2 enter the injury zone thanks to a different fractalkine receptor (CX3CR1), differentiating into **M2 macrophages** (**third wave**) (Orekhov et al., 2019; Stout & Suttles, 2004). These macrophages express anti-inflammatory cytokines, such as IL-10, IL-1RA, chemokine CC ligand 18 (CCL-18), or transforming growth factor ß (TGF-ß) that lessen inflammation and enable the start of the regenerative process. (Orekhov et al., 2019).

### 3.3. Anti-inflammatory phase: regenerative process

Then, the regenerative process starts. **Satellite cells** are the main contributors to muscle regeneration. They remain quiescent beneath the basal lamina expressing Pax7, adhesion proteins (NCAM, Mcad, VCAM-1, etc) and cell cycle inhibitors ($p27^{kip1}$) until called upon for regeneration. They also present self-renewal capacity, keeping the stem cells pool by expressing Pax7 and repressing myogenic genes such as myoblast determination protein (Myo-D). If activated after muscle injury, they migrate to the damaged zone and re-enter the cell cycle to start proliferating, suffering genetic and epigenetic changes in different gene expression patterns. A **proliferation stage** keeps Pax7 expression and induces satellite commitment to myoblasts by the activation of different proliferative and myogenic factors, such as myogenic factor 5 (Myf-5) and Myo-D (Dumont et al., 2015; Forcina et al., 2020). Then, myoblasts exit again the cell cycle and start the **differentiation stage**, downregulating Pax7 and increasing the expression of differentiation markers such as myogenin (Myo-G) and myogenic regulatory factor 4 (MRF-4). This is a complex process involving different factors (IL-4, TGF- ß), where myoblasts fuse to form new multinucleated myotubes, that will develop new myofibres and/or fuse with already existing damaged myofibres to regenerate damaged tissue. At this point, early differentiation markers decrease and typical myofibre proteins expression appear: myosin heavy chain (MHC), muscle creatine kinase (MCK), or enolase 3 (ENO3) (Agarwal et al., 2020; Dumont et al., 2015).

The skeletal muscle regenerative process is driven by satellite cells, but this is a complex and well-organized process, which also requires the combined and coordinated activity of different non-satellite cells. As mentioned before (see section 1.3), there are other cell populations (PIC cells, pericytes, etc) that in some way do also contribute to this process, complementing the satellite cells activity and keeping muscle homeostasis.

### 3.4. Remodelling phase and functional recovery

The remodelling phase takes place about 5-7 days after injury. During this phase, ECM remodelling guides myofibre maturation. TGF- ß chemotactically attracts **fibroblasts** to the injury site that will synthesize ECM proteins such as collagen, fibronectin and proteoglycans. These proteins will produce a newly organized ECM responsible for guiding myofibre alignment, maturation and functionality (Carnes & Pins, 2020). Functional recovery is completed when mature myofibres develop their functional performance and contractile activity. Re-innervation by neuromuscular junctions is essential for functional recovery since they provide the muscle with the APs necessary to generate muscle contraction and functionality. Nicotinic acetylcholine receptors (nAChR) are the main markers of neuromuscular junctions and functional recovery (Forcina et al., 2020).

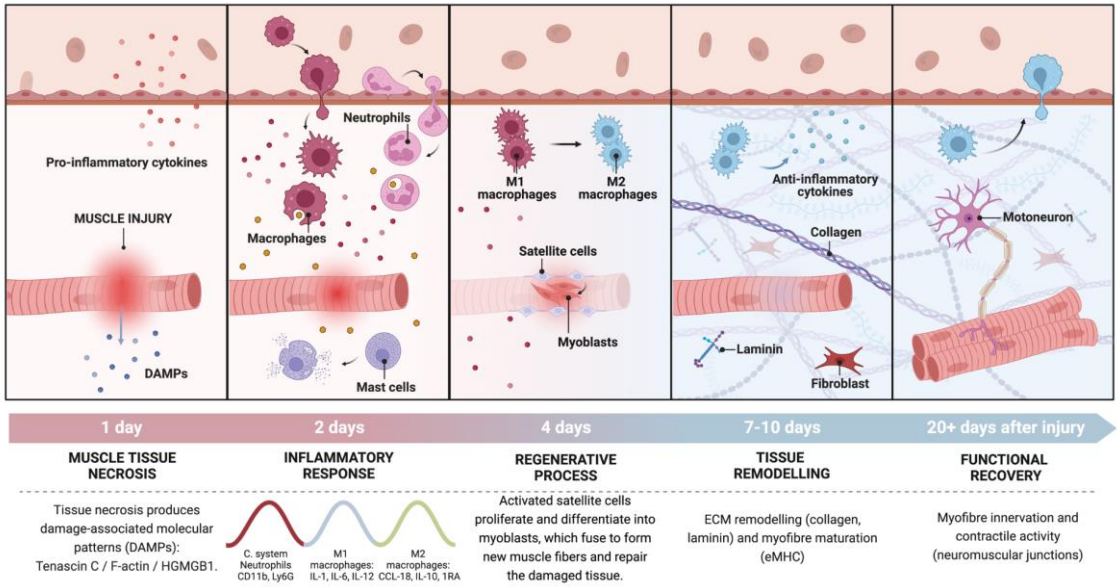


**Figure 4**. Simplified representation of the muscle healing process on a "wave by way" model remarking the different stages with different cell populations involved and their typical markers. Tissue necrosis produces damage-associated molecular patterns (DAMPs), which activate the inflammatory response, where neutrophils and macrophages carry out the necrotic tissue clearance and satellite cells activation. An anti-inflammatory stage enables the regenerative process, driven by satellite cell activation, proliferation and differentiation. This step is followed by tissue remodelling, where fibroblasts produce different structural extracellular matrix (ECM) components, and myofibres maturate. Finally, neuromuscular junctions (NMJs) produce innervation and muscle contraction, recovering tissue functionality. *Image adapted from (Forcina et al., 2020) and created with BioRender.*

## 4. Muscle tissue engineering

The skeletal muscle presents regenerative potential. It is able to reconstruct damaged tissue and recover its functionality, but after severe trauma with an important **volumetric muscle loss (VML)** (more than 20% of tissue loss) produced after traffic accidents, military conflicts or surgical trauma among others, the endogenous repairing system is not enough and the regenerative process leads to the formation of a non-functional fibrous and scar tissue. **Fibrosis** is understood as an excessive ECM deposition in the necrotic tissue, caused by an overproduction of ECM components (especially collagen) and/or by an aberrant degradation of necrotic ECM tissue (Alameddine & Morgan, 2016).

Muscle fibrosis is highly related to the inflammatory response to injury. As previously described, macrophages present two different heterogeneous phenotypes. While M1 macrophages are the first to be activated and produce pro-inflammatory cytokines, M2 macrophages are lately activated to produce anti-inflammatory molecules and TGF-ß cytokines, among others. TGF-ß produces fibroblast proliferation and inhibits apoptotic fibro adipogenic progenitors' cleavage, inducing its differentiation to fibrogenic cells. Therefore, post-injury fibrosis is caused by an **imbalance between M1-M2 macrophage subtypes**, producing an overactivation of the M2 subtype and its consequent increase in the TGF-ß levels and ECM deposition (Mahdy, 2019). Fibrosis impairs muscle functionality at the same time that lessens regeneration and increases the possibility of re-injuries.

Different therapeutic approaches based on muscle transplantations have been applied to deal with impaired muscle regeneration after VML. Allotransplants are defined as the transplantation of cells, tissues or organs between genetically different individuals within the same species. Human muscle allotransplants present genetic, immunological and

ethical concerns, along with the problems derived from the imbalance between patients and available donors. This last problem is avoided with xenotransplants, those transplants into a human body of cells, tissues and/or organs from a different animal source (Lu et al., 2020). Nevertheless, the risk of cross-species diseases or infection transmission (xenozoonosis), genetic differences and immunological rejections in muscle xenotransplants are still major problems to be solved.

**Autologous muscle transplants** from healthy tissues of the own patient (muscle flaps) remain the most feasible procedure to treat severe muscle injury. This approach avoids the genetic differences and immune response of the body against foreign tissues and ensures the presence of an established vascular network with already-formed neuromuscular junctions. Nevertheless, these treatments still present several problems, such as donor site morbidity and longer times to restore muscle functionality (Qazi et al., 2015).

In this context, tissue engineering represents a promising alternative to enhance muscle regeneration and prevent fibrosis. **Muscle tissue engineering** (MTE) is based on the combination of meticulously designed biomaterial scaffolds, muscle cells and bioactive molecules to reproduce a niche which mimics the *in vivo* environment and induces cell adhesion, proliferation and differentiation into mature myofibres. These constructs should be transferred to muscles and replace the damaged tissues to enhance guided tissue regeneration (Qazi et al., 2015).

MTE present different strategies to repair injured muscle tissue: *in vivo* MTE*, in situ* MTE and *in vitro* MTE (Carnes & Pins, 2020). Each of them is described in the upcoming sections, together with examples of different applications.

### 4.1. *In vivo* MTE

*In vivo* MTE is based on the direct *in vitro* seeding of biopsy muscle stem cells into a designed biomaterial scaffold and its immediate transplantation into the injury zone. There, the scaffold will provide the niche for encapsulated cells to treat regeneration, both inducing the endogenous regenerative system by paracrine signalling or directly differentiating into myotubes and myofibres. (Carnes & Pins, 2020; McCullen et al., 2011). Before this technique, direct cellular injections into the affected zone were studied, but the results reported low effectivity related to poor survival rates, low cell retention and lack of structural microenvironments in VML injuries.

Alberto Rossi and collaborators demonstrated that a hyaluronan-based hydrogel for *in vivo* delivery of satellite cells in a murine model with partially ablated tibialis anterior injury produced an increase in muscle myofibres and tissue contractile functionality (Rossi et al., 2011). Other researchers employed dextran/chitosan injectable hydrogels to encapsulate and deliver myoblasts in rat models with tibialis anterior defects, and the results showed enhanced myofibre number and organization (Baolin Guo et al., 2019).
*In vivo* MTE is an exciting approach as its cost is lower than other available options because cells are scarcely manipulated *in vitro*, but its scalability and transferability to the clinic still limit its use (Sengupta et al., 2014).

### 4.2. *In situ* MTE

This strategy follows the same idea as *in vivo* MTE, based on inducing muscle regeneration in the same injury zone. Nevertheless, *in situ* MTE is only focused in acellular scaffolds design without the presence of any cell type within the matrix. It is based on obtaining decellularized structures with specific physicochemical features to mimic the ECM and trigger *in vivo* endogenous muscle regeneration after implantation. As cells are not seeded within the scaffold, fabrication time is highly decreased and the regulatory pathway to commercialization may be easier and faster (Carnes & Pins, 2020). Collagen scaffolds are widely used in this area. Kin et al. implanted acellular collagen sponges into a rabbit model with vastus lateralis tight defect, and after 24 weeks all animals survived and presented no signs of inflammation and fibrosis but did not achieve complete muscle regeneration (Kin et al., 2007). The main challenge of this strategy is to effectively generate microstructural niches that imitate the endogenous environment and guide tissue regeneration.

Alternatively, acellular scaffolds can also be obtained after *in vitro* decellularization of endogenous organs or tissues. An important clinical trial employed acellular porcine urinary bladders as ECMs to treat VML injuries of 13 patients with different muscle injuries. The results showed that all patients presented cell infiltration into the scaffold and signs of muscle regeneration in the majority of them with improved strength, motion and functional tasks (Dziki et al., 2016). Nevertheless, systematic reviews demonstrated that acellular scaffolds are not enough to promote *de novo* myofibre formation (Eugenis et al., 2021).

Although this technique presents easier regulatory trials compared to the rest and its scalability is also easier, the cost-effectiveness is still unclear since it is uncertain how designed decellularized scaffolds induce tissue regeneration (Sengupta et al., 2014).

### 4.3. *In vitro* MTE

*In vitro* MTE seeks to obtain *in vitro* maturated and functional muscle grafts from culturing stem cells and bioactive factors into biomaterials and implanting them in the injury zone. To do so, muscle stem cells should be previously extracted (biopsy) and expanded in controlled *in vitro* conditions. Then, they are seeded intro polymeric scaffolds that provide a solid environment that simulates the ECM to enable cells to attach, proliferate and differentiate into 3D muscle structures. Tissue 3D conformation can be easily achieved by coculturing muscle stem cells with other cell types, such as fibroblasts, and with growth factors (EGF, FGF-2, VEGF, etc). Several studies have successfully employed this *in vitro* approach in MTE. They engineered different scaffold structures to match the cell microenvironment. For example, Gilbert-Honick et al. fabricated aligned electrospinning microfibres of sodium alginate and fibrinogen and cultured them with myoblasts to generate muscle grafts for implantation in murine models of VML. The results successfully demonstrated the effectiveness in terms of muscle recovery *in vivo* (Gilbert-Honick et al., 2018). Kroehne et al employed freeze-drying techniques to generate collagen gels with an aligned porous structure that enabled directional organized myotube formation after seeding with myoblasts. Again, these grafts proved *in vivo* muscle force regeneration after implantation in a VML murine model (Kroehne et al., 2008).

Moreover, other researchers generated pre-vascularized grafts before implantation to ensure oxygen and nutrient diffusion and increase survival after implantation. The scaffolds with myoblasts and vascular cells coculture improved vascularization. Shandalov et al. developed a polylactic acid/polyglycolic acid (PLA/PLGA) scaffold seeded with myoblasts, fibroblasts and endothelial cells. The mature muscle flap was implanted in a murine model and showed enhanced vasculature and anastomosis with host vessels (Shandalov et al., 2014). Muscle innervation is also vital to achieving muscle functionality, and some researchers have tried to generate neuromuscular junctions in muscle grafts before implantation. Kap Ko et al. proved that supplementing myoblast culture within fibrin hydrogels with a proteoglycan (agrin, in this study) enhanced nerve contacts in an *in vivo* rat model (Ko et al., 2013).

Nevertheless, *in vitro* MTE still presents various disadvantages that nowadays limit its translation to the clinic. In general, there is a huge variance in the regeneration level, as there is an almost infinite possible combination of biomaterials and cells which will produce different results. It is notably difficult to generate *in vitro* muscle grafts with specific biomechanical conditions that exactly imitate those found *in vivo.* Moreover, the contractile forces generated by implanted grafts are usually lower than in native tissue. The need of generating a pre-vascularized and innervated implant also requires time and difficulty. Cell biopsy, expansion and seeding into the scaffolds take time and notably reduce industry scalability. The regulatory pathway of these products to reach clinics is also more complicated than *in vivo* or *in situ* approaches (Carnes & Pins, 2020). These limitations need to be further investigated if MTE wants to fill the gap currently existing in muscle regeneration treatments, although it represents a promising approach with great potential.

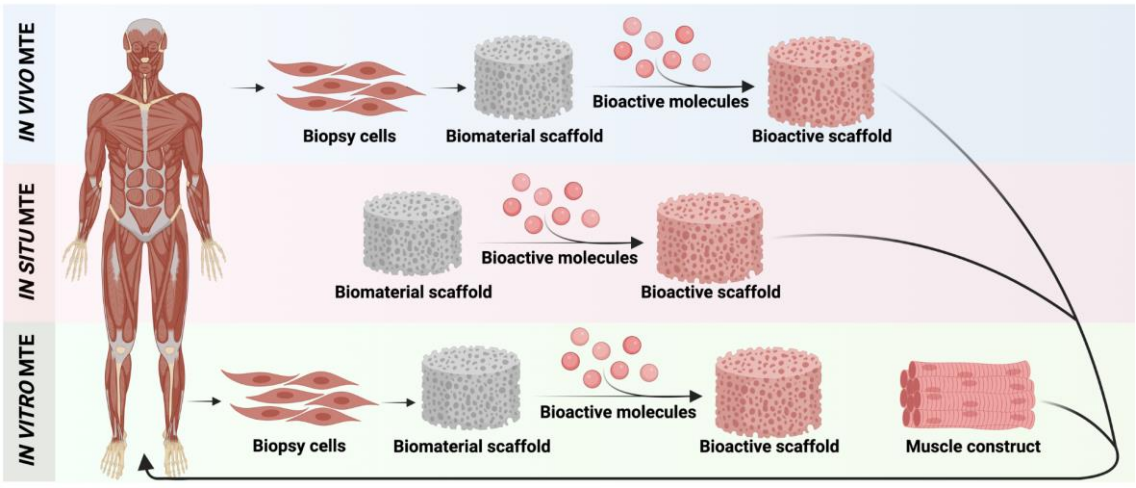


**Figure 5**. Representation of the different tissue engineering approaches. *In vivo MTE* seeks to extract and expand biopsy muscle stem cells and seed them into engineered scaffolds in combination with bioactive molecules to be implanted in the patient to regenerate muscle *in vivo*. *In situ MTE* avoids cell biopsy and directly implants an engineered scaffold with bioactive molecules to guide *in vivo* regeneration. *In vitro MTE* tries to generate an *in vitro* differentiated muscle construct from differentiated stem cells cultured in scaffolds with bioactive molecules that will be implanted in the muscle defect zone. *Image created with BioRender.*

## 4.4. Cell sources for skeletal muscle tissue engineering

A huge variety of cells have been used in skeletal muscle tissue engineering (SMTE). **Satellite cells** are widely employed since they are the main cell type enrolled in muscle regeneration. However, they present important heterogenicity and the purification process is difficult, resulting in very variable results in terms of regeneration. Its expansion *in vitro* produces cell senescence and a significant decrease in its proliferative activity, being an important limitation for these types of cells (Cezar & Mooney, 2015). Moreover, *in vitro* expanded satellite cells present lower regenerative potential when transplanted back into patients (Eugenis et al., 2021). Minced muscle grafts, described as bundles of single fibres containing satellite cells and other typical resident cells in muscle tissue have proved to enhance up to 55% the functional recovery of VML rat models (B. T. Corona et al., 2013). Other myogenic populations such as L8 or C2C12 (rat and murine myoblast cells, respectively) keep their proliferative activity *in vitro* and are considered alternative cell models to study muscle regeneration *in vitro*.

Induced pluripotent stem cells (iPSCs) are also used in MTE, since they present *in vitro* proliferating activity and can to differentiate into multiple cell types. They consist of adult somatic cells genetically reprogrammed with the worldwide famous *Yamanaka factors cocktail* (OCT4, KLF4, SOX2 and MYC) to a pluripotent stage where they can differentiate into any type of new somatic cell (Doss & Sachinidis, 2019). Different studies have shown that *in vitro* muscle constructs generated from iPSCs can fuse with existing myofibres and regenerate tissue *in vivo* (Rao et al., 2018; van der Wal et al., 2018). Nevertheless, IPSCs are controversial and difficult to be translated into clinics because of their genetical instability, mutagenesis, teratoma formation and tumorigenesis-derived problems (Attwood & Edel, 2019; Ben-David & Benvenisty, 2011; Galat et al., 2016).

Finally, mesenchymal stem cells (MSCs), fibro-adipogenic progenitors (FAPs), and pericytes are other cell types used in MTE (Carnes & Pins, 2020). Each cell type presents different advantages/disadvantages depending on the application, host or environment.

## 4.5. Bioactive molecules in skeletal muscle tissue engineering

The endogenous regeneration system is controlled by different signalling pathways where different biomolecules regulate cell behaviour and are involved in the control of cell adhesion, proliferation and differentiation. Therefore, these bioactive molecules are of great interest in MTE and regenerative medicine. Nevertheless, it is difficult to regulate the dosage of these molecules because an excess dose can result in fibrosis, oedema, hypertension or even tumours (Eugenis et al., 2021). In this context, biomaterials with specific compositions and conformations allow the controlled loading and delivery of these bioactive molecules and the subsequent optimization of their effects on muscle regeneration.

There is a great variety of bioactive molecules available for MTE. Some of the most important ones are insulin growth factor 1 (**IGF-1**) and fibroblast growth factor 2 (**FGF-2**). They regulate the recruitment and activation of satellite cells, and present synergic effects in cell proliferation. IGF-1 is also essential for myoblast fusion into myotubes and the production of new myofibres (Ahmad et al., 2020; Eugenis et al., 2021). When IGF-1 binds to its tyrosine kinase cell receptor (IGF1R), produces a transphosphorylation, which induces the coupling of the insulin receptor substrate 1 (IRS1). When IRS1 is

phosphorylated, it stimulates the **PI3K/Akt** pathway, which is related to muscle hypertrophy, cell proliferation and myoblast maturation to obtain new myofibres (Egerman & Glass, 2014; Mnatsakanyan et al., 2018; Ohashi et al., 2015). FGF-2 binds to its receptor FGF2R and activates different intracellular pathways: p38 α/ ß MAPK, PI3K/Akt and ERK/MAPK among others. p38 α/ ß MAPK stimulates both satellite cell activation and differentiation (Pawlikowski et al., 2017; Segalés et al., 2016); PI3K/Akt induces cell proliferation and myogenic differentiation (Mnatsakanyan et al., 2018), and ERK/MAPK promotes the cell cycle transition from cell growth (G1) to DNA replication (S1) (Pawlikowski et al., 2017).

Wnt7, hepatocyte growth factor (HGF) and nerve growth factor (NGF) are other growth factors with important roles in muscle development and regeneration, acting as signalling molecules that enhance satellite cells recruitment for muscle regeneration (Eugenis et al., 2021; Mnatsakanyan et al., 2018).

Nevertheless, the use of growth factors in regenerative medicine is quite controversial because they need supra-physiological dosages to be effective. This fact can result in several *off-target* effects and also increase tumour risk (Briquez et al., 2015; Mnatsakanyan et al., 2018; Simón-Yarza et al., 2012). An alternative to the use of growth factors might be the use of other bioactive elements, such as the called *therapeutic ions*. **Boron** (B), a metalloid essential for mammalian nutrition, growth and development has been used for different tissue engineering applications. Recent *in vitro* and *in vivo* studies have shown its potential in muscle tissue regeneration after boron receptor (NaBC1) activation and co-localization with fibronectin-binding integrins (Ciriza et al., 2021; Rico et al., 2015). **Zinc** (Zn), a transition metal and essential element which regulates different signalling and structural proteins in eukaryotic cells, has also proved to enhance *in vitro* myogenic proliferation and differentiation by stimulating the PI3K/Akt pathway through the zinc influx transporter (Zip7) (Briquez et al., 2015; Ohashi et al., 2015). Iron (Fe) is another transition metal with applicability in MTE, and also is widely used in imaging for *in vivo* monitoring techniques by magnetic resonance imaging after loading target cells with iron nanoparticles (Friedrich et al., 2021).

## 4.6. Biomaterials in skeletal muscle tissue engineering

The *National Institute of Biomedical Imaging and Bioengineering (NIBIB)* defines 'biomaterial' as any matter, surface or construct that interacts with biological systems (*https://www.nibib.nih.gov/science-education/glossary*). The scientific journal *Biomaterials* gives a more detailed biomedical definition: biomaterial is a substance that has been engineered to take a form which, alone or as a part of a complex system, is used to direct, by control of interactions with components of living systems, the course of any therapeutic/diagnostic procedure (*https://www.sciencedirect.com/journal/biomaterials*). Biomaterials need to perform their function without generating any toxic response in the host biological systems (biocompatibility) (Anderson, 2012). Moreover, most of them are biodegradable, naturally degraded by the biological machinery of living organisms into basic elements such as water, methane, carbon dioxide, etc. (Goswami & O'Haire, 2016).

Biomaterials are subdivided into ceramics, metals, polymers and/or composites formed by the combination of single biomaterials (Kulinets, 2015). Ceramics and metals are mainly employed in medical prostheses and dental implants, while polymers and

composites are essential in tissue engineering. Polymers are large chain molecules (macromolecules) composed of the union of multiple repeated units called monomers. Depending on its origin, there are synthetic and natural polymeric biomaterials.

**Natural polymers** are derived from structural components found in living systems, presenting inherent bioactivity and biocompatibility that induces cell response (Ullah & Chen, 2020). They are formed by polymeric chains of polysaccharides, proteins or polynucleotide subunits (Kulinets, 2015). Collagen, chitosan, alginate and keratin are among the most popular ones. Their properties can be modified depending on the tissue or application, but the possible modifications are lower than in synthetic polymers.

**Synthetic polymers** are those produced with specific structures and nanoscale topographies and are not naturally present in living organisms. They can be engineered and modified to match specific requirements depending on the application: degradation profile, mechanical properties, hydrophilicity, etc. Some of the most common synthetic biomaterials used in tissue engineering are polymers such as polylactic acid (PLA), polyethylene glycol (PEG), polycaprolactone (PCL) or polypropylene (PP). These biomaterials are easy to scale up, but their biocompatibility with cells and tissues might be lower compared to natural biomaterials, and sometimes they might present poor cell adhesion properties, needing functionalization with natural polymers or ECM proteins such as fibronectin, vitronectin or collagen (Carnes & Pins, 2020).

For MTE and other electrosensitive tissues, it is also noticeable the existence of different synthetic materials with conductive properties such as polypyrrole (PPy), polyaniline (PANI) or graphene (G) and their derivates, which can be combined with polymeric biomaterials to generate **electroactive composites** with enhanced biological response able to stimulate electro-sensitive cells growth, proliferation and differentiation. Further information on this aspect is provided in section 5.

Hydrophilicity is a property with a special interest in biomaterials and tissue engineering, which can be defined as the tendency of a molecule to be dissolved in water. There are natural and synthetic hydrophilic biomaterials based on polymers. Although hydrophilic polymers are soluble in water, different physicochemical reactions can produce interactions between their single chains, producing polymeric **hydrogels**. A hydrogel is a three-dimensional (3D) network of crosslinked polymeric chains able to retain large amounts of water without being dissolved (Ahmed, 2015). Depending on the manufacturing process, there are three main types of hydrogels (implantable, injectable or sprayable) with multiple industrial and biomedical applications: hemostatics, coatings, cosmetics, drug delivery, wound healing or tissue engineering (Correa et al., 2021).

In tissue engineering, though, hydrophilicity is related to low cell-biomaterial interactions. Highly hydrophilic surfaces hinder protein adsorption to the polymeric matrix, a key factor regulating cell attachment and behaviour (Rico et al., 2015; Ngandu Mpoyi et al., 2016). The combination of hydrophilic and hydrophobic polymers might result in novel composites, in the form of multipolymer networks (hydrogels), with moderate surface hydrophilicity, enhanced bioactive properties and broader ranges of applications in tissue engineering (Carnes & Pins, 2020).

There are two main types of multipolymer networks: i) **Interpenetrating polymer networks** (IPNs), defined as those polymeric blends comprising at least two crosslinked polymers entangled on a molecular scale but that are not bounded to each other by any

chemical bound, and ii) **Semi-interpenetrating polymer networks (semi-IPNs)**, a combination of at least one crosslinked polymer and one or more linear or branched polymers embedded within the matrix but not bounded to the crosslinked network, producing partial interlacing on the molecular scale. The difference between IPNs and semi-IPNs relies on that IPNs are comprised of different interwoven (but not bonded) networks that cannot be separated without breaking any chemical bond, while semi-IPNs contain networks and linear or branched polymers that can be effectively separated with no need of breaking chemical bonds (Aparicio-Collado et al., 2021).

In the next sections, different natural/synthetic biocompatible and biodegradable polymers with interesting properties in tissue engineering and especially SMTE are described. All of them have been approved by the *US Food and Drug Administration* (*FDA*) for their clinical use in humans and are employed in this Doctoral Thesis.

### 4.6.1. Polyhydroxyalkanoates

Polyhydroxyalkanoates (PHAs) are a family of natural aliphatic biopolyesters produced and stored by bacteria as an internal carbon and energy resource under nutrient-deprivation conditions. They show piezoelectric properties and present tuneable mechanical and thermal properties depending on the application. They also present moderate hydrophilicity, making them attractive materials for surface protein functionalization and cell adhesion (Aparicio-Collado et al., 2021; Pryadko et al., 2021).

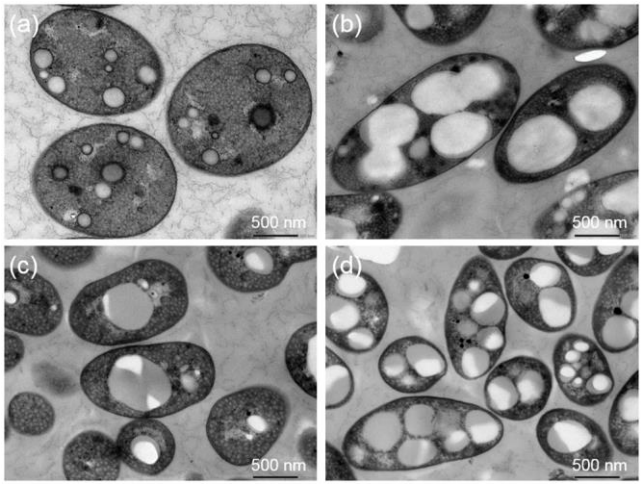


**Figure 6**. Different images taken with electron transmission microscopy (TEM) of PHA granules inside *Marichromatium bheemlicum* (**a**) and *Rhodovulum visakhpatnamense* (**b**,**c**,**d**) bacterial strains after cultivation with different nutrient-deficiency. Image from Higuchi-Takeuchi et al. (Higuchi-Takeuchi et al., 2016).

Within the PHAs family, only a few of them are commercially available at large-scale production: poly (hydroxubutyrate) (PHB), poly (3-hydroxybutyrate-co-3-hydroxuhexanoate) (PHBHHx) and poly (3-hydroxybutyrate-co-3-hydroxyvalerate) (PHBV). Although PHB is the most studied one, its poor mechanical properties, stiffness and brittleness limit its applications. **PHBV** presents improved mechanical properties than PHB (Young's Modulus between 1-5 GPa), being also tougher, more flexible and less stiff (Aparicio-Collado et al., 2021; Pryadko et al., 2021). Moreover, its physical and biological properties (mechanic behaviour, degradation, and cell attachment and growth)

can be modified by blending with other polymers or by the addition of nanoparticles such as carbon nanomaterials or ceramics (Hurtado et al., 2022; W. Li et al., 2014; Rivera-briso et al., 2022).

PHBV has been used in different biomedical areas varying from implants and biosensors to controlled drug delivery, stents, medical packaging and scaffolds for different tissue engineering applications (Rivera-Briso et al., 2022). In this regard, PHBV is traditionally used in bone tissue engineering alone or in combination with other polymers or bioactive molecules to develop cell constructs with different techniques such as electrospinning, microfluidics or solvent casting. Nevertheless, the state-of-the-art reveals that the application of PHBV in MTE is still to assess. Only a few studies have employed PHBV and other PHAs in muscle in cardiovascular tissue engineering, trying to develop fibres to mimic the fibres of the heart muscle or produce artificial blood vessels (Kaniuk & Stachewicz, 2021).

### 4.6.2. Polycaprolactone

Polycaprolactone (PCL) is a synthetic hydrophobic semi-crystalline and aliphatic polyester composed of repeated units of hexanoate. Its physicochemical properties depend on its molecular weight (from 530 to 630000 g/mol) and crystallinity (up to 69%). This polymer presents remarkable mechanical and thermal properties with relatively long degradation profiles. It is also easy to process and is soluble with various organic solvents and miscible with different polymers, increasing its range of applications (Labet & Thielemans, 2009; Mondal et al., 2016).

PCL has been widely employed in different tissue engineering areas: bone, cartilage, osteochondral, liver, skin cardiovascular and nerve tissue engineering. Each application requires specific properties and structure, but this is not an issue since PCL is easily processable according to the required function: high mechanical strength and slow degradation profiles for bone, high porosity and flexibility for cartilage, tubular conformation and flexibility for nerve or woven nanofibres for the heart (Siddiqui et al., 2018).

In MTE, electrospinning nanofibres are the most common way to process PCL, since differentiated myotubes and myofibres present tubular structures (see Figure 1) and the designed scaffold should promote cell guidance and alignment. PCL nanofibres with different properties and compositions have been used alone or in combination with other biomaterials and/or bioactive factors for muscle regeneration. For example, Perez-Puyana et al. managed to create an *ex vivo* skeletal tissue by combining PCL nanofibres with natural polymers gelatin and collagen. The addition of natural polymers resulted in lower-sized fibres and the consequent increase of the surface adhesion area and a decrease in the mechanical properties (Perez-Puyana et al., 2021). Drug-loaded PCL nanofibres containing 5-Aza cytidine for the upregulation of differentiated muscle genes produced by Fasolino and collaborators also enhanced the differentiation of human MSCs into myotubes (Fasolino et al., 2017). Another possibility in MTE tissues is the production of electroactive nanofibres to enhance tissue regeneration. Although it will be discussed later (section 5) an example of this approach was conducted by Chen et al., who engineered aligned PCL/PANI nanofibres and demonstrated its ability to induce myotube formation and maturation *in vitro* (M. C. Chen et al., 2013).

### 4.6.3. Poly (vinyl alcohol)

Poly (vinyl alcohol) (PVA) is a synthetic hydrophilic polymer made from vinyl acetate polymerization into poly (vinyl acetate) and posterior hydrolysis of the acetate groups. Its physicochemical properties can be modified according to the desired application by controlling the molecular weight and the partial hydrolysis of poly (vinyl acetate) in the synthesis procedure after free radical polymerization (Anuj Kumar & Han, 2017). High values of molecular weight and hydrolysis degree are related to increased viscosity, tensile strength and water resistance, while low values result in increased flexibility and water sensitivity (Thong et al., 2016).

PVA chains can be crosslinked chemically (e.g. glutaraldehyde), physically (freeze-thaw) or by high-energy irradiation to generate hydrogels. Like many synthetic hydrogels, PVA is a bio-inert polymer, which does not present cell interaction domains unless being functionalized or combined with other bioactive polymers. It has been used in different biomedical applications such as drug delivery, wound dressing, nerve tissue engineering, bone, nerve, cartilage and cardiovascular muscle tissue engineering (Curley et al., 2014; Gnanaprakasam et al., 2013; T. H. Kim et al., 2015).

### 4.6.4. Alginate

Alginate is one of the most popular polymers in tissue engineering. It is a natural linear anionic polysaccharide naturally found in cell walls of brown algae of the class *Phaeophyceae* providing flexibility and strength. It is also present in *Azotobacter vinelandii* and *Pseudomonas aeruginosa* bacterial strains forming a protection capsule which regulates biofilm development and bacterial adherence (Ahmad Raus et al., 2021; Serrano-Aroca et al., 2021). Its chemical structure consists of different combinations of arranged residues of 1,4-linked ß-D-mannuronic (M) acid and 1,4 α-L-guluronic acid (G). The disposition of the different M and G blocks and the physicochemical properties depend on the natural alginate resource. M blocks are responsible for the flexible and linear conformation, while G blocks correlate to the stiffness of the molecular chains (J. S. Yang et al., 2011). The molecular weight of alginate ranges between 32000 and 400000 g/mol, and it is related to the viscosity of the alginate solutions.

Since it is a hydrophilic polymer with functional $-COO^-$ and -COOH groups, alginate can be crosslinked to form hydrogels. The most common way is by ionic crosslinking with divalent cations such as calcium ($Ca^{2+}$) or sodium ($Na^{2+}$). At pH values lower than the disassociation $pK_a$ values of the uronic residues alginate can also form acid hydrogels by intermolecular hydrogen bonds (J. S. Yang et al., 2011). Covalent crosslinking by glutaraldehyde or adipic acid dihydrazine is another possibility to form alginate hydrogels (Serrano-Aroca et al., 2021).

The modifiable physicochemical properties, excellent biocompatibility and ability to form hydrogels and retain/deliver bioactive compounds have made alginate one of the most employed polymers in biomedical applications, alone or in combination with other polymers. Wound dressing is one clear example of alginate applicability. It keeps humidity at an optimal pH at the wound site, thus accelerating the healing process by keeping an hemostatic environment and facilitating debris removal. Kaltostat® is an example of an alginate-based gel commercialized for wound dressing (Ahmad Raus et al., 2021). Drug delivery is another area of application due to the possibility of

encapsulating bioactive molecules into alginate hydrogels within the gelation process. It has been used for the delivery of antibiotics into a wounded area, anticancer drugs, growth factors or even DNA transfection in combination with chitosan (Douglas et al., 2006).

Alginate is also extensively used to promote regeneration in different tissues: bone, cartilage, liver, cornea, nerve, heart and muscle. To repair skeletal muscle, the mechanical properties of alginate might not fit the biomechanical properties of muscle tissue *in vivo*. That is why alginate is combined with other polymers creating composites with enhanced mechanical features. Hualin Yi et al. developed alginate alginate/gelatin/heparin scaffolds where human skeletal muscle progenitor cells (hSMPCs) were able to grow and differentiate into mature myotubes (Yi et al., 2017). Furthermore, the bioactivity of alginate in terms of cell adhesion and proliferation is still unclear and, as in the case of PVA, different surface functionalization or combinations with other bioactive polymers are interesting approaches to increase its bioactivity. For example, a combination of sodium alginate (SA) with polycaprolactone (PCL) and conductive nanoparticles generated a novel biomaterial with enhanced mechanical, electrical and thermal properties that significantly enhanced cell adhesion and differentiation of murine C2C12 myoblasts into myotubes (Aparicio-Collado et al., 2022).

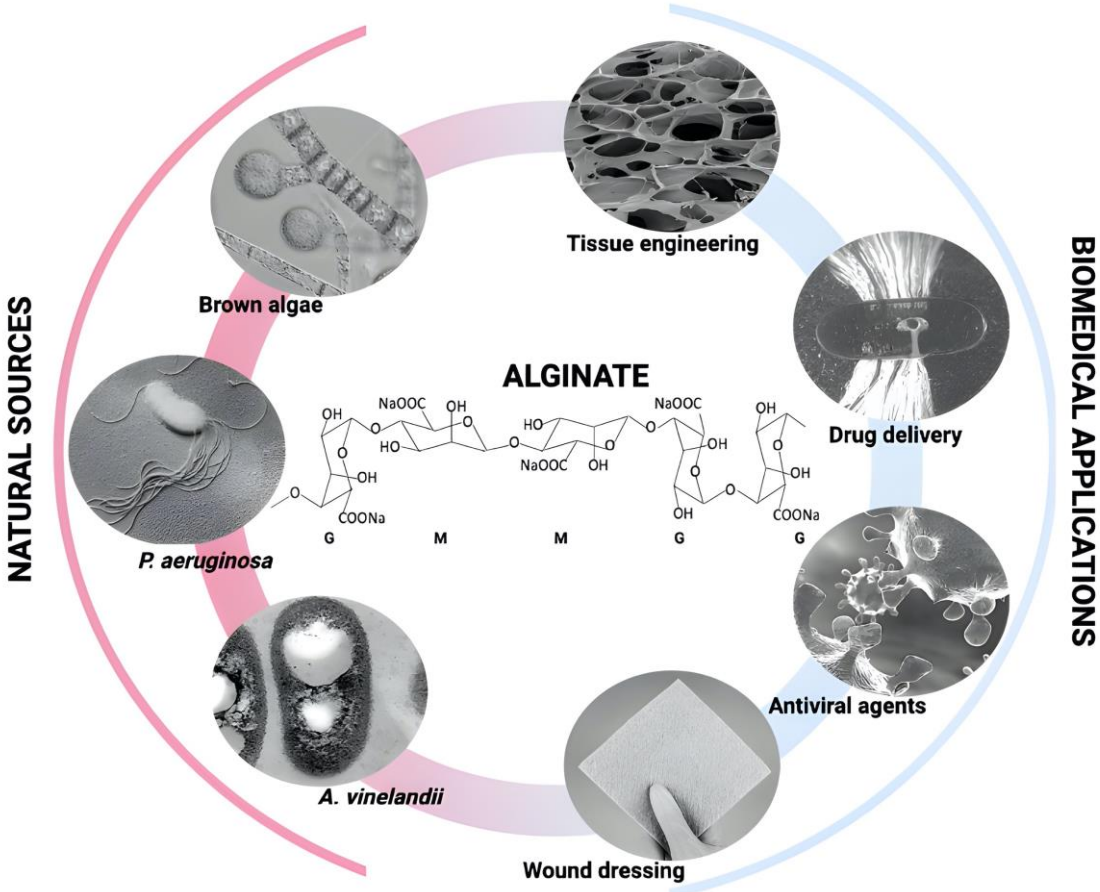


**Figure 7**. Schematic representation of alginate origin, structural conformation example (specific M/G blocks combination) and biomedical applications.

An ultimate promising application of alginate is its use as an antiviral agent. Different alginate compositions have shown antiviral activity against a broad range of viruses. For instance, alginate hydrogels were effective against different human viruses: herpes simplex virus type 1 and 2, influenza virus, hepatitis A, B and C, poliovirus type 1, rubella, etc. (Serrano-Aroca et al., 2021). SARS-CoV-2 pandemic has reactivated the focus on alginate as an antiviral agent and recently in 2022, A. Serrano-Aroca et al, showed the antiviral activity of calcium alginate hydrogels against the Delta variant of SARS-Cov-2 virus. The mechanism of this antiviral activity may rely on the negative alginate charges that bind to the virus envelope inactivating its membrane receptors (Cano-Vicent et al., 2022).

## 5. Conductive biomaterials for muscle tissue engineering

One of the unique properties of muscle tissues is their contractile activity to generate force and movement. This contraction is created in response to electrical signals from the nervous system (Dong et al., 2020). In this sense, the **muscle tissue is electrosensitive**, as it is bone, cardiovascular and neural tissues. Thus, an interesting approach to treating muscle regeneration in MTE is the development of **electrically conductive biomaterials** able to stimulate electrosensitive muscle cells in a similar way to native tissue and induce its proliferation and myogenic differentiation. It has been reported that conductive materials can stimulate the regeneration of electrosensitive tissues even without external electrical stimulation (J. L. Aparicio-Collado et al., 2022; J. Kim et al., 2019; H. S. Yang et al., 2016). Recommended conductivity values of electroactive materials for musculoskeletal tissue engineering are between 0,8 ~ 4,5 mS/m , range of values for human muscle tissue (C. Yu et al., 2022).

There are three main types of conductive biomaterials for muscle tissue engineering, which can be classified in conductive polymers, carbon nanomaterials and metal nanomaterials (Dong et al., 2020).

### 5.1. Conductive polymers

Conductive polymers (CPs) are synthetic polymers with unique properties such as electrical and optical activity similar to metals and semiconductors. They can be easily synthesized, and their surface can be chemically modified with bioactive species to enhance their biocompatibility and increase their feasibility to be used in biomedical applications, such as drug delivery, tissue engineering, neural probes, etc. (Kaur et al., 2015). CPs can be chemically or electrochemically synthesized.

Chemical synthesis offers different possibilities for synthesis and modifications of the CPs backbone although it is a complex technique. It can be performed by additive polymerization or condensation polymerization and it is easier to scale up. Electrochemical synthesis is currently the most common method for obtaining CPs (Kaur et al., 2015). It consists of applying positive potential or current to oxidize the monomer and allow the growth of the polymer at the anode in a simultaneous reaction with the insertion of dopant anions. This technique also allows the doping and embedding of bioactive molecules (Gvozdenović et al., 2014). However, the main drawbacks of CPs are their non-biodegradability and difficulty to process. These issues limit their application in biomedicine, so a solution might be its use at very low concentrations in

combination with other natural or synthetic polymers widely used in the biomedical field, such as alginate, chitosan, or polycaprolactone, among others. (Dong et al., 2020).

The most common conductive polymers used in tissue engineering applications are **polypyrrole** (PPy), polytiophene (PT) and polyaniline (PANI**).** PPy is one of the most investigated CP for tissue engineering due to its high electrical conductivity (up to 100 mS/m) and ease of synthesis by pyrrole oxidation, surface modification and scalability. It is crystalline, brittle, insoluble, and presents excellent mechanical properties (Kaur et al., 2015). Numerous studies have shown the effectivity of conductive biomaterials incorporating PPy for electrosensitive tissues regeneration, even without electrical stimulation: nerve tissue engineering (M. Patel et al., 2020; Vijayavenkataraman et al., 2019), bone tissue engineering (Maharjan et al., 2020; Sajesh et al., 2013) and cardiac tissue engineering (Liang & Goh, 2020).

In MTE, Gilmore et al. investigated whether flat PPy substrates doped with different compounds could promote C2C12 myoblast adhesion, proliferation and differentiation. While substrates with hyaluronic acid promoted cell proliferation but did not significantly enhance myotube formation, PPy films with dextran sulphate or dodecyl benzene sulphonic acid promoted cell adhesion, proliferation and differentiation (Gilmore et al., 2009). Moreover, other studies reported nanofibres engineered from a copolymer combination of PCL with different amounts of PPy for application in MTE (Browe & Freeman, 2019). The results showed an enhancement in terms of C2C12 cell adhesion and differentiation in PCL-PPy copolymer nanofibres compared to pure PCL, whereas there were no significant differences between the different PPy concentrations in the copolymer. It was suggested that electrical conductivity might not be the only key factor to induce myogenesis, but also the chemical and structural modifications as a consequence of PPy incorporation into polymeric scaffolds might play a relevant role. These results support the idea that conductive biomaterials with incorporated CPs enhance muscle regeneration even without external electrical stimulation.

## 5.2. Carbon nanomaterials

Carbon can be considered one of the most important chemical elements in life. It is the basis for life in nature, being present in every structure and living organism. **Carbon-based nanomaterials** (CBNs) are exciting materials for the scientific field due to their excellent properties, such as high electrical and thermal conductivity, flexibility, high surface area, and remarkable mechanical and optical properties. The capability to organize its four valence electrons in different hybridization stages (sp, sp2 and sp3) enable carbon to form structures with different bonds and allotropic conformations (mainly diamond and graphite) and thus generate different carbon-based structures: nanotubes, fibres, fullerenes, nanodiamonds or graphene nanosheets. This variety of structures leads to a full display of applications employing carbon-based nanomaterials (CBNs): electronics, environmental remediation, water treatments, bioimaging, electrochemical sensing, magnetic resonance, etc (Speranza, 2021). Recently, CBNs have also demonstrated their great potential for applications in the biomedical field for controlled drug delivery and especially in tissue engineering. For these kinds of applications, CBNs are used at low concentrations and in combination with polymeric matrices to enhance their conductivity and mechanical properties while avoiding cytotoxicity and biodegradability issues. **Carbon nanotubes (CNTs) and graphene (G)** are the most widely used CBNs in this field of research.

CNTs are highly hydrophobic cylindrical structures consisting of condensed benzene rings of carbon atoms which can be classified into single-walled CNTs (hollow cylindric structures with 1 atom thickness) or multi-walled CNTs (different multi-layers of CNTs surrounding a central CNT). Their remarkable mechanical properties, electrical conductivity and high thermal conductivity make CNTs very useful in biomedical applications, especially in tissue engineering for electrosensitive tissues (B. Huang, 2020; Z. Huang et al., 2020; Velasco-Mallorquí et al., 2020).

**Graphene** is a 2D polycyclic aromatic sp2 hydrocarbon presenting a typical nanosheet structure with a lateral size between 0,5-5 μm, firstly isolated from 3D graphite (Dong et al., 2020). Among its physicochemical properties, its high electrical conductivity (about $10^7$ mS/m), excellent mechanical properties and topographic roughness make graphene a reference material in tissue engineering (Bellet et al., 2021a). Nevertheless, the poor solubility and dispersibility limit graphene applications in this field. Alternatively, different strategies have been performed to obtain graphene derivates keeping the properties of pristine graphene but adopting functionalized surfaces with different oxygen functional groups to avoid the aggregation and low solubility. These derivates are typically named graphene-based materials (GBMs): graphene oxide (GO), reduced graphene oxide (rGO) and graphene quantum dots (GQDs). They are differently synthesized and possess different properties and applications (Smith et al., 2019). GO is typically obtained after oxidation and exfoliation of pristine graphite and presents an sp2 and sp3 altered carbon structure with different oxygen groups (hydroxyl, carbonyl, carboxylic acid, etc). This characteristic structure improves its solubility and enables surface modification with bioactive compounds. A further thermal treatment or chemical reduction can deplete most of the sp3 carbon and oxygen groups to generate rGO, with different properties and structure than pristine graphene, but even with high electric conductivity (Bellet et al., 2021a; Smith et al., 2019). Further processing of GO and rGO derive on GQDs (Tian et al., 2018).

GBMs are widely used for different biomedical applications: drug delivery carriers, gene therapy, biosensing, bioimaging, etc. Furthermore, they also find their application in tissue engineering, especially when combined with natural and/or synthetic polymers to generate biodegradable and non-cytotoxic nanocomposites. Some examples of GMBs in muscle tissue engineering are the use of graphene in combination with chitosan, gellan or PCL to induce myofibre formation, GO films to induce skeletal muscle differentiation (Lee et al., 2021) or semi-IPNs of alginate/polycaprolactone and rGO as electroactive substrates to induce musculoskeletal regeneration (J. L. Aparicio-Collado et al., 2022).

## 5.3. Metal nanomaterials

Gold (Au), silver (Ag) and copper (Cu) are among the most common nanometals in tissue engineering. They present remarkable biocompatibility, porosity and ability to be loaded with different drugs or bioactive factors for different applications. Moreover, they are easy to modify and adapt into different structures such as nanoparticles, nanotubes, nanowires or nanofibres. Nanoparticles have been of great interest in different biomedical areas ranging between drug delivery, tumour therapy, energy storage and tissue engineering. Recent studies showed that nanoparticles are can penetrate cell cytoplasm and produce mechanical stimulation of different biochemical routes and signalling pathways. Among them, the p38 α MAPK intracellular pathway is highly related

to the conversion of mechanic stimuli into biochemical cues (Ashok Kumar et al., 2002). Gold nanoparticles have been approved by the FDA for their use in patients and have already proved to enhance bone regeneration and differentiation of MSCs by stimulating the mechanosensitive p38 MAPK signalling pathway (Changqing et al., 2010). In skeletal muscle, single gold nanoparticles and combinations of gold-silver nanoparticles have been shown to enhance both *in vitro* and *in vivo* myogenic differentiation in a mechanism by which nanoparticles enter the cell cytoplasm and mechanically stimulate the p38 α MAPK pathway (Ge et al., 2018).

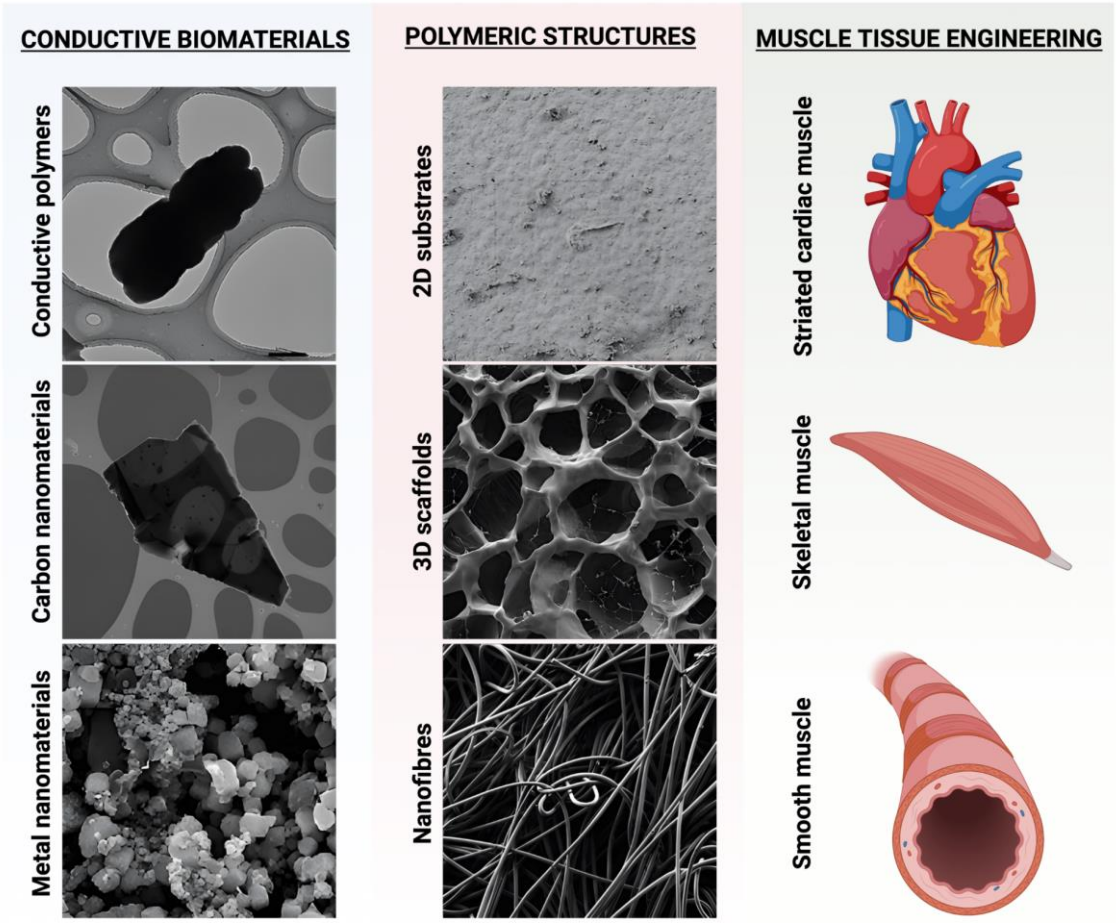


**Figure 8**. Representation of the different conductive biomaterials and their applications in muscle tissue engineering. Conductive polymers, carbon nanomaterials and metal nanomaterials are usually combined with polymeric constructs to generate novel electroactive composites with different structures, mainly 2D, 3D and electrospun nanofibres, etc. *Image created with BioRender.*

Thus, it can be concluded that muscle regeneration is a complex and hierarchically organized process able to recover muscle functionality after injury, but its regenerative potential is impaired in volumetric muscle loss, representing an open challenge to be addressed in the biomedical field. Muscle tissue engineering aims to restore, improve or keep muscle activity by generating functional biocompatible constructs combining biomaterials, cells and bioactive factors, which simulate the *in vivo* like tissue microenvironment where cells can attach, grow and differentiate into mature and functional muscle myofibres. Moreover, in the context of electro-sensitive tissues, such as skeletal muscle, conductive biomaterials represent a promising approach to generating novel polymeric composites with electroactive properties able to induce muscle regeneration even without electrical stimulation. The development of conductive

scaffolds and their combination with cells and bioactive molecules to assess their performance in terms of myogenic differentiation remains an exciting research opportunity to be further explored.

# Hypothesis and objectives

## 1. Hypothesis

The endogenous regenerative potential of skeletal muscle is controlled by satellite cells in a coordinated process involving different cells and biomolecules. In small-scale injuries, the musculoskeletal system is capable of activating its internal regeneration process and restoring muscle functionality. Nevertheless, in the case of considerable volumetric muscle loss (VML) after surgery, sports injuries or traumatic events such as military or traffic accidents, the innervation and vascularization are ablated. Therefore, the ability to activate different biochemical cues, muscle cells and growth factors in the injury zone to enable auto-regeneration is limited. Impaired muscle regeneration usually derives on necrosis, fibrosis, inflammation and functionality loss. Autologous muscle flap is the most common treatment for VML, as it restores at least partial functionality in the injury zone. However, this is a complex process requiring very expertise and quite commonly derive on infections, amputations, donor site morbidity or questionable effectivity. Hence, there is a clear clinical need in the treatment of VML.

Muscle tissue engineering represents a promising novel treatment for these muscle injuries. It aims to avoid scar tissue formation and enable regeneration by developing artificial muscle grafts generating an artificial microenvironment mimicking the *in vivo* conditions to guide muscle regeneration. This strategy requires biomaterial scaffolds with specific physicochemical features combined with cells and bioactive molecules. Its main goal is to generate an *in vitro*, *in vivo* or *in situ* biocompatible engineered muscle graft that will help to regenerate the damaged muscle.

Several biomimetic scaffolds have been developed for muscle tissue engineering in the last few years. Conductive biomaterials are of special interest in electrosensitive tissues such as skeletal muscle, as they enhance regeneration even without electrical stimulation. In addition, it has been reported different bioactive molecules with proven regenerative potential used in combination with conductive biomaterials and cells. Nevertheless, there is no evidence in the literature of specific combinations of conducting biomaterials as cell substrates together with zinc ions as a bioactive factor to evaluate its potential application in muscle tissue engineering.

In this Doctoral Thesis, it is hypothesized that the development of electroactive biomaterials based on different combinations of hydrophilic/hydrophobic polymers (semi-IPNs) with different conductive nanoparticles will produce novel cell substrates with electrical conductivity able to induce myogenic differentiation. Moreover, the combination of conductive cell substrates with extracellular zinc ions as bioactive molecules might produce promyogenic environments with a synergistic effect of electroactive surface-bioactive molecules in terms of *in vitro* myogenic differentiation, providing new promising insights to enhance muscle regeneration.

## 2. Objectives

To address the hypothesis, the main objective of this thesis is the development of novel conductive biomaterials, which will provide an electroactive cellular microenvironment that will promote myogenic differentiation *in vitro*. To meet this goal, different electroactive biomaterials with a semi-IPN structure or highly conductive single polymeric surfaces will be engineered based on biodegradable natural and synthetic polymers (PHBV, PVA, SA, PCL) with incorporated conductive nanoparticles based on conductive polymers (PPy nanoparticles) and carbon nanomaterials (G and rGO nanosheets). The physicochemical and morphological properties of the cell substrates will be analysed and the biological performance in terms of *in vitro* myoblast adhesion, proliferation and differentiation will be evaluated. In addition, the study of possible synergies between electrically conductive surfaces and therapeutic ions (particularly $Zn^{2+}$) as bioactive factors will be evaluated on the myogenic response by combining an electroactive PCL/G surface with a specific concentration of extracellular zinc ions to generate promyogenic environments.

To achieve the main objective, the next specific objectives have been carried out:

**I.** Design and development of novel electroactive biomaterials with different structures and compositions as cell substrates: semi-IPNs based on PHBV/PVA/PPy and SA/PCL/rGO, and conductive surfaces based on PCL/G nanocomposites.

**II.** Physicochemical characterization of the developed biomaterials.

**III.** Biological evaluation for skeletal muscle regeneration (with C2C12 murine cell line): biocompatibility (cytotoxicity assay), adhesion, proliferation and differentiation onto the PHBV/PVA/PPy, SA/PCL/rGO and PCL/G materials. Study of a possible correlation between nanoparticle content and biological performance.

**IV.** Combination of an electroactive surface (PCL/G nanocomposite) with extracellular zinc ions. Analysis of possible synergistic effects of a conductive interface cell-material combined with zinc ions on myoblast adhesion, proliferation and differentiation (using C2C12 cell line).

# Chapter 1

# Novel semi-interpenetrated polymer networks of poly(3-hydroxybutyrate-co-3-hydroxyvalerate)/poly (vinyl alcohol) with incorporated conductive polypyrrole nanoparticles

Chapter published in ***Polymers*** (excluding sections 2.6 and 3.5 regarding cell culture and biological evaluation)

José Luís Aparicio-Collado, Juan José Novoa, José Molina-Mateo, Constantino Torregrosa-Cabanilles, Ángel Serrano-Aroca, Roser Sabater i Serra. Novel semi-interpenetrated polymer networks of poly(3-hydroxybutyrate-co-3-hydroxyvalerate)/poly (vinyl alcohol) with incorporated conductive polypyrrole nanoparticles. *Polymers* 2021, 13, 57. DOI: 10.3390/polym13010057.

**Personal contributions**

Materials' synthesis was developed by J. L. Aparicio-Collado and J.J. Novoa. Morphological analysis, thermal properties, wettability, contact angle and spectroscopy were performed by J. L. Aparicio-Collado. Conductivity measurements were carried out at Biomaterials and Bioengineering Lab (Univeridad Católica de Valencia) by Á. Serrano-Aroca.

J. L. Aparicio-Collado wrote the first version of the manuscript. J. Molina-Mateo, C. Torregrosa-Cabanilles, Á. Serrano-Aroca and R. Sabater i Serra contributed in experimental conceptualization, manuscript revision and funding acquisition.

# Novel semi-interpenetrated polymer networks of poly(3-hydroxybutyrate-co-3-hydroxyvalerate)/poly (vinyl alcohol) with incorporated conductive polypyrrole nanoparticles

José Luis Aparicio-Collado [1], Juan José Novoa [2], José Molina-Mateo [1], Constantino Torregrosa-Cabanilles [1], Ángel Serrano-Aroca [3] and Roser Sabater i Serra [1,4]

[1]Centre for Biomaterials and Tissue Engineering, Universitat Politècnica de València, Spain

[2]University of Applied Sciences Technikum Wien, Vienna, Austria.

[3]Biomaterials and Bioengineering Lab, Centro de Investigación Traslacional San Alberto Magno, Universidad Católica de Valencia San Vicente Mártir, Valencia, Spain

[4]Biomedical Research Networking Centre in Bioengenieering, Biomaterials and Nanomedicine (CIBER-BBN), Spain

## Abstract

This paper reports the preparation and characterization of semi-interpenetrating polymer networks (semi-IPN) of poly(3-hydroxybutirate-co-3-hydroxyvalerate), PHBV, and poly (vinyl alcohol), PVA, with conductive polypyrrole (PPy) nanoparticles. Stable hybrid semi-IPN (PHBV/PVA 30/70 ratio) hydrogels were produced by solvent casting, dissolving each polymer in chloroform and 1-methyl-2-pyrrolidone respectively, and subsequent glutaraldehyde crosslinking of the PVA chains. The microstructure and physical properties of this novel polymeric system were analysed, including thermal behaviour and degradation, water sorption, wettability and electrical conductivity. The conductivity of these advanced networks rose significantly at higher PPy nanoparticles content. FTIR and calorimetry characterization indicated good miscibility and compatibility between all the constituents, with no phase separation and strong interactions between phases. A single glass transition was observed between those of pure PHBV and PVA, although PVA was dominant in its contribution to the glass transition process. Incorporating PPy nanoparticles significantly reduced the hydrogel swelling, even at low concentrations, indicating molecular interactions between the PPy nanoparticles and the hydrogel matrix. The PHBV/PVA semi-IPN showed higher thermal stability than the neat polymers and PHBV/PVA blend, which also remained in the tertiary systems.

**Keywords:** nanocomposite, semi-interpenetrating network, hydrogel, electroactive biomaterial, conductive polymer, poly (3-hydroxybutyrate-co-3-hydroxyvalerate), poly (vinyl alcohol), polypyrrole nanoparticles, tissue engineering.

## 1. Introduction

Polyhydroxyalkanoates (PHA) are a family of biodegradable aliphatic polyesters synthesised by bacteria and archaea as an intracellular carbon and energy storage compound (Anjum et al., 2016). The PHA copolymer poly (3-hydroxybutyrate-*co*-3-hydroxyvalerate) (PHBV) has emerged as a promising material for biomedical applications, due to its null cytotoxicity and its current large-scale production (Chang et al., 2014; Guo-Qiang & Qiong, 2005; L. Wang et al., 2013). PHBV's biocompatibility and biodegradability render it an excellent biomaterial with a wide range of applications in the fields of cardiovascular stents (Smith, J. R., & Lamprou, 2014), controlled drug release (Riekes et al., 2013), absorbable surgical sutures (Wu et al.,2013), tissue patches, biodegradable implants, and tissue engineering scaffolds (Hutmacher, 2000). It has also been proposed as a 'green' dielectric material (lead- and halogen-free) for capacitors in a wide range of applications, such as electric power circuits for implantable medical devices (Y. Yang et al., 2012). As a hydrophobic polymer, PHBV possess outstanding mechanical properties with a Young's modulus of about 1-5 GPa (Mohan & Nair, 2008). However, despite the excellent properties of PHBV, its biomedical use is still limited due to its lack of water sorption, brittleness and low thermal stability (Rivera-Briso et al., 2019; Rivera-Briso & Serrano-Aroca, 2018).

On the other hand, hydrophilic polymers networks, commonly known as hydrogels, are particularly useful and advantageous materials due to their capacity of being able to absorb and retain large amounts of water within their polymer network without being dissolved in aqueous solutions (Ahmed, 2015; Y. Li et al., 2012). These water sorption properties have made these three dimensional networks very promising biomaterials for a wide range of applications, such as drug delivery, tissue engineering (Keengwe & Onchwari, 2015) and wound dressing (Simões et al., 2018). More specifically, injectable hydrogels have been used in bone tissue engineering as carriers for bioactive factors, such as growth factors, that will be released after the hydrogel degradation (Zhu et al., 2020). The hydrophilic polymer poly (vinyl alcohol) (PVA) has been extensively studied in biomedicine applications due to its excellent water sorption properties, biocompatibility and biodegradability (T. H. Kim et al., 2015; X. Wang et al., 2010). PVA can be crosslinked by multiple methods, ranging from chemical agents like glutaraldehyde (GA) and other monoaldehydes to electron beams, gamma-irradiation or physical crosslinking due to crystallite formation (Hassan & Peppas, 2000). PVA hydrogels have been widely used in tissue engineering (Anuj Kumar & Han, 2017): neurogenesis and osteogenesis promotion (T. H. Kim et al., 2015), cardio myoblasts culture (Gnanaprakasam et al., 2013) and fibroblasts culture for knee implants (Curley et al., 2014). However, like most hydrogels, the mechanical properties of PVA are poor.

Multipolymer networks, also known as hybrid networks, such as semi-interpenetrating polymer networks (semi-IPNs), interpenetrating polymer networks (IPNs) and the so-called 'double networks' (DN), with a particular IPN structure, have emerged as an effective alternative to overcome the limitations of pure polymers (Dragan, 2014; Mishra et al., 2006). In this regard, semi-IPNs and IPNs can lead to reinforced interwoven polymer networks. An IPN can be defined as a polymeric matrix comprising two crosslinked networks interlaced on a molecular scale, whilst a semi-IPN is a matrix comprising only one crosslinked network, in which the linear or blanched polymer

penetrates the network on a molecular scale, i.e., the linear or branched macromolecules are dispersed into the polymer network (Zoratto & Matricardi, 2018). Mechanically enhanced DNs, characterized by good mechanical properties, are formed by a first densely cross-linked ionic hydrogel and a neutral loosely cross-linked network (Dragan, 2014). These DN hydrogels are composed of crosslinked polymers without covalent bonds between the polymer networks. Nevertheless, at least one of these polymer networks is synthesized and/or crosslinked within the presence of the second network (Merlin & Sivasankar, 2009; M. Wang et al., 2004).

These hybrid structures combine the advantageous properties of each polymeric component leading to a new material with properties that may be different from those of the pure components (Zoratto & Matricardi, 2018) (J. Zhang et al., 2009). Depending on the nature of the constituent polymers, the combination of synthetic and natural polymers, with hydrophobic and hydrophilic properties, can result in a broader range of properties and applications (Matricardi et al., 2013) (Mishra et al., 2006).

Hydrogel properties can be effectively modified by preparing hybrid networks (IPNs or semi-IPNs) due to their having better properties in a blend that those of their individual components (Dragan, 2014; Mishra et al., 2006). In aqueous environments, hydrogels formed by a crosslinked hydrophilic polymer with chains of a hydrophobic polymer dispersed into the network (i.e. a semi-IPN hydrogel) can be an interesting approach to combine the properties of both components. The hydrogel provides hydration while preventing dissolution of the hydrophilic polymer and the hydrophobic polymer provides improved physical properties. Semi-IPNs hydrogels synthetised from biocompatible polyurethane and acrylamide monomer (Merlin & Sivasankar, 2009), PVA with poly(caprolactone) (Mohan & Nair, 2008) or with poly(acrylamide-co-styrene) (A. K. Bajpai et al., 2003) with enhanced physical and biological properties have been reported for biomedical applications (particularly tissue engineering and drug release). However, no semi-IPNs of PHBV/PVA have been reported in the literature so far.

Conductive polymers (CPs) include a family of polymers with a mixture of the properties of metals (ability to conduct electrical charges) and conventional polymers (ease of synthesis and processing) (Balint et al., 2014). Conductive and semiconductive polymers, either alone or in combination with other polymers, have recently attracted growing interest in the field of biomedicine and regenerative medicine, particularly as cell substrates for cell culture with or without external electrical stimulation or conducting polymer-based biosensors (Dong et al., 2020; Waleed et al., 2020). Several studies have shown that cell substrates with conductive (or electroactive) properties can enhance bioactivity, promoting cell response in terms of proliferation and differentiation (J. Chen et al., 2018; Jun et al., 2009). Recently, electroactive composite scaffolds have been prepared to control the release of osteoinductive factors by external electrostimulation (Cui et al., 2020). In addition, infection produced by microbes have become a social problem due to the rise of antibiotic-resistant microorganisms (Frieria et al., 2017). Novel antimicrobial agents, among them conducting polymers, have been applied as a new tool to address this problem (F. A. G. Da Silva et al., 2016).

Conductive polymers such as polypyrrole (PPy), polyaniline and the family of polythiophene polymers have been reported for biomedical applications, both as bioactive and biocide agents (Guarino et al., 2016; Talikowska et al., 2019). PPy is a polymer with good electrical conductivity, insoluble in water, with proven *in vitro* and *in*

*vivo* biocompatibility (Guarino et al., 2016) and antimicrobial activity (F. A. G. Da Silva et al., 2016). However, problems related to their poor solubility and non-degradability can limit their use. One way to overcome these problems is the preparation of materials from blends and composites based on CPs and degradable polymers: such as PHBV, poly(caprolactone), polylactic acid, gelatin, or collagen (Balint et al., 2014; B Guo et al., 2012; Baolin Guo et al., 2013; Hardy et al., 2013; Nair et al., 2015), or also grafts, such as PPy grafted with oligo-3-hydroxybutyrate pendants reported in refs. (A. Domagala et al., 2014; Anna Domagala et al., 2016).

In this study, we explore the preparation and characterization of reinforced semi-IPN hydrogels based on PHBV/PVA with incorporated conductive nanoparticles of PPy with the aim of obtaining novel polymeric biomaterials with intrinsic bioactive and antimicrobial properties for potential application in the field of tissue engineering. The semi-IPN was prepared with the hydrophobic PHBV and the hydrophilic PVA in 30/70 ratio in order to provide structural reinforcement while preserving the major characteristics of hydrogels. To increase blend compatibility and simultaneously avoid PVA dissolution when the substrates are introduced into aqueous environments (such as a culture medium), PVA was chemically crosslinked with GA to form an insoluble 3D network, in which the PHVB chains were entwined within the PVA network. Neat PVA, PHBV and a 30/70 PHBV/PVA blend were also prepared as control materials. Since these semi-IPN networks lack conductive properties, the strategy of introducing conductive PPy nanoparticles is proposed here. Several PPy nanoparticles (diameter 300-500 nm) contents, ranging from 0 to 15% wt/wt, were incorporated into the substrates. The morphology and physicochemical properties (swelling, wettability and thermal behaviour/degradation) of these novel semi-IPN hydrogels were determined in this study. Semi-IPNs filled with conductive PPy nanoparticles were also analysed in terms of their microstructural properties and electrical behaviour.

## 2. Materials and methods

### 2.1. Materials

Poly (3-hydroxybutirate-*co*-3-hydroxyvalerate), PHBV, with 2% wt of 3-hydroxyvalerate (Mw 410,000 g/mol) was supplied by Goodfellow (UK), product code BV336010. Poly (vinyl alcohol), PVA, (Mw 13,000-23,000, 87-89% hydrolyzed, product code 363170), polypyrrole nanoparticles (PPy) doped with an organic sulfonic acid as dopant (conductivity 10-50 $*10^3$ mS/m and stable up to 290 ºC, product code 577030) and 1-metil-2-pyrrolidone (NMP) were purchased from Sigma Aldrich-Merck (USA). PVA with a low molecular weight was selected because it biodegrades faster (Matsumura et al., 1993). However, PVA with lower molecular weight exhibits lower mechanical performance (Ngadiman et al., 2015). Thus, since the mechanical properties and thermal stability of PHBV increases rapidly with molecular weight (Luo et al., 2002) we selected a PHBV with a high molecular weight to enhance the physical properties of PVA. Chloroform (99-99.6% pure), glutaraldehyde (GA) solution 25 wt. % in H2O, methanol and sulfuric acid (95-98% extra pure) and acetic acid glacial (99% extra pure) were supplied by Scharlab (Spain). All reagents were used as received.

### 2.2. Preparation of neat polymers and 30/70 PHBV/PVA blend films

PHBV, PVA and 30/70 PHBV/PVA blend films were prepared by solvent casting. PHBV was dissolved in chloroform (3% wt/wt) at 50ºC with constant stirring for 120 minutes. PVA was dissolved in NMP (5% wt/wt), also with constant stirring for 120 minutes, gradually raising the heating plate temperature from 25ºC to 150ºC. After complete dissolution, the neat polymer solutions were poured into petri dishes. Polymer films were obtained after solvent evaporation at room temperature for 24h (neat PHBV) and in an air oven at 60 ºC for 72h (PVA). PHBV/PVA blends were prepared by mixing PHBV/chloroform and PVA/NMP solutions (30/70 wt/wt ratio) with magnetic stirring for 24h at 50 ºC. The mixed solution was poured into a Petri dish and PHBV/PVA films were obtained after 24h of chloroform evaporation at room temperature followed by 72h in an air oven at 80 ºC to evaporate NMP. All the prepared films were dried at 60 ºC under vacuum to constant weight to completely remove all traces of solvent. The thickness of the samples (≈ 300 µ) was measured by a digital caliper (Acha, Spain).

### 2.3. Preparation of PHBV/PVA semi-IPN (PVA crosslinking)

PVA was crosslinked to achieve aqueous stability, forming a semi-IPN hydrogel with (uncrosslinked) PHBV. The crosslinking of the PVA phase in the semi-IPN was performed according to the procedure reported by Rudra et al. (Rudra et al., 2015), using GA as crosslinker (4% wt/wt GA with respect of the total PVA content). To accelerate the rate of the crosslinking reaction, sulfuric acid as catalyst, methanol as a quencher and acetic acid as pH controller were used. Four aqueous solutions were prepared: solution 1 with 25% GA (crosslinker) as a crosslinking solution, solution 2 with 10% sulfuric acid, solution 3 with 10% acetic acid and solution 4 with 50% methanol. These reagent solutions were mixed in a 2:1:3:2 volumetric ratio and then transferred to the mixed PHBV/chloroform and PVA/NMP solution with vigorous stirring. Using the same procedure as that used for 30/70 PHBV/PVA blends; the mixed solution was casted and left for 24h at room temperature to evaporate chloroform followed by 72h in an air-oven at 80º to completely evaporate NMP. The crosslinked films were then immersed twice in Milli-Q water at 37º C (24 hours) to remove any GA residue and left 48 h at room temperature to evaporate water. Finally, the semi-IPN films were dried at 60 ºC under vacuum to constant weight to remove residual moisture.

### 2.4. Electroconductive particles embedding

Four different concentrations of PPy (2, 5, 10 and 15% wt/wt based on the mass of the polymeric matrix) were introduced in the 30/70 PHBV/PVA matrix. First, PPy particles were dispersed in NMP solvent by sonication for 30 minutes, after which PVA was dissolved in the NMP-PPy suspension, and the PHBV/PVA/PPy semi-IPN films were prepared following the protocols described in Sections 2.2 and 2.3.

The notation and sample compositions are included in Table 1.

**Table 1.** Sample notation

| Identification | Sample description |
|---|---|
| PHBV | 100% PHBV |
| PVA | 100% PVA |
| PVA E | 100% crosslinked PVA |
| PHBV/PVA | 30% PHBV / 70% PVA blends |
| PHBV/PVA E | 30% PHBV / 70% PVA semi-IPN |
| PPy | PPy nanoparticles |
| PHBV/PVA E2 | 30% PHBV / 70% PVA semi-IPN with 2% PPy |
| PHBV/PVA E5 | 30% PHBV / 70% PVA semi-IPN with 5% PPy |
| PHBV/PVA E10 | 30% PHBV / 70% PVA semi-IPN with 10% PPy |
| PHBV/PVA E15 | 30% PHBV / 70% PVA semi-IPN with 15% PPy |

## 2.5. Characterisation technique

### 2.5.1. Electron microscopy

The surface and cross-section morphology of the samples were analysed in a GeminiSEM 500 High Resolution Field Emission Scanning Electron Microscope (HR-FESEM) (Carl Zeiss Microscopy, Jena, Germany) with an accelerating voltage of 0.8-1.0 kV. The samples were coated with a platinum layer by an EM MED020 sputter coater (Leica, Wetzlar, Germany). The cross-section was observed in samples previously immersed in liquid $N_2$ and cryofractured. The morphology of PPy nanoparticles was observed by HR-FESEM and TEM (transmission electron microscope JEM 2100F operated at 200 kV, JEOL, Tokyo, Japan). Previously, the nanoparticles were dispersed in an ultrasound bath for 1h. One drop was then placed on a SEM sample holder and carbon-coated TEM grid for 2h to ensure complete drying. An estimation of the size distribution of PPy nanoparticles was obtained from HR-FESEM micrographs with ImageJ software. The diameter of about 100 PPy nanoparticles (only those that show clear spherical shape) was measured to obtain the average diameter and its diameters' distribution.

### 2.5.2. Fourier Transformed Infrared Spectroscopy (FTIR)

Functional groups in the systems were determined by FTIR (Bruker Optics FTIR Alpha II). Samples underwent 24 scans at room temperature, and FTIR spectra were collected in transmittance mode from 4000 to 400 $cm^{-1}$ at a resolution of 2 $cm^{-1}$.

### 2.5.3. Swelling assay

Swelling experiments were performed gravimetrically in crosslinked samples: PHBV/PVA E and semi-IPNs with 2, 5, 10 and 15% of PPy nanoparticles with PVA E as reference. Square samples (10x10 mm and thickness ≈ 300 μm) were vacuum-dried at 60 ºC and immersed in Milli-Q water at 37 ºC until equilibrium. Redundant surface water was removed by filter paper. Experiments were performed in triplicate to ensure reproducibility.

Samples were weighed before ($W_0$) and after ($W_1$) swelling and the swelling degree ($W_{eq}$) was calculated as:

$$W_{eq}(\%) = \frac{W_1 - W_0}{W_0} \cdot 100 \quad (1)$$

### 2.5.4. Surface wettability

The surface wettability was determined by water contact angle (WCA) on the surface of films (thickness ≈ 300 μm) using the sessile drop method. Hydrophobic PHBV, hydrophilic PVA (non-crosslinked and crosslinked) were used as reference. 30/70 PHBV/PVA blend and semi-IPNs with and without PPy nanoparticles were analysed. To measure the contact angles, a 3 μL Milli-Q water drop was deposited onto the surface and stabilization was allowed (~10 s) at room temperature. WCA was measured by using an optical contact angle and contour analysis system (Dataphysics OCA 20, North Carolina, USA). All measurements were performed in triplicate.

### 2.5.5. Differential Scanning Calorimetry (DSC)

DSC analysis was carried out on a PerkinElmer DSC 8000 (PekinElmer, Massachusetts, USA) under a flowing nitrogen atmosphere (20 mL/min). After erasing the effects of any previous thermal history by heating at 220 ºC, the samples were subjected to a cooling scan down to −20 ºC, followed by a heating scan from this temperature to 220 ºC, both at 20 ºC/min. The glass transition temperature, $T_g$, was calculated from the heating scan as the inflexion point of the specific heat capacity, $C_p$, vs. temperature, which coincides with a maximum in the temperature derivative ($dc_p/dT$). The width of the glass transition, $\Delta T_g$, was obtained by the intersections of the tangent line at the inflexion point with the extrapolated glass and liquid lines. Finally, the specific heat capacity increment at the measured glass transition, $\Delta c_p(T_g)$, was determined as the difference in heat capacity between the extrapolated liquid and glass lines at $T_g$.

### 2.5.6. Thermogravimetric Analysis (TGA)

TGA was used to study the thermal decomposition of each sample related to gradual temperature increases. Vacuum-dried samples (5-10 mg weight) were heated from 30 to 600ºC at a rate of 10ºC/min in a Mettler Toledo TGA 2 (SF) system (Mettler Toledo, Ohio, USA). The mass of the samples was constantly measured as a function of temperature.

### 2.5.7. Conductivity Analysis

The electrical sheet resistance ($R_S$) of circular film samples of approximately 10 mm diameter was measured on a T2001A3-EU four-point probe system-EU plug (Ossila Limited, Sheffield, UK). The electrical conductivity ($\sigma$) in S/m was calculated according to the following formula:

$$\sigma = \frac{1}{R_S \times l} \quad (2)$$

Where *l* is the film thickness, which was measured by a digital calliper (Acha, Spain). The measurements were performed in triplicate in order to ensure reproducibility.

## 2.6. Cell culture and biological evaluation

The biological assessment of the engineered biomaterials was carried out with C2C12 murine myoblasts (Sigma Aldrich; Merck), a common cell line employed as a musculoskeletal cell model. Briefly, C2C12 were grown for expansion in high glucose Dulbeco's Modified Eagle's Medium (DMEM, Biowest) supplemented with 10% fetal bovine serum (FBS, ThermoFisher) and 1% Penicillin/Streptomycin (P/S, ThermoFisher) in a humidified atmosphere at 37 ºC and 5% $CO_2$. Cells were passaged during amplification at maximum 80% confluence.

### 2.6.1. Cytotoxicity

An indirect MTT assay was used to evaluate the materials' biocompatibility, adapting the ISO/EN10993 standard to evaluate *in vitro* toxicity of novel biomaterials. The protocol is based on the reduction of MTT (3-[4, 5-dimethylthiazol-2-yl]-2, 5 diphenyl tetrazolium bromide) by viable and metabolically active cells into formazan crystals in an enzymatic NADPH-dehydrogenases dependent reaction. The formazan crystals can be solubilized and quantified by measuring the absorbance at 570 nm, which is directly related to cell viability.

Prior to the assay, samples (150 µm thickness) were sterilized by autoclave (121º, 20 minutes) and left overnight incubating with growth medium (DMEM + 10% FBS + 1% P/S) with a material/medium ratio of 2,5 $cm^2$/mL to generate the medium extracts. Simultaneously, C2C12 cells were seeded in 96-well plates with 100 µL of growth medium ($10^4$ cells/well) and left incubating overnight at 37º and 5% $CO_2$. Then, medium was replaced by 100 µL of the medium extracts generated after the materials incubation and left incubating during 24 and 48 h. A negative control (C2C12 cells cultured with growth medium) and positive control (C2C12 cells incubated with natural rubber latex cytotoxic extract) were used to compare sample's viability.

After 24 and 48 h, supernatant was replaced by 100 µL of new growth medium without phenol red containing a 1:10 MTT dilution (Sigma Aldrich; Merck) and cells were left incubating for 4 h to allow MTT metabolization into formazan. Then, the medium was removed and 100 µL of solubilization buffer (10% SDS in 0.01 M HCl) (Sigma Aldrich; Merck) was added and left overnight at 37ºC to dissolve the formazan crystals. The next day, optical density was measured by a microplate reader (Victor Multilabel Plate Reader, Perkin Elmer) at 570 nm wavelength. Cell viability was calculated as:

$$Viability\ (\%) = \frac{OD\ test}{OD\ control} \cdot 100 \quad (3)$$

where *OD test* is the optical density of the sample and *OD control* is the optical density of the negative control.

### 2.6.2. Cell adhesion

A cell adhesion study was carried out to test the materials' feasibility to allow cell attachment and growth. Prior to cell culture, materials (3,8 $cm^2$ area) were functionalized with an overnight incubation in growth medium to allow typical serum proteins to adsorb to the materials' surface and allow the subsequent cell attachment. The next day, C2C12 cells were seeded onto the materials at a 5000 cells/$cm^2$ density with growth medium

and after 24 h of culture, the samples were rinsed with Dulbecco's phosphate-buffered saline (DPBS) and fixed with a 4% paraformaldehyde solution (1 h at room temperature). Samples were then permeabilized with 0.5% Triton-X-100/DPBS, blocked with 5% horse serum (HS) in DPBS (1 h, 37ºC) and stained with fluorescent Phalloidin (dil:1:100, Invitrogen/ThermoFisher A12379). Finally, samples were mounted in Vectashield mounting media (Palex Medical) and observed through a fluorescence microscope. Image quantification of cell areas (actin cytoskeleton stained with phalloidin) was performed on ImageJ software.

### 2.7. Statistical analysis

Statistical analyses were performed on swelling degree assay, static contact angle measurements and electric conductivity by one-way ANOVA tests on all samples using GraphPad Prism 6.0 software. Data were presented as mean ± standard deviation. If significant differences were noted between the samples, Tukey tests were used for pairwise comparisons with a 95% confidence interval ($p<0.05$).

## 3. Results and discussion

To obtain this novel hydrogel with improved structural enhancement, the semi-IPN PHBV/PVA was prepared with 30% of PHBV and 70% of PVA and subsequent crosslinking of PVA with GA. This ratio, with a high percentage of the hydrophilic polymer, was chosen to achieve the mechanical reinforcement provided by the hydrophobic PHBV but maintaining the water absorption capacity characteristic of hydrogels. As will be shown in this section, this ratio allowed obtaining a hybrid network with hydrogel characteristics. In PHBV/PVA blends with PVA percentage lower than 70%, the PVA crosslinking was not completely effective and the samples were partially dissolved after immersion in water.

### 3.1. Microstructure and Fourier Transform Infrared Spectroscopy

Figure 1 shows the HR-FESEM images of the surface and cross-section (from cryogenic fracture) of the PHBV/PVA semi-IPN hydrogels. A homogeneous structure can be seen in both the surface and cross-section (Figure 1a and 1b). The cross-section had some areas with a brittle fracture and few threads were identified between the brittle areas, as reported for semicrystalline polymers (Diani & Gall, 2012). Figure 1c and 1d present HR-FESEM and TEM images, respectively, of the PPy nanoparticles as received. The PPy nanoparticles show a rod-like morphology (see the TEM image), with an average diameter of 480 nm (in agreement with previous results (A. B. Da Silva et al., 2018)). The diameter distribution of the nanoparticles is shown in the inset of Figure 1c.

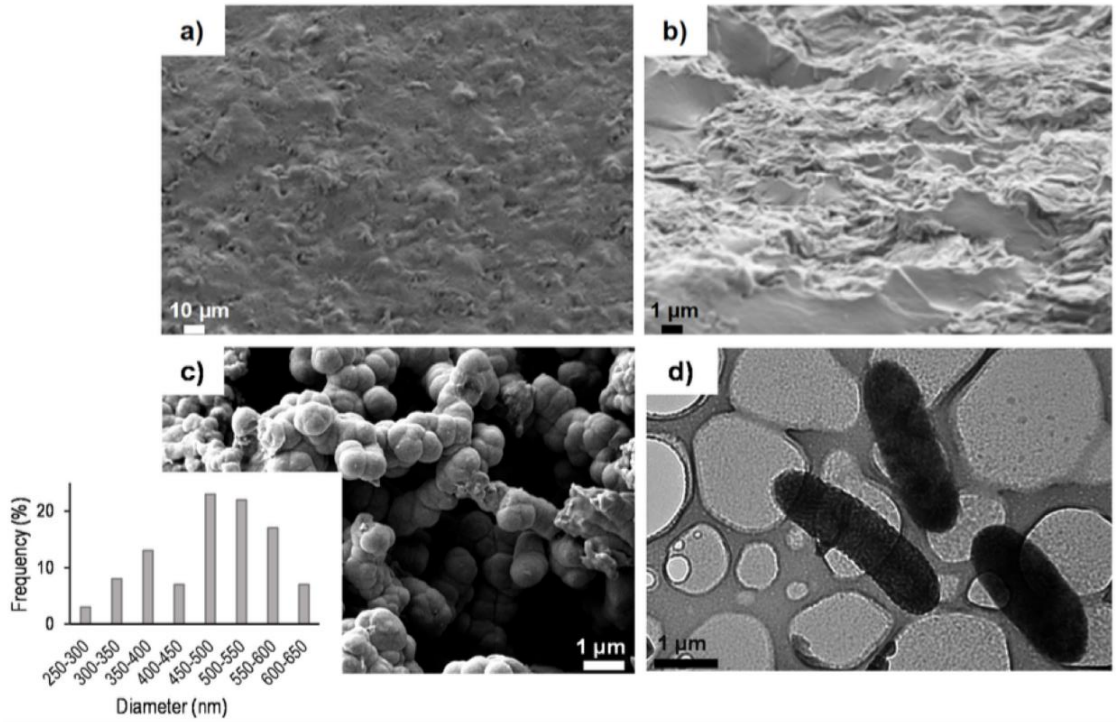


**Figure 1**. High-resolution field-emission scanning electron microscope (HR-FESEM) photomicrographs of semi-interpenetrating polymer network (IPN) poly (3-hydroxybutyrate-co-3-hydroxyvalerate) / poly (vinyl alcohol) (PHBV/PVA E). **a)** Surface and **(b)** cross-section. **(c)** HR-FESEM and **(d)** transmission electron microscope (TEM) photomicrographs of polypyrrole (PPy) nanoparticles. Inset in (c) shows diameter's distribution.

The images from the surface and cross-section of the PVBV/PVA semi-IPN samples with different percentages of PPy nanoparticles are included in Figure 2. The photomicrographs show that the surface morphology changes slightly after the addition of PPy nanoparticles. As the nanoparticle load content rises, the surface roughness increases progressively (Figure 2a, 2c and 2e, with 2, 10 and 15% of PPy nanoparticles respectively), although the nanocomposite surface appears fully covered by the polymer matrix. In Figure 2b and 2d, showing the cross-section of the semi-IPN after adding 2 and 10% of PPy nanoparticles, the nanoparticles can be seen tightly embedded in the polymer matrix (see the arrows), forming a uniform structure. However, in the composite with the highest PPy nanoparticle content (15%) the particles tended to form aggregates with some voids (Figure 2f and 2g), suggesting the need for a stronger PPy dispersion mixing at high PPy nanoparticle contents.

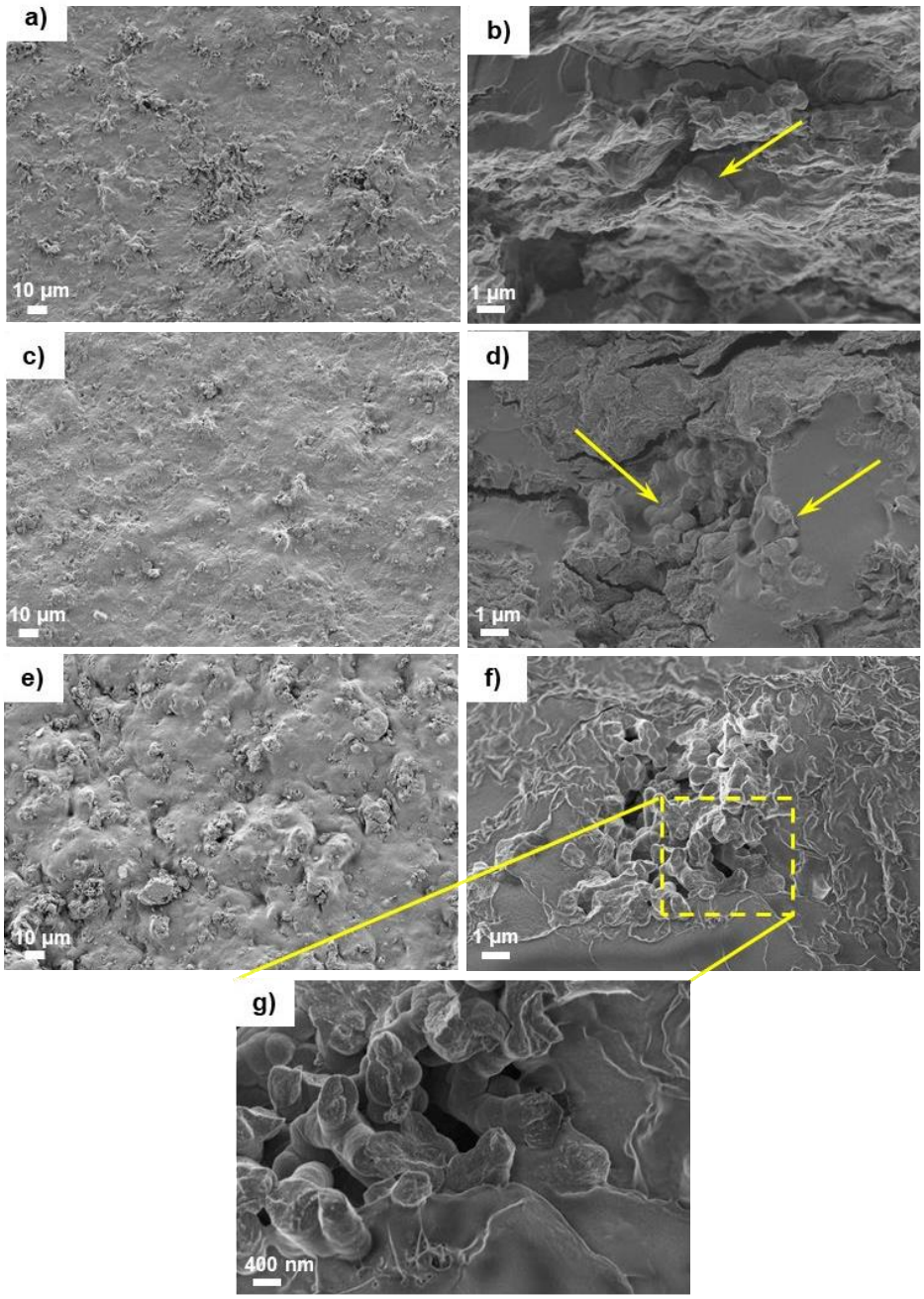


**Figure 2.** HR-FESEM photomicrographs of surface and impact fracture of semi-IPN PHBV/PVA with different percentage of PPy nanoparticles: (**a**) Surface of PHBV/PVA E2 composite; (**b**) Cross-section of PHBV/PVA E2 composite; (**c**) Surface of PHBV/PVA E10 composite; (**d**) Cross-section of PHBV/PVA E10 composite; (**e**) Surface of PHBV/PVA E15 composite; (**f**) Cross-section of PHBV/PVA E15 composite; (**g**) PPy nanoparticles embedded within the PHBV/PVA E15 composite in the cross-section at higher magnification. Arrows in b) and d) indicate PPy nanoparticles embedded in the matrix.

FTIR spectra of PHBV/PVA and the semi-IPN PHBV/PVA are shown for comparison in Figure 3 together with neat PVA, PVA crosslinked with GA and PHBV as reference.

For neat PVA, the spectrum reveals the major vibrational peaks associated with poly (vinyl alcohol). The large bands between wavenumbers 3600 and 3200 $cm^{-1}$ represent the stretching of OH groups due to the inter and intramolecular hydrogen bonds (H-bonds). The vibrational band between 2840 and 3000 $cm^{-1}$ is related to the stretching of the C-H bond in the alkyl group and the band between 1750-1735 $cm^{-1}$ is related to C=O

stretch. PVA crosslinking is produced by the formation of acetal bridges between the hydroxyl groups in PVA and the difunctional aldehyde molecule of GA (Mansur et al., 2008). After crosslinking PVA with GA, it was verified the reduction of the relative intensity of the O-H bands (3600-3200 $cm^{-1}$), which evidence that the reaction of the PVA with GA has occurred by forming acetal bonds (Mansur et al., 2004, 2008; Rudra et al., 2015). The PHBV spectrum shows a band at 1719 $cm^{-1}$, related to the C=O stretch of the ester group present in the molecular chain of highly ordered crystalline structure. The peaks between 800 and 1050 $cm^{-1}$ are characteristic of the -C-O-C- stretching vibration (Fei et al., 2003; Paşcu et al., 2013).

The spectrum of the PHBV/PVA blend shows the characteristic peaks related to both PVA and PHBV, confirming their presence in the blend. A reduction of the intensity of the O-H bands between 3600-3200 $cm^{-1}$ can be observed in the semi-IPN PHBV/PVA obtained after crosslinking the PVA chains, which is indicative of the reduced number of the hydroxyl groups after the crosslinking reaction and the formation of the acetal bonds.

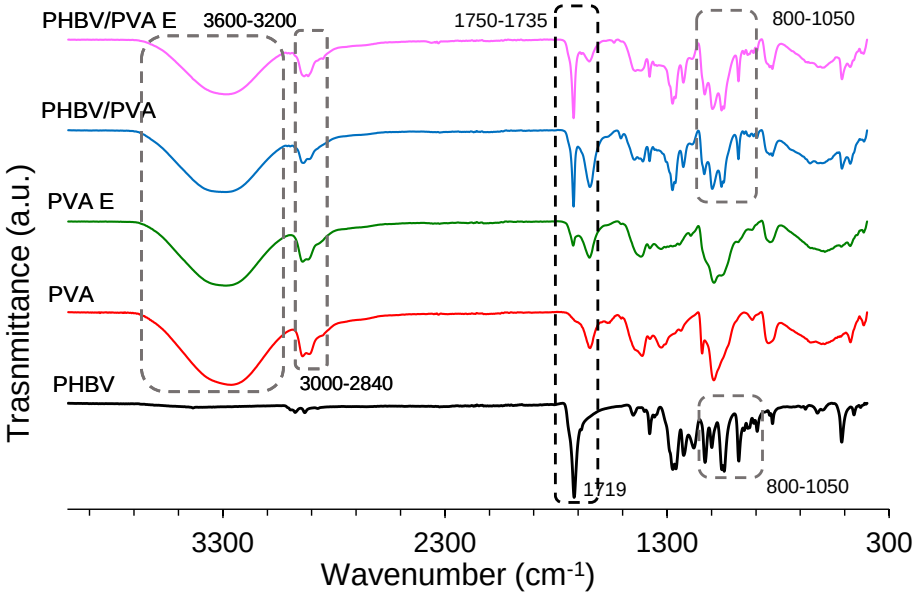


**Figure 3.** FTIR spectra in the region of 4000-300 $cm^{-1}$. PHBV, PVA, PHBV/PVA, PVA E and semi-IPN PHBV/PVA E.

The FTIR spectra of the composites after adding the PPy nanoparticles are depicted in Figure 4. The PPy particles show a peak at 1548 $cm^{-1}$ due to the C=C stretching. The peak at 1100 $cm^{-1}$ is related to C-C stretching and the peaks between 780 and 1050 $cm^{-1}$ (dotted box) are associated with the torsion of the polypyrrole's aromatic rings (Chougule et al., 2011; Håkansson et al., 2006; Yussuf et al., 2018). The composites revealed all the common peaks of the PHBV/PVA semi-IPN. The effect of the PPy nanoparticles in the PHBV/PVA network is more evident in composites with a concentration of 10% or higher, where the characteristic PPy peaks at 1100, 1548 $cm^{-1}$ and the band between 780-1050 $cm^{-1}$ can be identified. It can also be observed a slight reduction of the intensity of this band as the percentage of nanoparticles increases. This behaviour suggests the presence of hydrogen bonding between the polymer matrix and the PPy nanoparticles.

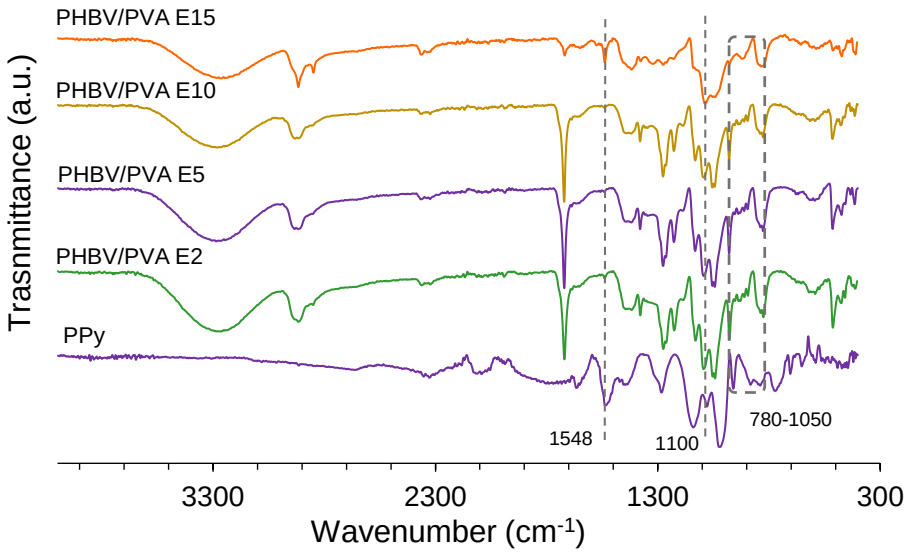


**Figure 4.** FTIR spectra in the region of 4000-300 $cm^{-1}$. PHBV/PVA E with different percentages of PPy nanoparticles (2, 5, 10 and 15% referred to the mass sample).

### 3.2. Swelling properties and surface wettability

The swelling degree of the crosslinked samples is depicted in Figure 5. Crosslinked PVA shows the highest swelling degree (560% of its initial weight) due to the well-known hydrophilic nature of PVA (Gaaz et al., 2015). Conversely, PHBV is a hydrophobic polymer, able to reduce the swelling ratio of pure hydrogels (Q. Zhang et al., 2009). As expected, PHBV/PVA semi-IPN, with 30% of PHBV, shows a swelling degree ca. 400%, a value significantly lower than the crosslinked PVA. Adding PPy nanoparticles reduces the swelling degree in all the composites. Increasing the percentage of nanoparticles reduces the swelling degree monotonically, with significant differences with respect to the semi-IPN without nanoparticle at 5% or higher PPy concentrations. These results suggest that in addition to the PPy's hydrophobic nature, PPy nanoparticles, embedded within the PHBV/PVA E matrix, entangle with PVA chains by hydrogen bonding (H-bonding) (Ding et al., 2018), forming a more compact structure with reduced swelling capacity (H. Takahashi et al., 2012). This behaviour could be associated with the slight reduction of the band related to -OH bonds (3600-3200 $cm^{-1}$) observed in the FTIR spectra when increasing the percentage of PPy nanoparticles (Figure 4). It is also worth noting that after the addition of the PPy nanoparticles, although the swelling capacity decreases, even in the semi-IPN with 15% nanoparticles, the swelling capacity is above 150%, which indicates that the nanocomposites retain the water absorption capacity, preserving their hydrogel properties.

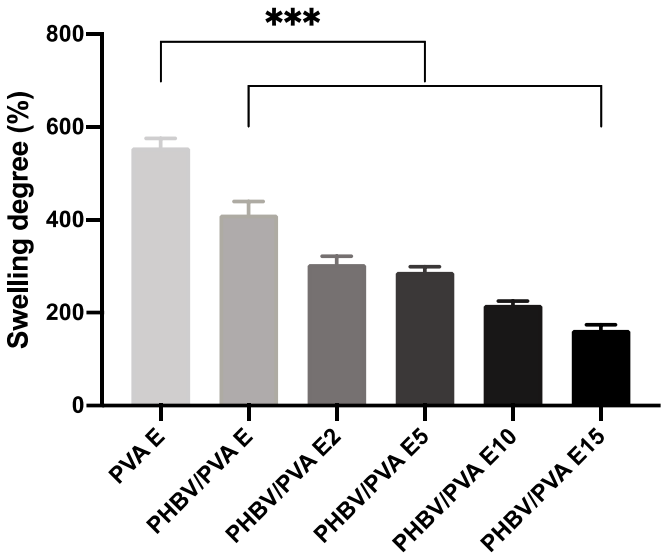


**Figure 5.** Swelling degree in equilibrium for PHBV/PVA E with different percentages of PPy nanoparticles ranging from 0 to 15 wt/wt %. PVA E is included as reference. Statistically significant differences ($p < 0.05$) are represented as (*).

The surface wettability, obtained from static water contact angle measurements, is included in Table 2. Contact angle of PHBV (~ 103º) and PVA with (~ 71º) are included as reference. The 30/70 PHBV PVA blend shows an increase in the contact angle, consistent with the presence of the hydrophobic chains of PHBV. As expected, crosslinking PVA increase the contact angle, for both neat PVA and the blend PHBV/PVA.

**Table 2.** Water contact angle measurement of PHBV/PVA blend, semi-IPN and composites with different percentages of PPy nanoparticles. PHBV and PVA (with and without crosslinking) are included as reference.

| **Sample** | **Contact angle** (º) |
|---|---|
| PHBV | 103.2±8.7 (◊) |
| PVA | 70.8±5.1 (*) |
| PVA E | 83.3±2.0 (*) |
| PHBV/PVA | 74.7±3.1 (**)(◊) |
| PHBV/PVA E | 93.5±6.3 (**)(♦)(◊) |
| PHBV/PVA E2 | 96.3±2.7 |
| PHBV/PVA E5 | 100.1±5.9 |
| PHBV/PVA E10 | 103.3±2.7 (♦) |
| PHBV/PVA E15 | 109.7±2.7 (♦) |

(*)(**)(♦)(◊) Significant differences ($p<0.05$) between samples

The incorporation of the PPy nanoparticles modifies the surface wettability. The contact angle increases with the percentage of nanoparticles, which have a hydrophobic nature. Compared to the semi-IPN without nanoparticles, the nanocomposites have a rougher surface (Figure 2) which may also slightly increase the WCA. These results are in good agreement with the swelling assay; the swelling degree decreases in the nanocomposites with incorporated PPy nanoparticles, which in turn present higher values of WCA.

## 3.3. Thermal properties

Differential scanning calorimetry and thermogravimetry were used to get further insight into the thermal behaviour and degradation of the PHBV/PVA/PPy system.

### 3.3.1 Differential Scanning Calorimetry (DSC)

#### 3.3.1.1. PHBV/PVA blends and semi-IPN PHBV/PVA

Among other different characterization techniques, DSC is one of the most widely used to determine miscibility of polymer blends and obtain further information on the molecular structure by studying the phase transformations. It is well established that two polymers are compatible with each other if they show a single glass transition temperature, $T_g$, intermediate between the glass transition temperatures of both polymers. Figure 6 shows the DSC scan (cooling and heating) of PHBV/PVA, PVA E and PHBV/PVA E samples in which PVA was crosslinked forming a network and a semi- IPN network respectively, together with the control polymers (neat PHBV and PVA).

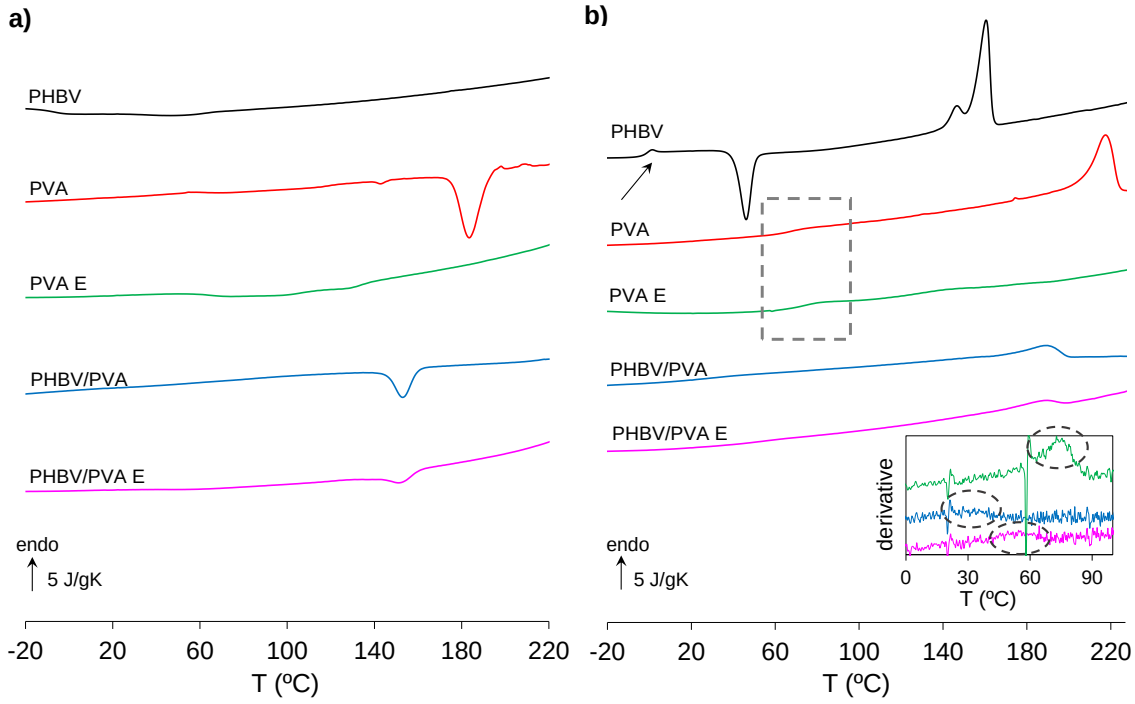


**Figure 6**. DSC thermograms at a rate of 20 ºC/min of neat PHBV and PVA, PHBV/PVA blend and PHBV/PVA E. (**a**) Normalized heat flow ($c_p$) on cooling. (**b**) Normalized heat flow ($c_p$) on heating. Arrows and rectangle mark the glass transition process. The inset shows the temperature derivative of the heat capacity from 0 to 100 ºC ($dc_p/dT$). The arrow and dotted area in b) and the inset indicate the glass transition process.

The glass transition and melting and crystallization processes can be observed in the thermograms. The 30/70 PHBV/PVA blend shows only one single $T_g$ (see the inset of Figure 6, where the inflexion point related to the glass transition is transformed into a maximum in the derivative) positioned in between the $T_g$ of the neat polymers (Table 3) showing the blends' good compatibility and miscibility. The experimental values of $T_g$, $\Delta c_{pi}$ and $\Delta T_g$, obtained from the heating scan (Figure 6b), are enlisted in Table 3.

**Table 3.** Glass transition temperature ($T_g$), width of the glass transition ($\Delta T_g$), heat capacity increment at the glass transition ($\Delta C_p$), crystallization ($T_c$) and melting ($T_m$) temperature, enthalpy of fusion ($\Delta H_f$), degree of crystallinity PHBV ($X_c$ *PHBV*) and PVA ($X_c$ *PVA*) and 50% weight loss decomposition temperature ($T_{d\text{-}50\%}$) for neat PHBV and PVA, crosslinked PVA, PHBV/PVA blend and semi-IPN PHBV/PVA.

| Sample | $T_g$ (ºC) | $\Delta T_g$ (ºC) | $\Delta C_p$ (J/g ºC) | $T_c$ (ºC) | $T_m$ (ºC) | $\Delta H_f$ (J/g) | $X_c$ PHBV | $X_c$ PVA | $T_{d\text{-}50\%}$ (ºC) |
|---|---|---|---|---|---|---|---|---|---|
| PHBV | 0.77 | 3.67 | 0.5 | 46.7(*) | 160.5 | 73.5 | 0.56 | - | 276.1 |
| PVA | 69.2 | 13.2 | 0.55 | 183.5 | 217.5 | 64.4 | - | 0.44 | 286.8 |
| PVA E | 74 | 36 | 2.05 | - | - | - | - | - | 386.9 |
| PHBV/PVA | 32.8 | 33.3 | 0.54 | 154 | 192.4 | 17.3 | - | 0.16 | 315.8 |
| PHBV/PVA E | 49.2(**) | - | - | 151.5 | 188.2 | 11.2 | - | 0.09 | 359.2 |

(*) Cold crystallization
(**) Obtained from the derivative curve ($dc_p/dT$ *vs.* $T$)

The Couchman and Karasz (CK) equation is a thermodynamic approach for predicting the glass transition temperature of blends (Couchman, 1978):

$$T_g = \frac{\omega_1 \Delta c_{p1} T_{g1} + \omega_2 \Delta c_{p2} T_{g2}}{\omega_1 \Delta c_{p1} + \omega_2 \Delta c_{p2}} \quad (3)$$

where $T_g$ is the glass transition of the blend, $\omega_i$ is the weight fraction of the component *i* and $\Delta c_{pi}$ is the specific heat capacity increment at the glass transition.

The $T_g$ obtained from the PHBV/PVA blend according to CK prediction is 48.5 ºC, which differs from that obtained experimentally (32.8 ºC), suggesting interactions between the components in the blend not considered in Eq. (3). It is therefore, more appropriate to consider the Kwei equation (Kwei, 1994):

$$T_g = \frac{\omega_1 T_{g1} + k\omega_2 T_{g2}}{\omega_1 + k\omega_2} + q\omega_1\omega_2 \quad (4)$$

where the parameter *k* can be obtained as the quotient between $\Delta c_{p2}$ and $\Delta c_{p1}$ and is related to the unequal contribution of each component in the mixture to the final $T_g$. The term $q\omega_1\omega_2$ represents the deviation of the glass transition temperature of the mixture from the linear weighted average of $T_{g1}$ and $T_{g2}$ and account for strong specific interactions within the mixture. The parameter *q* is used to model the effect of interaction between the components, such as H-bonding (Lin et al., 1989).

The value of $k$ = 1.1, obtained from the Kwei equation (Eq. 4) for the PHBV/PVA blend, suggests that PVA is dominant in its contribution to the $T_g$ in the mixture. The Kwei equation provides a good fit of the experimental value of $T_g$ with $q$ = -81.905. As indicated previously, $q$ is related to the strength of specific interactions, reflecting the balance between the breakdown of self-association and formation of inter-associations between the two components. The negative $q$ obtained indicates that the breaking of self-association (such as H-bonding between PVA molecules) reduces the $T_g$ more than the formation of H-bonds between PHBV and PVA can increase it (Weng et al., 2014).

PVA was chemically crosslinked to achieve aqueous stability and avoid the dissolution of the hydrophilic component in the blend, leading to a semi-IPN structure. As expected, $T_g$ increases in the crosslinked PVA sample (PVA E), from 69.2 to 74 ºC, because of the reduced mobility of the chains imposed by the crosslinking. In the PHBV/PVA semi-IPN

the glass transition process is difficult to detect, although it can be identified (as a maximum) in the derivative curves ($dc_p/dT$ vs. $T$) depicted in the inset of Figure 6b in the heating scan. The $T_g$ increases considerably with respect to the PHVB/PVA blend (from 32.8 to 49 ºC), in a similar way as the crosslinked PVA (PVA E sample), whose $T_g$ increases from 69.2 to 74 ºC. In the semi-IPN, both, the restricted of mobility in the PVA chains imposed by the crosslinking and the more rigid environment that surrounds the PHBV chains produced by the PVA network lead to a significant increase in the $T_g$. (Table 3).

Both PHBV and PVA are semicrystalline polymers. The thermograms depicted in Figure 6a show that neat PHBV exhibits no crystallization in the cooling ramp, but an exotherm crystallization (cold crystallization process) can be observed during heating (46.7 ºC), followed by melting (189.6 ºC) (Figure 6b). Neat PVA shows a crystallization process and subsequent melting in the cooling and heating ramp at 183.5 ºC and 217.5 ºC, respectively. The degree of crystallinity of neat polymers was estimated by using Equation (5).

$$X_c = \frac{\Delta H_f}{\Delta H_f^0} \tag{5}$$

Where $\Delta H_f$ is the enthalpy of fusion of the samples and $\Delta H_f^0$ the enthalpy of fusion of the totally crystalline PHBV and PVA. Considering $\Delta H_{PVA}^0$= 158 J/g (Enayati et al., 2016) and $\Delta H_{PHB}^0$= 132 J/g (assuming that only poly-hydroxybutyrate (PHB) crystals are produced in the PHBV copolymer due to the low percentage of hydroxyvalerate copolymer (2%)) (Requena et al., 2016), the degree of crystallinity of PHBV and PVA are 0.56 and 0.44 respectively (Table 3).

Crosslinked PVA (PVA E) shows no crystallization or melting process, indicating that crystallization was hampered by the crosslinking. The thermograms of the PHBV/PVA blend (Figure 6) show the presence of a crystallization process during the cooling followed by the subsequent melting on heating. In binary miscible semicrystalline polymer mixtures, the phase structure and morphology are affected by the crystallization processes of the components, determined by their different melting temperatures and ability to crystallize (Qiu, 2018). The PHBV/PVA blend under study shows a single crystallization peak (cooling) and melting peak (heating), and no cold crystallization was observed. The crystallization (153.9 ºC) and melting (189 ºC) temperatures are between those of the neat polymers, so the one with higher melt temperature, PVA, crystallizes, whereas the low melt-temperature component, PHBV, acts as a temporary amorphous diluent (Qiu, 2018). As only PVA crystallizes, the degree of crystallinity of the PHBV/PVA can be estimated (Equation 6) from the enthalpy of fusion ($\Delta H_f$), the PVA weight fraction in the sample ($\omega_2$), and the enthalpy of fusion of the total crystalline PVA.

$$X_c = \frac{\Delta H_f / \omega_2}{\Delta H_{PVA}^0} \tag{6}$$

The degree of crystallinity in the blend, $X_c$, is 0.16 (Table 3), lower than neat PVA, indicating that PHBV hampers PVA crystallization.

Since the crosslinked PVA (sample PVA E) does not crystallize, it would initially seem that in the semi-IPN PHBV/PVA, any process related to crystallization or melting should be related to the PHBV component. But there are important differences between the

thermograms of the semi-IPN and neat PHBV, which shows an exotherm crystallization process and subsequent melting during the heating, both at much lower temperatures than PVA crystallization and melting. In addition, the scan from the semi-IPN PHBV/PVA E and the blend PHBV/PVA are very similar, although the amplitude of both crystallization (endotherm) and melting peaks are smaller. Therefore, these results suggest that the processes observed are the crystallization and subsequent melting of PVA component. Crystallization and melting processes of the semi-IPN are weaker than in the blend due to the crosslinking of PVA, but still appear. The PVA chains, with reduced mobility imposed by the crosslinking, still are able to crystallize ($X_c$ = 0.09), although to a much lesser extent than in the blend.

#### 3.3.1.2. Semi-IPN PHBV/PVA with PPy

DSC thermograms during cooling and heating after the inclusion of PPy nanoparticles are shown in Figure 7. The PPy nanoparticles are also included in the figure, in which no $T_g$ was found in the temperature range analysed. The thermograms of PHBV/PVA semi-IPN composites with 2, 5, 10 and 15% PPy nanoparticles do not provide any thermal events that can be related to $T_g$, although crystallization (both endotherm and exotherm) and melting processes could be observed, indicating that the presence of the nanoparticles influences the overall crystallization of the semi-IPN matrix. The temperatures related to crystallization and melting are listed in Table 4. Samples with 2 and 5% of PPy nanoparticles show both a crystallization process on cooling, close to the crystallization peak in the semi-IPN without PPy nanoparticles (doted area in Figure 7a) and a cold crystallization process during the heating in the same temperature range as PHBV (doted area in Figure 7b). The melting process, with several peaks, can be observed in a wide area from 140 to 200 ºC. These results suggest that after the incorporation of small percentages of nanoparticles, PVA crystallization remains and the PPy nanoparticles act as nucleating agents for PHBV. The wide melting process suggest the melting of PHBV at lower temperature (the first two peaks) followed by the melt of PVA. The presence of these two peaks related to PHBV melting seems to indicate that PPy nanoparticles induce heterogeneous nucleation and lead to the formation of different sized crystals that melt at different temperatures, as has been reported for other nanoparticle-based fillers (Wilberforce et al., 2011; D. Wu et al., 2007). However, in samples with 10 and 15% of PPy nanoparticles, the crystallization peak related to PVA does not appear in the cooling scan and the cold crystallization peak related to PHBV is higher, indicating that when the amount of PPy nanoparticles increases, the PVA crystallization is prevented (maybe due to interactions between PVA chains and PPy nanoparticles), while the PHBV chains are able to crystallize to a larger extent due to the PPy nanoparticles acting as nucleating agents and the absence of PVA crystals. The degree of crystallinity (Tables 3 and 4) related to PVA (X*c-PVA)* does not change significantly after the incorporation of 2 and 5% of PPy nanoparticles. However, the degree of crystallization related to PHBV (X*c-PHBV)* increases from 0.31 to 0.42, as the percentage of PPy nanoparticles rises.

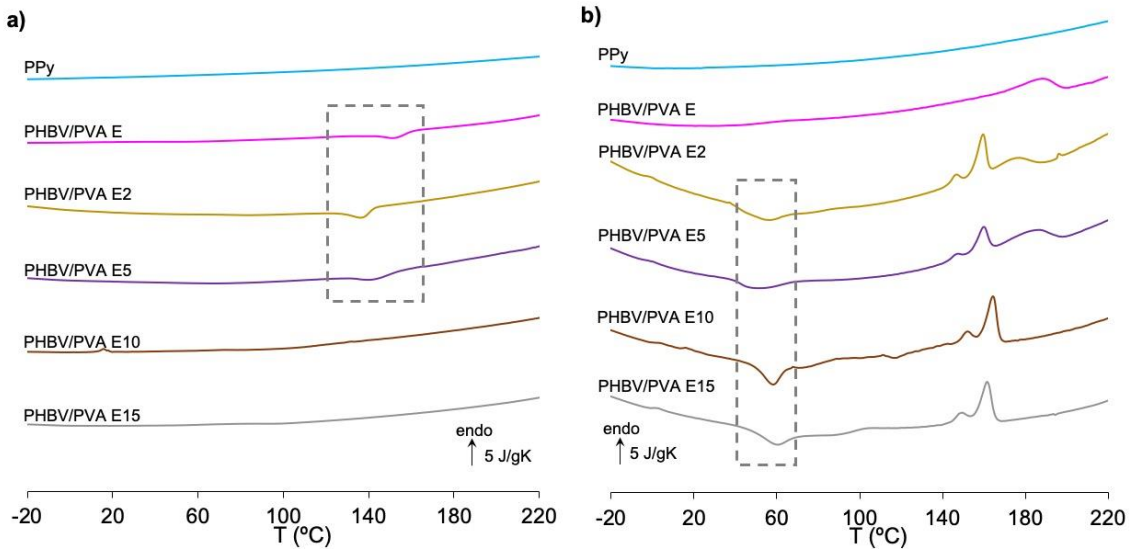


**Figure 7.** DSC thermograms at a rate of 20 ºC/min of PHBV/PVA E with different percentages of PPy nanoparticles ranging from 0 to 15 wt/wt %. (**a**) Normalized heat flow on cooling and (**b**) normalized heat flow on heating. Rectangles mark endo and exotherm crystallization peaks.

**Table 4.** Crystallization ($T_c$) and melting ($T_m$) temperature, enthalpy of fusion ($\Delta H_f$), degree of crystallinity PHBV ($X_c$ *PHBV*) and PVA ($X_c$ *PVA*) and 50% weight loss decomposition temperature ($T_d$-*50%*) for semi-IPN PHBV/PVA with different percentages of PPy nanoparticles.

| **Sample** | $T_c$ (ºC) | $T_m$ (ºC) | $\Delta H_f$(J/g) | $X_c$ *PHBV* | $X_c$ *PVA* | $T_{d\text{-}50\%}$(ºC) |
|---|---|---|---|---|---|---|
| PHBV/PVA E2 | 137.5/53.5(*) | 140-200 | 21.9 | 0.31 | 0.09 | 366.3 |
| PHBV/PVA E5 | 141.7/51.2(*) | 140-200 | 22.9 | 0.36 | 0.08 | 368.3 |
| PHBV/PVA E10 | 58.4(*) | 140-170 | 16.4 | 0.45 | - | 368.5 |
| PHBV/PVA E15 | 59.9(*) | 140-170 | 14.0 | 0.42 | - | 356.8 |

(*) Cold crystallization exotherm (heating scan)

### 3.3.2. Thermal degradation properties

The samples' thermal degradation and thermal stability were determined by TGA analysis. The relative weight loss and the derivative of the weight loss (DTG) curves in the temperature range from 30 to 600ºC (see Figures 8 and 9). The decomposition temperatures at which the weight loss is 50% ($T_{d\text{-}50\%}$) are indicated in Tables 3 and 4.

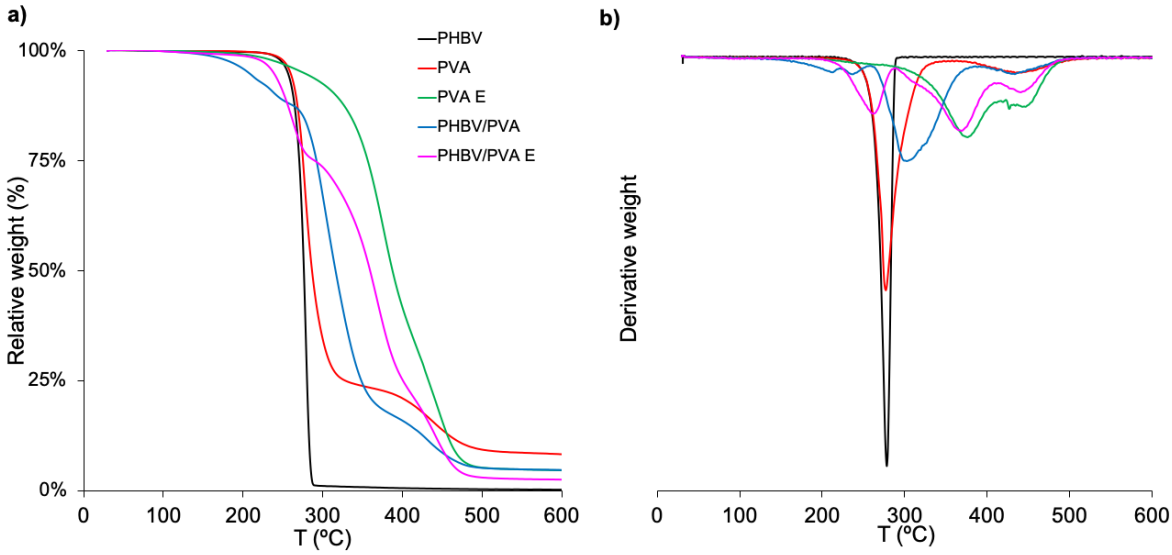


**Figure 8.** Thermogravimetry results of neat PHBV and PVA, PVA E, 30/70 PHBV/PVA blend and semi-IPN PHBV/PVA E. (**a**) Relative weight loss and (**b**) first derivative of the weight loss as a function of temperature (DTG).

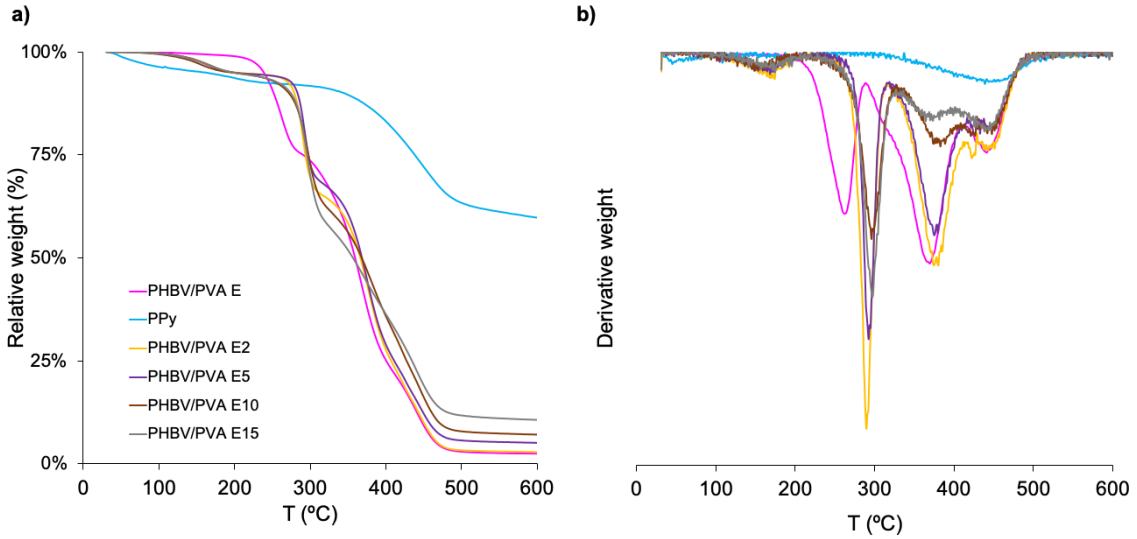


**Figure 9.** Thermogravimetry results of neat PPy nanoparticles and semi-IPN PHBV/PVA E with different percentages of PPy nanoparticles. PHBV/PVA E is included as reference. (**a**) Relative weight and (**b**) first derivative of the weight loss as a function of temperature (DTG).

#### 3.3.2.1. PVA/PHBA blend and PHBV/PVA semi-IPN

Neat PHBV shows a unique degradation stage, starting at 251ºC ($T_{onset}$) (Figure 8a). The 50% weight loss decomposition temperature is 276.1 ºC, and at 290 ºC the polymer is almost completely degraded, in good agreement with previous results (Q. S. Liu et al., 2009; Singh & Mohanty, 2007). It has been reported that PHBV is thermally unstable at temperatures above 250 ºC, with hydrolysis and chain scission, which leads to the formation of crotonic acid (Singh & Mohanty, 2007). PVA decomposition has been reported to be in three stages, with the one produced at temperatures between 50-130 ºC related to moisture vaporization, followed by two additional degradation processes at higher temperature (Lewandowska, 2009; Voronova et al., 2015). Figure 8a shows two-stage degradation depicted as two peaks in the DTG curve (Figure 8b), with no evidence

of moisture (the samples were previously vacuum-dried, so there was no moisture vaporization is not observed). The first degradation process, at temperatures higher than 200 ºC, is mainly due to the dehydration of hydroxyl groups and the formation of some volatile compounds followed by hydrocarbon products degradation, while the last stage, above 400 ºC, involves the breakage of the main chain. The 50% loss decomposition temperature, reported in Table 3, is $T_{d\text{-}50\%}$=286.8 ºC.

The PHBV/PVA blend, also depicted in Figure 8, shows the initial degradation process, at temperatures lower than 250 ºC, which may be related to the removal of moisture, mainly the water molecules bound to the PVA chains that remain trapped between the PHBV and PVA intertwined chains, even after previous vacuum drying. At higher temperature, the degradation profile contains the mixed characteristics of the blend components. However, the curve shifts to higher temperatures than those observed for both PHBV and PVA; $T_{d\text{-}50\%}$ is ca. 316 ºC, which can be attributed to hydrogen bonding interactions between the blend components that enhance thermal stability, as it has been reported for other polymers interacting with PHBV (Malmir et al., 2017; H. Yu et al., 2014; H. Y. Yu & Yao, 2016).

The PVA E and the PHBV/PVA E (semi-IPN) crosslinked samples show that degradation happened at higher temperature (Figure 8a). PVA E has the highest shift with two degradation processes ($T_{onset\ I}$ = 220 ºC and $T_{onset\ II}$ = 425 ºC). The 50% weight loss temperature ($T_{d\text{-}50\%}$ ~ 387 ºC) is 100 ºC higher than neat PVA (Table 3), which denotes a significant increase in its thermal stability after crosslinking, as has been reported previously (Figueiredo et al., 2009). As expected, after crosslinking the PVA chains in the PHBV/PVA blend, the degradation profile of the semi-IPN shifted to higher temperatures, close to 44 ºC (from 315.8 to 359.2 ºC after crosslinking) in $T_{d\text{-}50\%}$, which indicates enhanced thermal stability of the PHBV/PVA semi-IPN.

#### 3.3.2.2. PPy nanoparticles in the semi-IPN thermal degradation

The degradation behaviour in the PHBV/PVA semi-IPN before and after incorporating PPy nanoparticles is shown in Figure 9 together with the PPy thermal degradation profile, which has an initial weight loss (10%) below 220 ºC, which can be related to moisture and dopant evaporation (A. B. Da Silva et al., 2018).

Degradation begins above 350 ºC (Figure 9a), with a maximum around 450 º (Figure 9b). At 600 ºC, the final temperature of the scan performed, the weight loss is 40 %, in good agreement with previous results (Batool et al., 2012; A. B. Da Silva et al., 2018). Adding PPy nanoparticles to the PHBV/PVA semi-IPN does not significantly affect its degradation profile (Figure 9a). The first weight loss of around 10% can be related to the expulsion of moisture and the first stage of PPy degradation (dopant evaporation). The 50% weight loss temperature (Table 4) is in the same range as the semi-IPN matrix. At temperatures above 500 ºC, the residual weight is in proportion to composition and rises with higher percentages of nanoparticles. These results indicate that the semi-IPN's thermal stability is not significantly affected by the addition of PPy nanoparticles.

### 3.4. Electrical behaviour

Nanoparticles of the conductive polymer PPy were initially introduced into PHBV/PVA semi-IPNs with the aim of increasing its conductive properties. The surface electrical conductivity is reported in Table 5 for neat PHBV and PVA and semi-IPN with and without PPy nanoparticles.

Semi-IPN conductivity without nanoparticles shows values in proportion to the composition. Adding PPy nanoparticles significantly increases conductivity, which is PPy concentration-dependent (from 2.79 mS/m for neat PHBV/PVA semi-IPN to 6.35 mS/m for 15% PPy composite), although the percolation threshold was not reached (A. B. Da Silva et al., 2018). These values are in the same range as other electroactive biomaterials proposed for tissue engineering based on polymeric matrices that have shown an improved cellular response (L. P. da Silva et al., 2019; Song et al., 2016). It can thus be concluded that PPy nanoparticles incorporation leads to a significant enhancement of the surface electrical conductivity of the nanocomposites.

**Table 5.** Surface electrical conductivity of neat PHVA, PVA, PHBV/PVA 30/70 network and composites with from 2 up to 15% of PPy nanoparticles.

| **Sample** | $\sigma_s$ (mS/m) |
|---|---|
| PHBV | 2.38±0.05 |
| PVA | 3.55±0.14 |
| PHBV/PVA E | 2.79±0.03 |
| PHBV/PVA E2 | 3.48±0.06(*) |
| PHBV/PVA E5 | 3.76±0.04(*) |
| PHBV/PVA E10 | 4.93±0.12(*) |
| PHBV/PVA E15 | 6.35±0.15(*) |

(*) significant difference ($p<0.05$) with PHBV/PVA E

### 3.5. Biological evaluation

Both PHBV and PVA are FDA-approved biomaterials for biomedical applications. However, when developing a novel biomaterial, it is essential to test its biocompatibility, even if its components are already considered non cytotoxic. In the novel semi-IPN engineered in this study, nanoparticles of the conductive polymer polypyrrole have been added, which may result cytotoxic at high concentrations (Vaitkuviene et al., 2013). In this study, only 2% and 10% PPy concentrations were studied as a first screening of cell-material interactions.

The biocompatibility of the semi-IPNs was evaluated by an indirect MTT assay. Figure 10a represents the cytotoxicity results in terms of cell viability (%) after 24 and 48 h of cell incubation with the materials' extracts. There were not significant differences in any condition and time with respect to the positive control, considered as 100% viability. Thus, these results show that the engineered biomaterials are not cytotoxic and are feasible to be used in the biomedical field.

After proving their biocompatibility, a cell adhesion study was performed with C2C12 seeded at low density (5000 cells/cm2) on the surface of pre-functionalized materials during 24 h. Actin staining and cell area quantification (Figure 10 b and c) show that crosslinked PVA (PVA E) possess low attachment. However, PHBV incorporation into

the PVA crosslinked matrix (semi-IPN PHBV/PVA E) significantly enhanced cell adhesion area, in good agreement with previous studies (Kaniuk & Stachewicz, 2021). The decrease in surface hydrophilicity of the semi-IPNs after the incorporation of PHBV might improve cell attachment, since it has been reported that high hydrophilicity difficult protein adsorption and surface functionalization, hindering cell attachment (Mnatsakanyan et al., 2015; Ngandu Mpoyi et al., 2016).

Regarding the effect of PPy nanoparticles on cell attachment, the results show that low PPy concentrations (PHBV/PVA E2) also produced a significant increase in cell adhesion area respect to the semi-IPN without nanoparticles, as previously reported in literature (Basurto et al., 2021; Gilmore et al., 2009). Nevertheless, higher concentrations of PPy (PHBV/PVA E10) produced a fall in the adhesion values, reaching the same values as pure PVA E. The addition of PPy nanoparticles modifies the hydrophilic properties of the surface, as shown in surface wettability results (Table 2), thus affecting cell adhesion. Lower hydrophilic values result in more protein adsorption into the surface and an increase in cell attachment (Mnatsakanyan et al., 2015; Ngandu Mpoyi et al., 2016). Nevertheless, high PPy concentrations (10% and 15% PPy) did not significantly modify surface wettability in comparison with 2% PPy. The decrease in cell attachment might be due to the aggregation of nanoparticles at high concentrations, as can be seen in the microscopy photos Figure 2. These aggregates result in an irregular surface where cells might exhibit different attachment behaviour depending on the presence/absence of PPy aggregates, resulting in a general decrease of cell attachment. These results indicate that low PPy concentrations are the best option to obtain electroactive semi-IPNs with enhanced cell attachment for tissue engineering applications.

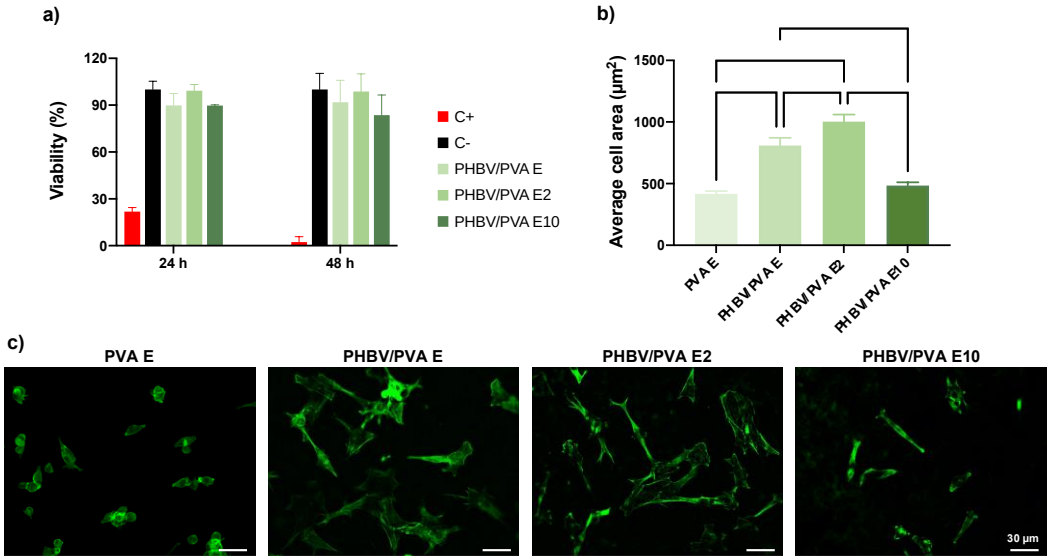


**Figure 10.** (**a**) MTT Cytotoxicity results of the semi-IPNs PHBV/PVA E, PHBV/PVA E2 and PHBV/PVA E10 represented as cell viability after 24 and 48 h incubation with extracts. Positive control: latex. Negative control: growth medium. (**b**) Average cell area quantification for PHBV/PVA E, PHBV/PVA E2 and PHBV/PVA E10 after actin staining. (**c**) Representative actin stained cells from PHBV/PVA E, PHBV/PVA E2 and PHBV/PVA E10 after 24 h culture. Graphs show mean ± standard deviation. (*) and (****) indicate significant differences ($p<0.05$ and $p<0.0001$, respectively).

## 4. Conclusions

Novel homogeneous PHBV/PVA semi-IPN hydrogels were prepared with different amounts of PPy nanoparticles by solvent casting using glutaraldehyde as PVA crosslinker. SEM images after PPy nanoparticle incorporation indicate that the particles were successfully embedded within the semi-IPN matrix. The FTIR and calorimetry results indicate good miscibility and compatibility between the components, with no phase separation. The parameters from the Kwei equation suggest the presence of strong specific interactions between the components, and that PVA is dominant in the glass transition process. The crystallinity of the semi-IPN PHBV/PVA, related to PVA, is less that of the neat polymers and the PHBV/PVA blend, which can be associated with the mobility restrictions imposed by the PVA crosslinking. The addition of PPy nanoparticles increases the PHBV crystallization with the nanoparticles acting as nucleation agent. The swelling assay indicates a significant reduction after adding PPy nanoparticles, even at low concentrations, indicating intermolecular interactions between the PPy nanoparticles and the semi-IPN hydrogel matrix. The hybrid hydrogel's structural organization show enhanced thermal stability, with no significant changes after adding PPy nanoparticles. The electrical conductivity is PPy concentration-dependent and increases significantly with the percentage of conductive polymer. Biological assessment proved the biocompatibility of the semi-IPNs for low (2%) and high (10%) PPy concentrations. Moreover, low nanoparticle concentrations significantly increased cell attachment of murine C2C12 myoblasts into the surface, while high concentrations resulted on a huge decrease of cell adhesion, maybe due to its tendency to form heterogeneous aggregates on the surface as confirmed by water contact angle measurement. Thus, electroactive semi-IPN PHBV/PVA with 2% PPy nanoparticles can be considered as promising biomaterials to further explore its potential in myogenic differentiation. Despite the results obtained, further studies are needed to demonstrate the potential applications of these stable electroactive hybrid hydrophilic networks in the biomedical field and especially in muscle tissue engineering.

## 5. Patents

Patent Application No. CN201811517745, filed on 02 October 2020 by R.S.S, Á.S-A, J. M-M and J.L.A-C.

## 6. Acknowledgments

This research was funded by the Spanish Ministry of Science, Innovations and Universities Economy, grant number RTI2018-097862-B-C21, including the FEDER financial support, (awarded to R.S.S. and J.M-M) and by the Fundación Universidad Católica de Valencia San Vicente Mártir, grant Nº 2019-231-003UCV (awarded to Á.S-A.). CIBER-BBN is an initiative funded by the VI National R&D&I Plan 2008–2011, Iniciativa Ingenio 2010, Consolider Program. CIBER Actions are financed by the Instituto de Salud Carlos III with assistance from the European Regional Development Fund.

## 7. References

Ahmed, E. M. (2015). Hydrogel: Preparation, characterization, and applications: A review. *Journal of Advanced Research*, *6*(2), 105–121. https://doi.org/http://dx.doi.org/10.1016/j.jare.2013.07.006

Anjum, A., Zuber, M., Zia, K. M., Noreen, A., Anjum, M. N., & Tabasum, S. (2016). International Journal of Biological Macromolecules Microbial production of polyhydroxyalkanoates ( PHAs ) and its copolymers : A review of recent advancements. *International Journal of Biological Macromolecules*, *89*, 161–174. https://doi.org/10.1016/j.ijbiomac.2016.04.069

Bajpai, A. K., Bajpai, J., & Shukla, S. (2003). Release dynamics of tetracycline from a loaded semi-interpenetrating polymeric material of polyvinyl alcohol and poly(acrylamide-co-styrene). *Journal of Materials Science: Materials in Medicine*, *14*(4), 347–357. https://doi.org/10.1023/A:1022983932548

Balint, R., Cassidy, N. J., & Cartmell, S. H. (2014). Conductive polymers: Towards a smart biomaterial for tissue engineering. *Acta Biomaterialia*, *10*(6), 2341–2353. https://doi.org/10.1016/j.actbio.2014.02.015

Batool, A., Kanwal, F., Imran, M., Jamil, T., & Anwar, S. (2012). Synthesis of polypyrrole / zinc oxide composites and study of their structural , thermal and electrical properties. *Synthetic Metals*, *161*(23–24), 2753–2758. https://doi.org/10.1016/j.synthmet.2011.10.016

Chang, H. M., Wang, Z. H., Luo, H. N., Xu, M., Ren, X. Y., Zheng, G. X., Wu, B. J., Zhang, X. H., Lu, X. Y., Chen, F., Jing, X. H., & Wang, L. (2014). Poly(3-hydroxybutyrate-co-3-hydroxyhexanoate)-based scaffolds for tissue engineering. *Brazilian Journal of Medical and Biological Research*, *47*(7), 533–539. https://doi.org/10.1590/1414-431X20143930

Chen, J., Yu, M., Guo, B., Ma, P. X., & Yin, Z. (2018). Conductive nanofibrous composite scaffolds based on in-situ formed polyaniline nanoparticle and polylactide for bone regeneration. *Journal of Colloid and Interface Science*, *514*, 517–527. https://doi.org/10.1016/j.jcis.2017.12.062

Chougule, M. A., Pawar, S. G., Godse, P. R., Mulik, R. N., Sen, S., & Patil, V. B. (2011). Synthesis and Characterization of Polypyrrole (PPy) Thin Films. *Soft Nanoscience Letters*, *01*(01), 6–10. https://doi.org/10.4236/snl.2011.11002

Couchman, P. R. (1978). Compositional Variation of Glass-Transition Temperatures. 2. Application of the Thermodynamic Theory to Compatible Polymer Blends. *Macromolecules*, *11*(6), 1156–1161. https://doi.org/10.1021/ma60066a018

Cui, L., Zhang, J., Zou, J., Yang, X., Guo, H., Tian, H., Zhang, P., Wang, Y., Zhang, N., Zhuang, X., Li, Z., Ding, J., & Chen, X. (2020). Electroactive composite scaffold with locally expressed osteoinductive factor for synergistic bone repair upon electrical stimulation. *Biomaterials*, *230*(November 2019), 119617. https://doi.org/10.1016/j.biomaterials.2019.119617

Curley, C., Hayes, J. C., Rowan, N. J., & Kennedy, J. E. (2014). An evaluation of the thermal and mechanical properties of a salt-modified polyvinyl alcohol hydrogel for a knee meniscus application. *Journal of the Mechanical Behavior of Biomedical Materials*,

*40*, 13–22. https://doi.org/10.1016/j.jmbbm.2014.08.003

Da Silva, A. B., Marini, J., Gelves, G., Sundararaj, U., Gregorio, R., & Bretas, R. (2018). Synergic effect in electrical conductivity using a combination of two fillers in PVDF hybrids composites. *European Polymer Journal*, *49*, 3318–3327. https://doi.org/10.1016/j.eurpolymj.2013.06.039

Da Silva, F. A. G., Queiroz, J. C., Macedo, E. R., Fernandes, A. W. C., Freire, N. B., Da Costa, M. M., & De Oliveira, H. P. (2016). Antibacterial behavior of polypyrrole: The influence of morphology and additives incorporation. *Materials Science and Engineering C*, *62*, 317–322. https://doi.org/10.1016/j.msec.2016.01.067

da Silva, L. P., Kundu, S. C., Reis, R. L., & Correlo, V. M. (2020). Electric Phenomenon: A Disregarded Tool in Tissue Engineering and Regenerative Medicine. *Trends in Biotechnology*, *38*(1), 24–49. https://doi.org/10.1016/j.tibtech.2019.07.002

Diani, J., & Gall, K. (2012). Properties of Linear Poly(Lactic Acid)/Polyethylene Glycol Blends. *Polymer Engineering and Science*, *51*, 108–116. https://doi.org/10.1002/pen

Ding, Q., Xu, X., Yue, Y., Mei, C., Huang, C., Jiang, S., Wu, Q., & Han, J. (2018). Nanocellulose-Mediated Electroconductive Self-Healing Hydrogels with High Strength, Plasticity, Viscoelasticity, Stretchability, and Biocompatibility toward Multifunctional Applications [Research-article]. *ACS Applied Materials and Interfaces*, *10*(33), 27987–28002. https://doi.org/10.1021/acsami.8b09656

Domagala, A., Maksymiak, M., Janeczek, H., Musiol, M., Turczyn, R., Ledwon, P., Kaczmarczyk, B., Kurcok, P., Adamus, G., Kowalczuk, M., & Lapkowski, M. (2014). Oligo-3-hydroxybutyrate functionalised pyrroles for preparation of biodegradable conductive polymers. *Journal of Materials Science*, *49*(14), 5227–5236. https://doi.org/10.1007/s10853-014-8241-0

Domagala, Anna, Domagala, W., Ledwon, P., Musiol, M., Janeczek, H., Stolarczyk, A., Kurcok, P., Adamus, G., & Lapkowski, M. (2016). N-Oligo(3-hydroxybutyrate)-functionalized polypyrroles: towards bio-erodible conducting copolymers. *Polymer International*, *65*(12), 1395–1404. https://doi.org/10.1002/pi.5190

Dong, R., Ma, P. X., & Guo, B. (2020). Conductive biomaterials for muscle tissue engineering. *Biomaterials*, *229*(October 2019), 119584. https://doi.org/10.1016/j.biomaterials.2019.119584

Dragan, E. S. (2014). Design and applications of interpenetrating polymer network hydrogels . A review. *Chemical Engineering Journal*, *243*, 572–590. https://doi.org/10.1016/j.cej.2014.01.065

Enayati, M. S., Behzad, T., Sajkiewicz, P., Bagheri, R., Ghasemi-Mobarakeh, L., Łojkowski, W., Pahlevanneshan, Z., & Ahmadi, M. (2016). Crystallinity study of electrospun poly (vinyl alcohol) nanofibers: effect of electrospinning, filler incorporation, and heat treatment. *Iranian Polymer Journal (English Edition)*, *25*(7), 647–659. https://doi.org/10.1007/s13726-016-0455-3

Fei, B., Chen, C., Wu, H., Peng, S., Wang, X., & Dong, L. (2003). Quantitative FTIR study of PHBV/bisphenol A blends. *European Polymer Journal*, *39*(10), 1939–1946. https://doi.org/10.1016/S0014-3057(03)00114-9

Figueiredo, K. C. S., Alves, T. L. M., & Borges, C. P. (2009). Poly ( vinyl alcohol ) Films Crosslinked by Glutaraldehyde Under Mild Conditions. *Journal of Applied Polymer Science*, *111*, 3074–3080. https://doi.org/10.1002/app

Frieria, Kumarb, K., & Boutin, A. (2017). Antibiotic resistance. *Journal of Infecction and Public Health*, *10*, 369–378. https://doi.org/10.1016/S0011-8532(03)00039-9

Gaaz, T. S., Sulong, A. B., Akhtar, M. N., Kadhum, A. A. H., Mohamad, A. B., Al-Amiery, A. A., & McPhee, D. J. (2015). Properties and applications of polyvinyl alcohol, halloysite nanotubes and their nanocomposites. *Molecules*, *20*(12), 22833–22847. https://doi.org/10.3390/molecules201219884

Gnanaprakasam, F., Muthu, J., Sankar, V., & Gopal, R. K. (2013). Growth and survival of cells in biosynthetic poly vinyl alcohol – alginate IPN hydrogels for cardiac applications. *Colloids and Surfaces B: Biointerfaces*, *107*, 137–145.

Guarino, V., Zuppolini, S., Borriello, A., & Ambrosio, L. (2016). Electro-active polymers (EAPs): A promising route to design bio-organic/bioinspired platforms with on demand functionalities. *Polymers*, *8*, 185. https://doi.org/10.3390/polym8050185

Guo-Qiang, C., & Qiong, W. (2005). The application of polyhydroxyalkanoates as tissue engineering materials. *Biomaterials*, *26*, 6565–6578.

Guo, B, Sun, Y., Finne-Wistrand, A., Mustafa, K., & Albertsson, A. (2012). Electroactive porous tubular scaffolds with degradability and non-cytotoxicity for neural tissue regeneration. *Acta Biomaterialia*, *8*, 144-153.

Guo, Baolin, Glavas, L., & Albertsson, A. C. (2013). Biodegradable and electrically conducting polymers for biomedical applications. *Progress in Polymer Science*, *38*(9), 1263–1286. https://doi.org/10.1016/j.progpolymsci.2013.06.003

H. Takahashi, S., M. Lira, L., & I. Córdoba de Torresi, S. (2012). Zero-Order Release Profiles from A Multistimuli Responsive Electro-Conductive Hydrogel. *Journal of Biomaterials and Nanobiotechnology*, *03*(02), 262–268. https://doi.org/10.4236/jbnb.2012.322032

Håkansson, E., Lin, T., Wang, H., & Kaynak, A. (2006). The effects of dye dopants on the conductivity and optical absorption properties of polypyrrole. *Synthetic Metals*, *156*(18–20), 1194–1202. https://doi.org/10.1016/j.synthmet.2006.08.006

Hardy, J. G., Lee, J. Y., & Schmidt, C. E. (2013). Biomimetic conducting polymer-based tissue scaffolds. *Current Opinion in Biotechnology*, *24*(5), 847–854. https://doi.org/10.1016/j.copbio.2013.03.011

Hassan, C. M., & Peppas, N. A. (2000). Structure and applications of poly(vinyl alcohol) hydrogels produced by conventional crosslinking or by freezing/thawing methods. *Advances in Polymer Science*, *153*, 37–65. https://doi.org/10.1007/3-540-46414-x_2

Hutmacher, D. W. (2000). Scaffolds in tissue engineering bone and cartilage. *Biomaterials*, *21*, 2529–2543.

Jun, I., Jeong, S., & Shin, H. (2009). The stimulation of myoblast differentiation by electrically conductive sub-micron fibers. *Biomaterials*, *30*(11), 2038–2047.

https://doi.org/10.1016/j.biomaterials.2008.12.063

Keengwe, J., & Onchwari, G. (2015). *Handbook of research on active learning and the flipped classroom model in the digital age*. IGI Global.

Kim, T. H., An, D. B., Oh, S. H., Kang, M. K., Song, H. H., & Lee, J. H. (2015). Creating stiffness gradient polyvinyl alcohol hydrogel using a simple gradual freezing-thawing method to investigate stem cell differentiation behaviors. *Biomaterials*, *40*, 51–60. https://doi.org/10.1016/j.biomaterials.2014.11.017

Kumar, A., & Han, S. S. (2017). PVA-based hydrogels for tissue engineering: A review. *International Journal of Polymeric Materials and Polymeric Biomaterials*, *66*(4), 159–182. https://doi.org/10.1080/00914037.2016.1190930

Kwei, T. . (1994). The effect of hydrogen bonding on the glass transtion temperatures of polymer mixtures. *Journal of Polymer Science Part C: Polymer Letters*, *22*, 307–313.

Lewandowska, K. (2009). Miscibility and thermal stability of poly ( vinyl alcohol )/ chitosan mixtures. *Thermochimica Acta*, *493*, 42–48. https://doi.org/10.1016/j.tca.2009.04.003

Li, Y., Rodrigues, J., & Tomás, H. (2012). Injectable and biodegradable hydrogels: Gelation, biodegradation and biomedical applications. *Chemical Society Reviews*, *41*(6), 2193–2221. https://doi.org/10.1039/c1cs15203c

Lin, A. A., Kwei, T. K., & Reiser, A. (1989). On the Physical Meaning of the Kwei Equation for the Glass Transition Temperature of Polymer Blends. *Macromolecules*, *22*(10), 4112–4119. https://doi.org/10.1021/ma00200a052

Liu, Q. S., Zhu, M. F., Wu, W. H., & Qin, Z. Y. (2009). Reducing the formation of six-membered ring ester during thermal degradation of biodegradable PHBV to enhance its thermal stability. *Polymer Degradation and Stability*, *94*(1), 18–24. https://doi.org/10.1016/j.polymdegradstab.2008.10.016

Luo, S., Grubb, D. T., & Netravali, A. N. (2002). The effect of molecular weight on the lamellar structure, thermal and mechanical properties of poly(hydroxybutyrate-co-hydroxyvalerates). *Polymer*, *43*(15), 4159–4166. https://doi.org/10.1016/S0032-3861(02)00242-2

Malmir, S., Montero, B., Rico, M., Barral, L., & Bouza, R. (2017). Morphology, thermal and barrier properties of biodegradable films of poly (3-hydroxybutyrate-co-3-hydroxyvalerate) containing cellulose nanocrystals. *Composites Part A: Applied Science and Manufacturing*, *93*, 41–48. https://doi.org/10.1016/j.compositesa.2016.11.011

Mansur, H. S., Oréfice, R. L., & Mansur, A. A. P. (2004). Characterization of poly(vinyl alcohol)/poly(ethylene glycol) hydrogels and PVA-derived hybrids by small-angle X-ray scattering and FTIR spectroscopy. *Polymer*, *45*(21), 7193–7202. https://doi.org/10.1016/j.polymer.2004.08.036

Mansur, H. S., Sadahira, C. M., Souza, A. N., & Mansur, A. A. P. (2008). FTIR spectroscopy characterization of poly (vinyl alcohol) hydrogel with different hydrolysis degree and chemically crosslinked with glutaraldehyde. *Materials Science and Engineering C*, *28*(4), 539–548. https://doi.org/10.1016/j.msec.2007.10.088

Matricardi, P., Di Meo, C., Coviello, T., Hennink, W. E., & Alhaique, F. (2013). Interpenetrating polymer networks polysaccharide hydrogels for drug delivery and tissue engineering. *Advanced Drug Delivery Reviews*, *65*(9), 1172–1187. https://doi.org/10.1016/j.addr.2013.04.002

Matsumura, S., Kurita, H., & Shimokobe, H. (1993). Anaerobic biodegradability of polyvinyl alcohol. *Biotechnology Letters*, *15*(7), 749–754. https://doi.org/10.1007/BF01080150

Merlin, D. L., & Sivasankar, B. (2009). Synthesis and characterization of semi-interpenetrating polymer networks using biocompatible polyurethane and acrylamide monomer. *European Polymer Journal*, *45*(1), 165–170. https://doi.org/10.1016/j.eurpolymj.2008.10.012

Mishra, S., Bajpai, R., Katare, R., & Bajpai, A. K. (2006). Preparation and characterization of polyvinyl alcohol based biomaterials: Water sorption and in vitro blood compatibility study. *Journal of Applied Polymer Science*, *100*(3), 2402–2408. https://doi.org/10.1002/app.23177

Mohan, N., & Nair, P. D. (2008). Polyvinyl Alcohol-Poly(caprolactone) Semi IPN Scaffold With Implication for Cartilage Tissue Engineering Neethu. *Journal of Biomedical Materials Research. Part B, Applied Biomaterials*, *84B*, 584–594. https://doi.org/10.1002/jbm.b.30906

Nair, M. B., Baranwal, G., Vijayan, P., Keyan, K. S., & Jayakumar, R. (2015). Colloids and Surfaces B : Biointerfaces Composite hydrogel of chitosan – poly ( hydroxybutyrate- co -valerate ) with chondroitin sulfate nanoparticles for nucleus pulposus tissue engineering. *Colloids and Surfaces B: Biointerfaces*, *136*, 84–92. https://doi.org/10.1016/j.colsurfb.2015.08.026

Ngadiman, N. H. A., Noordin, M. Y., Kurniawan, D., Idris, A., & Shakir, A. S. A. (2015). Influence of Polyvinyl Alcohol Molecular Weight on the Electrospun Nanofiber Mechanical Properties. *Procedia Manufacturing*, *2*(February), 568–572. https://doi.org/10.1016/j.promfg.2015.07.098

Paşcu, E. I., Stokes, J., & McGuinness, G. B. (2013). Electrospun composites of PHBV, silk fibroin and nano-hydroxyapatite for bone tissue engineering. *Materials Science and Engineering C*, *33*(8), 4905–4916. https://doi.org/10.1016/j.msec.2013.08.012

Qiu, Z. (2018). Chapter 8 - Crystallization Behavior of Miscible Semicrystalline Polymer Blends. In *Crystallization in Multiphase Polymer Systems*. Elsevier Inc. https://doi.org/10.1016/B978-0-12-809453-2.00008-6

Requena, R., Jiménez, A., Vargas, M., & Chiralt, A. (2016). Effect of plasticizers on thermal and physical properties of compression-moulded poly[(3-hydroxybutyrate)-co-(3-hydroxyvalerate)] films. *Polymer Testing*, *56*, 45–53. https://doi.org/10.1016/j.polymertesting.2016.09.022

Riekes, M. K., Junior, L. R., Pereira, R. N., Borba, P. A., Fernandes, D., & Stulzer, H. K. (2013). Development and evaluation of poly (3-hydroxybutyrate-co-3-hydroxyvalerate) and polycaprolactone microparticles of nimodipine. *Current Pharmaceutical Design*, *19*, 7264–7270.

Rivera-Briso, A. L., Aachmann, F. L., Moreno-Manzano, V., & Serrano-Aroca, Á. (2019). Graphene oxide nanosheets versus carbon nanofibers: Enhancement of physical and biological properties of poly(3-hydroxybutyrate-co-3-hydroxyvalerate) films for biomedical applications. *International Journal of Biological Macromolecules*. https://doi.org/10.1016/j.ijbiomac.2019.10.034

Rivera-Briso, A. L., & Serrano-Aroca, Á. (2018). Poly(3-Hydroxybutyrate-co-3-Hydroxyvalerate): Enhancement strategies for advanced applications. In *Polymers* (Vol. 10, Issue 7, p. 732). Multidisciplinary Digital Publishing Institute. https://doi.org/10.3390/polym10070732

Rudra, R., Kumar, V., & Kundu, P. P. (2015). Acid catalysed cross-linking of poly vinyl alcohol (PVA) by glutaraldehyde: effect of crosslink density on the characteristics of PVA membranes used in single chambered microbial fuel cells. *RSC Advances*, *5*(101), 83436–83447. https://doi.org/10.1039/c5ra16068e

Simões, D., Miguel, S. P., Ribeiro, M. P., Coutinho, P., Mendonça, A. G., & Correia, I. J. (2018). Recent advances on antimicrobial wound dressing: A review. *European Journal of Pharmaceutics and Biopharmaceutics*, *127*, 130–141. https://doi.org/10.1016/j.ejpb.2018.02.022

Singh, S., & Mohanty, A. K. (2007). Wood fiber reinforced bacterial bioplastic composites: Fabrication and performance evaluation. *Composites Science and Technology*, *67*(9), 1753–1763. https://doi.org/10.1016/j.compscitech.2006.11.009

Smith, J. R., & Lamprou, D. A. (2014). Polymer coatings for biomedical applications: a review. *Transactions of the IMF*, *92*, 9–19.

Song, J., Sun, B., Liu, S., Chen, W., Zhang, Y., Wang, C., Mo, X., Che, J., Ouyang, Y., Yuan, W., & Fan, C. (2016). Polymerizing pyrrole coated poly (l-lactic acid-co-ε-caprolactone) (PLCL) conductive nanofibrous conduit combined with electric stimulation for long-range peripheral nerve regeneration. *Frontiers in Molecular Neuroscience*, *9*, 117. https://doi.org/10.3389/fnmol.2016.00117

Talikowska, M., Fu, X., & Lisak, G. (2019). Application of conducting polymers to wound care and skin tissue engineering: A review. *Biosensors and Bioelectronics*, *135*(February), 50–63. https://doi.org/10.1016/j.bios.2019.04.001

Vilos, C., Morales, F. A., Solar, P. A., Herrera, N. S., Gonzalez-Nilo, F. D., Aguayo, D. A., ... & Kato, S. (2013). Paclitaxel-PHBV nanoparticles and their toxicity to endometrial and primary ovarian cancer cells. *Biomaterials*, *34*, 4098–4108.

Voronova, M. I., Surov, O. V., Guseinov, S. S., Barannikov, V. P., & Zakharov, A. G. (2015). Thermal stability of polyvinyl alcohol/nanocrystalline cellulose composites. *Carbohydrate Polymers*, *130*, 440–447. https://doi.org/10.1016/j.carbpol.2015.05.032

Waleed, E.-S., Abdelshakour, M., Choi, J.-H., & Choi, J.-W. (2020). Application of Conducting Polymer Nanostructures to. *Molecules*, *25*, 307. https://doi.org/10.3390/molecules25020307

Wang, L., Du, J., Cao, D., & Wang, Y. (2013). Recent Advances and the Application of Poly(3-hydroxybutyrate- co -3-hydroxyvalerate) as Tissue Engineering Materials. *Journal of Macromolecular Science, Part A*, *50*(8), 885–893. https://doi.org/10.1080/10601325.2013.802540

Wang, M., Pramoda, K. P., & Goh, S. H. (2004). Mechanical Behavior of Pseudo-Semi-Interpenetrating Polymer Networks Based on Double-C 60 -End-Capped Poly ( ethylene oxide ) and Poly ( methyl methacrylate ). *Chem. Mater.*, *16*, 3452–3456.

Wang, X., Yucel, T., Lu, Q., Hu, X., & Kaplan, D. L. (2010). Biomaterials Silk nanospheres and microspheres from silk / pva blend films for drug delivery. *Biomaterials*, *31*(6), 1025–1035. https://doi.org/10.1016/j.biomaterials.2009.11.002

Weng, L., Vijayaraghavan, R., MacFarlane, D. R., & Elliott, G. D. (2014). Application of the Kwei equation to model the Tg behavior of binary blends of sugars and salts. *Cryobiology*, *68*(1), 155–158. https://doi.org/10.1016/j.cryobiol.2013.12.005

Wilberforce, S. I. J., Finlayson, C. E., Best, S. M., & Cameron, R. E. (2011). The in fl uence of hydroxyapatite ( HA ) microparticles ( m ) and nanoparticles ( n ) on the thermal and dynamic mechanical properties of poly- L -lactide. *Polymer*, *52*(13), 2883–2890. https://doi.org/10.1016/j.polymer.2011.04.028

Wu, J., Xue, K., Li, H., Sun, J., & Liu, K. (2013). Improvement of PHBV scaffolds with bioglass for cartilage tissue engineering. *PloS One*, *8*, e71563.

Wu, D., Wu, L., Wu, L., Xu, B. I. N., Zhang, Y., & Zhang, M. (2007). Nonisothermal Cold Crystallization Behavior and Kinetics of Polylactide / Clay Nanocomposites. *Journal of Polymer Science Part B-Polymer Physics*, *45*, 1100–1113. https://doi.org/10.1002/polb

Yang, Y., Ke, S., Ren, L., Wang, Y., Li, Y., & Huang, H. (2012). Dielectric spectroscopy of biodegradable poly ( 3-hydroxybutyrate-co-3-hydroxyhexanoate ) films. *European Polymer Journal*, *48*(1), 79–85. https://doi.org/10.1016/j.eurpolymj.2011.10.002

Yu, H., Sun, B., Zhang, D., Chen, G., Yang, X., & Yao, J. (2014). Reinforcement of biodegradable poly(3-hydroxybutyrate-co-3-hydroxyvalerate) with cellulose nanocrystal/silver nanohybrids as bifunctional nanofillers. *Journal of Materials Chemistry B*, *2*(48), 8479–8489. https://doi.org/10.1039/c4tb01372g

Yu, H. Y., & Yao, J. M. (2016). Reinforcing properties of bacterial polyester with different cellulose nanocrystals via modulating hydrogen bonds. *Composites Science and Technology*, *136*, 53–60. https://doi.org/10.1016/j.compscitech.2016.10.004

Yussuf, A., Al-Saleh, M., Al-Enezi, S., & Abraham, G. (2018). Synthesis and Characterization of Conductive Polypyrrole: The Influence of the Oxidants and Monomer on the Electrical, Thermal, and Morphological Properties. *International Journal of Polymer Science*, *2018*. https://doi.org/10.1155/2018/4191747

Zhang, J., Bhat, R., & Jandt, K. D. (2009). Temperature-sensitive PVA / PNIPAAm semi-IPN hydrogels with enhanced responsive properties. *Acta Biomaterialia*, *5*(1), 488–497. https://doi.org/10.1016/j.actbio.2008.06.012

Zhang, Q., Zhao, Y., & Chen, L. (2009). Effect of PHBV content on the transparency and swelling behavior of polymer/hectorite nanocomposite hydrogel. *International Journal of Modern Physics*, *23*, 1365–1370.

Zhu, T., Cui, Y., Zhang, M., Zhao, D., Liu, G., & Ding, J. (2020). Engineered three-dimensional scaffolds for enhanced bone regeneration in osteonecrosis. *Bioactive Materials*, *5*(3), 584–601. https://doi.org/10.1016/j.bioactmat.2020.04.008

Zoratto, N., & Matricardi, P. (2018). Semi-IPNs and IPN-based hydrogels. In I. B. Kunal Pal (Ed.), *Polymeric Gels. Characterization, Properties an Biomedical Applications* (pp. 91–124). Elsevier Ltd. https://doi.org/10.1016/B978-0-08-102179-8.00004-1

# Chapter 2

# Electroactive calcium-alginate/polycaprolactone/reduced graphene oxide nanohybrid hydrogels for skeletal muscle tissue engineering

Chapter published in ***Colloids and Surfaces B: Biointerfaces***

José Luís Aparicio-Collado, Natalia García-San-Martín, José Molina-Mateo, Constantino Torregrosa-Cabanilles, Vicente Donderis-Quiles, Ángel Serrano-Aroca, Roser Sabater i Serra. Electroactive calcium-alginate/polycaprolactone/reduced graphene oxide nanohybrid hydrogels for skeletal muscle tissue engineering. *Colloids and Surfaces B: Biointerfaces*. 2022, 214, 112455. DOI: 10.1016/j.colsurfb.2022.112455.

**Personal contributions**

Materials' synthesis was developed by N. García-San-Martín and J. L. Aparicio-Collado. Morphological analysis, thermal properties, wettability, contact angle and spectroscopy were performed by N. García-San-Martín and J. L. Aparicio-Collado. Conductivity measurements were carried out at Department of Electrical Engineering by R. Sabater i Serra. Biological evaluation was performed by J. L. Aparicio-Collado.

J. L. Aparicio-Collado wrote the first version of the manuscript. J. Molina-Mateo, C. Torregrosa-Cabanilles, Á. Serrano-Aroca and R. Sabater i Serra contributed in experimental conceptualization, manuscript revision and funding acquisition.

# Electroactive calcium-alginate/polycaprolactone/reduced graphene oxide nanohybrid hydrogels for skeletal muscle tissue engineering

José Luís Aparicio-Collado[1], Natalia García-San Martín[1], José Molina-Mateo[1], Constantino Torregrosa Cabanilles[1], Vicente Donderis Quiles[2], Ángel Serrano-Aroca[3], Roser Sabater i Serra[1,2,4]

[1]Centre for Biomaterials and Tissue Engineering, Universitat Politècnica de València, Spain

[2]Department of Electrical Engineering, Universitat Politècnica de València, Spain

[3]Biomaterials and Bioengineering Lab, Centro de Investigación Traslacional San Alberto Magno, Universidad Católica de Valencia San Vicente Mártir, Valencia, Spain

[4]Biomedical Research Networking Centre in Bioengenieering, Biomaterials and Nanomedicine (CIBER-BBN), Spain

**Abstract**

Graphene derivatives such as reduced graphene oxide (rGO) are used as components of novel biomaterials for their unique electrical properties. Electrical conductivity is a crucial factor for muscle cells, which are electrically active. This study reports the development of a new type of semi-interpenetrated polymer network based on two biodegradable FDA-approved biomaterials, sodium alginate (SA) and polycaprolactone (PCL), with $Ca^{2+}$ ions as SA crosslinker. Several drawbacks such as the low cell adhesion of SA and weak structural stability can be improved with the incorporation of PCL. Furthermore, this study demonstrates how this semi-IPN can be engineered with rGO nanosheets (0.5 and 2% wt/wt rGO nanosheets) to produce electroactive nanohybrid composite biomaterials. The study focuses on the microstructure and the enhancement of physical and biological properties of these advanced materials, including water sorption, surface wettability, thermal behaviour and thermal degradation, mechanical properties, electrical conductivity, cell adhesion and myogenic differentiation. The results suggest the formation of a complex nano-network with different interactions between the components: bonds between SA chains induced by $Ca^{2+}$ ions (*egg-box* model), links between rGO nanosheets and SA chains as well as between rGO nanosheets themselves through $Ca^{2+}$ ions, and strong hydrogen bonding between rGO nanosheets and SA chains. The incorporation of rGO significantly increases the electrical conductivity of the nanohybrid hydrogels, with values in the range of muscle tissue. *In vitro* cultures with C2C12 murine myoblasts revealed that the conductive nanohybrid hydrogels are not cytotoxic and can greatly enhance myoblast adhesion and myogenic differentiation. These results indicate that these novel electroactive nanohybrid hydrogels have great potential for biomedical applications related to the regeneration of electroactive tissues, particularly in skeletal muscle tissue engineering.

**Keywords:** reduced graphene oxide, nanohybrid hydrogel, myoblast differentiation, alginate, semi-interpenetrated networks.

## 1. Introduction

Alginate-based hydrogels are usually produced by crosslinking alginate polymer chains with divalent cations such as $Ca^{2+}$ (X. Sun et al., 2020). Although alginate-based hydrogels possess excellent properties for a broad range of industrial applications (Llorens-Gámez & Serrano-Aroca, 2018; Serrano-Aroca et al., 2021), $Ca^{2+}$ ionically cross-linked alginate hydrogels possess weak mechanical properties within a few hours in physiological solution or immersed in distilled water at body temperature (37ºC) (Llorens-Gámez et al., 2020). In addition, the hydrophilic nature of alginate hydrogels leads to a lack of cell adhesion (Abalymov et al., 2020)(Rowley et al., 1999). Several reinforcing strategies can be used to overcome these issues such as incorporating a hydrophobic polymer with good mechanical properties in the form of semi-interpenetrated polymer networks (semi-IPNs), in which only the hydrophilic polymer networks are crosslinked (José Luis Aparicio-Collado et al., 2021) and/or incorporating Carbon-based nanomaterials (CBNs) (Llorens-Gámez et al., 2020; Martí et al., 2019). Among hydrophobic polymers, the synthetic and biodegradable polymer polycaprolactone (PCL) has good mechanical performance and have shown great potential in biomedical applications such as tissue engineering and drug delivery (Dwivedi et al., 2020; Mondal et al., 2016). PCL possesses low melting temperature and superior viscoelastic performance, which render it easy to process into a broad range of shapes and sizes (Mondal et al., 2016). Furthermore, alginate and PCL are Food and Drug Administration-approved materials for biomedical applications (Siddiqui et al., 2018; Tyagi et al., 2022). Previous studies found that CBNs combined with natural or synthetic polymers can reinforce the biomaterials' mechanical properties, enhance cell adhesion, proliferation (Rivera-Briso et al., 2019) and differentiation into several lineages (Palmieri et al., 2020), such as osteo-, neural- (Ku et al., 2013) or skeletal muscle (Hwang et al., 2019).

Graphene (G), one of the most promising CBNs is a two-dimensional material forming a lattice with unique properties (K. P. Loh et al., 2010). The family of G related materials include graphene oxide (GO), and reduced graphene oxide (rGO), obtained after GO reduction (Ku et al., 2013). Graphene-based composites have been suggested as a promising novel biomaterial in the field of regenerative medicine (Bellet et al., 2021b), particularly in skeletal muscle regeneration (S. Bin Jo et al., 2020; Kang et al., 2021; E. A. Lee et al., 2021; Y. C. Shin et al., 2018). Composites based on natural polymers, such as gelatin with graphene oxide (GO) nanosheets (J. H. Lee et al., 2016) and aligned polysaccharides with graphene fibres (A. Patel et al., 2018), have been shown to promote spontaneous differentiation of C2C12 myoblasts. Shin et al. (Y. C. Shin et al., 2015) fabricated hybrid fibres matrices composed of poly(lactic-co-glycolic acid)-Collagen impregnated with GO which stimulated cell attachment and myogenic differentiation of murine myoblast cultured in growth medium; moreover, myogenesis was further enhanced using differentiation medium.

Among the properties of G and rGO nanomaterials, its exceptional conductivity stands out (Novoselov et al., 2004; Zeng et al., 2019), which make them useful for producing conductive polymer-based composites (X. Wu et al., 2017; L. Yang et al., 2020; L. L. Zhang et al., 2012). Although rGO sheets have certain structural defects, lower conductivity and mechanical strength than pristine G sheets, their lower cost and

excellent scalable synthesis has enabled many advanced nanocomposites containing rGO to be developed with excellent physical properties (Compton & Nguyen, 2010). Electrical conductivity is essential for muscle cells, just as it is for neural and cardiac cells. It has been postulated that electrically conductive cell environments could, by themselves, facilitate electrical communication between muscle cells, thus stimulating myogenesis (Palmieri et al., 2020). Composites based on rGO and polyacrylamide (PAAm) enhanced myogenic differentiation compared with GO/PAAm (H. Jo et al., 2017), however, it has also been reported that cell response can be conditioned by the reduction method employed to obtain rGO (Palmieri et al., 2020).

In this study, we have prepared novel nanohybrid hydrogels based on sodium alginate and polycaprolactone (SA/PCL semi-IPN with $Ca^{2+}$ ions as alginate crosslinker) with incorporated conductive rGO nanosheets with the aim to overcome the drawback of alginate hydrogels (weak structural stability in aqueous environments and poor cell adhesion) and stimulate bioactivity. The incorporated rGO nanosheets will provide bioactivity (in the form intrinsic electrical conductivity) suitable for the regeneration of electroactive tissues, such as skeletal muscle, cardiac and neural tissue. We hypothesise that the combination of alginate and a very small amount of PCL (10% *wt*/*wt*) in the form of semi-IPN with embedded rGO nanoparticles (0.5 or 2% with respect to the total mass of polymers) could produce highly stable conductive nanohybrid hydrogels with enhanced physical and biological properties with promising prospects for skeletal muscle tissue engineering. This percentage (10% of PCL) was chosen to keep the hydrophilic properties of calcium alginate, while enhancing its mechanical and cell adhesion properties. Since carbon-based materials, such as rGO, are still quite expensive materials, low percentages of rGO were also selected to reduce production costs as much as possible and avoid potential biocompatibility issues. The physico-chemical properties of the nanohybrid composites were characterized by field emission scanning electron microscopy (HRFESEM), atomic force microscopy (AFM), Fourier transformed infrared spectroscopy (FTIR), water sorption, surface wettability, differential scanning calorimetry (DSC), thermogravimetry (TGA), dynamic mechanical thermal analysis (DMTA) and impedance analysis (electrical conductivity). Furthermore, the biological behaviour of C2C12 skeletal myoblast cultures in the nanohybrid hydrogels were analysed to explore their biocompatibility and bioactivity (in terms of cell adhesion and myogenic differentiation).

## 2. Materials and methods

### 2.1. Materials

Polyaprolactone (PCL) (molecular weight 43-50 kDa, Product Code 19561) was purchased from Polysciences. Sodium Alginate from brown algae (SA) (538 kDa, ~250 cP, M/G ratio: 0.85, product code 71238) was supplied by Merck. Dioxane and anhydrous calcium chloride ($CaCl_2$) were provided by Scharlab. Reduced graphene oxide (product code C459/rGOB070) was purchased from Graphenea (Spain). Water was purified with a Milli-Q Direct Q 3, 5, 8 system from Millipore. All reagents were used as received.

### 2.2. Fabrication of crosslinked SA and semi-IPN SA/PCL 90/10

SA was dissolved in ultrapure water (Milli-Q) (2% *wt/wt*) at room temperature with constant stirring overnight. PCL was dissolved in dioxane (1% *wt/wt*), also with constant

stirring for 2 h at room temperature. To obtain the SA/PCL blends, SA and PCL solutions were mixed with magnetic stirring for 24 h at 85 ºC with a 90/10 *wt/wt* ratio. SA/PCL 90/10 blend films were obtained after the solvent evaporation in an air oven at 50 ºC for 72h. Reference samples (pristine SA and PCL) were obtained from the initial polymer solutions poured into Petri dishes. Pristine SA films were kept at 50ºC in an air oven and PCL films were placed at room temperature until solvent evaporation (72 h in both cases).

SA and SA/PCL 90/10 blend films were ionically crosslinked by immersion in a 2% *wt/wt* $CaCl_2$ solution for 2 h (sodium alginate turns into calcium alginate after crosslinking). After that, the films were rinsed three times in Milli-Q water to remove any salt residue, left 48 h at room temperature to evaporate water and dried at 50 ºC under vacuum until constant weight to remove traces of moisture.

### 2.3. Production of electroactive SA/PCL semi-IPN with embedded rGO nanosheets

The semi-IPNs with incorporated rGO nanosheets were prepared following the same procedure described in Section 2.2 but including an additional previous step. Two different concentrations of rGO (0,5% *wt/wt* and 2% *wt/wt* of the total polymeric weight) were first dispersed (ultrasonic bath for 6h) in the specific amount of Milli-Q water needed to dissolve SA to obtain a homogeneous dispersion of the nanoparticles and avoid aggregates. Then, the nanohybrid composites were obtained following the same procedure described previously.

The scheme with the different steps followed to prepare the semi-IPN and the nanohybrid hydrogels is shown in Figure 1a, and the notation and sample compositions are indicated in Table 1.

**Table 1.** Sample notation and composition.

| Identification | Sample description |
|---|---|
| PCL | 100% Polycaprolactone |
| SA | 100% Sodium Alginate |
| SA E | 100% crosslinked SA |
| SA/PCL | Blend 90% SA 10% PCL |
| SA/PCL E | Semi-IPN (90% SA/10% PCL) |
| SA/PCL E(0.5 rGO) | Semi-IPN nanohybrid hydrogel SA/PCL 90/10 +0.5% rGO nanosheets |
| SA/PCL E(2rGO) | Semi-IPN nanohybrid hydrogel SA/PCL 90/10 +2% rGO nanosheets |

### 2.4. Characterization techniques

#### 2.4.1. Electron Microscopy

The morphology of the samples was analysed by HRFESEM (GeminiSEM 500, Carl Zeiss Microscopy) with an accelerating voltage of 0.8-1.0 kV. The samples were coated with a platinum layer (EM MED020, Leica). Samples were previously hydrated until equilibrium and then freeze-dried to preserve the porous structure. The cross-section was observed after cryogenic fracture.

### 2.4.2. Atomic Force Microscopy

The surface topography of the semi-IPN SA/PCL-E and the nanohybrid hydrogel with 2% of rGO nanosheets was analysed by AFM (NanoScope IIIa, Veeco) operating in tapping mode in air (75 kHz resonance frequency and 2.8 N/m constant force). Drive amplitude (600 mV), amplitude set point Asp (1.8 V) and A∞/A0 (0.8) were set. Nanoscope 5.30r2 software was used for image processing. Roughness of samples was measured from AFM images (300 nm×300 nm). Root-mean-square average of height deviations taken from the mean image data plane ($R_q$) was calculated using the roughness subroutine of Nanoscope software.

### 2.4.3. Fourier Transformed Infrared Spectroscopy (FTIR)

The presence of specific (chemical) groups was determined by FTIR spectroscopy (Bruker Optics FTIR Alpha II). FTIR spectra were collected in transmittance mode from 4000 to 400 $cm^{-1}$ after 24 scans at a resolution of 2 $cm^{-1}$.

### 2.4.4. Swelling assay

Swelling experiments were performed in crosslinked samples. Circular samples (ca. 3,8 $cm^2$) were vacuum-dried at 60 ºC and subsequently immersed in Milli-Q water at 37 ºC for 24 h until equilibrium. Experiments were performed in triplicate.

Samples were weighed before ($W_0$) and after ($W_1$) swelling. The swelling degree ($W_{eq}$) was calculated as follows:

$$W_{eq}(\%) = \frac{W_1 - W_0}{W_0} \cdot 100 \quad (1)$$

### 2.4.5. Surface wettability

Surface wettability was determined by water contact angle (WCA) using the sessile drop method. A Milli-Q water drop (3 µL) was deposited gravimetrically onto the surface to measure the contact angle and stabilization was allowed (~5 s). WCA was measured by an optical contact angle and contour analysis system (Dataphysics OCA 20). All measurements were performed in quintuplicate to ensure reproducibility.

### 2.4.6. Differential Scanning Calorimetry (DSC)

DSC analysis was carried out by a PerkinElmer DSC 8000 under a flowing nitrogen atmosphere (20 mL/min). Samples were subjected to a single heating scan from -80 to 240 ºC at 20 ºC/min.

### 2.4.7. Thermogravimetric Analysis (TGA)

Thermal stability and decomposition were analysed by a thermogravimetric analyser Mettler Toledo TGA 2 (SF) system. Vacuum-dried samples (5-10 mg weight) were heated from 30 to 600ºC at a rate of 30ºC/min. The mass of the samples was constantly measured as a function of temperature.

### 2.4.8. Mechanical properties

Dynamic mechanical thermal analysis (DMTA) was performed with a Perking Elmer DMA 8000 at a frequency of 1 Hz on sample bars (20 × 5 × 0.01 mm) in an immersion bath (Milli-Q water). The storage modulus (*E'*) and loss modulus (*E''*) was measured in the temperature range 35 to 39 ºC at a heating rate of 1 ºC/min.

### 2.4.9. Electrical properties

Electrical characterization was performed by the Agilent 16451B parallel plates (circular electrodes 5 mm in diameter) connected to an impedance analyser Hewlett Packard 4284A LCR Meter. Complex impedance was obtained at frequencies 20, 50 and 100 kHz at room temperature. Electrical conductivity ($\sigma$) was calculated (S/m) as:

$$\sigma = \frac{l}{R_S \cdot A} \quad (2)$$

Where *l* is the sample thickness, $R_s$ is the real part of the complex impedance and *A* is the electrode area. The measurements were performed in triplicate.

## 2.5. Cell culture and biological characterization

Murine myoblasts (C2C12, Sigma Aldrich; Merck) were cultured in high glucose Dulbeco's Modified Eagle's Medium (DMEM, Biowest) supplemented with 10% fetal bovine serum (FBS, ThermoFisher) and 1% Penicillin/Streptomycin (P/S, ThermoFisher) in a humidified atmosphere at 37ºC and 5% $CO_2$. Cells were passed during amplification at maximum 80% confluence.

### 2.5.1. Cytotoxicity

Cytotoxicity was performed by adapting the ISO/EN10993 standard to evaluate *in vitro* toxicity from the extracts (indirect method) by mean of an MTT (3-[4, 5-dimethylthiazol-2-yl]-2, 5 diphenyl tetrazolium bromide) assay. The ratio of material surface to extraction fluid was 2,5 $cm^2$/mL (sample thickness ca. 200 µm). 96-well plates were seeded with $10^4$ cells/well with 100 µL of growth medium (DMEM + 10% FBS + 1% P/S) and placed in the incubator. At the same time, autoclaved crosslinked samples (121ºC, 20 min) were cultured overnight in growth medium to generate the extracts. After 24 h of culture, the medium was replaced by 100 µL of the extracts. Culture medium (growth medium) was used as negative control (life) and natural rubber latex extract was the positive control (death). Each sample was studied with three biological replicates.

After 24, 48 and 72 h, supernatant was replaced by 100 µL of new growth medium without phenol red containing a 1:10 MTT dilution (Sigma Aldrich; Merck). Viable cells were stained with water-insoluble formazan dye. After incubation for 4 h, the solution was removed and 100 µL of solubilization buffer (10% SDS in 0.01 M HCl) (Sigma Aldrich; Merck) was added to each well and left overnight at 37ºC to dissolve the formazan crystals. Optical density was then measured by a microplate reader (Victor Multilabel Plate Reader, Perkin Elmer) at 570 nm wavelength. Cell viability was calculated as:

$$Viability\ (\%) = \frac{OD\ test}{OD\ control} \cdot 100 \quad (3)$$

where *OD test* is the optical density of the sample and *OD control* is the optical density of the negative control.

### 2.5.2. Cell adhesion

Cell adhesion was studied by fluorescence microscopy (Nikon Microscope Eclipse 80i). Sterilized samples were left overnight at 37ºC and 5% $CO_2$ growth medium (DMEM, 10% FBS, 1% P/S) to allow protein adsorption and surface functionalization. Culture medium was then renewed and C2C12 cells were seeded at a 5000 cells/$cm^2$ density on the materials' surface (3,8 $cm^2$). After 24 h of culture, wells were rinsed with Dulbecco's phosphate-buffered saline (DPBS) and fixed with a 4% paraformaldehyde solution (1 h at room temperature). Samples were then permeabilized with 0.5% Triton-X-100/DPBS, blocked with 5% horse serum (HS) in DPBS (1 h, 37ºC) and stained with fluorescent Phalloidin (dil:1:100, Invitrogen/ThermoFisher A12379). Finally, samples were mounted in Vectashield mounting media (Palex Medical) and observed through a fluorescence microscope. Image quantification of cell areas (actin cytoskeleton stained with phalloidin) was performed on ImageJ software.

### 2.5.3. Myogenic differentiation

To assess myogenic differentiation, C2C12 cells were seeded in growth medium at 20000 cells/$cm^2$ on the materials' surface (3,8 $cm^2$), previously pre-treated with overnight incubation with growth medium to facilitate protein adsorption. After 24 h of culture the medium was changed to supplemented differentiation medium containing insulin transferrin selenium (ITS liquid media supplement, Sigma) (DMEM, 1% ITS, 1% P/S) for 6 days, with medium changes every 2 days. Cells were then fixed with paraformaldehyde for 1 h and blocked with 5% HS in DPBS for 1 h, permeabilized with 0,5% Triton-X-100 in DPBS and incubated with sarcomeric α-actinin mouse monoclonal antibody (Invitrogen/Thermofisher MA1-22863, clone EA-53, 1:200) for 1 h at 37ºC. Then, samples were rinsed with DPBS and incubated with secondary Alexa 488 conjugated goat anti-mouse IgG polyclonal antibody (Invitrogen/Thermofisher A11029, 1/500) for 1 h at 37ºC. Finally, samples were mounted with Vectashield containing DAPI and analysed by fluorescence microscopy. Image quantification of myogenic differentiation was performed on ImageJ software.

The nanohybrid hydrogels with rGO nanosheets showed a strong auto fluorescence background on the same wavelength as DAPI (358⁄461 nm, blue), hindering the correct visualization of the cell nucleus. To overcome this issue and be able to adequately identify the differentiated myoblasts (myotubes), an adapted method from H. Inoue et al. (Inoue et al., 2018) was used. The average area of myotubes with two nuclei from the semi-IPN hydrogel (average area: 550 $\mu m^2$), which did not show auto fluorescence background and cell nuclei could be observed by DAPI staining, was first calculated. Differentiated myoblasts were considered as those with cell area ≥ 550 $\mu m^2$ and elongate shape while undifferentiated cells remained with round shape. Myogenic differentiation was quantified as the number of myotubes/$cm^2$, mean myotube area and diameter and the ratio between the areas of myotubes and the area of total sarcomeric α-actinin positive cells.

## 2.6. Statistical analysis

One-way ANOVA tests were performed on GraphPad Prism 8.0.2 software. Data were presented as mean ± standard deviation. Statistical significance was indicated by (*) $p<0.05$, (**) $p<0.01$, and (***) $p<0.001$ according to the analysis of variance.

## 3. Results and Discussion

### 3.1. Microstructure

HRFESEM images (Figure 1b) show the cross-section and surface morphology of the semi-IPN and nanohybrid hydrogels with incorporated rGO nanosheets (0.5 and 2% wt/wt) previously swollen in water and freeze-dried to preserve the porous structure. The images show a uniform structure in all samples (no evidence of phase separation is observed), with micropores along the cross-section (Fig. 1b, left column), with pore size < 0.25 µm. This small pore size is related to a very compact structure, which indicates that the system is highly crosslinked. This feature is expected to limit the swelling capacity and the formation of large pores, as will be verified in the swelling assay (section 3.3). A homogenous surface, with low porosity, can be observed in the semi-IPN and nanohybrids hydrogels (Figure 1b, right column) with a slight increase in surface roughness after the incorporation of rGO nanosheets. In addition, the image of pristine rGO nanosheets after dispersion in water by ultrasonic bath shows that their length can reach 3-4 µm and that they tend to wrinkle, forming small aggregates. The surface roughness observed in the nanohybrid hydrogels suggests the presence of rGO nanosheets close to the surface highly embedded in the polymeric matrix.

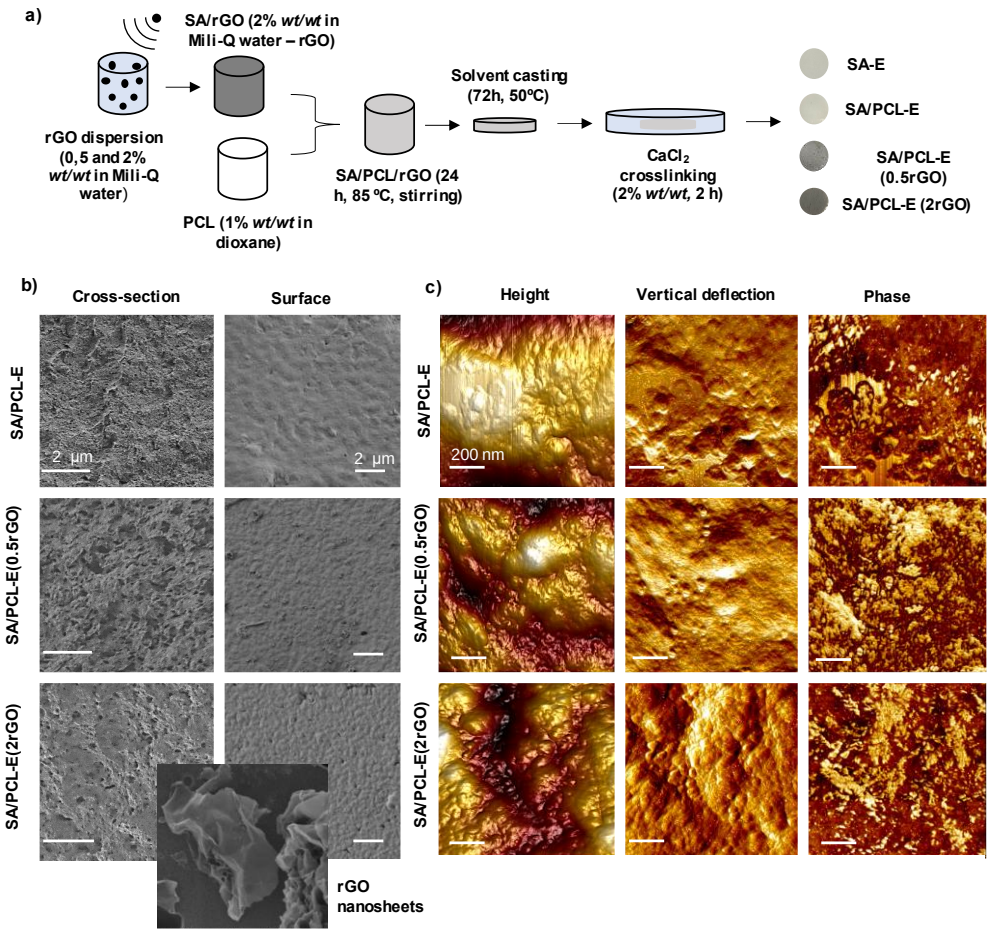


**Figure 1.** (**a**) Scheme with the steps followed to prepare the semi-IPN and the nanohybrid hydrogels. (**b**) High-resolution field-emission scanning electron microscopy (HRFSEM) images of the cross-section (left column) and surface (right column) in freeze-dried samples. The image at the bottom shows pristine rGO nanosheets dispersed previously in water. (**c**) Representative Atomic Force microscopy (AFM) images (height, vertical deflection, and phase) of the semi-IPN SA/PCL-E and nanohybrid hydrogels with 0.5 and 2% of rGO.

Dry samples obtained after solvent casting were analysed by AFM to study the surface topography (Figure 1c). The porous alginate-based hydrophilic structures collapsed during drying, as expected (see Fig. 3 in ref (Serrano-Aroca et al., 2017)). On the nanoscale, the surfaces of the semi-IPN and nanocomposites with rGO nanosheets show a fairly homogeneous structure with rough areas, as can be seen in Figure 1c, consistent with the presence of two materials and two solvents (water and dioxane) with different evaporation dynamics during sample preparation. The roughness parameter, $R_q$, rises from 4.14 nm for the semi-IPN SA/PCL-E to 9.33 nm for the nanocomposite with 2% of rGO nanosheets.

### 3.2. Fourier Transform Infrared Spectroscopy

Figure 2a shows the FTIR spectra of neat PCL, SA, SA/PCL blend and semi-IPN SA/PCL-E with and without rGO nanosheets. The neat PCL spectrum shows the characteristic peaks related to asymmetric and symmetric stretching of the $CH_2$ groups, which belong to the bands at 2945 and 2865 $cm^{-1}$ (Elzein et al., 2004; Tranquillo et al., 2019). The distinctive peak around 1720 due to carbonyl stretching of the –COOH group can be clearly identified, together with asymmetric COC stretching at 1240 $cm^{-1}$ and symmetric COC stretching at 1170 $cm^{-1}$ (Elzein et al., 2004; Z. Yang et al., 2010). Neat SA shows a wide band between 3700 and 3000 $cm^{-1}$ associated with O-H stretching. The peaks at 2919 $cm^{-1}$ and 1417 $cm^{-1}$are due to C–H stretch $sp^3$ and C-OH stretch, respectively (Rashtchian et al., 2020; Xiao et al., 2002). Alginate gelation takes place when divalent ions interact ionically with the guluronic acid block, which produce a three-dimensional network (S. K. Bajpai & Sharma, 2004). Crosslinking SA replaces sodium with calcium ions, resulting in a change in ion density, diameter and weight, affecting the stretch forces applied to the C=O carboxylic salt functional groups (Pathak et al., 2010). This phenomenon can be identified as a slight shift from 1593 $cm^{-1}$ in pristine SA to 1590 $cm^{-1}$ in the crosslinked samples (Gomaa et al., 2018; Rashtchian et al., 2020).

The SA/PCL blend spectrum shows the characteristic peaks related to both SA and PCL, confirming their presence in the blend. The semi-IPN (SA/PCL-E) obtained after crosslinking SA with $CaCl_2$ also shows the slight shift related to the stretch in the C=O carboxylic salt functional groups (asymmetric stretching vibrations), with the peak located at 1590 $cm^{-1}$. After the addition of rGO nanosheets, the position and intensity of the main characteristic absorption peaks did not change substantially because they shared the same functional groups and the amount of filler is small. The spectra show a slight reduction of the intensity of the band between 3700 and 3000 $cm^{-1}$, more noticeable after the addition of 2% of rGO (SA/PCL-E(2rGO) sample) (W. Zhao et al., 2018). This behaviour suggests an interactions between the polymer matrix and rGO nanoparticles through oxygen-containing functional groups, such as –OH and –COO groups, forming interfacial hydrogen bonds between both components (W. Zhao et al., 2018). An additional shift of the peak related to carbonyl stretching (C=O) can be seen in the nanohybrid composites, from 1593 to 1588 $cm^{-1}$, which may have been produced by further interactions between SA chains and rGO nanosheets through $Ca^{2+}$ ions. Specific ions, such $Ca^{2+}$, $Zn^{2+}$ and $Fe^{3+}$, are able to crosslink alginate chains and GO nanosheets simultaneously, generating hydrogels with crosslinked GO networks inside the alginate hydrogel (Sabater i Serra et al., 2020; Serrano-Aroca et al., 2018; Zheng et al., 2016). It has also been reported that the oxygen-containing functional groups of GO can bond to divalent ions, particularly $Mg^{2+}$ and $Ca^{2+}$ (Park et al., 2008). The nanocomposite spectra

suggest that although the number of functional groups in rGO nanosheets is lower than in GO, they still remain.

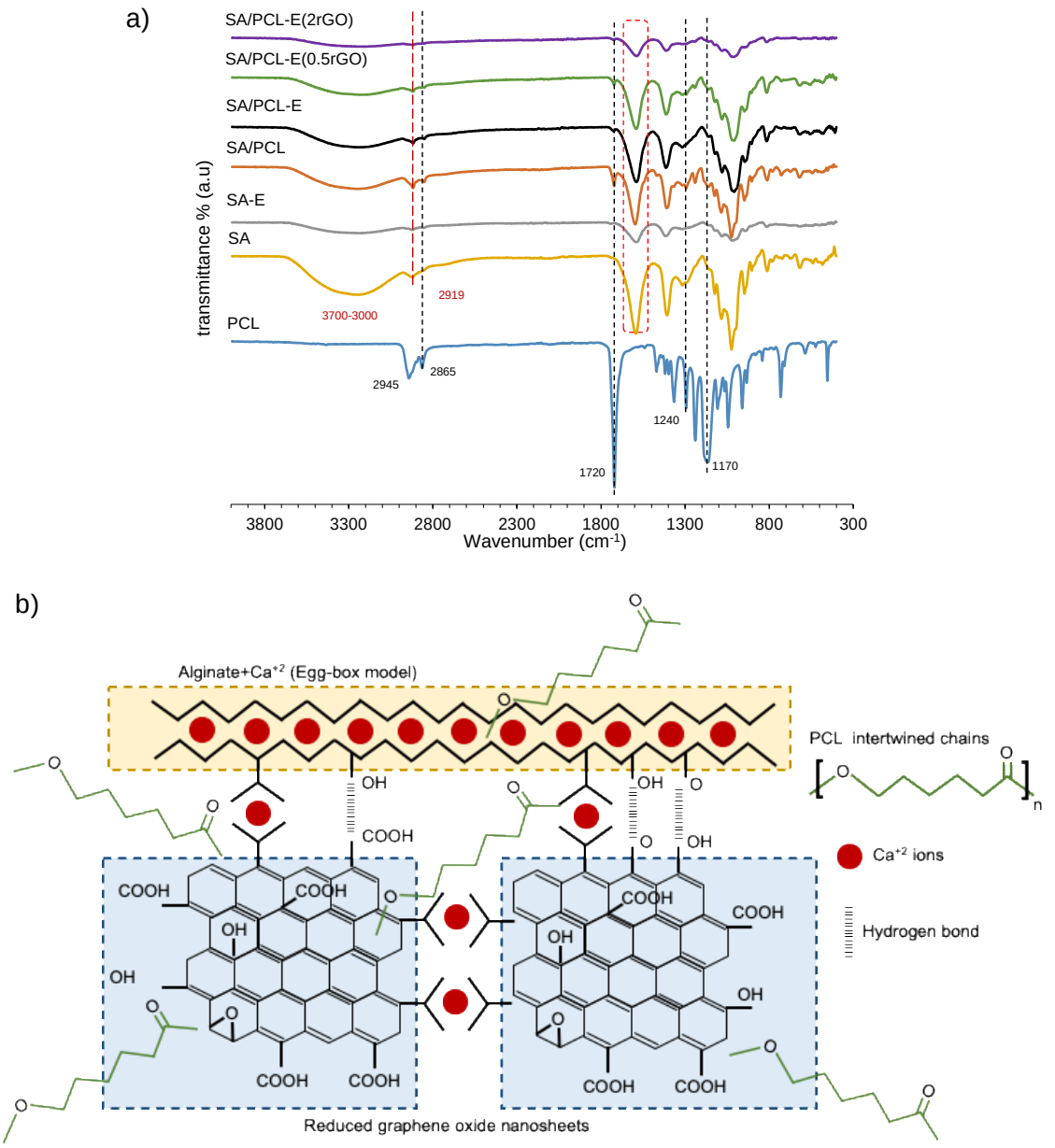


**Figure 2.** (**a**) Fourier transform infrared (FTIR) spectroscopy spectra in the region 4000-300 $cm^{-1}$: SA/PCL blend, semi-IPN SA/PCL (SA/PCL-E) and nanohybrid composites with 0.5 and 2% of rGO nanosheets. Neat PCL and SA, crosslinked SA (SA-E) have been included as reference. (**b**) Schematic diagram of the structure of nanohybrid hydrogels.

We therefore hypothesized that the nanocomposites present a complex nano-network structure (Figure 2b) formed by bonds between SA chains induced by $Ca^{2+}$ ions (the well-known *egg-box* structure (Cao et al., 2020)), links between rGO nanosheets and SA chains and also between rGO nanosheets themselves through $Ca^{2+}$ ions, and finally hydrogen bonds between rGO nanosheets and SA chains (-OH and –COOH groups). In this structure, the PCL chains are trapped inside the calcium alginate-rGO nano-network. The results of the characterization of the system using additional techniques are presented below. These confirmed the proposed structure of the nanohybrid hydrogels.

### 3.3. Swelling and surface wettability

Water sorption (Figure 3a) was obtained gravimetrically as the amount of water absorbed from the dry to the swollen state in crosslinked samples (SA/PCL-E and nanohybrid hydrogels). Crosslinked alginate (SA-E) was included as reference. The swelling degree of the systems is moderate (between 50 and 70%), indicating high crosslinking density. The mean swelling degree in the semi-IPN SA/PCL-E does not present significant differences with respect to the crosslinked alginate, probably due to the fact that the system is highly crosslinked and the amount of PCL is low. The addition of rGO nanosheets affects the swelling capacity as expected, according to previous water sorption results obtained with other composite hydrogels of alginate/carbon nanomaterials (Llorens-Gámez & Serrano-Aroca, 2018; Serrano-Aroca et al., 2017). Nanohybrids with 0.5% of rGO did not show a statistically significant reduction of water swelling. However, the nanohybrids with 2% of rGO exhibited a statistically significant decrease of 16% with respect to the swelling degree of the semi-IPN SA-E. These results are in good agreement with the porous microstructure shown in Fig. 1b (cross-section images), where the small pore size shown by the semi-IPN and the nanohybrid hydrogels results in moderate swelling capacity.

Figure 3b shows the surface wettability obtained from the static water contact angle measurement. The contact angle for the reference samples is 92 ± 3º for smooth surface PCL (low wettability) (Šišková et al., 2021) and 52 ± 4º for crosslinked SA. In the semi-IPN SA/PCL with 10% PCL, the contact angle increases to 61 ± 4º. The addition of rGO nanosheets does not significantly influence the hydrophilic behaviour of the nanohybrid composites, in good agreement with previous results (Du et al., 2018).

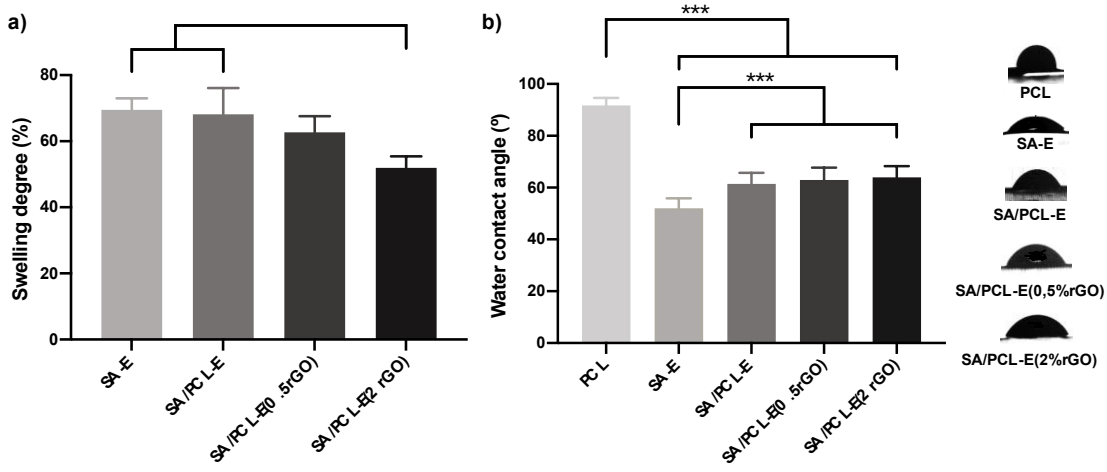


**Figure 3.** (**a**) Swelling degree in equilibrium. (**b**) Water contact angle of semi-IPN SA/PCL-E and nanohybrid hydrogels with 0.5 and 2% of rGO. Crosslinked SA (SA E) and PCL have been included as reference. Graphs show mean ± standard deviation. (*) and (***) indicate significant differences ($p<0.05$ and $p<0.001$, respectively).

The reduced swelling in the nanohybrid hydrogels suggest that the remaining functional groups of rGO nanosheets (after reduction) embedded in the SA/PCL matrix are able to generate a more compact network (Jia et al., 2018; Zheng et al., 2016), consistent with the structure proposed in the previous section. However, surface wettability is not altered, probably due to the particles being completely covered by the polymer matrix and not showing up on the surface.

## 3.4. Thermal and mechanical properties

### 3.4.1. Differential Scanning Calorimetry (DSC)

Figure 4a shows the normalized heat flow on heating. SA/PCL blend shows a small endotherm peak around 60 ºC followed by a large one at 180 ºC; finally, thermal degradation can be identified at temperatures higher than 220 ºC. Alginates have a strong affinity for water and the molecular structure determines their hydration properties (El-Houssiny et al., 2016). Water can be released at different temperatures according to the interactions between water and alginate chains (Dong et al., 2017). Free water can be released at temperatures lower than 80 ºC, water linked through hydrogen bonds can be released in the interval between 80-120 ºC and more tightly linked water through polar interaction with carboxyl groups at higher temperatures (El-Houssiny et al., 2016; Laurienzo et al., 2005). The samples were vacuum dried at 60 ºC for 24h to remove free water, however, in neat SA, crosslinked SA and SA/PCL blend, a peak appeared at temperatures higher than 150 ºC, related to the evaporation of the tightly linked water. This was not found in the semi-IPN SA/PCL and the nanocomposites with rGO nanosheets, indicating their lower hydrophilic character. Both alginate and rGO nanosheets possess -COOH groups that can bond with water molecules and also with each other through hydrogen bonds. The lower intensity of this peak after the ionic crosslinking of the carboxyl groups of alginate and $Ca^{2+}$ ions (samples SA E and SA/PCL E) indicates a reduction of bonded water molecules (Sabater i Serra et al., 2020). In the nanohybrid hydrogels, the endotherm peak related to the evaporation of tightly bonded water molecules can scarcely be seen. This behaviour indicates strong links between the SA chain, $Ca^{2+}$ ions and rGO nanosheets, resulting in a high crosslinked network with reduced capacity to bond with water molecules. The results are in good agreement with those obtained from the swelling assay, in which incorporating 2% rGO nanosheets significantly reduced the swelling capacity. These results reinforced the proposed structure of the nanohybrid hydrogels based on complex nano-networks with multiple interactions between the components through $Ca^{2+}$ ions and hydrogen bonding (Fig. 2b).

**Table 2.** 50% weight loss decomposition temperature from the thermogravimetric assay ($T_{d\text{-}50\%}$). Melting temperature ($T_m$), enthalpy of fusion ($\Delta H_f$) and degree of crystallinity related to PCL content (from DSC thermograms).

| **Sample** | $T_{d\text{-}50\%}$ (ºC) | $T_m$(ºC) | $\Delta H_f$ (J/g) | $X_c$ PCL |
|---|---|---|---|---|
| PCL | 405 | 64.5 | 89.8 | 0.64 |
| SA | 311 | - | - | - |
| SA-E | 339 | - | - | - |
| SA/PCL | 299 | 62.8 | 2.68 | 0.18 |
| SA/PCL-E | 332 | 67.3 | 1.4 | 0.1 |
| SA/PCL-E(0.5rGO) | 351 | 64.2 | 0.9 | 0.06 |
| SA/PCL-E(2rGO) | 350 | 64.2 | 0.6 | 0.04 |

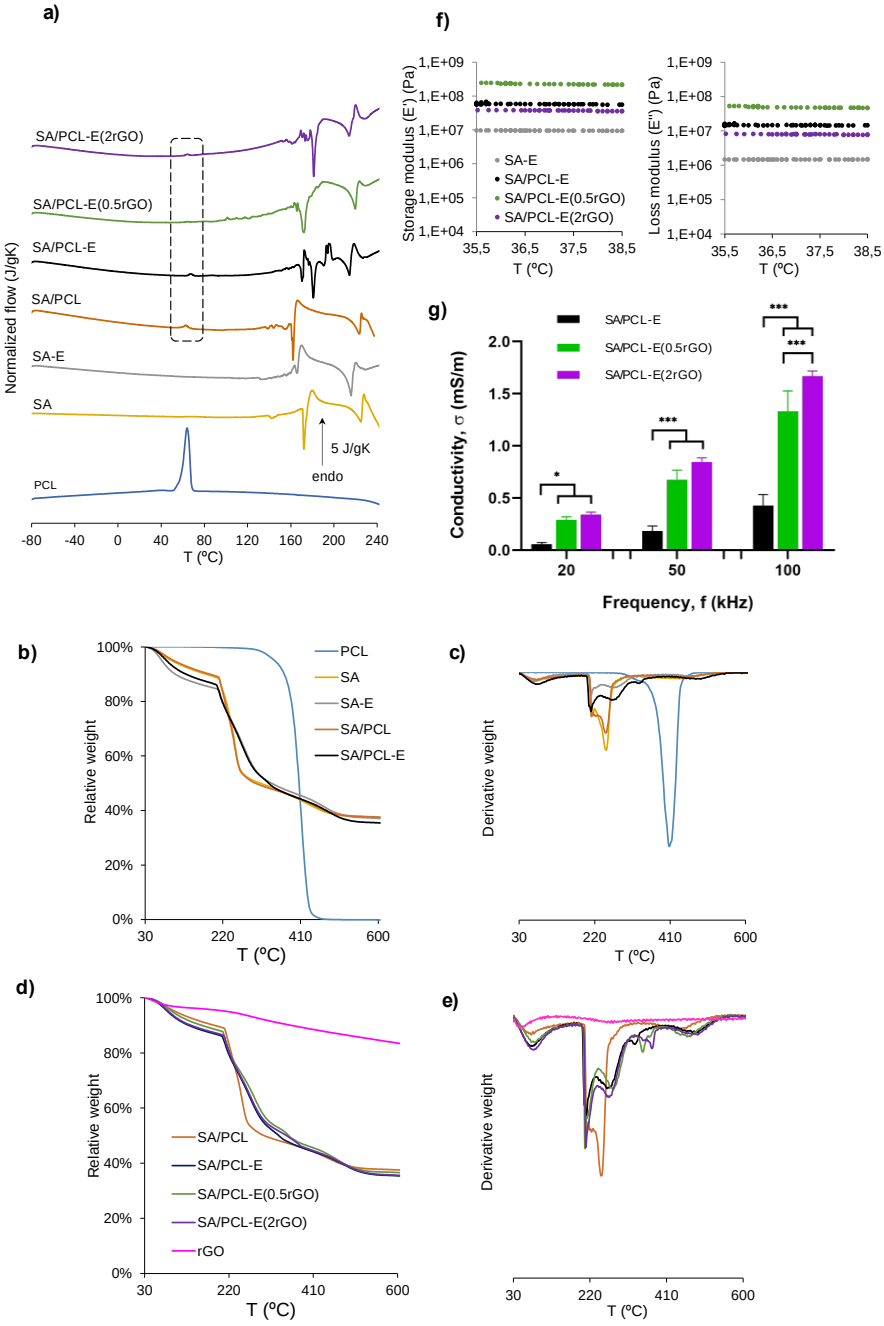


**Figure 4.** (**a**) DSC thermograms at a rate of 20 °C/min. Normalized heat flow on heating of SA/PCL blend, semi-IPN SA/PCL (SA/PCL-E) and nanohybrid composites with 0.5 and 2% of rGO nanosheets. Thermogravimetry results (TGA): (**b**) SA/PCL blend, semi-IPN SA/PCL (SA/PCL-E) and (**c**) derivative. (**d**) Nanohybrid hydrogels with 0.5 and 2% of rGO and (**e**) derivative. SA/PCL-E has been also included in (d) and (e) to facilitate comparison. Neat SA and PCL and crosslinked SA (SA-E) have been included as reference in DSC and TGA results. (**f**) Dynamic mechanical analysis. Storage modulus (*E'*) and loss modulus (*E''*) in the interval 35 to 39 ºC performed on samples immersed in water. (**g**) Electrical conductivity of semi-IPN SA/PCL (SA/PCL-E) and nanohybrid composites with 0.5% and 2% of rGO nanosheets at different frequencies (20, 50 and 100 kHz). Graph shows mean ± standard deviation. (*), (**) and (***) indicate significant differences ($p$<0.05, $p$<.01 and $p$<0.001, respectively).

The melting process in the blend is related to PCL crystallization (only 10% *wt/wt*) and in the semi-IPN and nanohybrid composites. The melting temperature, enthalpy of fusion and crystallinity are collected in Table 2. There are no significant changes in the PCL melting temperature, although the crystallinity of the embedded PCL is strongly affected

by alginate chains, ionic crosslinking and rGO nanosheets, hindering the reorganization of the PCL chains (see the dotted box in Fig. 4a). PCL crystallinity in the SA/PCL blend is reduced from $X_C$=0.64 for neat PCL to $X_C$=0.18, with an additional reduction after crosslinking ($X_C$=0.1). The crystallinity continues to decrease after incorporating rGO nanosheets to $X_C$=0.06 for the nanohybrid composite with 0.5% rGO and 0.04 for the 2% sample.

### 3.4.2. Thermogravimetry analysis (TGA)

The thermal degradation profile in the SA/PCL blend and the semi-IPN SA/PCL is dominated by the SA profile (Fig. 4b and 4c), consistent with the 90% SA in the sample. SA, SA/PCL blend and crosslinked samples (SA-E, semi-IPN SA/PCL-E and nanohybrid composites) show an initial weight loss due to the removal of water molecules at temperatures below 200 ºC (free and linked water) [13], in good agreement with the DSC thermogram. The first degradation step occurred in the interval 200-275 ºC followed by a second step in the range between 290 and 525 ºC, both related to the degradation of the SA matrix. The third process was at temperatures above 525 ºC, attributed to the formation of metal carbonates (Pathak et al., 2010; Sabater i Serra et al., 2020). Crosslinking, in both SA and SA/PCL blends shifts the first process of the thermal degradation to higher temperatures. The 50% weight loss temperature, $T_{d\text{-}50\%}$, is more than 30 ºC higher in the crosslinked samples (Sabater i Serra et al., 2020). The nanohybrid composites (Fig. 4d and 4e) with 0.5 and 2% rGO nanosheets show an additional shift in $T_{d\text{-}50\%}$, ca. 50 ºC, although the degradation profile is quite similar to the semi-IPN. It can therefore be concluded that thermal stability increases after adding both $Ca^{2+}$ ions and rGO nanosheets.

### 3.4.3. Mechanical properties

The mechanical properties of hydrogels on wet environments (e.g. under *in vitro* or *in vivo* conditions) may be completely different from those in the dry state. Thus, the complex modulus (storage modulus (*E'*) and loss modulus (*E''*)) was obtained in the interval between 35 and 39 ºC, simulating physiological conditions (Figure 4f). The storage modulus of crosslinked SA is $9.55\cdot10^6\pm1.1\cdot10^5$ Pa, in good agreement with previous results of highly crosslinked calcium alginate films (Russo et al., 2007). As expected, the semi-IPN SA/PCL-E shows an increase in the mechanical properties in both *E'* and *E''* ($5.84\cdot10^7\pm 2.6\cdot10^6$ Pa and $1.47\cdot10^7\pm 5.9\cdot10^5$ Pa, respectively) due to the presence of 10% of PCL, which possess higher mechanical strength. This enhancement in the mechanical properties indicates that the PCL chains are homogeneously dispersed in the alginate network, reinforcing its structure. It can be observed that the addition of rGO nanosheets affects the mechanical properties of the polymeric matrix, though not in the same manner. The nanohybrid hydrogel with 0.5% of rGO shows a substantial rise in the storage modulus and loss modulus ($2.28\cdot10^8\pm1.1\cdot10^7$ Pa and $4.92\cdot10^7\pm2.4\cdot10^6$ Pa, respectively). However, the addition of 2% of rGO does not increase the mechanical behaviour (*E'*=$3.70\cdot10^7\pm1\cdot10^6$ Pa and *E''*=$7.87\cdot10^6\pm2.2\cdot10^5$ Pa), but even decrease slightly its value. This deterioration of the mechanical properties may be attributed to the aggregation of rGO during the preparation of the nanohybrid hydrogel with higher amount of nanosheets. These results are consistent with other studies with graphene-based nanocomposites, where high concentrations of GO or rGO

produced a decline in the mechanical properties (Abzan et al., 2019; Mansouri et al., 2019) due to a poor dispersion of the nanoparticles in the composite matrix.

### 3.5. Electrical conductivity

rGO nanosheets were introduced into the semi-IPN SA/PCL-E with the aim of increasing its conductive properties. Conductivity was measured at frequencies of 20, 50 and 100 kHz in dry samples (Figure 4g). The semi-IPN SA/PCL-E has low conductivity, which increases significantly after adding rGO nanosheets, which have been reported to promote electronic conduction across the entire range of frequencies (H. Jo et al., 2017; Mac Kenna et al., 2015). At 100 kHz, conductivity rises from 0.43 mS/m for the semi-IPN SA/PCL to 1.33 mS/m for the nanohybrid 0.5% rGO composite and to 1.67 mS/m after adding 2% rGO nanosheets, although without reaching the percolation threshold. The results suggest possible aggregation of the rGO nanosheets, more noticeable at the higher concentration, which moderately increases conductivity in this sample (in good agreement with DMTA results). The conductivity obtained for the nanohybrid hydrogels is in the same range as other electroactive biomaterials for tissue engineering applications that have induced a cell response (L. P. da Silva et al., 2019; Song et al., 2016) and those recommended specifically for skeletal muscle applications ($8.0x10^{-4}$~$4.5x10^{-3}$ S/m) (C. Yu et al., 2021).

### 3.6. Biocompatibility

It is essential to evaluate the biomaterial cytotoxicity for biomedical applications, which was assessed for murine myoblast (C2C12 cell line) exposed to the extracts of the semi-IPN SA/PCL-E and the nanohybrid hydrogels. Both components of the polymer matrix, SA and PCL are biocompatible and biodegradable polymers widely used in the biomedical field (Farokhi et al., 2020; Siddiqui et al., 2018; Venkatesan et al., 2015). However, the cytotoxicity of carbon nanomaterials such as graphene, GO or rGO have been reported to depend not only on the concentration but to a large extent on the processing techniques used to prepare the biomaterial (Gies et al., 2019).
Figure 5a shows the cytotoxicity results after 24, 48 and 72 h exposure to the extracts. According to the ISO standard 109935, the materials are considered cytotoxic when cell viability shows values lower than 70% than the negative control. The semi-IPN SA/PCL-E and the nanohybrid hydrogels have viability values over 80% in the three evaluated times, with no significant differences from the negative control (considered as 100 % viability). This allows us to conclude that the materials are biocompatible, in good agreement with previous results in which rGO nanoparticles entrapped in polymeric matrices (Chakraborty et al., 2018; Díaz et al., 2021) were not cytotoxic even at concentrations higher than those administered in form of a solution (Mukherjee et al., 2015).

### 3.7. Myoblast adhesion on semi-IPN SA/PCL-E and nanohybrid hydrogels

Cell adhesion was studied after 24h of culture on samples pre-conditioned with protein adsorbed on the surface (Figure 5b and 5c). Myoblasts C2C12 were seeded at a low density (5000 cells/$cm^2$) to minimize cell contact. Actin staining showed that the average cell area increases significantly in the semi-IPN SA/PCL-E (mean cell area ca. 1190 $\mu m^2$) compared to the SA-E hydrogel, included as reference (mean cell area ca. 930 $\mu m^2$). The surface of hydrogels are known to show poor cell adhesion due to poor mechanical

properties, high hydrophilicity or the absence of binding sites (Abalymov et al., 2020; K. Y. Lee & Mooney, 2012). High hydrophilicity hinders protein adsorption on the biomaterial surface, a key factor in regulating cell behaviour (Mnatsakanyan, Rico, Grigoriou, Maturana Candelas, et al., 2015; Ngandu Mpoyi et al., 2016; Sahoo & Biswal, 2021; van Wachem et al., 1985), which can be overcome by combining the hydrogel with a hydrophobic polymer. Optimal hydrophilicity has been reported to enhance cell adhesion (X. J. Loh et al., 2010), which is maximized on surfaces with moderate wettability (50-70º). The wettability of the semi-IPN SA/PCL, which contains 10% of PCL, is significantly lower than that of the SA-E hydrogel (as shown by the increase in the water contact angle), which is at the limit of what is considered moderate surface wettability. The rise in the cell area in the semi-IPN SA/PCL-E seems to be related to reduced surface hydrophilicity, which facilitates protein adsorption and increases bioactivity, improving cell adhesion.

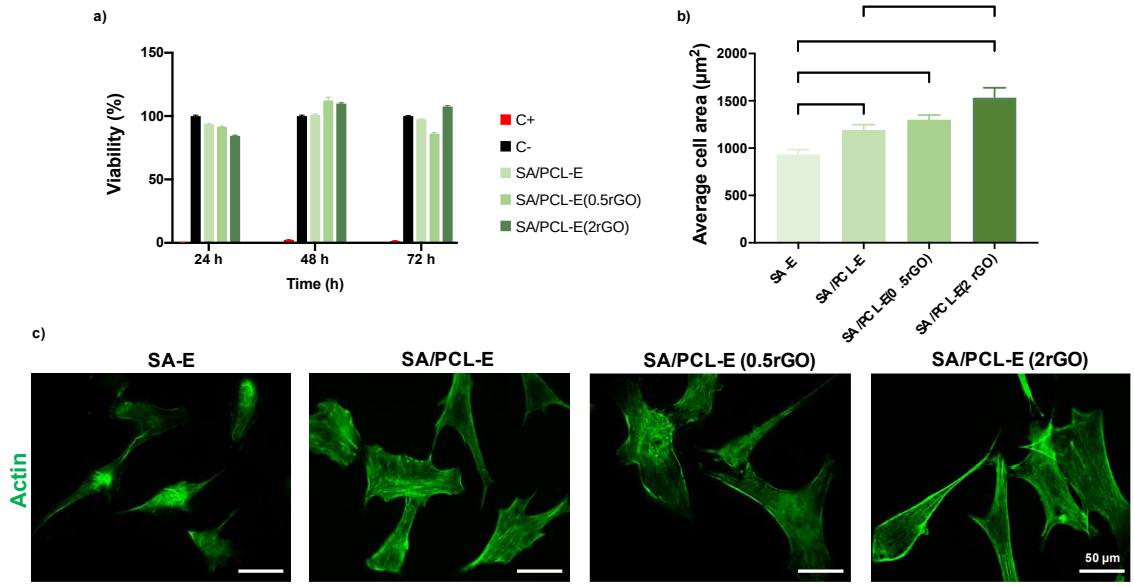


**Figure 5.** Cytotoxicity results and cell adhesion. (**a**) MTT cytotoxicity results represented as cell viability after 24, 48 and 72 h incubation with extracts from semi-IPN and nanohybrid hydrogels with 0.5% and 2% of rGO nanosheets. Positive control: latex extract, negative control: growth medium. (**b**) Average cell adhesion area for each condition from actin staining after 24 h of culture. (**c**) Representative immunofluorescence images of cells attached to the different hydrogels (actin staining) after 24 h of culture. SA-E was considered as reference. Graphs show mean ± standard deviation. (*), (**) and (***) indicate significant differences ($p<0.05$, $p<0.01$ and $p<0.001$, respectively).

After adding rGO, there was a clear trend towards higher average cell area (Fig. 5b). Both nanohybrid hydrogels (with 0.5 and 2% of rGO nanosheets) present significant differences in their average cell area to the SA-E hydrogel. The nanohybrid hydrogel with 2% rGO increases ca. by 65% and 28% with respect to the SA-E hydrogel and the semi-IPN SA/PCL-E, respectively. It has been shown that cell adhesion is enhanced in rGO-based hybrid nanomaterials (Jin et al., 2016; S. R. Shin et al., 2016; Y. Wang et al., 2017). It has also been hypothesized that rGO enables certain proteins from the culture medium to be adsorbed on the rGO surface, promoting cell adhesion (Shi et al., 2012; S. R. Shin et al., 2016). Protein adsorption is highly dependent on the physicochemical properties of the surfaces and interactions such as electrostatic forces, hydrophobic interactions and hydrogen bonding (Shi et al., 2012; Star et al., 2003). rGO nanosheets

are able to form hydrogen bonds with proteins through oxygenous groups along with electrostatic forces and hydrophobic interactions (Shi et al., 2012). The results obtained suggest that the higher cell-spreading during adhesion in the nanohybrid hydrogels after adding rGO could be related to enhanced adsorption of proteins involved in cell adhesion onto the surface of rGO-containing hydrogels.

### 3.8. Myoblast differentiation on semi-IPN SA/PCL-E and nanohybrid hydrogels

Figure 6 shows immunofluorescence images (Fig. 6a) and the quantification of myoblast differentiation on the semi-IPN and nanohybrid hydrogels with rGO nanosheets assessed after 6 days of culture in ITS-containing medium (Fig. 6b to 6e). Differentiation medium was specifically used to analyse whether, under culture conditions that favor cell differentiation, the conductive properties of the nanohybrid hydrogels stimulate myogenesis.

The semi-IPN SA/PCL-E shows a dramatic rise in myogenic differentiation of C2C12 cells compared to the SA-E hydrogel (included as reference), with a 400% increase in the number of myotubes/$cm^2$ (Fig. 6b). The ratio between the area of the myotubes and the sarcomeric α-actinin positive cells in the semi-IPN is also more than twice the ratio in the SA-E hydrogel (Fig. 6d). The morphology of the myotubes is also affected; the average myotube area and diameter in the semi-IPN is respectively 280% and 150% higher compared to the values obtained in the SA-E hydrogel (Fig. 6c and 6e). These results indicate that the cell-adhesion behaviour, with a higher cell-spreading area, is reflected in cell differentiation, as reported elsewhere (Ayala et al., 2011; Mnatsakanyan, Rico, Grigoriou, Maturana Candelas, et al., 2015). The reduced surface hydrophilicity (increased water contact angle) promotes adsorption of proteins, among them cell adhesive glycoproteins (such as fibronectin and laminin), which in turn, enhances cell adhesion (larger spreading areas) and stimulates cell differentiation (Mnatsakanyan, Rico, Grigoriou, Maturana Candelas, et al., 2015)(Ngandu Mpoyi et al., 2016) .

The nanohybrids hydrogels with 0.5 and 2% rGO nanosheets also show considerably more myoblast differentiation than both the SA-E hydrogel and the semi-IPN SA/PCL-E without nanoparticles (Fig. 6a). Conducting cell substrates have been shown to promote myogenic differentiation (Dong et al., 2017; Baolin Guo & Ma, 2018; H. S. Yang et al., 2016). The conductivity in both nanohybrid hydrogels increased substantially after adding rGO nanoparticles, as can be seen in Fig. 4f. The nanohybrid hydrogels with 2% rGO shows significant differences in cell differentiation in all the parameters analysed. The number of myotubes per $cm^2$ increase by 700% compared to the SA-E hydrogel and almost 200% as compared with the semi-IPN SA/PCL (Fig. 6b). The ratio between the area of the myotubes and the sarcomeric α-actinin positive cells in this nanohybrid hydrogel is also more than four times the ratio in the SA-E hydrogel and almost twice the ratio in the semi-IPN SA/PCL-E (Fig. 6d).

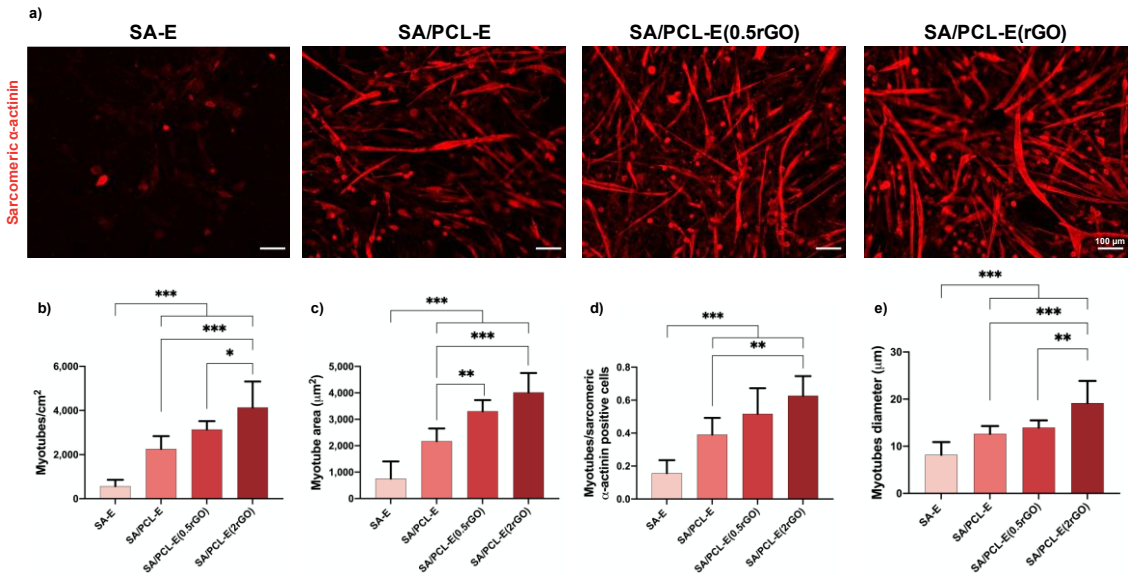


**Figure 6.** Results of myoblast differentiation. (**a**) Immunofluorescence images of differentiated myoblasts (sarcomeric α-actinin staining) after 6 days of culture in differentiation medium (DMEM+1% P/S+1%ITS). (**b**) Myotubes density represented as number of myotubes/cm$^2$. (**c**) Average myotubes area. (**d**) Ratio between the area of differentiated myotubes/area of total sarcomeric α-actinin positive cells. (**e**) Mean diameter of myotubes after analysis of 80 random myotubes per hydrogel. SA-E was considered as reference. Graphs show mean ± standard deviation. (*), (**) and (***) indicate significant differences ($p<0.05$, $p<0.01$ and $p<0.001$, respectively).

Regarding the morphology, the average area of the myotubes and the diameter show a 180% and 150% increase, respectively, compared to the semi-IPN SA/PCL (Fig. 6c and 9e). The nanohybrid hydrogels with 0.5% rGO nanosheets also show an improvement in terms of myogenic differentiation. The results, although not as marked as with 2% rGO, indicate that the average area of myotubes increases significantly. These results are in good agreement with those reported in several previous studies, where it has been suggested that electrically conductive environments, even without external electrostimulation, facilitate electrical communication between myoblasts, leading to increased myogenic differentiation (Du et al., 2018; H. Jo et al., 2017; Palmieri et al., 2020). The polymeric matrix served as elastomeric environment and rGO provided the electric conductivity. The better myoblast differentiation in the nanohybrid hydrogels than in the semi-IPN SA/PCL-E could be attributed to the increased conductivity of the cell substrate after adding rGO nanoparticles to the polymeric matrix. It should be noted that even under conditions that favor myogenic differentiation (myogenic culture medium), the conductive properties of rGO stimulate myogenesis over and above what occurs with cell substrates without conductive properties.

These results demonstrate that the combination of calcium alginate and a very small amount of PCL in the form of semi-IPN and rGO produce stable conductive nanohybrid hydrogels with enhanced physical and biological properties that show great promise for muscle tissue engineering, in good agreement with our hypothesis.

## 4. Conclusions

We developed electroactive cell substrates consisting of a novel semi-IPN SA/PCL crosslinked with $Ca^{2+}$ ions and rGO nanosheets (0.5 and 2% wt/wt rGO nanosheets) to assess its potential to stimulate cell adhesion and myogenic differentiation. Freeze-dried samples showed a homogeneous porous structure with an increase in surface roughness after adding rGO nanosheets. The FTIR, calorimetry and swelling results suggest the formation of a complex nano-network structure formed by bonds between SA chains induced by $Ca^{2+}$ ions (*egg-box* model), links between rGO nanosheets and SA chains and also between rGO nanosheets themselves through $Ca^{2+}$ ions and strong hydrogen bonding between rGO nanosheets and SA chains. Thermal stability was improved both after crosslinking though $Ca^{2+}$ ions and incorporating rGO nanosheets. The resulting electric conductivity of the nanohybrid hydrogels is expected to be suitable for electroactive tissues, including skeletal muscle. The *in vitro* biological studies with murine myoblasts revealed that the nanohybrid hydrogels are not cytotoxic and can greatly promote myoblast adhesion and myogenic differentiation. These novel nanohybrid hydrogels have shown to be promising biomaterials for the development of biomedical applications, particularly in skeletal muscle tissue engineering. Regeneration of electroactive tissues like neural and cardiac ones, are also potential applications of the nanohybrid biomaterials engineered, however, further studies are needed to explore their full potential.

## 5. Acknowledgements

Financial support from the Spanish Ministry of Science and Innovation (MCINN, AEI/FEDER funds) through the projects RTI2018-097862-B-C21 and PID2020-119333RB-I00/AEI/10.13039/501100011033 are acknowledged. CIBER-BBN initiative is funded by the VI National R&D&I Plan 2008-2011, Iniciativa Ingenio 2010, Consolider Program. CIBER actions are financed by the Instituto de Salud Carlos III with assistance from the European Regional Development Fund.

## 6. References

Abalymov, Anatolii A., Bogdan V. Parakhonskiy, and Andre G. Skirtach. 2020. “Colloids-at-Surfaces: Physicochemical Approaches for Facilitating Cell Adhesion on Hybrid Hydrogels.” *Colloids and Surfaces A: Physicochemical and Engineering Aspects* 603.

Abzan, Nadia, Mahshid Kharaziha, and Sheyda Labbaf. 2019. “Development of Three-Dimensional Piezoelectric Polyvinylidene Fluoride-Graphene Oxide Scaffold by Non-Solvent Induced Phase Separation Method for Nerve Tissue Engineering.” *Materials and Design* 167:107636.

Aparicio-Collado, José Luis, Juan José Novoa, José Molina-Mateo, Constantino Torregrosa-Cabanilles, Ángel Serrano-Aroca, and Roser Sabater I Serra. 2021. “Novel Semi-Interpenetrated Polymer Networks of Poly(3-Hydroxybutyrate-Co-3-Hydroxyvalerate)/Poly (Vinyl Alcohol) with Incorporated Conductive Polypyrrole Nanoparticles.” *Polymers* 13(1):1–21.

Ayala, Ramses, Chao Zhang, Darren Yang, Yongsung Hwang, Aereas Aung, Sumeet S. Shroff, Fernando T. Arce, Ratnesh Lal, Gaurav Arya, and Shyni Varghese. 2011. “Engineering the Cell-Material Interface for Controlling Stem Cell Adhesion,

Migration, and Differentiation." *Biomaterials* 32(15):3700–3711.

Bajpai, S. K., and Shubhra Sharma. 2004. "Investigation of Swelling/Degradation Behaviour of Alginate Beads Crosslinked with Ca2+ and Ba2+ Ions." *Reactive and Functional Polymers* 59(2):129–40.

Bellet, Pietro, Matteo Gasparotto, Samuel Pressi, Anna Fortunato, Giorgia Scapin, Miriam Mba, Enzo Menna, and Francesco Filippini. 2021. "Graphene-Based Scaffolds for Regenerative Medicine." *Nanomaterials* 11(2):1–41.

Cao, Lianqi, Wei Lu, Analucia Mata, Katsuyoshi Nishinari, and Yapeng Fang. 2020. "Egg-Box Model-Based Gelation of Alginate and Pectin: A Review." *Carbohydrate Polymers* 242:116389.

Chakraborty, S., T. Ponrasu, S. Chandel, M. Dixit, and V. Muthuvijayan. 2018. "Reduced Graphene Oxide-Loaded Nanocomposite Scaffolds for Enhancing Angiogenesis in Tissue Engineering Applications." *Royal Society Open Science* 5(5).

Compton, Owen C., and Sonbinh T. Nguyen. 2010. "Graphene Oxide, Highly Reduced Graphene Oxide, and Graphene: Versatile Building Blocks for Carbon-Based Materials." *Small* 6(6):711–23.

Díaz, Esperanza, Naroa Iglesias, Sylvie Ribeiro, and Senentxu Lanceros-Méndez. 2021. "Cytocompatible Scaffolds of Poly(L-Lactide)/Reduced Graphene Oxide for Tissue Engineering." *Journal of Biomaterials Science, Polymer Edition* 32(11):1406–19.

Dong, Ruonan, Xin Zhao, Baolin Guo, and Peter X. Ma. 2017. "Biocompatible Elastic Conductive Films Significantly Enhanced Myogenic Differentiation of Myoblast for Skeletal Muscle Regeneration." *Biomacromolecules* 18(9):2808–19.

Du, Yuzhang, Juan Ge, Yannan Li, Peter X. Ma, and Bo Lei. 2018. "Biomimetic Elastomeric, Conductive and Biodegradable Polycitrate-Based Nanocomposites for Guiding Myogenic Differentiation and Skeletal Muscle Regeneration." *Biomaterials* 157:40–50.

Dwivedi, Ruby, Sumit Kumar, Rahul Pandey, Aman Mahajan, Deepti Nandana, Dhirendra S. Katti, and Divya Mehrotra. 2020. "Polycaprolactone as Biomaterial for Bone Scaffolds: Review of Literature." *Journal of Oral Biology and Craniofacial Research* 10(1):381–88.

El-Houssiny, A. S., A. A. Ward, D. M. Mostafa, S. L. Abd-El-Messieh, K. N. Abdel-Nour, M. M. Darwish, and W. A. Khalil. 2016. "Drug-Polymer Interaction between Glucosamine Sulfate and Alginate Nanoparticles: FTIR, DSC and Dielectric Spectroscopy Studies." *Advances in Natural Sciences: Nanoscience and Nanotechnology* 7:025014.

Elzein, Tamara, Mohamad Nasser-Eddine, Christelle Delaite, Sophie Bistac, and Philippe Dumas. 2004. "FTIR Study of Polycaprolactone Chain Organization at Interfaces." *Journal of Colloid and Interface Science* 273(2):381–87.

Farokhi, Maryam, Farinaz Jonidi Shariatzadeh, Atefeh Solouk, and Hamid Mirzadeh. 2020. "Alginate Based Scaffolds for Cartilage Tissue Engineering: A Review." *International Journal of Polymeric Materials and Polymeric Biomaterials* 69(4):230–47.

Gies, Valerie, Gregory Lopinski, Jerry Augustine, Timothy Cheung, Oltion Kodra, and Shan Zou. 2019. “The Impact of Processing on the Cytotoxicity of Graphene Oxide.” *Nanoscale Advances* 1(2):817–26.

Gomaa, Mohamed, Awatief F. Hifney, Mustafa A. Fawzy, and Khayria M. Abdel-Gawad. 2018. “Use of Seaweed and Filamentous Fungus Derived Polysaccharides in the Development of Alginate-Chitosan Edible Films Containing Fucoidan: Study of Moisture Sorption, Polyphenol Release and Antioxidant Properties.” *Food Hydrocolloids* 82:239–47.

Guo, Baolin, and Peter X. Ma. 2018. “Conducting Polymers for Tissue Engineering.” *Biomacromolecules* 19(6):1764–82.

Hwang, Taeseon, Zachary Frank, Justin Neubauer, and Kwang Jin Kim. 2019. “High-Performance Polyvinyl Chloride Gel Artificial Muscle Actuator with Graphene Oxide and Plasticizer.” *Scientific Reports* 9(1):2–10.

Inoue, Haruki, Katsuyuki Kunida, Naoki Matsuda, Daisuke Hoshino, Takumi Wada, Hiromi Imamura, Hiroyuki Noji, and Shinya Kuroda. 2018. “Automatic Quantitative Segmentation of Myotubes Reveals Single-Cell Dynamics of S6 Kinase Activation.” *Cell Structure and Function* 43(2):153–69.

Jia, Li Chuan, Wen Jin Sun, Chang Ge Zhou, Ding Xiang Yan, Quan Chao Zhang, and Zhong Ming Li. 2018. “Integrated Strength and Toughness in Graphene/Calcium Alginate Films for Highly Efficient Electromagnetic Interference Shielding.” *Journal of Materials Chemistry C* 6(34):9166–74.

Jin, Lin, Dingcai Wu, Shreyas Kuddannaya, Yilei Zhang, and Zhenling Wang. 2016. “Fabrication, Characterization, and Biocompatibility of Polymer Cored Reduced Graphene Oxide Nanofibers.” *ACS Applied Materials and Interfaces* 8(8):5170–77.

Jo, Hyerim, Myeongbu Sim, Semin Kim, Sumi Yang, Youngjae Yoo, Jin Ho Park, Tae Ho Yoon, Min Gon Kim, and Jae Young Lee. 2017. “Electrically Conductive Graphene/Polyacrylamide Hydrogels Produced by Mild Chemical Reduction for Enhanced Myoblast Growth and Differentiation.” *Acta Biomaterialia* 48:100–109.

Jo, Seung Bin, Uyanga Erdenebileg, Khandmaa Dashnyam, Guang Zhen Jin, Jae Ryung Cha, Ahmed El-Fiqi, Jonathan C. Knowles, Kapil Dev Patel, Hae Hyoung Lee, Jung Hwan Lee, and Hae Won Kim. 2020. “Nano-Graphene Oxide/Polyurethane Nanofibers: Mechanically Flexible and Myogenic Stimulating Matrix for Skeletal Tissue Engineering.” *Journal of Tissue Engineering* 11.

Kang, Moon Sung, Jeon Il Kang, Phuong Le Thi, Kyung Min Park, Suck Won Hong, Yu Suk Choi, Dong Wook Han, and Ki Dong Park. 2021. “Three-Dimensional Printable Gelatin Hydrogels Incorporating Graphene Oxide to Enable Spontaneous Myogenic Differentiation.” *ACS Macro Letters* 10(4):426–32.

Mac Kenna, Nicky, Paul Calvert, Aoife Morrin, Gordon G. Wallace, and Simon E. Moulton. 2015. “Electro-Stimulated Release from a Reduced Graphene Oxide Composite Hydrogel.” *Journal of Materials Chemistry B* 3(12):2530–37.

Ku, Sook Hee, Minah Lee, and Chan Beum Park. 2013. “Carbon-Based Nanomaterials for Tissue Engineering.” *Advanced Healthcare Materials* 2(2):244–60.

Laurienzo, P., M. Malinconico, A. Motta, and A. Vicinanza. 2005. “Synthesis and

Characterization of a Novel Alginate-Poly(Ethylene Glycol) Graft Copolymer." *Carbohydrate Polymers* 62:274–82.

Lee, Eunjee A., Seon Yeong Kwak, Jin Kyoung Yang, Yoon Sik Lee, Jong Ho Kim, Hwan D. Kim, and Nathaniel S. Hwang. 2021. "Graphene Oxide Film Guided Skeletal Muscle Differentiation." *Materials Science and Engineering C* 126(February).

Lee, Jong Ho, Yunki Lee, Yong Cheol Shin, Min Jeong Kim, Ji Hoon Park, Suck Won Hong, Bongju Kim, Jin Woo Oh, Ki Dong Park, and Dong Wook Han. 2016. "In Situ Forming Gelatin/Graphene Oxide Hydrogels for Facilitated C2C12 Myoblast Differentiation." *Applied Spectroscopy Reviews* 51(7–9):527–39.

Lee, Kuen Yong, and David J. Mooney. 2012. "Alginate: Properties and Biomedical Applications." *Progress in Polymer Science (Oxford)* 37(1):106–26.

Llorens-Gámez, Mar, Beatriz Salesa, and Ángel Serrano-Aroca. 2020. "Physical and Biological Properties of Alginate/Carbon Nanofibers Hydrogel Films." *International Journal of Biological Macromolecules* 151:499–507.

Llorens-Gámez, Mar, and Ángel Serrano-Aroca. 2018. "Low-Cost Advanced Hydrogels of Calcium Alginate/Carbon Nanofibers with Enhanced Water Diffusion and Compression Properties." *Polymers* 10(4):405.

Loh, Kian Ping, Qiaoliang Bao, Priscilla Kailian Ang, and Jiaxiang Yang. 2010. "The Chemistry of Graphene." *Journal of Materials Chemistry* 20(12):2277–89.

Loh, Xian Jun, Priscilla Peh, Susan Liao, Colin Sng, and Jun Li. 2010. "Controlled Drug Release from Biodegradable Thermoresponsive Physical Hydrogel Nanofibers." *Journal of Controlled Release* 143(2):175–82.

Mansouri, Negar, Said F. Al-Sarawi, Jagan Mazumdar, and Dusan Losic. 2019. "Advancing Fabrication and Properties of Three-Dimensional Graphene-Alginate Scaffolds for Application in Neural Tissue Engineering." *RSC Advances* 9(63):36838–48.

Martí, M., B. Frígols, B. Salesa, and Á. Serrano-Aroca. 2019. "Calcium Alginate/Graphene Oxide Films: Reinforced Composites Able to Prevent Staphylococcus Aureus and Methicillin-Resistant Staphylococcus Epidermidis Infections with No Cytotoxicity for Human Keratinocyte HaCaT Cells." *European Polymer Journal* 110.

Mnatsakanyan, Hayk, Patricia Rico, Eleni Grigoriou, Aarón Maturana Candelas, Aleixandre Rodrigo-Navarro, Manuel Salmeron-Sanchez, and Roser Sabater I Serra. 2015. "Controlled Assembly of Fibronectin Nanofibrils Triggered by Random Copolymer Chemistry." *ACS Applied Materials & Interfaces* 7(32):18125–35.

Mondal, Debasish, May Griffith, and Subbu S. Venkatraman. 2016. "Polycaprolactone-Based Biomaterials for Tissue Engineering and Drug Delivery: Current Scenario and Challenges." *International Journal of Polymeric Materials and Polymeric Biomaterials* 65(5):255–65.

Mukherjee, Sudip, Pavithra Sriram, Ayan Kumar Barui, Susheel Kumar Nethi, Vimal Veeriah, Suvro Chatterjee, Kattimuttathu Ittara Suresh, and Chitta Ranjan Patra. 2015. "Graphene Oxides Show Angiogenic Properties." *Advanced Healthcare Materials*

4(11):1722–32.

Ngandu Mpoyi, Elie, Marco Cantini, Paul M. Reynolds, Nikolaj Gadegaard, Matthew J. Dalby, and Manuel Salmerón-Sánchez. 2016. “Protein Adsorption as a Key Mediator in the Nanotopographical Control of Cell Behavior.” *ACS Nano* 10(7):6638–47.

Novoselov, K. S., A. K. Geim, S. V Morozov, D. Jiang, Y. Zhang, S. V Dubonos, I. V Grigorieva, and A. A. Firsov. 2004. “Electric Field Effect in Atomically Thin Carbon Films.” *Science (New York, N.Y.)* 306(5696):666–69.

Palmieri, Valentina, Francesca Sciandra, Manuela Bozzi, Marco De Spirito, and Massimiliano Papi. 2020. “3D Graphene Scaffolds for Skeletal Muscle Regeneration: Future Perspectives.” *Frontiers in Bioengineering and Biotechnology* 8(May):1–8.

Park, Sungjin, Kyoung Seok Lee, Gulay Bozoklu, Weiwei Cai, Son Binh T. Nguyen, and Rodney S. Ruoff. 2008. “Graphene Oxide Papers Modified by Divalent Ions - Enhancing Mechanical Properties via Chemical Cross-Linking.” *ACS Nano* 2(3):572–78.

Patel, Akhil, Yingfei Xue, Rebecca Hartley, Vinayak Sant, James R. Eles, Xinyan Tracy Cui, Donna Beer Stolz, and Shilpa Sant. 2018. “Hierarchically Aligned Fibrous Hydrogel Films through Microfluidic Self-Assembly of Graphene and Polysaccharides.” *Biotechnology and Bioengineering* 115(10):2654–67.

Pathak, Tara Sankar, Jung Ho Yun, Joonbae Lee, and Ki Jung Paeng. 2010. “Effect of Calcium Ion (Cross-Linker) Concentration on Porosity, Surface Morphology and Thermal Behavior of Calcium Alginates Prepared from Algae (Undaria Pinnatifida).” *Carbohydrate Polymers* 81(3):633–39.

Rashtchian, Morvarid, Ahmad Hivechi, S. Hajir Bahrami, Peiman B. Milan, and Sara Simorgh. 2020. “Fabricating Alginate/Poly(Caprolactone) Nanofibers with Enhanced Bio-Mechanical Properties via Cellulose Nanocrystal Incorporation.” *Carbohydrate Polymers,* 233, 115873.

Rivera-Briso, Ariagna L., Finn Lillelund Aachmann, Victoria Moreno-Manzano, and Ángel Serrano-Aroca. 2019. “Graphene Oxide Nanosheets versus Carbon Nanofibers: Enhancement of Physical and Biological Properties of Poly(3-Hydroxybutyrate-Co-3-Hydroxyvalerate) Films for Biomedical Applications.” *International Journal of Biological Macromolecules*.

Rowley, Jon A., Gerard Madlambayan, and David J. Mooney. 1999. “Alginate Hydrogels as Synthetic Extracellular Matrix Materials.” *Biomaterials* 20(1):45–53.

Russo, R., M. Malinconico, and G. Santagata. 2007. “Effect of Cross-Linking with Calcium Ions on the Physical Properties of Alginate Films.” *Biomacromolecules* 8(10):3193–97.

Sabater i Serra, R., J. Molina-mateo, C. Torregrosa-cabanilles, A. Andrio-Balado, JM Meseguer Dueñas, and A. Serrano-Aroca. 2020. “Bio-Nanocomposite Hydrogel Based on Zinc Conformation , Thermal Behavior / Degradation , and Dielectric Properties.” *Polymers* 12:702.

Sahoo, Deepti Rekha, and Trinath Biswal. 2021. “Alginate and Its Application to Tissue Engineering.” *SN Applied Sciences* 3(1):1–19.

Serrano-Aroca, Ángel, María Ferrandis-Montesinos, and Ruibing Wang. 2021. “Antiviral Properties of Alginate-Based Biomaterials: Promising Antiviral Agents against SARS-CoV-2.” *ACS Applied Bio Materials* 4(8):5897–5907.

Serrano-Aroca, Ángel, Lilis Iskandar, and Sanjukta Deb. 2018. “Green Synthetic Routes to Alginate-Graphene Oxide Composite Hydrogels with Enhanced Physical Properties for Bioengineering Applications.” *European Polymer Journal* 103:198–206.

Serrano-Aroca, Ángel, Juan Francisco Ruiz-Pividal, and Mar Llorens-Gámez. 2017. “Enhancement of Water Diffusion and Compression Performance of Crosslinked Alginate Films with a Minuscule Amount of Graphene Oxide.” *Scientific Reports* 7(1):1–8.

Shi, Xuetao, Haixin Chang, Song Chen, Chen Lai, Ali Khademhosseini, and Hongkai Wu. 2012. “Regulating Cellular Behavior on Few-Layer Reduced Graphene Oxide Films with Well-Controlled Reduction States.” *Advanced Functional Materials* 22(4):751–59.

Shin, Su Ryon, Claudio Zihlmann, Mohsen Akbari, Pribpandao Assawes, Louis Cheung, Kaizhen Zhang, Vijayan Manoharan, Yu Shrike Zhang, Mehmet Yüksekkaya, Kai Tak Wan, Mehdi Nikkhah, Mehmet R. Dokmeci, Xiaowu Shirley Tang, and Ali Khademhosseini. 2016. “Reduced Graphene Oxide-GelMA Hybrid Hydrogels as Scaffolds for Cardiac Tissue Engineering.” *Small* 12(27):3677–89-

Shin, Yong Cheol, Seok Hee Kang, Jong Ho Lee, Bongju Kim, Suck Won Hong, and Dong Wook Han. 2018. “Three-Dimensional Graphene Oxide-Coated Polyurethane Foams Beneficial to Myogenesis.” *Journal of Biomaterials Science, Polymer Edition* 29(7–9):762–74.

Shin, Yong Cheol, Jong Ho Lee, Linhua Jin, Min Jeong Kim, Yong Joo Kim, Jung Keun Hyun, Tae Gon Jung, Suck Won Hong, and Dong Wook Han. 2015. “Stimulated Myoblast Differentiation on Graphene Oxide-Impregnated PLGA-Collagen Hybrid Fibre Matrices Matrices.” *Journal of Nanobiotechnology* 13(1):1–11.

Siddiqui, Nadeem, Simran Asawa, Bhaskar Birru, Ramaraju Baadhe, and Sreenivasa Rao. 2018. “PCL-Based Composite Scaffold Matrices for Tissue Engineering Applications.” *Molecular Biotechnology* 60(7):506–32.

da Silva, Lucília P., Subhas C. Kundu, Rui L. Reis, and Vitor M. Correlo. 2020. “Electric Phenomenon: A Disregarded Tool in Tissue Engineering and Regenerative Medicine.” *Trends in Biotechnology* 38(1):24–49.

Šišková, Alena Opálková, Mária Bučková, Zuzana Kroneková, Angela Kleinová, Štefan Nagy, Joanna Rydz, Andrej Opálek, Monika Sláviková, and Anita Eckstein Andicsová. 2021. “The Drug-Loaded Electrospun Poly(ε-Caprolactone) Mats for Therapeutic Application.” *Nanomaterials* 11(4).

Song, Jialin, Binbin Sun, Shen Liu, Wei Chen, Yuanzheng Zhang, Chunyang Wang, Xiumei Mo, Junyi Che, Yuanming Ouyang, Weien Yuan, and Cunyi Fan. 2016. “Polymerizing Pyrrole Coated Poly (l-Lactic Acid-Co-ε-Caprolactone) (PLCL) Conductive Nanofibrous Conduit Combined with Electric Stimulation for Long-Range Peripheral Nerve Regeneration.” *Frontiers in Molecular Neuroscience* 9:117.

Star, Alexander, Yi Liu, Kevin Grant, Ludek Ridvan, J. Fraser Stoddart, David W.

Steuerman, Michael R. Diehl, Akram Boukai, and James R. Heath. 2003. “Noncovalent Side-Wall Functionalization of Single-Walled Carbon Nanotubes.” *Macromolecules* 36(3):553–60.

Sun, Xiaoqing, Chao Ma, Wenli Gong, Yanan Ma, Yanhong Ding, and Lin Liu. 2020. “Biological Properties of Sulfanilamide-Loaded Alginate Hydrogel Fibers Based on Ionic and Chemical Crosslinking for Wound Dressings.” *International Journal of Biological Macromolecules* 157:522–29.

Tranquillo, Elisabetta, Federico Barrino, Giovanni Dal Poggetto, and Ignazio Blanco. 2019. “Sol-Gel Synthesis of Silica-Based Materials with Different Percentages of PEG or PCL and High Chlorogenic Acid Content.” *Materials* 12(1).

Tyagi, Nishant, Kirtida Gambhir, Rakesh Pandey, Gurudutta Gangenahalli, and Yogesh Kumar Verma. 2022. “Minimizing the Negative Charge of Alginate Facilitates the Delivery of Negatively Charged Molecules inside Cells.” *Journal of Polymer Research* 29(1).

Venkatesan, Jayachandran, Ira Bhatnagar, Panchanathan Manivasagan, Kyong Hwa Kang, and Se Kwon Kim. 2015. “Alginate Composites for Bone Tissue Engineering: A Review.” *International Journal of Biological Macromolecules* 72:269–81.

van Wachem, P. B., T. Beugeling, J. Feijen, A. Bantjes, J. P. Detmers, and W. G. van Aken. 1985. “Interaction of Cultured Human Endothelial Cells with Polymeric Surfaces of Different Wettabilities.” *Biomaterials* 6(6):403–8.

Wang, Yifan, Ying Xiao, Guorong Gao, Jing Chen, Ruixia Hou, Qiang Wang, Li Liu, and Jun Fu. 2017. “Conductive Graphene Oxide Hydrogels Reduced and Bridged by L-Cysteine to Support Cell Adhesion and Growth.” *Journal of Materials Chemistry B* 5(3):511–16.

Wu, Xu, Shirui Tan, Yuqian Xing, Qinqin Pu, Min Wu, and Julia Xiaojun Zhao. 2017. “Graphene Oxide as an Efficient Antimicrobial Nanomaterial for Eradicating Multi-Drug Resistant Bacteria in Vitro and in Vivo.” *Colloids and Surfaces B: Biointerfaces* 157:1–9.

Xiao, Chaobo, Lihui Weng, and Lina Zhang. 2002. “Improvement of Physical Properties of Crosslinked Alginate and Carboxymethyl Konjac Glucomannan Blend Films.” *Journal of Applied Polymer Science* 84(13):2554–60.

Yang, Hee Seok, Bora Lee, Jonathan H. Tsui, Jesse Macadangdang, Seok Young Jang, Sung Gap Im, and Deok Ho Kim. 2016. “Electroconductive Nanopatterned Substrates for Enhanced Myogenic Differentiation and Maturation.” *Advanced Healthcare Materials* 5(1):137–45.

Yang, Lijun, Wei Weng, Xiang Fei, Liang Pan, Xinao Li, Wenting Xu, Zexu Hu, and Meifang Zhu. 2020. “Revealing the Interrelation between Hydrogen Bonds and Interfaces in Graphene/PVA Composites towards Highly Electrical Conductivity.” *Chemical Engineering Journal* 383:123126.

Yang, Zhe, Hongdan Peng, Weizhi Wang, and Tianxi Liu. 2010. “Crystallization Behavior of Poly(ε-Caprolactone)/Layered Double Hydroxide Nanocomposites.” *Journal of Applied Polymer Science* 116(5):2658–67.

Yu, Chaojie, Fanglian Yao, and Junjie Li. 2021. “Rational Design of Injectable

Conducting Polymer-Based Hydrogels for Tissue Engineering.” *Acta Biomaterialia*.

Zeng, Yuqiang, Tian Li, Yonggang Yao, Tangyuan Li, Liangbing Hu, and Amy Marconnet. 2019. “Thermally Conductive Reduced Graphene Oxide Thin Films for Extreme Temperature Sensors.” *Advanced Functional Materials* 29(27):1901388.

Zhang, Li Li, Xin Zhao, Meryl D. Stoller, Yanwu Zhu, Hengxing Ji, Shanthi Murali, Yaping Wu, Stephen Perales, Brandon Clevenger, and Rodney S. Ruoff. 2012. “Highly Conductive and Porous Activated Reduced Graphene Oxide Films for High-Power Supercapacitors.” *Nano Letters* 12(4):1806–12.

Zhao, Wanting, Yan Qi, Yue Wang, Yun Xue, Peng Xu, Zichao Li, and Qun Li. 2018. “Morphology and Thermal Properties of Calcium Alginate/Reduced Graphene Oxide Composites.” *Polymers* 10(9):1–11.

Zheng, Haicheng, Jisheng Yang, and Suya Han. 2016. “The Synthesis and Characteristics of Sodium Alginate / Graphene Oxide Composite Films Crosslinked with Multivalent Cations.” *Journal of Applied Polymer Science* 43616.

# Chapter 3

# Pro-myogenic environment promoted by the synergistic effect of conductive polymer nanocomposites combined with extracellular zinc ions

Chapter published in **Biology**

José Luís Aparicio-Collado, José Molina-Mateo, Constantino Torregrosa-Cabanilles, Ana Vidaurre-Garayo, Beatriz Salesa, Ángel Serrano-Aroca, Roser Sabater i Serra. Pro-Myogenic Environments Promoted by the Synergistic Effect of Conductive Polymer Nanocomposites Combined with Extracellular Zinc Ions. *Biology* 2022, 11, 1706. DOI: 10.3390/biology11121706.

**Personal contributions**

Materials' synthesis, morphological analysis, physicochemical characterization and biological evaluation were carried out by J. L. Aparicio-Collado. B. Salesa performed data curation from gene expression analysis experiments.

J. L. Aparicio-Collado wrote the first version of the manuscript. J. Molina-Mateo, C. Torregrosa-Cabanilles, A. Vidaurre-Garayo, Á. Serrano-Aroca and R. Sabater i Serra contributed in experimental conceptualization, manuscript revision and funding acquisition.

# Pro-myogenic environment promoted by the synergistic effect of conductive polymer nanocomposites combined with extracellular zinc ions

José Luis Aparicio-Collado [1], José Molina-Mateo [1], Constantino Torregrosa Cabanilles [1], Ana Vidaurre [1,3], Beatriz Salesa [4], Ángel Serrano-Aroca [4] and Roser Sabater i Serra [1,2,3]

[1]Centre for Biomaterials and Tissue Engineering, Universitat Politècnica de València, Spain

[2]Department of Electrical Engineering, Universitat Politècnica de València, Spain

[3]Biomaterials and Bioengineering Lab, Centro de Investigación Traslacional San Alberto Magno, Universidad Católica de Valencia San Vicente Mártir, Valencia, Spain

[4]Biomedical Research Networking Centre in Bioengenieering, Biomaterials and Nanomedicine (CIBER-BBN), Spain

**Abstract**

A new strategy based on the combination of electrically conductive polymer nanocomposites and extracellular $Zn^{2+}$ ions as a myogenic factor was developed to assess its ability to synergically stimulate myogenic cell response. The conductive nanocomposite was prepared with a polymeric matrix and a small amount of graphene (G) nanosheets (0.7% *wt/wt*) as conductive filler to produce an electrically conductive surface. The nanocomposites' surface electrical conductivity presented values in the range of human skeletal muscle tissue. The biological evaluation of the cell environment created by the combination of the conductive surface and extracellular $Zn^{2+}$ ions showed no cytotoxicity and good cell adhesion (murine C2C12 myoblasts). Amazingly, the combined strategy, cell–material interface with conductive properties and Zn bioactive ions, was found to have a pronounced synergistic effect on myoblast proliferation and the early stages of differentiation. The ratio of differentiated myoblasts cultured on the conductive nanocomposites with extracellular $Zn^{2+}$ ions added in the differentiation medium (serum-deprived medium) was enhanced by more than 170% over that of non-conductive surfaces (only the polymeric matrix), and more than 120% over both conductive substrates (without extracellular $Zn^{2+}$ ions) and non-conductive substrates with extracellular $Zn^{2+}$. This synergistic effect was also found to increase myotube density, myotube area and diameter, and multinucleated myotube formation. MyoD-1 gene expression was also enhanced, indicating the positive effect in the early stages of myogenic differentiation. These results demonstrate the great potential of this combined strategy, which stands outs for its simplicity and robustness, for skeletal muscle tissue engineering applications.

**Keywords:** pro-myogenic environment, bioactive cell-material interface, conductive polymer nanocomposites, zinc ions, carbon nanomaterials, graphene, skeletal muscle tissue engineering.

## 1. Introduction

The musculoskeletal system, responsible for the movement and support of any vertebrate model, is a complex tissue composed of aligned multinucleated and contractile cells known as myofibres (Palmieri et al., 2020). Musculoskeletal tissue can self-regenerate after injury in a coordinated process by recruiting immature and quiescent satellite cells (Francesco et al., 2010). These cells proliferate, fuse, and differentiate into myoblasts that reorganize themselves to form, first, myotubes, and then myofibres. However, this self-renewal capacity is limited in degenerative diseases or volumetric muscle loss, resulting in fibrosis and muscular impairment (Corona et al., 2013). Although different treatments (cell and gene therapies, autotransplants, allotransplants, or xenotransplants) are able to enhance muscle regeneration, none of them seems to successfully overcome the issue due to immunogenicity, poor cell survival or lack of stability (Mertens et al., 2014; Qazi et al., 2015). Tissue engineering (TE) has emerged as a tool to regenerate damaged or lost tissue by providing cells with an environment that mimics the extracellular matrix (ECM) so that they can proliferate and differentiate into new tissue (Eltom et al., 2019; J. L. Guo et al., 2019; McCullagh & Perlingeiro, 2015). Skeletal muscle TE has been shown to stimulate survival and differentiation of myoblasts towards tissue regeneration both in vitro and in vivo (Cezar & Mooney, 2015; Langridge et al., 2021; Qazi et al., 2015).

Functional muscle tissue contracts in response to the electrical signals produced by motoneurons. Electrochemical cues are essential for both myofibre motility and myoblast differentiation in a still unknown mechanism that seems to be related to the induction of the calcineurin pathway mediated by ion flow through the cell membrane (Dong et al., 2020; Flaibani et al., 2009; X. Zhao et al., 2017) In this context, electroconductive scaffolds based on polymeric matrices with incorporated conductive polymers, such as poly(3,4-ethylenedioxythiophene), polypyrrole (PPy), polyaniline or carbon nanomaterials (CNMs), have been developed for muscle regeneration (José Luis Aparicio-Collado et al., 2021; Berti et al., 2017; McKeon-Fischer et al., 2015; Ostrovidov et al., 2017; Velasco-Mallorquí et al., 2020; Y. Wu et al., 2018). Graphene nanomaterials are a family of CNMs that include few-layer graphene, graphene nanosheets, graphene quantum dots, graphene oxide (GO), and reduced-graphene oxide (rGO) (Smith et al., 2019). Graphene (G) is a polycyclic aromatic hydrocarbon with potential applications in TE thanks to its excellent mechanical properties, high conductivity, biocompatibility, and nanoscale surface roughness able to match cell receptors and mimic the ECM (Bellet et al., 2021). It has been used in combination with different polymers, such as chitosan, gellan gum, or polycaprolactone (PCL) to prepare composite biomaterials that induced muscle regeneration (Palmieri et al., 2020; A. Patel et al., 2016, 2018). However, its cellular toxicity and immunological effects are both concerns that must be taken into account when CNMs are proposed for biomedical (Raja et al., 2019; Yuan et al., 2019). It has been reported that CNM biocompatibility is highly dependent on the concentration and processing techniques used to obtain the biomaterial (Chaudhuri et al., 2015; Gies et al., 2019). Cardiac, neural, and skeletal muscle tissues have electrical stimuli-responsible properties. Thus, the conductive properties of in vitro models are an important tool in the reproduction of in vivo environments, which have electrical properties related to the diffusion of electrical charges within the ECM (L. P. da Silva et al., 2019). Conductive biomaterials, such as graphene-based biomaterials, even in the

absence of electrical stimulation, have been shown to stimulate cell response in skeletal muscle cell differentiation (Kim et al., 2019; Yang et al., 2016). In a recent study, we engineered electroactive nanohybrid hydrogels based on sodium alginate/PCL semi-IPNs with rGO nanosheets, which possess conductive properties in the range of muscle tissue (Aparicio-Collado et al., 2022). Myoblast adhesion and myogenic differentiation were greatly enhanced with the incorporation of 2% of conductive rGO nanosheets.
The role of biomaterials is not only to provide structural support for tissue regeneration, but also to include some biophysical and biochemical cues that enhance cell proliferation and/or differentiation into different tissues. The use of growth factors, such as vascular endothelial growth factor (VEGF) and insulin-like growth factor (IGF), have been reported to stimulate myoblast proliferation, differentiation, and myotube formation (Rybalko et al., 2015; Syverud et al., 2016) although they can also generate problems related to alteration in cell homeostasis and risk of cancer (Briquez et al., 2015). Bioactive molecules, including bio-ceramics and therapeutic inorganic ions, have been investigated for tissue regeneration due to their ability to stimulate tissue regeneration without the disadvantages of growth factors (Baino et al., 2015; Mouriño et al., 2012). Promising results have been obtained with biometals in the field of regenerative medicine, due mainly to their stability and ability to induce cell response. Trace elements, such as copper, iron, or zinc, are considered therapeutic ions (Ramalingam & Hwang, 2020; Salesa et al., 2021; Su et al., 2019). In particular, zinc biometal, both as inorganic ion ($Zn^{2+}$) and zinc oxide nanoparticles, is being studied for its role as myogenic factor, since it has been shown to induce cell proliferation, differentiation, and migration, accelerating in vitro muscle formation (Mnatsakanyan et al., 2018; Salesa et al., 2021). Zinc homeostasis is essential for skeletal muscle tissue (Jinno et al., 2014) and regulates different metabolic signalling pathways, such as the phosphoinositide 3′-kinase (PI3K)/Akt pathway, directly involved in skeletal myogenesis (Briata et al., 2012; Sumitani et al., 2002). Extracellular $Zn^{2+}$ stimulates the PI3K/Akt pathway through stimulating the Zip7 transporter in murine C2C12 cells, considerably raising proliferation and myogenic differentiation (Mnatsakanyan et al., 2018).

Although both electrically conductive surfaces and extracellular zinc ions have been reported to stimulate myoblast differentiation (as we showed in previous studies ( Aparicio-Collado et al., 2022; Mnatsakanyan et al., 2018), to the best of our knowledge, there is no evidence in the literature on their possible synergistic effects in myogenesis when used together.

In this study, we engineered electrically conductive nanocomposites based on a polymeric matrix with incorporated G nanosheets, which will enhance bioactivity in the form of intrinsic surface conductivity, close to that of human skeletal muscle tissue. In addition, extracellular $Zn^{2+}$ ions were incorporated in the cell microenvironment (culture medium) as myogenic factor. The concentration of $Zn^{2+}$ ions in the culture medium (40 µM) was based on previous results (Mnatsakanyan et al., 2018), which showed that this specific concentration induced a positive effect on myogenesis stimulation.

We have chosen a polymer matrix based on PCL, the well-known biomaterial approved by the Food and Drug Administration (FDA), widely used in biomedical applications due to its excellent biocompatibility, physicochemical properties, and good processability (Abedalwafa et al., 2013). TE approaches have used PCL extensively as a cell substrate to enhance the regeneration of different bone, cartilage, skin, nerve, dental, or skeletal muscle tissue (Aragón et al., 2018; Oh et al., 2007; Siddiqui et al., 2018) with different

configurations, such as flat substrates (Siddiqui et al., 2018), nanofibres (Fasolino et al., 2017), interconnected channel networks (Zein et al., 2002), or 3D printed supports (Ostrovidov et al., 2019). Highly conductive CNMs, particularly G and rGO nanoparticles, are good candidates for engineering electrically conductive nanocomposites, although the conductive properties of G are higher than those of rGO. Thus, a very small percentage of G nanosheets was selected to avoid potential cytotoxicity effects, and to reduce costs, since CNMs are still expensive materials.

The aim of this work was thus to test a new strategy for skeletal muscle TE based on the combination of conductive polymer nanocomposites (electrically conductive surface) together with a specific extracellular zinc ($Zn^{2+}$) concentration on myoblast adhesion, proliferation, and the early stages of myogenic differentiation. We hypothesized that the combination of both approaches would act synergically to generate enhanced cell microenvironments, promote myogenesis, and so become a simple, effective, and low-cost tool applicable to skeletal muscle TE.

## 2. Materials and methods

### 2.1. Materials

Polycaprolactone (MW: 43–50 kDa) was supplied by Polysciences, Warrington, USA (Reference 19561). Graphene powder in the form of nanosheets (Reference 900561), and Zinc Chloride ($ZnCl_2$) (Reference Z0152) were purchased from Merk. Tetrahydrofuran (THF) was bought from Scharlab, Spain (Reference TE02282500). All the reagents were used as received.

### 2.2. Preparation of conductive cell substrates

Polycaprolactone was dissolved at a 3% *wt/wt* concentration in THF under constant stirring at 25 °C for two hours and transferred into Petri dishes. Neat PCL films (reference sample) were obtained after 72 h of solvent evaporation at room temperature (RT). The protocol for preparing cell substrates with a conductive surface was adapted from previous studies (Aparicio-Collado et al., 2021, 2022). Briefly, 14 mg of G nanosheets (0.7% *wt/wt* of the polymer mass) were dispersed in 72.2 mL of THF in an ultrasonic bath for 6 h. Then, 2 g of PCL was added to the previous dispersion, left with constant stirring at RT for two hours, and finally poured into Petri dishes. PCL/G films (thickness between 120 and 140 µm) were obtained after solvent evaporation at RT for 72 h. The G nanosheets were expected to precipitate during solvent evaporation, forming a conductive surface layer of G nanosheets wrapped by the polymer matrix. The samples were finally vacuum-dried until constant weight to eliminate any residual solvent.

### 2.3. Morphological and physicochemical characterization of conductive cell substrates

The cell substrates morphology was analysed by field emission scanning electron microscopy (FESEM) (Zeiss Ultra 55, Carl Zeiss Microscopy, Germany) with an accelerating voltage of 3 kV. Samples were coated with a platinum layer using a sputter coating (EM MED020, Leica, Germany). The cross-section was observed by cryogenic fracture with liquid nitrogen. The morphology of the G nanosheets, previously dispersed in THF, was studied by high-resolution field-emission scanning electron microscopy

(HRFSEM) (GeminiSEM 500, Carl Zeiss Microscopy, Germany) at acceleration voltages ranging between 0.7 and 1.5 kV.

Differential scanning calorimetry (DSC) (Perkin-Elmer DSC 8000, Perkin Elmer, USA) was performed under a flowing nitrogen atmosphere (20 mL/min) to analyse thermal behaviour. Samples were first heated up to 100 °C to erase the thermal history, followed by a cooling scan from 100 °C to −80 °C, ending with a second heating scan from –80 °C to 100 °C. All the scans were carried out at 20 °C/min. The glass transition temperature, $T_g$, was calculated from the second heating scan as the inflexion point of the specific heat capacity, $C_p$, vs. temperature, which coincides with a peak in the derivative heat capacity ($dC_p/dT$).

The PCL degree of crystallinity was obtained as:

$$X_c(\%) = \frac{\Delta H_f}{\Delta H_f^0} \cdot 100 \quad (1)$$

where $\Delta H_f$ is the enthalpy of fusion of the samples and $\Delta H_f^0$ the enthalpy of fusion of totally crystalline PCL (139.5 J/g) (Sabater I Serra et al., 2011).

The thermal stability and decomposition were analysed by thermogravimetric analysis (TGA) (Mettler Toledo TGA 2 (SF), Mettler Toledo, USA). Vacuum-dried samples (≈ 5 mg mass) were heated from ambient temperature to 600 °C at a heating rate of 30 °C/min. The mass of the samples was recorded over the temperature range.

The mechanical properties of the substrates were studied by dynamic mechanical thermal analysis (DMA 8000, Perkin Elmer, Waltham, Massachusetts, USA) in sample bars (30 × 10 × 0,1 mm) operating in traction mode. The temperature dependence of the complex modulus E* (storage modulus (*E'*) and loss modulus (*E''*) was measured from −80 °C to 50 °C with a rate of 3 °C/min under a nitrogen atmosphere.

The electrical sheet resistance ($R_S$) of neat PCL and PCL/G samples (10 mm diameter) was measured on a four-point probe system (T2001A3-EU, Ossila Ltd., Sheffield, UK). The electrical conductivity ($\sigma$) was obtained using the following expression:

$$\sigma = \frac{1}{R_S \times l} \quad (2)$$

where *l* is the film thickness, obtained with a digital caliper (Acha, Guipúzcoa, Spain). The measurements were carried out in triplicate to ensure reproducibility.

## 2.4. Biological Evaluation

### 2.4.1. Cell Culture

Murine C2C12 myoblasts (Sigma-Aldrich-Merck) were expanded in a growth medium composed of high glucose Dulbecco's Modified Eagle's Medium (DMEM), (Biowest) supplemented with 10% fetal bovine serum (FBS, ThermoFisher), and 1% penicillin/streptomycin (P/S) (ThermoFisher) (growth medium) in 5% $CO_2$ at 37 °C. Cells were passed during amplification upon reaching 80% confluence. All the experiments were performed on cells between six and eight passages. Four conditions were evaluated: non-conductive surfaces without additional extracellular $Zn^{2+}$ ions (PCL condition), conductive nanocomposite surfaces (PCL/G) without extracellular $Zn^{2+}$

(PCL/G condition), non-conductive surfaces with extracellular $Zn^{2+}$ (PCL/Zn condition), and conductive nanocomposite surfaces with extracellular $Zn^{2+}$ (PCL/G/Zn condition). $ZnCl_2$ (concentration 40 µM), added to the culture medium, was used as the source of $Zn^{2+}$ ions. This $Zn^{2+}$ concentration was chosen from previous satisfactory results, in which this specific concentration was found to be suitable as myogenic factor for promoting myoblast proliferation and differentiation (Mnatsakanyan et al., 2018).

### 2.4.2. Cytotoxicity

A direct MTS (3-[4,5, dimethylthiazol-2-yl]-5-[3-carboxymethoxy-phenyl]-2-[4-sulfophenyl]-2H-tetrazolium, inner salt) assay was performed to study the cytotoxicity of the engineered materials' surface after 3 and 6 days.. This colorimetric assay is based on the reduction of MTS by viable and metabolically active cells into formazan dye in an enzymatic reaction carried out by NADPH-dehydrogenases. The formazan dye is quantified by measuring the absorbance at 490–500 nm.

Neat PCL and nanocomposites' PCL/G cell substrates (three replicates with an area of 4 $cm^2$) were first sterilized with three consecutive washings in 70% ethanol (10 min each) followed by a 30 min UV exposure for each sample surface. C2C12 at a density of 20,000 cells/$cm^2$ were then cultured on the materials' surface with growth medium (DMEM high glucose, 10% FBS, 1% P/S) in a humidified atmosphere at 37 °C and 5% $CO_2$. Samples containing exogeneous $Zn^{2+}$ (PCL/Zn and PCL/G/Zn) were inoculated into the culture medium with $ZnCl_2$ 40 µM. After 3 and 6 days of culture (with medium renewal every 2 days), the growth medium was replaced by a medium without phenol red containing a 1:10 MTS dilution and left to incubate for 2 h to metabolize the MTS into formazan. The supernatant content of each well (three biological replicates per condition) was then transferred to a P96 plate (three technical replicates of each biological replicate), and absorbance at 490 nm was recorded using a fluorescence microplate reader (Victor Multilabel Plate Reader, Perkin Elmer, USA). Cell viability was calculated as:

$$Viability\ (\%) = \frac{OD\ test}{OD\ control} \cdot 100 \quad (3)$$

where *OD test* is the optical density of the sample and *OD control* (life) is the optical density of the negative control (cells in growth media cultured on neat PCL substrates). Positive control (death) consisted of cells cultured in growth media with 2% Triton-X100 supplement, added 1 h before inoculating materials and controls with MTS.

### 2.4.3. Cell Adhesion

Cell adhesion was evaluated in C2C12 myoblasts seeded at low density on the materials' surface (5000 cells/$cm^2$) to minimize cell contact. The materials (three replicates with 4 $cm^2$ area) had been sterilized previously, as described in Section 2.4.2 and incubated overnight in growth media to ensure protein adsorption and surface functionalization. C2C12 myoblast were seeded on non-conductive substrates and conductive nanocomposites without additional extracellular $Zn^{2+}$ (PCL and PCL/G conditions), and non-conductive and conductive cell substrates with $Zn^{2+}$ ($ZnCl_2$ 40 µM) in the culture medium (growth medium) (PCL/Zn, PCL/G/Zn conditions). After 24 h of culture at 37 °C and 5% $CO_2$, the samples were fixed with 4% paraformaldehyde solution (1 h at RT), permeabilized with 0.5% Triton-X-100/DPBS, blocked with 5% horse serum (HS) in

DPBS (1 h at 37 °C), and stained with fluorescent Phalloidin (dil:1:100, Thermo Fisher) to visualize the actin cytoskeleton. They were finally mounted with Vectashield containing DAPI (Palex Medical) and observed under a fluorescence microscope (Nikon Microscope Eclipse 80i). Cell area (actin cytoskeleton stained with phalloidin) was quantified on ImageJ software.

### 2.4.4. Proliferation

C2C12 myoblasts were seeded at 10,000 cells/cm$^2$ in previously sterilized and functionalized materials with 24 h incubation in growth medium to assess the proliferative effects of conductive cell surfaces and extracellular $Zn^{2+}$ ions. We again assessed non-conductive substrates and conductive nanocomposites without extracellular $Zn^{2+}$ ions (PCL and PCL/G conditions), and cell substrates supplemented with $ZnCl_2$ 40 µM upon seeding and in each additional medium change (PCL/Zn and PCL/G/Zn conditions). After 1, 3 and 5 days of culture in growth medium to allow cells to grow and proliferate on the materials' surface, the cells were fixed with paraformaldehyde solution (1 h at RT), permeabilized with 0.5% Triton-X-100/DPBS, blocked with 5% horse serum (HS) in DPBS (1 h at 37 °C), and mounted with Vectashield with DAPI to stain cell nuclei and quantify cell density after observation by fluorescence microscopy.

### 2.4.5. Myogenic Differentiation

Myogenic differentiation was evaluated for the different conditions: non-conductive substrates and conductive surface nanocomposites with and without extracellular $Zn^{2+}$ using two differentiation culture media. C2C12 were seeded at 20,000 cell/cm$^2$ onto the surface of all sterilized materials previously incubated overnight in growth media (three replicates with area 4 cm$^2$) for 24 h in growth medium. The culture medium was then changed to differentiation medium: DMEM supplemented with 2% FBS, 1% P/S (DMEM 2% FBS 1% P/S) as the first differentiation medium, and DMEM supplemented with 1% of insulin transferrin selenium (ITS, Sigma) and 1% P/S (DMEM 1% ITS 1% P/S) as the second differentiation medium. Again, PCL/Zn and PCL/G/Zn samples were supplemented with $ZnCl_2$ 40 µM in the medium. The cells were cultured for 72 h, and then fixed with 4% paraformaldehyde (1 h at RT) and blocked with 5% HS in DPBS (1 h), permeabilized with 0.5% Triton-X-100 in DPBS and incubated with sarcomeric α-actinin antibody (Thermo Fisher, 1:200) (37 °C, 1 h), rinsed with DPBS, and incubated with secondary Alexa 488 antibody (Thermo Fisher, 1/500) (37 °C, 1 h). All samples were mounted with Vectashield mounting medium with DAPI and analysed by fluorescence microscopy. Image quantification of myogenic differentiation was performed on ImageJ software.

The number of myotubes/cm$^2$, mean myotube area, ratio of differentiated cells (number of nucleus inside differentiated cells/total nucleus), myotube diameter, average number of nuclei per myotube, and the ratio between multinucleated myotubes (≥2 nuclei)/mononucleated sarcomeric α-actinin positive cells area was used to quantify myoblast differentiation.

### 2.4.6. Gene Expression Analysis

The expression of mTOR and MyoD-1 was analysed after 3 days of cell culture following the procedure described in Section 2.4.5 using DMEM 2% FBS 1% P/S as differentiation medium. Total RNA was extracted by a RNeasy® Mini Kit (Qiagen, Hilden, Germany)

and quantified by the NanoDrop One microvolume UV/Vis Spectrophotometer system (Thermo Fisher). It was then reversed transcribed to cDNA (SimpliAmp thermal cycler, Applied Biosystems) and RT-qPCR was performed by the SYBR Select Master Mix (Applied Biosystems) by a QuantStudio 5 Real-Time PCR System (Applied Biosystems). The expression of mTOR and MyoD-1 was analysed, with GAPDH as the housekeeping gene. Data analysis was performed on QuantStudioTM software. The primers used for amplification were as follows: MyoD-1 (forward: 5′-GCA CTA CAG TGG CGA CTC AGA T-3′, reverse: 5′- TAG TAG GCG GTG TCG TAG CCA T-3′), mTOR (forward: 5′- AGA AGG GTC TCC AAG GAC GAC T-3, reverse: 5′- GCA GGA CAC AAA GGC AGC ATT G) and GAPDH (forward: 5′- CAT CAC TGC CAC CCA GAA GAC TG-3′, reverse: 5′- ATG CCA GTG AGC TTC CCG TTC AG-3′).

Quantification of gene expression was carried out by the comparative $C_T$ method. Samples were normalized to the $C_T$ value of the housekeeping gene (GAPDH): $\Delta C_T$ = $C_T$ (sample)- $C_T$ (GAPDH). $C_T$ control values were those of the pristine PCL without extracellular zinc and/or graphene: $\Delta\Delta C_T = \Delta C_T$ (sample)-$\Delta C_T$(PCL). mRNA expression was calculated according to the expression:

$$Fold\ change = \ 2^{\Delta\Delta C_T} \quad (4)$$

### 2.5. Statistical analysis

The experiments were performed at least three times unless noted. All data are expressed as mean ± standard deviation. GraphPad Prism 8.0.2 software was used for statistical analysis. Differences between groups were analysed by one-way analysis of variance (ANOVA tests). Statistical significance is indicated by (*) $p < 0.05$, (**) $p < 0.01$, and (***) $p < 0.001$.

## 3. Results

### 3.1. Morphology and physicochemical Properties of PCL/G Nanocomposites

#### 3.1.1. Morphology

Figure 1 shows electron microscopy images of the surface of the PCL/G nanocomposite and pristine PCL substrates.

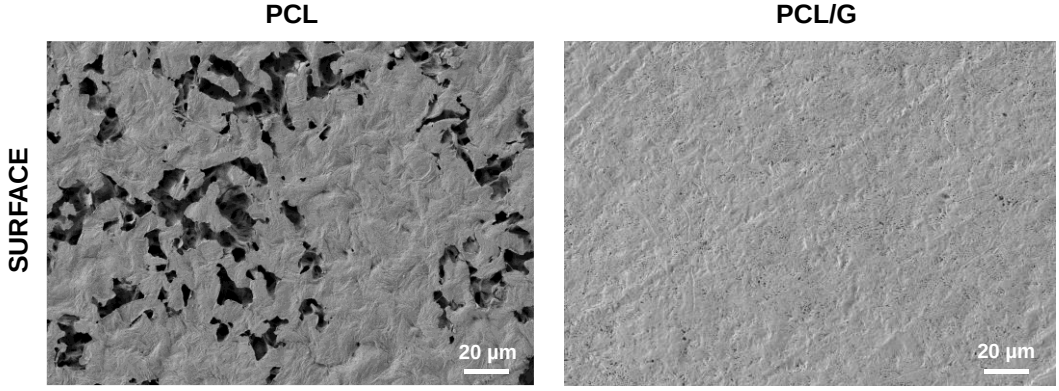


**Figure 1.** FESEM images of the surface of neat PCL and nanocomposites with 0.7 wt% of G nanosheets (PCL/G).

The PCL surface shows a porous structure (with pore size up to 10 µm) formed during solvent evaporation and the formation of crystallites, which can also be seen in the cross-section (Supplementary Figure S1a). The layer containing PCL and G nanosheets, highly wrapped, can also be seen at the top of the cross-sectional image of the composite (Supplementary Figure S1a). Images of pristine G nanosheets after dispersion in THF in an ultrasonic bath show that they are around 3–4 µm long, tending to form small aggregates (Supplementary Figure S1b).

### 3.1.2. Thermal properties and degradation

The thermal behavior of neat PCL (considered as reference) and PCL/G nanocomposites analysed by DSC is shown in Supplementary Figure S2a. The melting process, between 45 and 60 °C, can be seen in the heating thermogram, while no cold crystallization took place during the heating. PCL glass transition emerged after applying the derivative, located ca. −60 °C. The experimental values of the glass transition temperature ($T_g$) and the peak related to the melting process ($T_m$) are given in Table 1. The addition of graphene nanosheets does not affect the PCL glass transition process (see the dotted area in the inset of Supplementary Figure S2a), although PCL crystallization is affected by its incorporation. The nanocomposites with 0.7% *wt/wt* of G nanosheets thus show slightly higher crystallinity, from 34.8% for pristine PCL to 38.3%.

**Table 1.** Glass transition temperature ($T_g$), melting temperature ($T_m$), enthalpy of fusion ($\Delta H_f$), degree of crystallinity ($X_c$ %) and storage modulus (E') at 37 °C.

| Sample | $T_g$ (°C) | $T_m$ (°C) | $\Delta H_f$ (J/g) | $X_c$ (%) | E' (Pa) at 37 °C |
|---|---|---|---|---|---|
| PCL | −64.8 | 53.8 | 48.5 | 34.8 | $3.9 \cdot 10^8$ |
| PCL/G | −64.4 | 55.2 | 53.1 | 38.3 | $8.2 \cdot 10^8$ |

The thermal decomposition of the nanocomposites, analysed by TGA, are depicted in Supplementary Figure S2b (relative weight loss % and derivative of weight loss). The degradation profile of the nanocomposites is similar to that of pristine PCL, which degrades in a single weight loss step (320–480 °C).

### 3.1.3. Mechanical and electrical properties

Dynamic mechanical thermal analysis (DMTA) was carried out between −80 and 50 °C to study the mechanical properties (Supplementary Figure S3 and Table 1). Both the storage modulus (*E')* and loss modulus (*E''*) increased substantially after adding G nanosheets.

G nanosheets were introduced into the polymeric matrix to increase its surface electrical conductivity. The surface of PCL/G nanocomposites was prepared to obtain suitable electrical conductivity values for skeletal TE with a very small amount of G nanosheets to avert non-biocompatibility problems. The nanocomposite preparation procedure was designed to achieve a surface layer with large amount of G nanoparticles, which were darker in color, which considerably increased the surface conductivity of the PCL/G nanocomposite (7.5 ± 0.9 mS/m) (Figure 2), as reported elsewhere (Istrate et al., 2014; Soltani & Kharazi, 2016.). The biological assessment was performed with cells seeded on the conductive surface of the polymer nanocomposites.

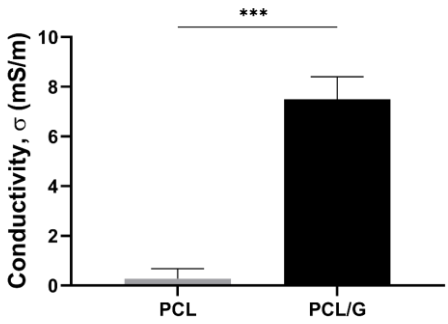


**Figure 2.** Electrical surface conductivity of PCL/G nanocomposites compared to pristine PCL substrate. (***) $p < 0.001$.

### 3.2. Biological performance

Flat substrates of neat PCL and nanocomposite PCL/G were used as non-conductive and conductive surfaces, respectively (the morphology of the substrates and physico-chemical properties are included below). In addition, $ZnCl_2$, as the source of $Zn^{2+}$ ions, was added to the culture medium. Murine myoblasts C2C12 were chosen as the cell line to study the response in terms of adhesion, proliferation, and early myogenic differentiation. Four conditions were evaluated: non-conductive and conductive surfaces without exogeneous $Zn^{2+}$ ions (PCL and PCL/G condition, respectively), and non-conductive and conductive surface with exogeneous $Zn^{2+}$ ions (concentration: 40 µM) (PCL/Zn and PCL/G/Zn condition, respectively).

#### 3.2.1. Effect of a conductive surface and exogeneous Zn ions on biocompatibility and cell adhesion

The biocompatibility of the substrates and the extracellular $Zn^{2+}$ concentration added to the culture medium was assessed by an MTS assay in both non-conductive and conductive polymer nanocomposites (PCL/Zn and PCL/G/Zn conditions) by the direct method. The cells were seeded on the surface of the engineered substrates and $Zn^{2+}$ ions (in the form of $ZnCl_2$, 40 µM concentration) were added to the culture medium. Neat PCL substrates were used as reference (C-).

Figure 3a shows the cytotoxicity after 3 and 6 days of culture. Cell viability less than 70% of the positive control is considered cytotoxic (ISO standard 109935). The G-based nanocomposites (PCL/G), as well as the addition of 40 µM of $Zn^{2+}$ in the culture medium (PCL/Zn condition), show viability values of over 80% in both evaluations, with no significant differences from the PCL substrates (considered as 100% viability). Combining the polymeric matric with 0.7% *wt/wt* of G nanosheets as cell surface and 40 µM of exogeneous $Zn^{2+}$ (PCL/G/Zn condition), the viability is still above 80%.

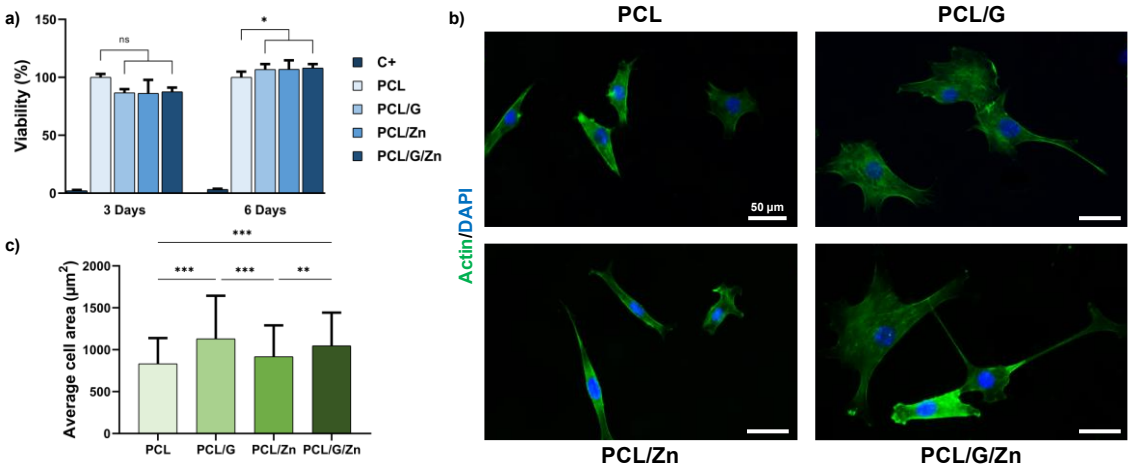


**Figure 3.** (**a**) MTS cytotoxicity. Cell viability after 3 and 6 days. Positive control: latex extract, negative control: neat PCL surface; (**b**) Immunofluorescence images of cell adhesion (actin staining); (**c**) Average cell adhesion area for the different conditions. (*) $p < 0.05$, (**) $p < 0.01$ and (***) $p < 0.001$.

Cell adhesion was analysed after 24 h of culture on samples pre-conditioned with protein adsorbed on the material surfaces (Figure 3b,c). Actin staining showed a significant increase in average cell area (>13%) in G nanocomposites (PCL/G) compared to neat PCL substrates (considered as reference). Conversely, PCL substrates with exogenous $Zn^{2+}$ ions (PCL/Zn) did not show a significant enhancement of cell adhesion. Finally, the combination of conductive cell substrate and exogeneous $Zn^{2+}$ ions (PCL/G/Zn) results in similar cell spreading to the conductive nanocomposite (PCL/G).

### 3.2.2. Effect of a conductive surface and exogeneous $Zn^{2+}$ ions on myoblast proliferation and differentiation

Cell proliferation experiments were performed on myoblasts seeded onto the surface of non-conductive PCL substrates and conductive PCL/G nanocomposites with and without extracellular $Zn^{2+}$ ions (concentration: 40 µM) to investigate the potential mitogenic effect of the combined strategy proposed in this study. Proliferation ratio (cell density/initial cell density) was analysed after 1, 3 and 5 days of culture (Figure 4).

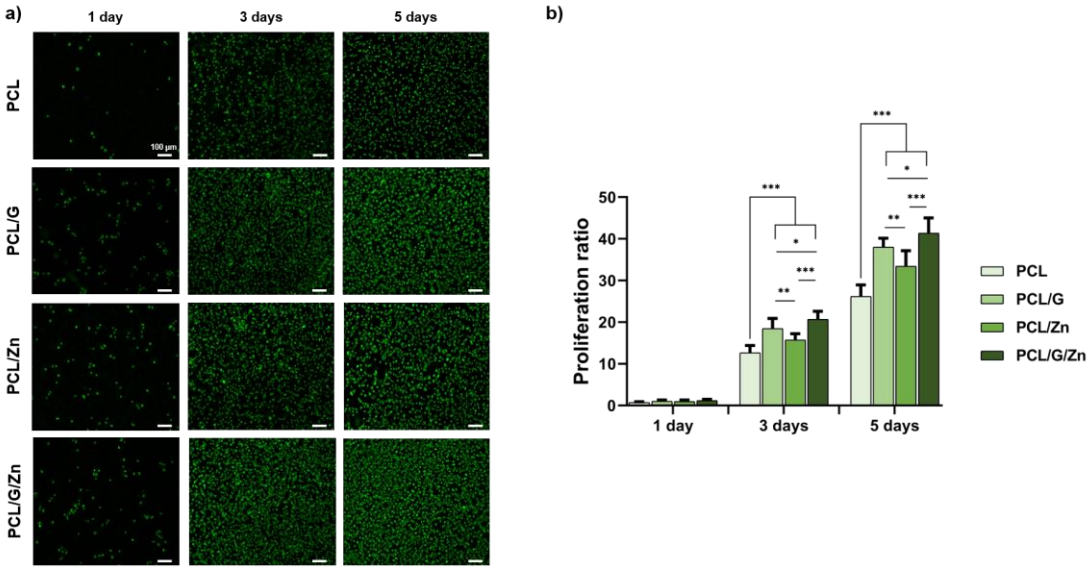


**Figure 4**. Myoblast proliferation seeding in growth medium. (**a**) Representative cell density (DAPI nuclei staining in green) at 1, 3 and 5 days after culture; (**b**) Proliferation ratio obtained as the ratio between total cell density and initial cell density. (*) $p < 0.05$, (**) $p < 0.01$, and (***) $p < 0.001$.

No significant differences were found after 1 day of culture, although the conductive PCL/G substrates (without extracellular $Zn^{2+}$) and PCL substrates with extracellular $Zn^{2+}$ significantly increased in cell density with respect to pristine PCL after 3 and 5 days of culture. Finally, the combination of the conductive properties of the substrate and the presence of extracellular $Zn^{2+}$ ions (PCL/G/Zn condition) was found to significantly enhance cell proliferation, compared to both conditions applied separately.

To investigate the synergies of a conductive nanocomposite surface and exogeneous $Zn^{2+}$ ions (40 µM concentration) in inducing myoblast differentiation in the early stages of commitment to differentiation, C2C12 cells were first cultured in DMEM supplemented with 2% of FBS (serum-deprived medium), a conventional way of inducing myoblast differentiation (Patel et al., 2016). Figure 5a shows immunofluorescence images and quantification of myoblast differentiation after 3 days of culture on non-conductive substrates and conductive substrates, with and without exogeneous $Zn^{2+}$. Conductive PCL/G nanocomposites (without extracellular $Zn^{2+}$), and non-conductive substrates with extracellular $Zn^{2+}$ (PCL/Zn condition) showed increased values for several parameters related to myogenic differentiation.

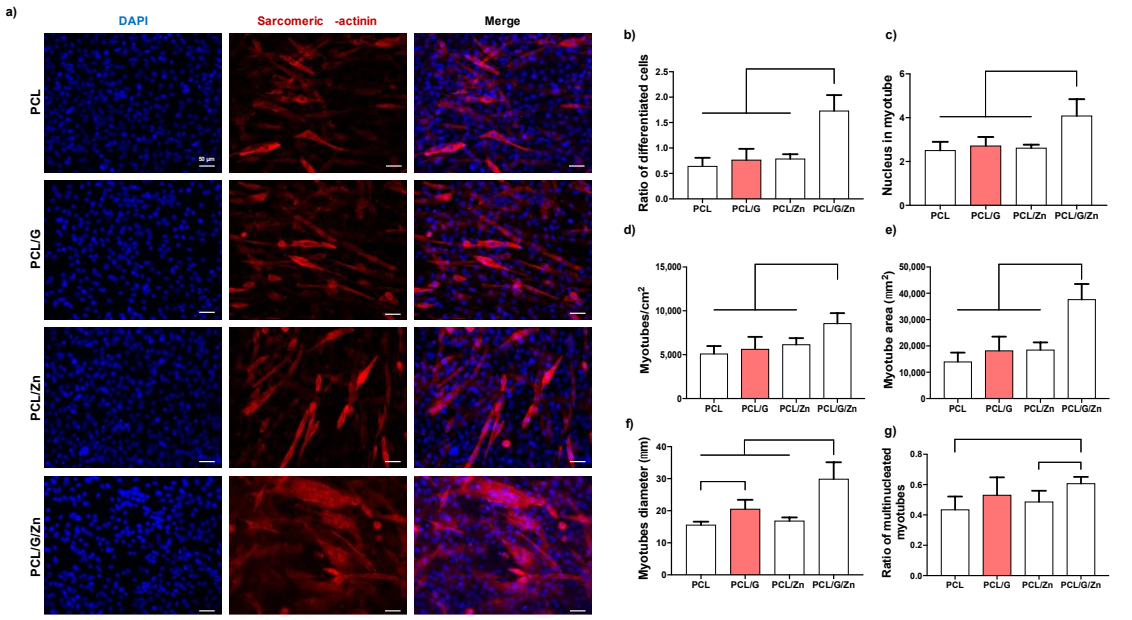


**Figure 5.** Myoblast differentiation (DMEM +2%FBS +1% P/S culture medium). (**a**) Immunofluorescence images of differentiated myoblasts (sarcomeric α-actinin staining) after 3 days of culture; (**b**) Ratio of differentiated cells relative to initial cell density; (**c**) Average number of nuclei inside myotubes; (**d**) Myotube density; (**e**) Myotube area; (**f**) Myotube diameter analysis of 80 random myotubes per condition; (**g**) Ratio of multinucleated myotubes. (*) $p < 0.05$, (**) $p < 0.01$, and (***) $p < 0.001$.

The combination of a conductive nanocomposite surface and exogeneous $Zn^{2+}$ ions (PCL/G/Zn condition) provided an outstanding result. The ratio of differentiated cells was around 170% higher than that of neat PCL (from 0.64 to 1.73), with an increase of ca. 126% and 120% over PCL/G and PCL/Zn conditions, respectively. Regarding the average number of nuclei per myotube (Figure 5c), it was found that the combined strategy substantially raised the number of fused cells, while an enhancement close to 70% was found between the combination of both effects and neat PCL substrates with regard to the number of myotubes/$cm^2$ (Figure 5d). The average myotube area and diameter (Figure 5e,f) were also significantly enhanced in PCL/G/Zn condition over all

other conditions. The mean myotube diameter (Figure 5f) was higher in the conductive substrates (PCL/G) than in neat PCL (from 15.5 to 20.5 µm). Again, the combination of a conductive surface and exogeneous $Zn^{2+}$ significantly raised the average myotube diameter to ca. 30 µm (more than 90% higher than the average myotube diameter on pristine PCL substrates). Finally, the combination of a conductive nanocomposite surface and extracellular $Zn^{2+}$ ions (PCL/G/Zn condition) (Figure 5g) significantly increased the ratio of multinucleated myotubes compared to neat PCL (ca. 40%), and PCL/Zn (ca. 25%).

Similar results were obtained in C2C12 myoblasts cultured in DMEM supplemented with 1% of insulin-transferrin-selenium (ITS) as differentiation medium (Figure 6). The differentiated cell ratio of conductive substrates supplemented with extracellular $Zn^{2+}$ was ca. 140% higher than that of non-conductive PCL, and 69% and 55% higher than PCL/G and PCL/Zn conditions, respectively. In addition, the combination of a conductive surface and exogeneous $Zn^{2+}$ ions significantly increased the number of nuclei inside myotubes, number of myotubes/cm$^2$, myotube area, myotube diameter, and the ratio of multinucleated myotubes over those of all the other conditions.

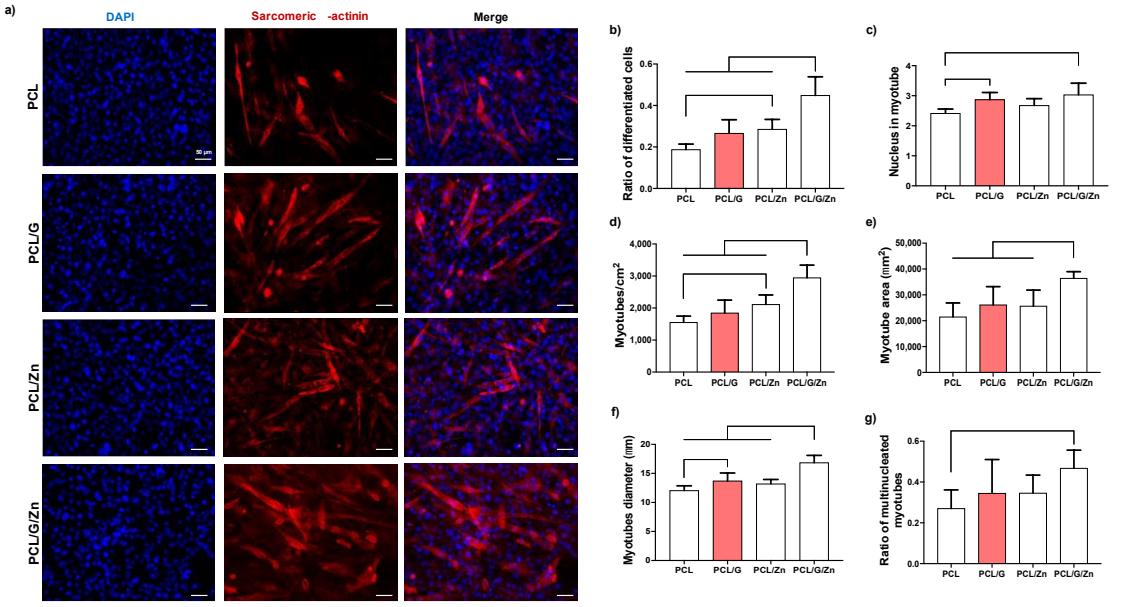


**Figure 6.** Myoblast differentiation in differentiation medium (DMEM +1% ITS +1% P/S. (**a**) Immunofluorescence images of differentiated myoblasts (sarcomeric α-actinin staining) after 3 days of culture; (**b**) Ratio of differentiated cells relative to initial cell density; (**c**) Average number of nuclei inside myotubes; (**d**) Myotube density; (**e**) Myotube area; (**f**) Myotube diameter analysis of 80 random myotubes per condition; (**g**) Ratio of multinucleated myotubes. Graphs show mean ± standard deviation. (*), (**) and (***) indicate significant differences ($p < 0.05$, $p < 0.01$, and $p < 0.001$, respectively).

## 4. Discussion

Our aim was to analyse the synergies between an electrically conductive biomaterial surface (polymeric matrix and G nanosheets as conductive filler) and extracellular $Zn^{2+}$ ions as bioactive factor to stimulate myoblast response.

Nanocomposites based on a biodegradable polymer matrix (PCL) and G nanosheets were first prepared to obtain flat cell substrates with surface conductive properties suitable for musculoskeletal TE. As stated previously, PCL-based polymers have been used as biomaterials to develop numerous strategies to generate skeletal muscle tissues in vitro and, in this study, was used as reference cell substrate in the biological evaluation. Classical solvent casting was a suitable method to prepare the flat cell

substrates with conductive surface properties. Thus, highly diluted PCL-THF solutions were used in the manufacturing process (3% *wt/wt* PCL/THF) incorporating G nanosheets at a concentration of 0.7% *wt/wt* (with respect to the mass of PCL). The diluted solution favors the deposition of the highly conductive G nanosheets on the bottom of the Petri dish during solvent evaporation, forming a superficial layer of G nanosheets wrapped by the polymer chains. As expected, after solvent evaporation, a darker coloration was observed on the surface in contact with the Petri dish, which indicated the presence of a higher amount of G nanosheets highly embedded within the polymeric matrix. Adding G nanosheets significantly changed the morphology, so that the PCL/G nanocomposites had a smooth surface without pores, which suggests the presence of G nanosheets precipitated during solvent evaporation, forming a uniform layer of PCL/nanoparticles.

The DSC thermogram of the PCL/G nanocomposites (Figure S2a and Table 1) showed that the crystallization of PCL increases after the addition of G nanosheets, indicating that the G nanosheets act as a nucleating agent, in good agreement with previous results (Wang et al., 2019). However, the thermal stability of the polymer matrix, shown in Figure S2b, is not substantially affected by adding very small amounts of G nanosheets (Hou et al., 2020). As expected, the mechanical properties increased in the nanocomposite compared to the neat PCL substrates, in agreement with previous results, which showed that a low G content can improve the mechanical properties (Ginestra, 2019; Sánchez-Correa et al., 2018). This increase can be attributed to the intrinsic properties of the filler, i.e., the dispersion and distribution of the G nanosheets embedded within the polymeric matrix (Martínez-Ramón et al., 2020). At 37 °C, the storage modulus of the nanocomposite is more than double that of the pristine PCL (Table 1). However, the improvement obtained is lower than that reported in other studies with composites containing carbon nanomaterials (Istrate et al., 2014; Papageorgiou et al., 2017), which could indicate the presence of G aggregates within the sample (Mansouri et al., 2019). This result is consistent with the aim of our study, in which the nanocomposite preparation procedure used allows obtaining a greater amount of G nanosheets on the surface. Thus, the surface conductivity in the smooth face of the PCL/G nanocomposite (Figure 2), where the G nanosheets precipitated, is in the range of other reported electroactive biomaterials that have stimulated cell response (da Silva et al., 2019; Song et al., 2016), and particularly close to that of natural human skeletal muscle ($0.8 \times 10^{-3}$~$4.5 \times 10^{-3}$ S/m) (Yu et al., 2022). The biological evaluation was carried out using this conductive smooth surface of the nanocomposite as cell substrate.

The biological assessment was performed in mouse myoblast cell line (C2C12), a well-established model to study myogenesis in vitro (Girgis et al., 2014), with conductive and non-conductive substrates, and with and without the addition of $Zn^{2+}$ ions in the culture medium. Previous results had shown that exogeneous $Zn^{2+}$ ions, in particular, 40 µM of $Zn^{2+}$ added to culture medium, enhanced myoblast proliferation and differentiation (Mnatsakanyan et al., 2018), which was why we used this specific $Zn^{2+}$ concentration as exogeneous bioactive factor.

The biocompatibility of PCL is well known (Siddiqui et al., 2018), although the cytotoxicity of biomaterials that include carbon nanomaterials still has to be verified. Both the concentration and the method used to prepare the biomaterial have been reported to be directly related to the performance in biological environments (Gies et al., 2019). The

biocompatibility assay (Figure 3a) showed that neither the conductive polymer nanocomposites, the addition of exogenous Zn at 40 µM in the culture medium, nor the cellular microenvironment created by the combined strategy is cytotoxic.

Cell adhesion on PCL/G nanocomposites increased compared to neat PCL substrates (Figure 3b,c). Due to its high specific surface area, graphene possesses a large capacity for protein adsorption. It is well known that the protein coating induces changes in surface charges, hydrophilicity or topography, affecting the bioactivity (Cheng et al., 2017). The enhancement in cell attachment on PCL/G nanocomposites, specifically the cell area, may be attributed to an increase in the adhesion of adsorption proteins, such as fibronectin and vinculin (Aryaei et al., 2014; Mnatsakanyan et al., 2018). In the other hand, neat PCL with $Zn^{2+}$ ions added in the culture medium had no effect on cell adhesion. It has been reported that $Zn^{2+}$ provides a positive effect on cell adhesion, depending on its content and cell line. Cell adhesion correlates with the concentration of $Zn^{2+}$ ions, and small amount of Zn may not enhance cell adhesion (Mnatsakanyan et al., 2018). These results suggest that the small amount of extracellular $Zn^{2+}$ used in this study (40 µM) is not enough to increase cell adhesion. In line with the above, the combination of conductive substrates and extracellular $Zn^{+2}$ has no impact on myoblast adhesion.

The significant increase of proliferation after 3 and 5 days of cell culture on PCL/G substrates (Figure 4) is in line with previous results that demonstrated that cell substrates containing conductive materials, such as conductive polymers, carbon-based nanomaterials or metal-based nanomaterials, induced proliferation in several cell lines (Baheiraei et al., 2015; W. Liu et al., 2016; Zhao et al., 2018). Likewise, an increase in cell proliferation was expected after the addition of extracellular $Zn^{2+}$ in PCL substrates (PCL/Zn condition), as reported elsewhere (Mnatsakanyan et al., 2018). The significant increase in myoblast proliferation after the addition of extracellular $Zn^{2+}$ on cells seeded on conductive substrates (PCL/G/Zn condition) with respect to both conditions separately, confirms the synergistic mitogenic effect of the combined strategy. This finding indicates that the molecular mechanism involved in myoblast proliferation is stimulated by the cell microenvironment created by the conductive substrates and the extracellular $Zn^{2+}$.

The synergistic effect of the combined strategy was assessed in C2C12 cultured in two differentiation media (serum-deprived medium and DMEM+ITS) after 3 days of culture (Figures 5 and 6). Conductive substrates and non-conductive substrates with extracellular $Zn^{2+}$ showed enhanced behavior in some parameters of myogenic differentiation in both culture media. However, as expected since it is a 3-day cell culture (early differentiation stage), the effect of the incorporation of G nanosheets and extracellular $Zn^{2+}$ ions was therefore lower than that obtained in previous studies (with longer culture time), in which both G (Kim et al., 2019; Patel et al., 2016) and exogeneous $Zn^{2+}$ (Mnatsakanyan et al., 2018) were shown to promote myogenic differentiation. Interestingly, a substantial increase was found by the combined strategy, with significant differences in most of the characteristic parameters with respect to all the other conditions, regardless of the differentiation medium used for the cell culture. These results confirm that the synergistic effect of the conductive surface and extracellular zinc promote the early stages of myogenic differentiation.

To further analyse the effect of the combined proposed strategy, gene expression analysis was performed by RT-qPCR to evaluate regulatory factors mTOR and MyoD-1, both related to the widely studied IGF/PI3K/Akt pathway, albeit with different functions (Karalaki et al., 2009; Mnatsakanyan et al., 2018). The activation (phosphorylation) of protein kinase Akt-1 by the IGF/PI3K signalling cascade has been reported to lead to an increase in the activity of mTOR protein kinase, related to myogenic protein biosynthesis and cell growth, survival, and proliferation (Goldbraikh et al., 2020; Li et al., 2019; Li et al., 2014). In vitro and in vivo experiments showed that mTOR activity not only promotes cell proliferation, but also inhibits myogenic differentiation in muscle development (Li et al., 2019). In addition, several studies have proven that Akt-1 activation by IGF/PI3K cascade increases the activity of MyoD-1, a transcriptional factor involved in the early stages of commitment to myogenic differentiation, establishing a signalling cascade that induces cell cycle arrest, a prerequisite for myogenesis initiation (Karalaki et al., 2009; Mnatsakanyan et al., 2018; Puri & Sartorelli, 2000; Sun et al., 2004; Zammit, 2017). Figure 7a depicts the chain of events following the IGF/PI3K/Akt signalling pathway leading to mTOR expression, related to muscle protein expression (cell growth/proliferation), and MyoD-1 expression (involved in the early stages of myogenic differentiation).

The qPCR results, shown in Figure 7b, are consistent with those reported previously, as the cells cultured in differentiation medium (serum-deprived medium in this assay) did not produce significant differences in mTOR expression in any of the condition tested. Neither PCL/G, PCL/Zn or PCL/G/Zn showed significant differences compared to PCL, indicating no proliferative activity induced by conductive substrates or extracellular $Zn^{2+}$ (Li et al., 2019). Nevertheless, MyoD-1 expression behaved differently, with a remarkable increase in PCL/G/Z condition with respect to neat PCL substrates. Thus, MyoD-1 expression in PCL/G/Zn condition was twice that of neat PCL substrates, while PCL/G and PCL/Zn conditions showed no significant differences in MyoD-1 expression compared to neat PCL.

PI3K/Akt is well known as an essential pathway in proliferation, differentiation, and cell survival, through the activation of Akt protein (Maleki-Ghaleh et al., 2021). Neuronal differentiation of bone marrow mesenchymal stem cells (BMSCs) has been reported to be promoted by the electrical properties of a collagen/hyaluronan hydrogel with conductive PPy nanoparticles and electrical stimulation, which is related to the PI3K/Akt signalling pathway (Wu et al., 2021). Liu et al. showed that the PI3K/Akt pathway is involved in cell growth induced by conducive graphene in representative cell lines (HepG2, A549, MCF-7 and HeLa) (Liu et al., 2016). Graphene has also been suggested to promote stem cell differentiation through the activation of PI3/Akt signalling pathway (Maleki-Ghaleh et al., 2021), while several studies have indicated the important role of Zn ions in this signalling pathway (Barthel et al., 2007). In fact, extracellular $Zn^{2+}$ ions have been shown to stimulate myoblast response via the PI3K/Akt signalling cascade (Mnatsakanyan et al., 2018; Ohashi et al., 2015). The results obtained suggest that the combined strategy applied in the present study (cell–substrate interface with conductive properties and extracellular $Zn^{2+}$) synergically stimulate PI3K/Akt, which result in an early commitment to myoblast differentiation. Further analyses will be necessary to reveal the cell mechanisms triggered by this combined strategy, including the analysis of myoblast differentiation for longer periods of time (later stages of myogenic differentiation) and the

role of the combined strategy on specific signalling pathways, as well as the effect of external electrostimulation.

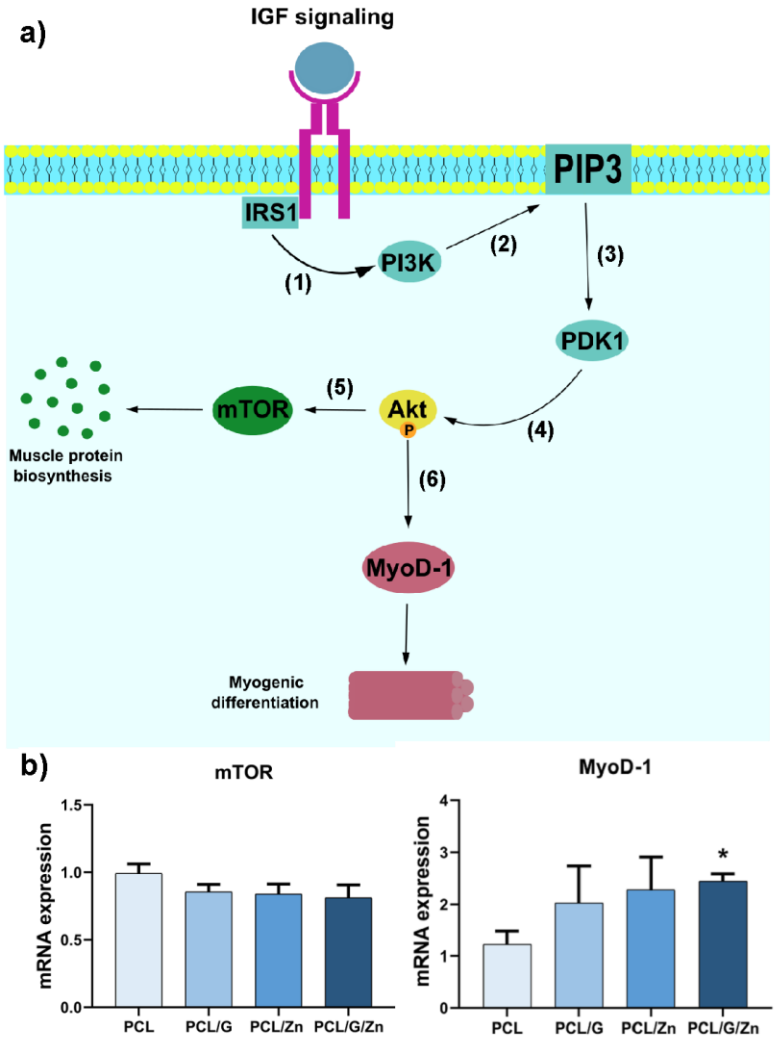


**Figure 7.** (**a**) Representative scheme of the simplified IGF/PI3K/Akt signalling pathway and its enrolment in muscle growth and myogenic differentiation. (1), (2) (Mnatsakanyan et al., 2018); (3), (4) (Dieterle et al., 2014; Mnatsakanyan et al., 2018); (5) (Li et al., 2019); (6) reference (Sun et al., 2004); (**b**) Gene expression analysis results (RT-qPCR) for mTOR and MyoD-1 after culture in serum-deprived medium (DMEM +2% FBS +1% P/S) with GAPDH as housekeeping gene. (*) $p < 0.05$ between PCL and PCL/G/Zn conditions.

## 5. Conclusions

In this study, we developed new cell environments based on the combination of a 2D conductive polymer nanocomposite and extracellular Zn ions as myogenic factor. The conductive nanocomposite surface was prepared from a polymeric matrix and a small percentage of graphene nanosheets (0.7% *wt/wt*) to evaluate the effect of this synergistic approach on myoblast adhesion, proliferation, and differentiation when combined with extracellular $Zn^{2+}$ ions (concentration 40 µM). PCL/G nanocomposites showed a smooth surface with no porosity. As expected, electrical properties of the cell substrates significantly increased in terms of surface conductivity, after graphene nanosheets addition, with conductivity in the range of biological skeletal muscle tissue. Biocompatibility was confirmed in murine C2C12 myoblasts after 3 and 6 days of culture. The novel cell microenvironment showed good cell adhesion and spreading. A strong

synergistic effect induced by the combined strategy was found on myoblast proliferation and cell differentiation (performed in two differentiation media), in which early myoblast differentiation was induced by this novel strategy. However, further studies are required to optimize the system by varying the conductive properties of the substrates and the concentration of mount of extracellular $Zn^{2+}$. From those results, 3D substrates will be engineered, using electrospinning or 3D printing as potential techniques, including both conductive surfaces and the release of Zn ions previously loaded in the substrate. In conclusion, considering the in vitro results obtained in this study, this straightforward and efficient strategy combining a conductive surface and extracellular zinc ions shows great potential for applications in skeletal muscle tissue engineering.

## 6. Acknowledgments

This research was funded by Spanish Ministry of Science and Innovation (MCINN, Agencia Estatal de Investigación/FEDER funds) through the RTI2018-097862-B-C21.) and PID2020-119333RB-I00/AEI/10.13039/501100011033 projects. CIBER-BBN is an initiative funded by the VI National R & D & I Plan 2008–2011, *Iniciativa Ingenio 2010*, Consolider Program, CIBER Actions were financed by the *Instituto de Salud Carlos III* with assistance from the European Regional Development Fund.

## 7. Supplementary information

**Figure S1**: (**a**) Cross-section of neat PCL and nanocomposites with 0.7 wt% of G nanosheets (PCL/G). (**b**) HRFESEM representative images of pristine graphene nanosheets (aggregated and single form) previously dispersed in THF; **Figure S2**: (**a**) Differential scanning calorimetry (DSC) thermograms of neat PCL and PCL/G nanocomposites. Normalized heat flow (Cp) (2nd scan, heating). Inset: temperature derivative of the heat capacity (dCp/dT) from −70 to 0 °C; the dotted lines indicate the glass transition process. (**b**) Thermogravimetry results (TGA). Relative weight loss of PCL and PCL/G nanocomposites; **Figure S3**: Dynamic mechanical thermal analysis (DMTA traction assay). *E'* and *E''* vs. temperature at 1 Hz.

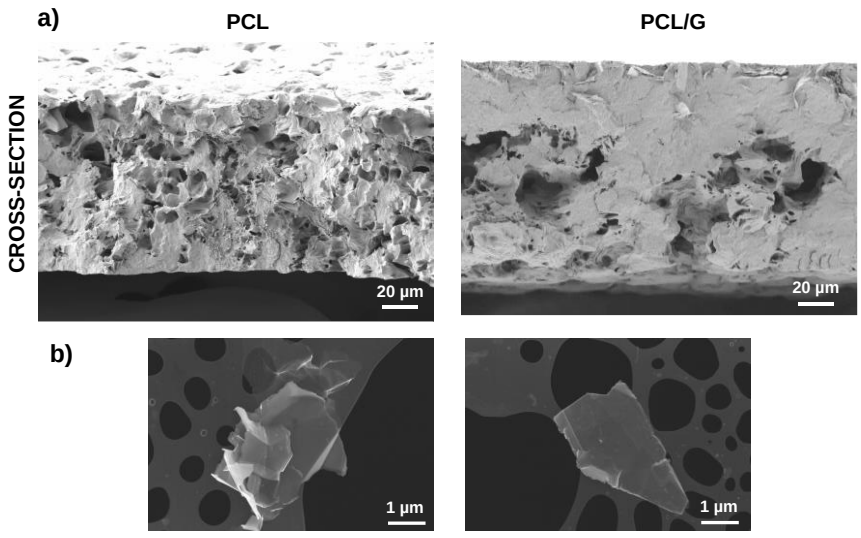

**Figure S1. (a)** Cross-section of neat PCL and nanocomposites with 0.7 wt% of G nanosheets (PCL/G). **(b)** HRFESEM representative images of pristine graphene nanosheets (aggregated and single form) previously dispersed in THF.

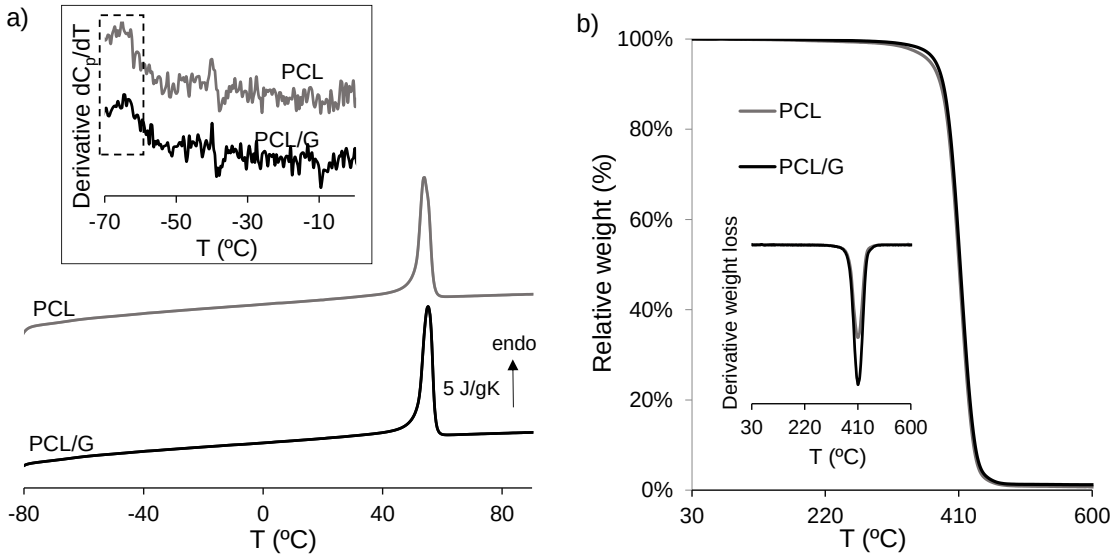


**Figure S2. (a)** Differential scanning calorimetry (DSC) thermograms of neat PCL and PCL/G nanocomposites. Normalized heat flow (Cp) (2nd scan, heating). Inset: temperature derivative of the heat capacity (dCp/dT) from -70 to 0 ºC; the dotted lines indicate the glass transition process. **(b)** Thermogravimetry results (TGA). Relative weight loss of PCL and PCL/G nanocomposites. Inset: derivative of weight loss.

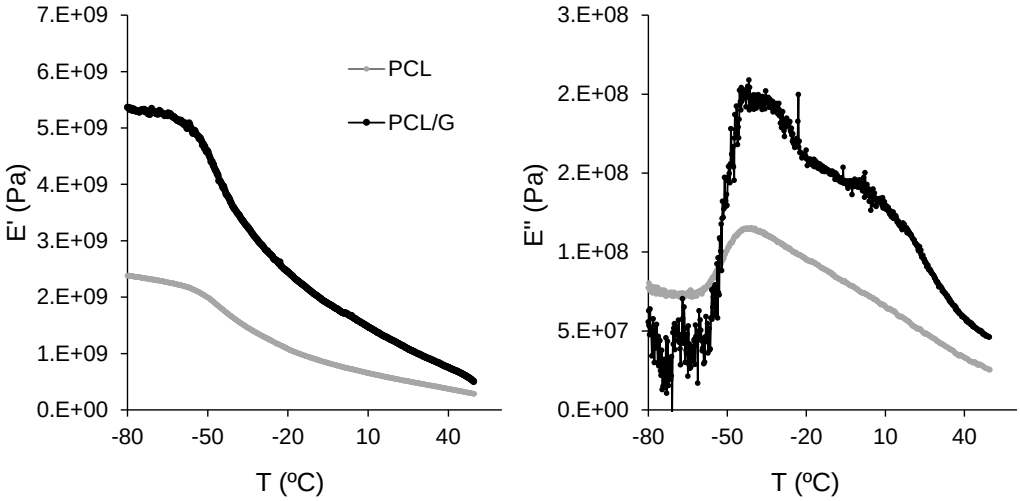


**Figure S3.** Dynamic mechanical thermal analysis (DMTA traction assay). E' and E'' vs. temperature at 1 Hz.

## 8. References

Abedalwafa, M., Wang, F., Wang, L., & Li, C. (2013). Biodegradable PCL for tissue engineering applications: A review. *Reviews on Advanced Materials Science*, *34*(2012), 123–140.

Aparicio-Collado, J. L., García-San-Martín, N., Molina-Mateo, J., Torregrosa Cabanilles, C., Donderis Quiles, V., Serrano-Aroca, A., & Sabater i Serra, R. (2022). Electroactive calcium-alginate/polycaprolactone/reduced graphene oxide nanohybrid hydrogels for skeletal muscle tissue engineering. *Colloids and Surfaces B: Biointerfaces*, *214*. https://doi.org/10.1016/j.colsurfb.2022.112455

Aparicio-Collado, José Luis, Novoa, J. J., Molina-Mateo, J., Torregrosa-Cabanilles, C., Serrano-Aroca, Á., & Sabater I Serra, R. (2021). Novel semi-interpenetrated polymer networks of poly(3-hydroxybutyrate-co-3-hydroxyvalerate)/poly (vinyl alcohol) with incorporated conductive polypyrrole nanoparticles. *Polymers*, *13*(1), 1–21. https://doi.org/10.3390/polym13010057

Aragón, J., Salerno, S., De Bartolo, L., Irusta, S., & Mendoza, G. (2018). Polymeric electrospun scaffolds for bone morphogenetic protein 2 delivery in bone tissue engineering. *Journal of Colloid and Interface Science*, *531*, 126–137. https://doi.org/10.1016/j.jcis.2018.07.029

Aryaei, A., Jayatissa, A. H., & Jayasuriya, A. C. (2014). The effect of graphene substrate on osteoblast cell adhesion and proliferation. *Journal of Biomedical Materials Research - Part A*, *102*(9), 3282–3290. https://doi.org/10.1002/jbm.a.34993

Baheiraei, N., Yeganeh, H., Ai, J., Gharibi, R., Ebrahimi-Barough, S., Azami, M., Vahdat, S., & Baharvand, H. (2015). Preparation of a porous conductive scaffold from aniline pentamer-modified polyurethane/PCL blend for cardiac tissue engineering. *Journal of Biomedical Materials Research - Part A*, *103*(10), 3179–3187. https://doi.org/10.1002/jbm.a.35447

Baino, F., Novajra, G., & Vitale-Brovarone, C. (2015). Bioceramics and scaffolds: A winning combination for tissue engineering. *Frontiers in Bioengineering and Biotechnology*, *3*, 1–17. https://doi.org/10.3389/fbioe.2015.00202

Barthel, A., Ostrakhovitch, E. A., Walter, P. L., Kampkötter, A., & Klotz, L. O. (2007). Stimulation of phosphoinositide 3-kinase/Akt signaling by copper and zinc ions: Mechanisms and consequences. *Archives of Biochemistry and Biophysics*, *463*(2), 175–182. https://doi.org/10.1016/j.abb.2007.04.015

Bellet, P., Gasparotto, M., Pressi, S., Fortunato, A., Scapin, G., Mba, M., Menna, E., & Filippini, F. (2021). Graphene-based scaffolds for regenerative medicine. *Nanomaterials*, *11*(2). https://doi.org/10.3390/nano11020404

Berti, F. V., Srisuk, P., Da Silva, L. P., Marques, A. P., Reis, R. L., & Correlo, V. M. (2017). Synthesis and characterization of electroactive Gellan gum spongy-like hydrogels for skeletal muscle tissue engineering applications. *Tissue Engineering - Part A*, *23*(17–18), 968–979. https://doi.org/10.1089/ten.tea.2016.0430

Briata, P., Lin, W. J., Giovarelli, M., Pasero, M., Chou, C. F., Trabucchi, M., Rosenfeld, M. G., Chen, C. Y., & Gherzi, R. (2012). PI3K/AKT signaling determines a dynamic switch between distinct KSRP functions favoring skeletal myogenesis. *Cell*

*Death and Differentiation*, *19*(3), 478–487. https://doi.org/10.1038/cdd.2011.117

Briquez, P. S., Hubbell, J. A., & Martino, M. M. (2015). Extracellular Matrix-Inspired Growth Factor Delivery Systems for Skin Wound Healing. *Advances in Wound Care*, *4*(8), 479–489. https://doi.org/10.1089/wound.2014.0603

Cezar, C. A., & Mooney, D. J. (2015). Biomaterial-based delivery for skeletal muscle repair. *Advanced Drug Delivery Reviews*, *84*, 188–197. https://doi.org/10.1016/j.addr.2014.09.008

Chaudhuri, B., Bhadra, D., Moroni, L., & Pramanik, K. (2015). Myoblast differentiation of human mesenchymal stem cells on graphene oxide and electrospun graphene oxide-polymer composite fibrous meshes: Importance of graphene oxide conductivity and dielectric constant on their biocompatibility. *Biofabrication*, *7*(1). https://doi.org/10.1088/1758-5090/7/1/015009

Cheng, C., Li, S., Thomas, A., Kotov, N. A., & Haag, R. (2017). Functional Graphene Nanomaterials Based Architectures: Biointeractions, Fabrications, and Emerging Biological Applications. *Chemical Reviews*, *117*(3), 1826–1914. https://doi.org/10.1021/acs.chemrev.6b00520

Corona, B. T., Wu, X., Ward, C. L., McDaniel, J. S., Rathbone, C. R., & Walters, T. J. (2013). The promotion of a functional fibrosis in skeletal muscle with volumetric muscle loss injury following the transplantation of muscle-ECM. *Biomaterials*, *34*(13), 3324–3335. https://doi.org/10.1016/j.biomaterials.2013.01.061

da Silva, L. P., Kundu, S. C., Reis, R. L., & Correlo, V. M. (2019). Electric Phenomenon: A Disregarded Tool in Tissue Engineering and Regenerative Medicine. *Trends in Biotechnology*, *38*(1), 24–49. https://doi.org/10.1016/j.tibtech.2019.07.002

Dieterle, A. M., Böhler, P., Keppeler, H., Alers, S., Berleth, N., Drießen, S., Hieke, N., Pietkiewicz, S., Löffler, A. S., Peter, C., Gray, A., Leslie, N. R., Shinohara, H., Kurosaki, T., Engelke, M., Wienands, J., Bonin, M., Wesselborg, S., & Stork, B. (2014). PDK1 controls upstream PI3K expression and PIP 3 generation. *Oncogene*, *33*(23), 3043–3053. https://doi.org/10.1038/onc.2013.266

Dong, R., Ma, P. X., & Guo, B. (2020). Conductive biomaterials for muscle tissue engineering. *Biomaterials*, *229*(March 2019). https://doi.org/10.1016/j.biomaterials.2019.119584

Eltom, A., Zhong, G., & Muhammad, A. (2019). Scaffold Techniques and Designs in Tissue Engineering Functions and Purposes: A Review. *Advances in Materials Science and Engineering*, *2019*. https://doi.org/10.1155/2019/3429527

Fasolino, I., Guarino, V., Cirillo, V., & Ambrosio, L. (2017). 5-Azacytidine-mediated hMSC behavior on electrospun scaffolds for skeletal muscle regeneration. *Journal of Biomedical Materials Research - Part A*, *105*(9), 2551–2561. https://doi.org/10.1002/jbm.a.36111

Flaibani, M., Boldrin, L., Cimetta, E., Piccoli, M., & Coppi, P. De. (n.d.). *Muscle differentiation and myotubes alignment is influenced by micro-patterned surfaces and exogenous electrical stimulation . AUTHORS : SHORT TITLE : Topological and electrical stimuli improve muscle cell differentiation ABSTRACT :* 1–27.

Gies, V., Lopinski, G., Augustine, J., Cheung, T., Kodra, O., & Zou, S. (2019).

The impact of processing on the cytotoxicity of graphene oxide. *Nanoscale Advances*, *1*(2), 817–826. https://doi.org/10.1039/c8na00178b

Ginestra, P. (2019). Manufacturing of polycaprolactone - Graphene fibers for nerve tissue engineering. *Journal of the Mechanical Behavior of Biomedical Materials*, *100*(August), 103387. https://doi.org/10.1016/j.jmbbm.2019.103387

Girgis, C. M., Clifton-Bligh, R. J., Mokbel, N., Cheng, K., & Gunton, J. E. (2014). Vitamin D signaling regulates proliferation, differentiation, and myotube size in C2C12 skeletal muscle cells. *Endocrinology*, *155*(2), 347–357. https://doi.org/10.1210/en.2013-1205

Goldbraikh, D., Neufeld, D., Eid-Mutlak, Y., Lasry, I., Gilda, J. E., Parnis, A., & Cohen, S. (2020). USP 1 deubiquitinates Akt to inhibit PI 3K-Akt-FoxO signaling in muscle during prolonged starvation . *EMBO Reports*, *21*(4), 1–16. https://doi.org/10.15252/embr.201948791

Guo, J. L., Kim, Y. S., & Mikos, A. G. (2019). Biomacromolecules for Tissue Engineering: Emerging Biomimetic Strategies. *Biomacromolecules*, *20*(8), 2904–2912. https://doi.org/10.1021/acs.biomac.9b00792

Hou, Y., Wang, W., & Bártolo, P. (2020). Novel Poly(-caprolactone)/Graphene Scaffolds for Bone Cancer Treatment and Bone Regeneration. *3D Printing and Additive Manufacturing*, *7*(5), 222–229. https://doi.org/10.1089/3dp.2020.0051

Istrate, O. M., Paton, K. R., Khan, U., O'Neill, A., Bell, A. P., & Coleman, J. N. (2014). Reinforcement in melt-processed polymer-graphene composites at extremely low graphene loading level. *Carbon*, *78*(0), 243–249. https://doi.org/10.1016/j.carbon.2014.06.077

Jinno, N., Nagata, M., & Takahashi, T. (2014). Marginal zinc deficiency negatively affects recovery from muscle injury in mice. *Biological Trace Element Research*, *158*(1), 65–72. https://doi.org/10.1007/s12011-014-9901-2

Karalaki, M., Fili, S., Philippou, A., & Koutsilieris, M. (2009). Muscle regeneration: Cellular and molecular events. *In Vivo*, *23*(5), 779–796.

Kim, J., Leem, J., Kim, H. N., Kang, P., Choi, J., Haque, M. F., Kang, D., & Nam, S. W. (2019). Uniaxially crumpled graphene as a platform for guided myotube formation. *Microsystems and Nanoengineering*, *5*(1). https://doi.org/10.1038/s41378-019-0098-6

Langridge, B., Griffin, M., & Butler, P. E. (2021). Regenerative medicine for skeletal muscle loss: a review of current tissue engineering approaches. *Journal of Materials Science: Materials in Medicine*, *32*(1). https://doi.org/10.1007/s10856-020-06476-5

Li, S., Fu, Y., Pang, Y., Tong, H., Li, S., & Yan, Y. (2019). GRP94 promotes muscle differentiation by inhibiting the PI3K/AKT/mTOR signaling pathway. *Journal of Cellular Physiology*, *234*(11), 21211–21223. https://doi.org/10.1002/jcp.28727

Li, X., Liu, H., Wang, H., Sun, L., Ding, F., Sun, W., Han, C., & Wang, J. (2014). Follistatin could promote the proliferation of duck primary myoblasts by activating PI3K/Akt/mTOR signalling. *Bioscience Reports*, *34*(5), 609–620. https://doi.org/10.1042/BSR20140085

Liu, W., Sun, C., Liao, C., Cui, L., Li, H., Qu, G., Yu, W., Song, N., Cui, Y., Wang, Z., Xie, W., Chen, H., & Zhou, Q. (2016). Graphene Enhances Cellular Proliferation through Activating the Epidermal Growth Factor Receptor. *Journal of Agricultural and Food Chemistry*, *64*(29), 5909–5918. https://doi.org/10.1021/acs.jafc.5b05923

Lo, K. W. H., Ashe, K. M., Kan, H. M., & Laurencin, C. T. (2012). The role of small molecules in musculoskeletal regeneration. *Regenerative Medicine*, *7*(4), 535–549. https://doi.org/10.2217/rme.12.33

Maleki-Ghaleh, H., Hossein Siadati, M., Fallah, A., Zarrabi, A., Afghah, F., Koc, B., Dalir Abdolahinia, E., Omidi, Y., Barar, J., Akbari-Fakhrabadi, A., Beygi-Khosrowshahi, Y., & Adibkia, K. (2021). Effect of zinc-doped hydroxyapatite/graphene nanocomposite on the physicochemical properties and osteogenesis differentiation of 3D-printed polycaprolactone scaffolds for bone tissue engineering. *Chemical Engineering Journal*, *426*(July), 131321. https://doi.org/10.1016/j.cej.2021.131321

Mansouri, N., Al-Sarawi, S. F., Mazumdar, J., & Losic, D. (2019). Advancing fabrication and properties of three-dimensional graphene-alginate scaffolds for application in neural tissue engineering. *RSC Advances*, *9*(63), 36838–36848. https://doi.org/10.1039/c9ra07481c

Martínez-Ramón, V., Castilla-Cortázar, I., Vidaurre, A., & Campillo-Fernández, A. J. (2020). Production and enzymatic degradation of poly(ε-caprolactone)/graphene oxide composites. *Materials Express*, *10*(6), 866–876. https://doi.org/10.1166/mex.2020.1702

McCullagh, K. J. A., & Perlingeiro, R. C. R. (2015). Coaxing stem cells for skeletal muscle repair. *Advanced Drug Delivery Reviews*, *84*, 198–207. https://doi.org/10.1016/j.addr.2014.07.007

McKeon-Fischer, K. D., Browe, D. P., Olabisi, R. M., & Freeman, J. W. (2015). Poly(3,4-ethylenedioxythiophene) nanoparticle and poly(ε-caprolactone) electrospun scaffold characterization for skeletal muscle regeneration. *Journal of Biomedical Materials Research - Part A*, *103*(11), 3633–3641. https://doi.org/10.1002/jbm.a.35481

Mertens, J. P., Sugg, K. B., Lee, J. D., & Larkin, L. M. (2014). Engineering muscle constructs for the creation of functional engineered musculoskeletal tissue. *Regenerative Medicine*, *9*(1), 89–100. https://doi.org/10.2217/rme.13.81

Mnatsakanyan, H., Serra, R. S. i., Rico, P., & Salmerón-Sánchez, M. (2018). Zinc uptake promotes myoblast differentiation via Zip7 transporter and activation of Akt signalling transduction pathway. *Scientific Reports*, *8*(1), 1–14. https://doi.org/10.1038/s41598-018-32067-0

Mouriño, V., Cattalini, J. P., & Boccaccini, A. R. (2012). Metallic ions as therapeutic agents in tissue engineering scaffolds: An overview of their biological applications and strategies for new developments. *Journal of the Royal Society Interface*, *9*(68), 401–419. https://doi.org/10.1098/rsif.2011.0611

Oh, S. H., Park, I. K., Kim, J. M., & Lee, J. H. (2007). In vitro and in vivo characteristics of PCL scaffolds with pore size gradient fabricated by a centrifugation method. *Biomaterials*, *28*(9), 1664–1671. https://doi.org/10.1016/j.biomaterials.2006.11.024

Ohashi, K., Nagata, Y., Wada, E., Zammit, P. S., Shiozuka, M., & Matsuda, R. (2015). Zinc promotes proliferation and activation of myogenic cells via the PI3K/Akt and ERK signaling cascade. *Experimental Cell Research*, *333*(2), 228–237. https://doi.org/10.1016/j.yexcr.2015.03.003

Ostrovidov, S., Ebrahimi, M., Bae, H., Nguyen, H. K., Salehi, S., Kim, S. B., Kumatani, A., Matsue, T., Shi, X., Nakajima, K., Hidema, S., Osanai, M., & Khademhosseini, A. (2017). Gelatin-Polyaniline Composite Nanofibers Enhanced Excitation-Contraction Coupling System Maturation in Myotubes. *ACS Applied Materials and Interfaces*, *9*(49), 42444–42458. https://doi.org/10.1021/acsami.7b03979

Ostrovidov, S., Salehi, S., Costantini, M., Suthiwanich, K., Ebrahimi, M., Sadeghian, R. B., Fujie, T., Shi, X., Cannata, S., Gargioli, C., Tamayol, A., Dokmeci, M. R., Orive, G., Swieszkowski, W., & Khademhosseini, A. (2019). 3D Bioprinting in Skeletal Muscle Tissue Engineering. *Small*, *15*(24), 1–14. https://doi.org/10.1002/smll.201805530

Palmieri, V., Sciandra, F., Bozzi, M., De Spirito, M., & Papi, M. (2020). 3D Graphene Scaffolds for Skeletal Muscle Regeneration: Future Perspectives. *Frontiers in Bioengineering and Biotechnology*, *8*(May), 1–8. https://doi.org/10.3389/fbioe.2020.00383

Papageorgiou, D. G., Kinloch, I. A., & Young, R. J. (2017). Mechanical properties of graphene and graphene-based nanocomposites. *Progress in Materials Science*, *90*, 75–127. https://doi.org/10.1016/j.pmatsci.2017.07.004

Patel, A., Xue, Y., Hartley, R., Sant, V., Eles, J. R., Cui, X. T., Stolz, D. B., & Sant, S. (2018). Hierarchically aligned fibrous hydrogel films through microfluidic self-assembly of graphene and polysaccharides. *Biotechnology and Bioengineering*, *115*(10), 2654–2667. https://doi.org/10.1002/bit.26801

Patel, A., Xue, Y., Mukundan, S., Rohan, L. C., Sant, V., Stolz, D. B., & Sant, S. (2016). Cell-Instructive Graphene-Containing Nanocomposites Induce Multinucleated Myotube Formation. *Annals of Biomedical Engineering*, *44*(6), 2036–2048. https://doi.org/10.1007/s10439-016-1586-6

Puri, P. L., & Sartorelli, V. (2000). Regulation of muscle regulatory factors by DNA-binding, interacting proteins, and post-transcriptional modifications. *Journal of Cellular Physiology*, *185*(2), 155–173. https://doi.org/10.1002/1097-4652(200011)185:2<155::AID-JCP1>3.0.CO;2-Z

Qazi, T. H., Mooney, D. J., Pumberger, M., Geißler, S., & Duda, G. N. (2015). Biomaterials based strategies for skeletal muscle tissue engineering: Existing technologies and future trends. *Biomaterials*, *53*, 502–521. https://doi.org/10.1016/j.biomaterials.2015.02.110

Raja, I. S., Song, S. J., Kang, M. S., Lee, Y. Bin, Kim, B., Hong, S. W., Jeong, S. J., Lee, J. C., & Han, D. W. (2019). Toxicity of zero-and one-dimensional carbon nanomaterials. *Nanomaterials*, *9*(9), 1–24. https://doi.org/10.3390/nano9091214

Ramalingam, V., & Hwang, I. (2020). Zinc oxide nanoparticles promoting the formation of myogenic differentiation into myotubes in mouse myoblast C2C12 cells. *Journal of Industrial and Engineering Chemistry*, *83*, 315–322.

https://doi.org/10.1016/j.jiec.2019.12.004

Rybalko, V. Y., Pham, C. B., Hsieh, P. L., Hammers, D. W., Merscham-Banda, M., Suggs, L. J., & Farrar, R. P. (2015). Controlled delivery of SDF-1α and IGF-1: CXCR4+ cell recruitment and functional skeletal muscle recovery. *Biomaterials Science*, *3*(11), 1475–1486. https://doi.org/10.1039/c5bm00233h

Sabater I Serra, R., Kyritsis, A., Escobar Ivirico, J. L., Gómez Ribelles, J. L., Pissis, P., & Salmerón-Sánchez, M. (2011). Molecular mobility in biodegradable poly (ε -caprolactone)/ poly(hydroxyethyl acrylate) networks. *European Physical Journal E*, *34*(4). https://doi.org/10.1140/epje/i2011-11037-4

Salesa, B., Serra, R. S. I., & Serrano-Aroca, Á. (2021). Zinc chloride: Time-dependent cytotoxicity, proliferation and promotion of glycoprotein synthesis and antioxidant gene expression in human keratinocytes. *Biology*, *10*(11). https://doi.org/10.3390/biology10111072

Sánchez-Correa, F., Vidaurre-Agut, C., Serrano-Aroca, & Campillo-Fernández, A. J. (2018). Poly(2-hydroxyethyl acrylate) hydrogels reinforced with graphene oxide: Remarkable improvement of water diffusion and mechanical properties. *Journal of Applied Polymer Science*, *135*(15), 1–11. https://doi.org/10.1002/app.46158

Siddiqui, N., Asawa, S., Birru, B., Baadhe, R., & Rao, S. (2018). PCL-Based Composite Scaffold Matrices for Tissue Engineering Applications. *Molecular Biotechnology*, *60*(7), 506–532. https://doi.org/10.1007/s12033-018-0084-5

Smith, A. T., LaChance, A. M., Zeng, S., Liu, B., & Sun, L. (2019). Synthesis, properties, and applications of graphene oxide/reduced graphene oxide and their nanocomposites. *Nano Materials Science*, *1*(1), 31–47. https://doi.org/10.1016/j.nanoms.2019.02.004

Soltani, S., & Kharazi, A. Z. (n.d.). *Chitosan / Graphene and Poly ( D , L-Lactic-co-Glycolic Acid )/ Graphene Nano-Composites for Nerve Tissue Engineering*. 684–690.

Song, J., Sun, B., Liu, S., Chen, W., Zhang, Y., Wang, C., Mo, X., Che, J., Ouyang, Y., Yuan, W., & Fan, C. (2016). Polymerizing pyrrole coated poly (l-lactic acid-co-ε-caprolactone) (PLCL) conductive nanofibrous conduit combined with electric stimulation for long-range peripheral nerve regeneration. *Frontiers in Molecular Neuroscience*, *9*, 117. https://doi.org/10.3389/fnmol.2016.00117

Su, Y., Cockerill, I., Wang, Y., Qin, Y. X., Chang, L., Zheng, Y., & Zhu, D. (2019). Zinc-Based Biomaterials for Regeneration and Therapy. *Trends in Biotechnology*, *37*(4), 428–441. https://doi.org/10.1016/j.tibtech.2018.10.009

Sumitani, S., Goya, K., Testa, J. R., Kouhara, H., & Kasayama, S. (2002). Akt1 and Akt2 differently regulate muscle creatine kinase and myogenin gene transcription in insulin-induced differentiation of C2C12 myoblasts. *Endocrinology*, *143*(3), 820–828. https://doi.org/10.1210/endo.143.3.8687

Sun, L., Liu, L., Yang, X. J., & Wu, Z. (2004). Akt binds prohibitin 2 and relieves its repression of MyoD and muscle differentiation. *Journal of Cell Science*, *117*(14), 3021–3029. https://doi.org/10.1242/jcs.01142

Syverud, B. C., VanDusen, K. W., & Larkin, L. M. (2016). Growth factors for skeletal muscle tissue engineering. *Cells Tissues Organs*, *202*(3–4), 169–179.

https://doi.org/10.1159/000444671

Tedesco, F. S., Dellavalle, A., Diaz-Manera, J., Messina, G., & Cossu, G. (2010). Repairing skeletal muscle: Regenerative potential of skeletal muscle stem cells. *Journal of Clinical Investigation*, *120*(1), 11–19. https://doi.org/10.1172/JCI40373

Velasco-Mallorquí, F., Fernández-Costa, J. M., Neves, L., & Ramón-Azcón, J. (2020). New volumetric CNT-doped gelatin-cellulose scaffolds for skeletal muscle tissue engineering. *Nanoscale Advances*, *2*(7), 2885–2896. https://doi.org/10.1039/d0na00268b

Wang, W., Huang, B., Byun, J. J., & Bártolo, P. (2019). Assessment of PCL/carbon material scaffolds for bone regeneration. *Journal of the Mechanical Behavior of Biomedical Materials*, *93*(October 2018), 52–60. https://doi.org/10.1016/j.jmbbm.2019.01.020

Wu, C., Chen, S., Zhou, T., Wu, K., Qiao, Z., Zhang, Y., Xin, N., Liu, X., Wei, D., Sun, J., Luo, H., Zhou, L., & Fan, H. (2021). Antioxidative and Conductive Nanoparticles-Embedded Cell Niche for Neural Differentiation and Spinal Cord Injury Repair. *ACS Applied Materials and Interfaces*, *13*(44), 52346–52361. https://doi.org/10.1021/acsami.1c14679

Wu, Y., Wang, L., Hu, T., Ma, P. X., & Guo, B. (2018). Conductive micropatterned polyurethane films as tissue engineering scaffolds for Schwann cells and PC12 cells. *Journal of Colloid and Interface Science*, *518*, 252–262. https://doi.org/10.1016/j.jcis.2018.02.036

Yang, H. S., Lee, B., Tsui, J. H., Macadangdang, J., Jang, S. Y., Im, S. G., & Kim, D. H. (2016). Electroconductive Nanopatterned Substrates for Enhanced Myogenic Differentiation and Maturation. *Advanced Healthcare Materials*, *5*(1), 137–145. https://doi.org/10.1002/adhm.201500003

Yu, C., Yao, F., & Li, J. (2021). Rational design of injectable conducting polymer-based hydrogels for tissue engineering. *Acta Biomaterialia*. https://doi.org/10.1016/j.actbio.2021.04.027

Yuan, X., Zhang, X., Sun, L., Wei, Y., & Wei, X. (2019). Cellular Toxicity and Immunological Effects of Carbon-based Nanomaterials. *Particle and Fibre Toxicology*, *16*(1). https://doi.org/10.1186/s12989-019-0299-z

Zammit, P. S. (2017). Function of the myogenic regulatory factors Myf5, MyoD, Myogenin and MRF4 in skeletal muscle, satellite cells and regenerative myogenesis. *Seminars in Cell and Developmental Biology*, *72*, 19–32. https://doi.org/10.1016/j.semcdb.2017.11.011

Zein, I., Hutmacher, D. W., Tan, K. C., & Teoh, S. H. (2002). Fused deposition modeling of novel scaffold architectures for tissue engineering applications. *Biomaterials*, *23*(4), 1169–1185. https://doi.org/10.1016/S0142-9612(01)00232-0

Zhao, M., Dai, Y., Li, X., Li, Y., Zhang, Y., Wu, H., Wen, Z., & Dai, C. (2018). Evaluation of long-term biocompatibility and osteogenic differentiation of graphene nanosheet doped calcium phosphate-chitosan AZ91D composites. *Materials Science and Engineering C*, *90*(August 2017), 365–378. https://doi.org/10.1016/j.msec.2018.04.082

Zhao, X., Dong, R., Guo, B., & Ma, P. X. (2017). Dopamine-Incorporated Dual Bioactive Electroactive Shape Memory Polyurethane Elastomers with Physiological Shape Recovery Temperature, High Stretchability, and Enhanced C2C12 Myogenic Differentiation. *ACS Applied Materials and Interfaces*, *9*(35), 29595–29611. https://doi.org/10.1021/acsami.7b10583

# Discussion

Volumetric Muscle Loss (VML) results in impaired muscle regeneration and loss of tissue functionality. Different therapeutic approaches based on tissue transplantations (xenotransplants, allotransplants, and auto transplants) have been proposed, but none of them seems to overcome the regenerative issue. Problems derived from these strategies, such as immunogenicity, comorbidity, and/or genetic rejection evidence the need to explore new approaches to deal with VML. Tissue Engineering is an emerging trend that seeks to regenerate damaged tissues/organs by developing *in vitro* biocompatible and implantable biomaterial scaffolds combined with cell sources and bioactive molecules to generate an *in vivo*-like environment that will allow cell proliferation and differentiation into a specific tissue/organ type. In electrosensitive tissues (muscle, cardiac, neural, bone), it has been proven that electroactive biomaterials promote tissue regeneration even without external electrical stimulation (J. Chen et al., 2015; Pinho et al., 2021; Samadian et al., 2020).

This Doctoral Thesis was conceived with the main purpose of developing electroactive biomaterials to study their applicability in musculoskeletal tissue engineering as novel cell substrates with electrical activity able to promote cell differentiation into the myogenic lineage. To do so, different cell constructs based on biocompatible and biodegradable polymers (PHBV, PCL, SA, PVA) combined with conductive polymeric nanoparticles (PPy, rGO, G) were engineered to obtain electroactive composites with reinforced physicochemical properties (Chapters 1 and 2). The biological properties of the developed electroactive cell substrates were assessed in terms of myoblast adhesion, proliferation, and myogenic differentiation with a murine C2C12 myoblast cell line. Moreover, the combination between a polymeric nanocomposite PCL/G surface and extracellular zinc ions as bioactive factors was investigated to develop novel promyogenic environments based on the synergistic effect between electroactive surfaces and bioactive molecules in terms of myogenic differentiation (Chapter 3).

Semi-interpenetrating polymer networks (semi-IPNs) are polymeric composites formed by the combination of at least one hydrophilic crosslinked polymer (hydrogel) and one or more non-crosslinked polymers entangled into the matrix. The combination of hydrophilic and hydrophobic polymers enables the development of novel cell substrates with enhanced physicochemical and biological properties for tissue engineering (Carnes & Pins, 2020). Moreover, since electrically active biomaterials are of special interest for electrosensitive tissues such as skeletal muscle, the idea of combining semi-IPNs with different conductive polymers results in a promising approach for muscle regeneration.

Chapter 1 describes de development of a novel semi-IPN based on the combination of PHBV and crosslinked PVA (ratio PHBV/PVA 30/70) along with the incorporation of different percentages of PPy nanoparticles as an electroactive filler (up to 15%). The morphological characterization reveals a homogeneous structure for the semi-IPNs with and without PPy nanoparticles. Nevertheless, the highest PPy concentration (15%) tends to form nanoparticle aggregates into the matrix, suggesting the need for a stronger PPy dispersion for concentrations above 10%. The infrared spectroscopy (FTIR)

confirms the presence of every single component on the semi-IPN PHBV/PVA and the effective PVA crosslinking, which produces a reduction in the relative intensity of the O-H bands (3600-3200 $cm^{-1}$). PPy incorporation does not produce significant changes in the spectra but they are visible in it with characteristic peaks at 1100, 1548, and 780-1050 $cm^{-1}$ band. A slight reduction in this band may indicate hydrogen bonding between PPy and the semi-IPN matrix. Swelling and surface wettability confirm that both PHBV and PPy increase the composites' hydrophobicity gradually. Moreover, thermogravimetry results (TGA) indicate that PVA crosslinking and combination with PHBV increases thermal stability, while the addition of PPy nanoparticles does not produce significant changes in the degradation profile. Differential scanning calorimetry (DSC) elucidates a homogeneous structure with no phase separation where PPy affects the crystallization process, especially at high concentrations (10% and 15%). Finally, electrical conductivity analysis shows that PPy nanoparticles significantly increase conductivity in a concentration-dependent manner, reaching conductivity values in the range of electroactive biomaterial suitable for tissue engineering (L. P. da Silva et al., 2019).

Biological assessment of the semi-IPN PHBV/PVA/PPy was evaluated with C2C12 murine myoblasts. MTT cytotoxicity assay confirms the biocompatibility of the semi-IPN even with PPy nanoparticles (2% and 10%). Cell adhesion studies reveal that PHBV increases cell adhesion area in comparison with PVA hydrogels after 24 h culture. Moreover, semi-IPNs with low PPy concentrations (2%) present an even more enhanced cell spreading area than the semi-IPN PHBV/PVA, while high concentrations (10%) reflect an important decrease in these values. These results might be due to the irregular PPy dispersion and its tendency to form aggregates at high nanoparticle concentrations, suggesting the semi-IPN PHBV/PVA with 2% PPy as the best choice for musculoskeletal tissue engineering. Nevertheless, further biological assessment must be performed in order to confirm the feasibility of the nanocomposites to support and enhance myogenic differentiation.

Chapter 2 develops a different conductive semi-IPN. In this case, the composite is formed by a SA hydrogel mixed with hydrophobic PCL (ratio SA/PCL 90/10) to obtain a semi-IPN with reinforced thermal, mechanical, and biological properties compared to SA hydrogels. Hydrogels are very important for various applications, such as drug release and tissue engineering, but when it comes to cell attachment and growth, crucial factors for some tissue engineering applications, their high hydrophilic nature produces a lack of cell adhesion (Abalymov et al., 2020). Therefore, their combination with hydrophobic polymers, such as PCL, may produce a composite with improved physicochemical and biological properties while keeping hydrogel characteristics. In addition, conductive rGO nanoparticles were introduced into the hydrogels at different concentrations to evaluate their effect on the physicochemical and biological properties of the semi-IPN SA/PCL/rGO.

The microstructure analysis by atomic force microscopy and scanning electron microscopy (SEM) reveals a compact and homogeneous microporous structure with no phase separation. Although rGO nanoparticles scarcely modify the composites' inner structure, the surface roughness is increased, pointing out a probable deposition of nanoparticles forming a conductive surface covered by the polymeric matrix. These

results correlate with swelling, wettability, and spectroscopy analysis (FTIR), as rGO nanoparticles (and hydrophobic PCL) decrease the hydrophilicity and surface wettability, due to their hydrophobic nature and the interaction rGO-rGO and rGO-SA, with SA ionically crosslinked with divalent ions (*egg-box* model) (Cao et al., 2020). Moreover, the thermal and mechanical properties of the hydrogel increase after PCL incorporation. rGO enhances mechanical performance at low concentrations (0,5%), while 2% rGO nanosheets produce a slight decrease in the mechanical properties, probably due to the aggregation of rGO during the manufacturing process, as it has been reported in different studies (Abzan et al., 2019; Mansouri et al., 2019). Electrical conductivity measurements prove that rGO increases significantly the electrical conductivity of the semi-IPN, reaching values specifically recommended for musculoskeletal applications (0,8∼4.5 mS/m) (C. Yu et al., 2022).

Biological evaluation with murine myoblasts (C2C12 cell line) shows a biocompatible semi-IPN with no cytotoxic effect of rGO nanoparticles after their addition within the polymeric matrix SA/PCL. Cell adhesion area is improved after PCL and 2% rGO incorporation, probably due to the decreased hydrophilicity of the networks, enabling better protein adsorption. In addition, C2C12 differentiation studies were also performed to study the myogenic potential of these nanohybrid hydrogels. rGO autofluorescence on the 358-641 wavelength range prevented us from identifying cell nuclei with DAPI and performing the typical myogenic differentiation analysis based on the multinucleated myotubes study. To overcome the problem, an adapted method developed by Inoue et al. based on analysing myotubes' density, size, and morphology was used (Inoue et al., 2018). The results reveal a massive enhancement of cell differentiation of the semi-IPN SA/PCL in comparison with SA. While no myotube formation can be observed on the SA hydrogels, the SA/PCL semi-IPN presents a dramatic increase in myotubes density and size. This improvement in myotube formation is even more evident after the addition of 0,5% and 2% rGO nanosheets, with ca. 700% more myotubes/cm$^2$ and 450% average myotube area increase compared to pristine SA hydrogels. These results, in good agreement with previous literature, confirm that electroactive biomaterials enhance myoblast differentiation even without external electrostimulation (Du et al., 2018; Palmieri et al., 2020). Thus, these novel electroactive SA/PCL/rGO nanohybrid hydrogels can be considered promising biomaterials for skeletal muscle tissue engineering.

Chapters 1 and 2 focused on developing novel hydrogels with a semi-IPN structure based on different polymeric combinations (PHBV/PVA and SA/PCL) and electroactive nanoparticles (PPy and rGO) to generate electroactive scaffolds with improved physicochemical and biological properties for musculoskeletal tissue engineering. The results postulate that both PHBV/PVA/PPy and SA/PCL/rGO hydrogel nanonetworks can support C2C12 culture and enhance cell adhesion. Moreover, SA/PCL/rGO nanohybrid hydrogels, also enhance myoblast differentiation extraordinarily. Thus, both electroactive semi-IPNs can be considered strong candidates for muscle tissue engineering applications.

Looking forward to developing new strategies for the stimulation of muscle regeneration, Chapter 3 focuses on studying possible interactions between conductive biomaterials

and bioactive molecules to induce myogenic differentiation. Firstly, an electrically bioactive surface based on PCL combined with high conductive graphene nanosheets (G) at low concentrations (0,7% wt/wt), was prepared. The electroactive surface was obtained by an intentioned deposition of G nanoparticles in the bottom surface during the manufacturing process. The PCL/G nanocomposite was morphologically characterized by electron microscopy and physiochemical properties (thermal, mechanical, and electrical) were obtained. Electron microscopy confirms G nanoparticles deposition on the bottom surface and a homogeneous structure. Thermal characterization by DSC and TGA indicates that graphene nanosheets do not produce a significant change in thermal degradation and do not affect PCL glass transition, although the crystallinity is slightly increased. Both mechanical properties and electrical conductivity were also increased with graphene incorporation, as expected.

To generate a promyogenic cell environment, during biological evaluation, a pre-established zinc ions ($Zn^{2+}$) concentration (40 μm) was employed as an extracellular therapeutic molecule with an already proven promyogenic effect on C2C12 proliferation and differentiation (Mnatsakanyan et al., 2018). Different culture conditions were employed to assess biocompatibility, cell adhesion, proliferation, and differentiation of C2C12 myoblasts seeded on the conductive PCL/G surface with extracellular $Zn^{2+}$. The results show good biocompatibility, and cell adhesion analysis reveals that only nanocomposites with graphene nanosheets (PCL/G) presented an increased cell adhesion area (with no influence of Zn ions). Proliferation assays point out that graphene and zinc individually produce a significant increase in cell density after 3 and 5 days, and the combination of both components surprisingly results in even more enhanced cell density, confirming a synergistic effect of the PCL/G/Zn combination in terms of cell proliferation. Finally, myogenic differentiation was assessed in two different cell culture mediums, and the results were quite interesting. Again, the combination PCL/G/Zn produces a synergistic effect on early myogenic differentiation after 3 days if compared to each individual component and single PCL as the control substrate. These outstanding results are confirmed by gene expression analysis (RT-qPCR) of two genes enrolled on the well-known IGF/PI3K/Akt signalling pathway, related to cell proliferation (mTOR) and early-stage muscle differentiation (MyoD-1) (S. Li et al., 2019; Mnatsakanyan et al., 2018; L. Sun et al., 2004). Overexpression of MyoD-1 and constant mTOR expression levels suggest that the PCL/G/Zn composites, under myogenic cell culture conditions, produce a synergic stimulation of early myogenic differentiation through the activation of the IGF/PI3K/Akt signalling cascade. Nevertheless, further studies need to be carried out to further describe de molecular mechanisms and long-term effects in muscle differentiation of the combined strategy.

# Conclusions

This Doctoral Thesis focused on the development of electroactive biomaterials for skeletal muscle tissue engineering able to support and stimulate cell culture and myogenic differentiation. Additionally, the effects of the combination of a conductive cell surface and extracellular bioactive molecules on skeletal muscle differentiation were also evaluated. The conclusions for each chapter are described below.

## Chapter 1

- PHBV/PVA semi-IPN structure: PVA crosslinking imposes mobility restrictions in the matrix and avoids dissolution in aqueous environments.
- The semi-IPN presents enhanced thermal stability and homogeneous structure with no phase separation.
- Polypyrrole nanoparticles embedded within the semi-IPNs (PHBV/PVA/PPy) interact with the polymer matrix and increase electrical conductivity.
- The electroactive substrates are biocompatible and support C2C12 cell culture. PHBV increases cell adhesion area compared to pure PVA hydrogels. Low PPy concentrations (2%) increase cell adhesion of the semi-IPN PHBV/PVA.
- Further biological studies must be performed to confirm the applicability of these electroactive hydrogels in skeletal muscle tissue engineering applications.

## Chapter 2

- This chapter presents the combination of SA and PCL into a semi-IPN hydrogel with incorporated rGO nanoparticles as strong candidates for skeletal muscle tissue engineering applications.
- Microstructure analysis reveals a homogeneous nanoporous structure with an increased surface roughness after rGO incorporation.
- Spectroscopy, calorimetry, and swelling results suggest the formation of an *egg-box* structure with SA-SA, SA-rGO, and rGO-rGO bonds.
- Thermal stability increases after both SA crosslinking and rGO embedding into the polymer matrix.
- rGO enhances the electrical conductivity of the semi-IPNs reaching typical skeletal muscle conductivity values.
- Biological assessment demonstrates the biocompatibility of the semi-IPNs. The nanohybrid hydrogels SA/PCL/rGO increase cell adhesion and promote myogenic differentiation compared to SA hydrogels, especially after rGO addition.

## Chapter 3

- Cell microenvironments based on the combination of a conductive surface (based on PCL/G nanosheets), together with extracellular $Zn^{2+}$ ions generate a promyogenic environment able to stimulate myogenic differentiation.
- Graphene nanosheets deposit on the bottom surface of the PCL matrix generating a smooth surface with barely any porosity. This surface shows enhanced electrical properties in the same range as skeletal muscle. The mechanical performance also improves with G nanosheets embedding.
- The engineered cell microenvironments are biocompatible after 3 and 6 days of culture. Conductive surfaces (PCL/G) improve cell spreading, with no influence of $Zn^{2+}$ ions.
- Both conductive cell substrates (PCL/G) and non-conductive cell substrates with extracellular $Zn^{2+}$ ions (PCL/Zn) stimulate cell proliferation and myogenic differentiation individually, but the PCL/G/Zn microenvironment produces a synergic enhancement of these values.
- New processing techniques to develop different 2D/3D biological constructs based on the combined strategy (conductive cell microenvironments with $Zn^{2+}$ ions) to mimic the *in vivo* muscle tissue microstructure and the possibility of using an external electrical source to stimulate the engineered electroactive microenvironments are under consideration.

# Future perspectives

In this Doctoral Thesis, different electroactive cell supports based on combinations between polymeric biomaterials and conductive nanoparticles have been developed to obtain a biomimetic cell environment able to enhance skeletal muscle regeneration by stimulating myogenic differentiation. The potential synergies between electroactive biomaterials and extracellular therapeutic ions have also been studied.

Choosing the right combinations of biomaterials to generate new semi-IPNs is quite challenging. The nanoparticles' dispersion into the right solvents and its miscibility with the other polymeric solvents, as well as other crucial parameters, such as materials concentrations, crosslinking methods, and solvent casting conditions, are crucial steps. Nevertheless, the obtained results reflect the success of generating different electroactive platforms with applicability in skeletal muscle tissue engineering. The combination of electroactive cell substrates with bioactive molecules to enhance cell differentiation, such as zinc ions, is a very exciting discovery for the field.

The evaluation of the composites' biological performance with different human cell lines and animal models in terms of cell attachment, proliferation, and myogenic differentiation is crucial. The semi-IPN SA/PCL/rGO and the PCL/G/Zn microenvironments already showed remarkable results with C2C12 murine myoblast cells, enhancing cell spreading, proliferation, and differentiation. In the case of PHBV/PVA/PPy hydrogels, further proliferation and differentiation studies must be performed to prove their potential in skeletal muscle tissue engineering. Antimicrobial properties can also be explored since the different materials from the presented works are composed in part of components with proven antimicrobial activity. This is the case of alginate and the conductive polypyrrole nanoparticles, graphene, and reduced graphene oxide nanosheets (Cabuk et al., 2014; Salem et al., 2019; Zou et al., 2016).

The structure of the electroactive composites is also an open question. The developed novel biomaterials (PHBV/PVA/PPy and SA/PCL/rGO) present a compact nanoporous structure with water sorption capacity. This small pore size is probably due to the manufacturing process. Solvent casting generates collapsed structures suitable for supporting monolayer cell culture. This approach is very useful when testing the biological performance of a novel biomaterial for the first time, which was our case for all materials. However, once we have successfully proved its bioactivity, it is time to optimize the protocol to generate 3D scaffolds based on the same biomaterial compositions, obtaining porous structures similar to the *in vivo* environment. Different manufacturing techniques will be considered (electrospinning, bioprinting), or are already being explored (directional freeze drying, swollen lyophilization) along with the necessary adaptations in the cell culture conditions (cell density, cell line, culture time, etc.). Directional freeze drying is of special interest for skeletal muscle tissue engineering since it can provide a parallel aligned microporous structure to guide myofibre formation after myoblasts differentiation. For instance, we have prepared the first freeze-dried constructs of SA/PCL/rGO, and results present an extremely organized microporous structure. The technique consists of a directional freezing of SA/PCL/rGO (SA/PCL 90/10 and 1% rGO) solution in a cylindrical tube with only one extreme of the tube in close

contact with liquid nitrogen to produce directional freezing of the solution. After that, quick storage at -80º followed by a 72 hours lyophilization and crosslinking process generates the directional freeze-dried hydrogels from Figure 9.

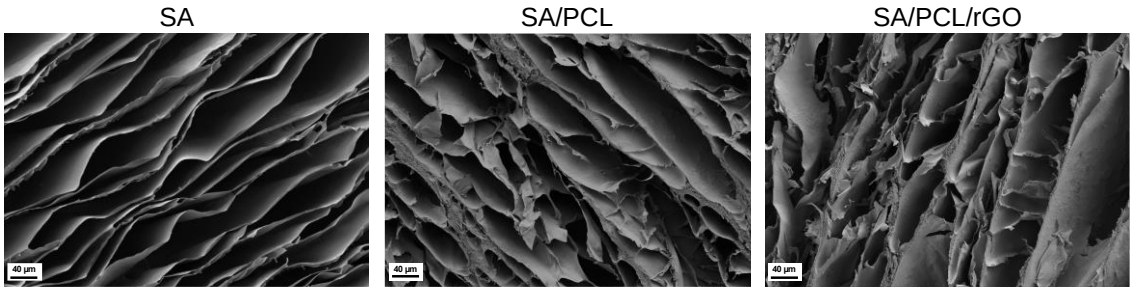


**Figure 9**. Field emission scanning electron microscopy (FESEM) photomicrographs of directional freeze-dried SA, SA/PCL, and SA/PCL/rGO hydrogels.

Moreover, although the engineered electroactive surfaces (PCL/G) from Chapter 3 and their combination with extracellular zinc ions enhance myoblast differentiation without needing an external electrical stimulation source, the study of how electrostimulation (with and without bioactive molecules) could affect the regenerative potential will be soon analysed. First studies are already being conducted with a C-Pace EP cell culture stimulator (IONOptix, Westwood, USA) testing different biomaterials and stimulation parameters.

The combination of 3D electroactive scaffolds with different bioactive molecules, such as therapeutic ions, to enhance myogenic differentiation also needs to be assessed. In the case of zinc ions, since their effect on myogenic differentiation in combination with 2D electroactive surfaces is already proved, it would be interesting to develop 3D electroactive hydrogels with a controlled release of zinc ions to enhance muscle regeneration in a VML defect.

Finally, the implantation of the developed materials with proven *in* vitro enhancement of myogenic differentiation to an *in vivo* model of VML is a must. Generating murine models of VML to later implant the developed materials and evaluate their potential in muscle regeneration would be an interesting starting point since all *in vitro* experiments have been carried out employing murine cells (C2C12 myoblasts).

# Scientific contributions

During this Doctoral Thesis, several experimental results have been produced and diffused through different publications in scientific journals, patents, international conferences and academic works.

## 1. Publications in scientific journals.

The publications as a first author are listed below:

- **Aparicio-Collado, J.L**.; Novoa, J.J.; Molina-Mateo, J.; Torregrosa-Cabanilles, C.; Serrano-Aroca, Á.; Sabater i Serra, R. *Novel semi-interpenetrated polymer networks of poly(3-hydroxybutyrate-co-3-hydroxyvalerate)/poly (vinyl alcohol) with incorporated conductive polypyrrole nanoparticles*. Polymers. 2021, 13, 1–21.
- **Aparicio-Collado, J.L**.; García San-Martín, N.; Molina-Mateo, J.; Torregrosa Cabanilles, C.; Donderis Quiles, V.; Serrano-Aroca, A.; Sabater i Serra, R. *Electroactive calcium-alginate/polycaprolactone/reduced graphene oxide nanohybrid hydrogels for skeletal muscle tissue engineering*. Colloids and Surfaces B: Biointerfaces. 2022, 214.
- **Aparicio-Collado, J.L**.; Molina-Mateo, J.; Cabanilles, C.T.; Vidaurre, A.; Salesa, B.; Serrano-Aroca, Á.; Sabater i Serra, R. *Pro-Myogenic environment promoted by the synergistic effect of conductive polymer nanocomposites combined with extracellular zinc ions*. Biology. 2022, 11.
- **Aparicio-Collado, J.L.;** Zheng, Q.; Molina-Mateo, J.L.; Torregrosa-Cabanilles, C.; Vidaurre, A.; Serrano-Aroca, Á.; Sabater i Serra, R.; *Engineering hihgly porous polyvinyl alcohol hydrogels with poly(3-hydroxybutyrate-co-3-hydroxyvalerate) and graphene nanosheets for musculoskeletal tissue engineering: morphology, water sorption, thermal, mechanical, electrical properties and biocompatibility*. Materials. 2023, 16, 3114.

Other contributions:

- Takayama, K.; Tuñón-Molina, A.; Cano-Vicent, A.; Muramoto, Y.; Noda, T.; **Aparicio-Collado, J. L**.; Sabater i Serra, R.; Martí, M.; Serrano-Aroca, Á. *Non-woven infection prevention fabrics coated with biobased cranberry extracts inactivate enveloped viruses such as SARS-CoV-2 and multidrug-resistant bacteria*. International Journal of Molecular Science. 2021, 22, 12729.
- Rivera-briso, A.L.; **Aparicio-Collado, J.L**.; Sabater i Serra, R. *Graphene Oxide versus carbon nanofibres in simulated intestinal environments*. Polymers. 2022, 14.
- Hurtado, A.; Cano-Vicent, A.; Tuñón-Molina, A.; **Aparicio-Collado, J.L**.; Salesa, B.; i Serra, R.; Serrano-Aroca, Á. *Engineering alginate hydrogel films with poly(3-hydroxybutyrate-co-3-valerate) and graphene nanoplatelets: Enhancement of antiviral activity, cell adhesion and electroactive properties*. International Journal of Biological Macromolecules. 2022, 219, 694–708.

## 2. Intellectual property

- Patent: WO 2022/069783 A1. *Biodegradable biomaterial*. Sabater i Serra, R.; Serrano-Aroca, Á.; Molina-Mateo, J.; **Aparicio-Collado, J.L**.
- Patent: WO 2022/243586 A1. *Device for the release of bioactive agents in the digestive tract, method of preparation and use thereof*. Sabater i Serra, R.; Serrano-Aroca, Á.; Molina-Mateo, J.; Vidaurre-Garayo, A. J.; **Aparicio-Collado, J.L**.; Guillén-Sánchez, L.; Galiana-Cabrera, A. J.

## 3. International conferences

- Poster presentation. *PCL/PVA semi-interpenetrated networks with conductive and antibacterial polypyrrole microparticles for bone tissue engineering: synthesis and physicochemical characterization*. **Aparicio-Collado, J.L**.; Mollá-Robles, A.; Molina-Mateo, J. Sabater i Serra, R. 11th World Biomaterials Congress 2020. Virtual edition.
- Poster presentation. *Nanocomposite zinc alginate/graphene oxide networks: synthesis and physicochemical properties*. **Aparicio-Collado**, **J.L**.; Molina-Mateo, J. Sabater i Serra, R. 11th World Biomaterials Congress 2020. Virtual edition.
- Oral presentation. *Novel hydrogels based on PHBV/PVA with incorporated electroactive nanoparticles for regenerative medicine*. **Aparicio-Collado, J.L**.; Molina-Mateo, J. Sabater i Serra, R. Polymer Connect Conference. Virtual edition.
- Poster presentation. *Zinc alginate/graphene oxide nanocomposite hydrogels for tissue engineering: physicochemical and morphological characterization*. **Aparicio-Collado, J.L**.; Molina-Mateo, J.; Fernández-García, C.; Sabater i Serra, R. Polymer Connect Conference 2021. Virtual edition.
- Poster presentation. *Minimal non-markovian computational model to further understand polymeric biomaterials properties around the glass transition*. **Aparicio-Collado, J.L**.; Molina-Mateo, J.; Sabater i Serra, R.; Meseguer Dueñas, J. M.; Gómez Ribelles, J. L.; Torregrosa-Cabanilles, C. T. 6th Termis World Congress 2021. Virtual edition.
- Poster presentation. *Semi-IPN PHBV/PVA nanocomposite hydrogels with conductive nanoparticles for tissue engineering*. **Aparicio-Collado, J.L**.; Novoa, J. J.; Molina-Mateo, J.; Torregrosa-Cabanilles, C.; Serrano-Aroca, Á.; Sabater i Serra, R. 6th Termis World Congress 2021. Virtual edition.
- Poster participation. *Bio-nanocomposite hydrogels based on zinc alginate/graphene oxide for tissue engineering*. Sabater i Serra, R.; **Aparicio-Collado, J.L**.; Molina-Mateo, J.; Torregrosa-Cabanilles, C.; Meseguer Dueñas, J. M.; Serrano-Aroca, Á. 6th Termis World Congress 2021. Virtual edition.
- Poster participation. *Novel PHBV/PVA based emi-IPN hydrogels with conductive nanoparticles: synthesis and physicochemical characterization*. **Aparicio-Collado, J.L**.; Nova, J. J.; Molina-Mateo, J.; Torregrosa-Cabanilles, C.; Serrano-Aroca, Á.; Sabater i Serra, R. 6th Termis World Congress 2021. Virtual edition.

- Oral presentation. *Electroactive polycaprolactone-graphene nanocomposites combined with zinc ions trigger myogenic differentiation*. **Aparicio-Collado, J. L**.; Molina-Mateo, J. M.; Serrano-Aroca, Á.: Sabater i Serra, R. TERMIS EU 2022, Kraków.
- Poster presentation. *Electroactive SA/PCL hydrogels with conductive rGO nanoparticles for musculoskeletal tissue engineering*. **Aparicio-Collado, J. L**.; García San-Martín, N.; Molina-Mateo, J. M.; Torregrosa-Cabanilles, C.; Serrano-Aroca, Á.: Sabater i Serra, R. TERMIS EU 2022, Kraków.

## 4. Academic contributions

- Final University Degree Thesis co-supervision. *Development of novel semi-interpenetrated polymer networks with electroactive properties for muscle tissue engineering*. Student: García San-Martín, N. Supervisors: Molina-Mateo, J.; Sabater i Serra, R.; **Aparicio-Collado, J. L**. Universitat Politècnica de València, Biomedical Engineering degree.
- Final University Degree Thesis co-supervision. *Synthesis and characterisation of electroactive nanocomposites based on semi-interpenetrated polymer networks and carbon nanoparticles for muscle regeneration*. Student: Zheng, Q. Supervisors: Molina-Mateo, J.; Sabater i Serra, R.; **Aparicio-Collado, J. L**. Universitat Politècnica de València, Biomedical Engineering degree.
- Final Master's Degree Thesis co-supervision. *Development of biomimetic three-dimensional structures with electroactive properties for muscle regeneration*. Student: N. García San-Martín. Supervisors: Vilariño-Feltrer, G.; Sabater i Serra, R.; **Aparicio-Collado, J. L**. Universitat Politècnica de València, Biomedical Engineering Master's.

# References


Abalymov, A. A., Parakhonskiy, B. V., & Skirtach, A. G. (2020). Colloids-at-surfaces: Physicochemical approaches for facilitating cell adhesion on hybrid hydrogels. *Colloids and Surfaces A: Physicochemical and Engineering Aspects*, *603*. https://doi.org/10.1016/j.colsurfa.2020.125185

Abzan, N., Kharaziha, M., & Labbaf, S. (2019). Development of three-dimensional piezoelectric polyvinylidene fluoride-graphene oxide scaffold by non-solvent induced phase separation method for nerve tissue engineering. *Materials and Design*, *167*, 107636. https://doi.org/10.1016/j.matdes.2019.107636

Agarwal, M., Sharma, A., Kumar, P., Kumar, A., Bharadwaj, A., Saini, M., Kardon, G., & Mathew, S. J. (2020). Myosin heavy chain-embryonic regulates skeletal muscle differentiation during mammalian development. *Development*, *147*(7), 1–14. https://doi.org/10.1242/dev.184507

Ahmad Raus, R., Wan Nawawi, W. M. F., & Nasaruddin, R. R. (2021). Alginate and alginate composites for biomedical applications. *Asian Journal of Pharmaceutical Sciences*, *16*(3), 280–306. https://doi.org/10.1016/j.ajps.2020.10.001

Ahmad, S. S., Ahmad, K., Lee, E. J., Lee, Y. H., & Choi, I. (2020). Implications of Insulin-Like Growth Factor-1 in Skeletal Muscle and Various Diseases. *Cells*, *9*. https://doi.org/10.3390/cells9081773

Ahmed, E. M. (2015). Hydrogel: Preparation, characterization, and applications: A review. *Journal of Advanced Research*, *6*(2), 105–121. https://doi.org/10.1016/j.jare.2013.07.006

Alameddine, H. S., & Morgan, J. E. (2016). Matrix Metalloproteinases and Tissue Inhibitor of Metalloproteinases in Inflammation and Fibrosis of Skeletal Muscles. *Journal of Neuromuscular Diseases*, *3*(4), 455–473. https://doi.org/10.3233/JND-160183

Anderson, J. . (2012). Biocompatibility. In *Polymer Science: A Comprehensive Reference* (pp. 363–383). https://doi.org/10.1016/B978-0-444-53349-4.00229-6

Aparicio-Collado, J. L., García-San-Martín, N., Molina-Mateo, J., Torregrosa Cabanilles, C., Donderis Quiles, V., Serrano-Aroca, A., & Sabater i Serra, R. (2022). Electroactive calcium-alginate/polycaprolactone/reduced graphene oxide nanohybrid hydrogels for skeletal muscle tissue engineering. *Colloids and Surfaces B: Biointerfaces*, *214*(February). https://doi.org/10.1016/j.colsurfb.2022.112455

Aparicio-Collado, José Luis, Novoa, J. J., Molina-Mateo, J., Torregrosa-Cabanilles, C., Serrano-Aroca, Á., & Sabater I Serra, R. (2021). Novel semi-interpenetrated polymer networks of poly(3-hydroxybutyrate-co-3-hydroxyvalerate)/poly (vinyl alcohol) with incorporated conductive polypyrrole nanoparticles. *Polymers*, *13*(1), 1–21. https://doi.org/10.3390/polym13010057

Attwood, S. W., & Edel, M. J. (2019). Ips-Cell Technology and the Problem of Genetic Instability—Can It Ever Be Safe for Clinical Use? *Journal of Clinical Medicine*, *8*(3). https://doi.org/10.3390/jcm8030288

Bellet, P., Gasparotto, M., Pressi, S., Fortunato, A., Scapin, G., Mba, M., Menna, E., & Filippini, F. (2021a). Graphene-based scaffolds for regenerative medicine.

*Nanomaterials*, *11*(2). https://doi.org/10.3390/nano11020404

Ben-David, U., & Benvenisty, N. (2011). The tumorigenicity of human embryonic and induced pluripotent stem cells. *Nature Reviews Cancer*, *11*(4), 268–277. https://doi.org/10.1038/nrc3034

Briquez, P. S., Hubbell, J. A., & Martino, M. M. (2015). Extracellular Matrix-Inspired Growth Factor Delivery Systems for Skin Wound Healing. *Advances in Wound Care*, *4*(8), 479–489. https://doi.org/10.1089/wound.2014.0603

Browe, D., & Freeman, J. (2019). Optimizing C2C12 myoblast differentiation using polycaprolactone–polypyrrole copolymer scaffolds. *Journal of Biomedical Materials Research - Part A*, *107*(1), 220–231. https://doi.org/10.1002/jbm.a.36556

Cabuk, M., Alan, Y., Yavuz, M., & Unal, H. I. (2014). Synthesis, characterization and antimicrobial activity of biodegradable conducting polypyrrole-graft-chitosan copolymer. *Applied Surface Science*, *318*, 168–175. https://doi.org/10.1016/j.apsusc.2014.02.180

Calderón, J. C., Bolaños, P., & Caputo, C. (2014). The excitation-contraction coupling mechanism in skeletal muscle. *Biophysical Reviews*, *6*(1), 133–160. https://doi.org/10.1007/s12551-013-0135-x

Cano-Vicent, A., Hashimoto, R., Takayama, K., & Serrano-Aroca, Á. (2022). Biocompatible Films of Calcium Alginate Inactivate Enveloped Viruses Such as SARS-CoV-2. *Polymers*, *14*(7). https://doi.org/10.3390/polym14071483

Carnes, M. E., & Pins, G. D. (2020). Skeletal muscle tissue engineering: Biomaterials-based strategies for the treatment of volumetric muscle loss. *Bioengineering*, *7*(3), 1–39. https://doi.org/10.3390/bioengineering7030085

Cezar, C. A., & Mooney, D. J. (2015). Biomaterial-based delivery for skeletal muscle repair. *Advanced Drug Delivery Reviews*, *84*, 188–197. https://doi.org/10.1016/j.addr.2014.09.008

Changqing Yi, Dandan Liu, Chi-Chun Fong, Jinchao Zhang, and M. Y. (2010). Gold Nanoparticles Promote Osteogenic Differentiation of Mesenchymal Stem Cells through p38 MAPK Pathway. *ACS Nano*, *4*(11), 6439–6448. https://doi.org/ 10.1021/nn101373r

Chen, J., Dong, R., Ge, J., Guo, B., & Ma, P. X. (2015). Biocompatible, Biodegradable, and Electroactive Polyurethane-Urea Elastomers with Tunable Hydrophilicity for Skeletal Muscle Tissue Engineering. *ACS Applied Materials and Interfaces*, *7*(51), 28273–28285. https://doi.org/10.1021/acsami.5b10829

Chen, M. C., Sun, Y. C., & Chen, Y. H. (2013). Electrically conductive nanofibers with highly oriented structures and their potential application in skeletal muscle tissue engineering. *Acta Biomaterialia*, *9*(3), 5562–5572. https://doi.org/10.1016/j.actbio.2012.10.024

Ciriza, J., Rodríguez-Romano, A., Nogueroles, I., Gallego-Ferrer, G., Cabezuelo, R. M., Pedraz, J. L., & Rico, P. (2021). Borax-loaded injectable alginate hydrogels promote muscle regeneration in vivo after an injury. *Materials Science and Engineering C*, *123*. https://doi.org/10.1016/j.msec.2021.112003

Corona, B. T., Garg, K., Ward, C. L., McDaniel, J. S., Walters, T. J., & Rathbone, C. R. (2013). Autologous minced muscle grafts: A tissue engineering therapy for the volumetric loss of skeletal muscle. *American Journal of Physiology - Cell Physiology*, *305*(7), 761–775. https://doi.org/10.1152/ajpcell.00189.2013

Correa, S., Grosskopf, A. K., Lopez Hernandez, H., Chan, D., Yu, A. C., Stapleton, L. M., & Appel, E. A. (2021). Translational Applications of Hydrogels. *Chemical Reviews*, *121*(18), 11385–11457. https://doi.org/10.1021/acs.chemrev.0c01177

Correra, R. M., Ollitrault, D., Valente, M., Mazzola, A., Adalsteinsson, B. T., Ferguson-Smith, A. C., Marazzi, G., & Sassoon, D. A. (2018). The imprinted gene Pw1/Peg3 regulates skeletal muscle growth, satellite cell metabolic state, and self-renewal. *Scientific Reports*, *8*(1), 1–14. https://doi.org/10.1038/s41598-018-32941-x

Curley, C., Hayes, J. C., Rowan, N. J., & Kennedy, J. E. (2014). An evaluation of the thermal and mechanical properties of a salt-modified polyvinyl alcohol hydrogel for a knee meniscus application. *Journal of the Mechanical Behavior of Biomedical Materials*, *40*, 13–22. https://doi.org/10.1016/j.jmbbm.2014.08.003

da Silva, L. P., Kundu, S. C., Reis, R. L., & Correlo, V. M. (2019). Electric Phenomenon: A Disregarded Tool in Tissue Engineering and Regenerative Medicine. *Trends in Biotechnology*, *38*(1), 24–49. https://doi.org/10.1016/j.tibtech.2019.07.002

Dong, R., Ma, P. X., & Guo, B. (2020). Conductive biomaterials for muscle tissue engineering. *Biomaterials*, *229*(March 2019). https://doi.org/10.1016/j.biomaterials.2019.119584

Doss, M. X., & Sachinidis, A. (2019). Current Challenges of iPSC-Based Disease Modeling and Therapeutic Implications. *Cells*, *8*(406). https://doi.org/doi:10.3390/cells8050403

Douglas, K. L., Piccirillo, C. A., & Tabrizian, M. (2006). Effects of alginate inclusion on the vector properties of chitosan-based nanoparticles. *Journal of Controlled Release*, *115*(3), 354–361. https://doi.org/10.1016/j.jconrel.2006.08.021

Du, Y., Ge, J., Li, Y., Ma, P. X., & Lei, B. (2018). Biomimetic elastomeric, conductive and biodegradable polycitrate-based nanocomposites for guiding myogenic differentiation and skeletal muscle regeneration. *Biomaterials*, *157*, 40–50. https://doi.org/10.1016/j.biomaterials.2017.12.005

Dulhunty, A. F., Beard, N. A., & Casarotto, M. G. (2018). Recent advances in understanding the ryanodine receptor calcium release channels and their role in calcium signalling [version 1; peer review: 4 approved]. *F1000Research*, *7*, 1–9. https://doi.org/10.12688/f1000research.16434.1

Dumont, N. A., Bentzinger, C. F., Sincennes, M. C., & Rudnicki, M. A. (2015). Satellite cells and skeletal muscle regeneration. *Comprehensive Physiology*, *5*(3), 1027–1059. https://doi.org/10.1002/cphy.c140068

Dziki, J., Badylak, S., Yabroudi, M., Sicari, B., Ambrosio, F., Stearns, K., Turner, N., Wyse, A., Boninger, M. L., Brown, E. H. P., & Rubin, J. P. (2016). An acellular biologic scaffold treatment for volumetric muscle loss: results of a 13-patient cohort study. *Npj Regenerative Medicine*, *1*(1), 1–12. https://doi.org/10.1038/npjregenmed.2016.8

Egerman, M. A., & Glass, D. J. (2014). Signalling pathways controlling skeletal muscle mass. *Critical Reviews in Biochemistry and Molecular Biology*, *49*(1), 59–68. https://doi.org/10.3109/10409238.2013.857291

Eugenis, I., Wu, D., & Rando, T. A. (2021). Cells, scaffolds, and bioactive factors: Engineering strategies for improving regeneration following volumetric muscle loss. *Biomaterials*, *278*(February). https://doi.org/10.1016/j.biomaterials.2021.121173

Fasolino, I., Guarino, V., Cirillo, V., & Ambrosio, L. (2017). 5-Azacytidine-mediated hMSC behavior on electrospun scaffolds for skeletal muscle regeneration. *Journal of Biomedical Materials Research - Part A*, *105*(9), 2551–2561. https://doi.org/10.1002/jbm.a.36111

Forcina, L., Cosentino, M., & Musarò, A. (2020). Mechanisms Regulating Muscle Regeneration: Insights into the Interrelated and Time-Dependent Phases of Tissue Healing. *Cells*, *9*(5). https://doi.org/10.3390/cells9051297

Friedrich, R. P., Cicha, I., & Alexiou, C. (2021). Iron oxide nanoparticles in regenerative medicine and tissue engineering. *Nanomaterials*, *11*(9). https://doi.org/10.3390/nano11092337

Frismantiene, A., Philippova, M., Erne, P., & Resink, T. J. (2018). Smooth muscle cell-driven vascular diseases and molecular mechanisms of VSMC plasticity. *Cellular Signalling*, *52*(July), 48–64. https://doi.org/10.1016/j.cellsig.2018.08.019

Frontera, W. R., & Ochala, J. (2015). Skeletal Muscle: A Brief Review of Structure and Function. *Calcified Tissue International*, *45*(2), 183–195. https://doi.org/10.1007/s00223-014-9915-y

Fu, X., Xiao, J., Wei, Y., Li, S., Liu, Y., Yin, J., Sun, K., Sun, H., Wang, H., Zhang, Z., Zhang, B. T., Sheng, C., Wang, H., & Hu, P. (2015). Combination of inflammation-related cytokines promotes long-term muscle stem cell expansion. *Cell Research*, *25*(6), 655–673. https://doi.org/10.1038/cr.2015.58

Galat, V., Galat, Y., Perepitchka, M., Jennings, L. J., Iannaccone, P. M., & Hendrix, M. J. C. (2016). Transgene Reactivation in Induced Pluripotent Stem Cell Derivatives and Reversion to Pluripotency of Induced Pluripotent Stem Cell-Derived Mesenchymal Stem Cells. *Stem Cells and Development*, *25*(14), 1060–1072. https://doi.org/10.1089/scd.2015.0366

Ge, J., Liu, K., Niu, W., Chen, M., Wang, M., Xue, Y., Gao, C., Ma, P. X., & Lei, B. (2018). Gold and gold-silver alloy nanoparticles enhance the myogenic differentiation of myoblasts through p38 MAPK signalling pathway and promote in vivo skeletal muscle regeneration. *Biomaterials*, *175*, 19–29. https://doi.org/10.1016/j.biomaterials.2018.05.027

Gilbert-Honick, J., Iyer, S. R., Somers, S. M., Lovering, R. M., Wagner, K., Mao, H. Q., & Grayson, W. L. (2018). Engineering functional and histological regeneration of vascularized skeletal muscle. *Biomaterials*, *164*, 70–79. https://doi.org/10.1016/j.biomaterials.2018.02.006

Gilmore, K. J., Kita, M., Han, Y., Gelmi, A., Higgins, M. J., Moulton, S. E., Clark, G. M., Kapsa, R., & Wallace, G. G. (2009). Skeletal muscle cell proliferation and differentiation on polypyrrole substrates doped with extracellular matrix components.

*Biomaterials*, *30*(29), 5292–5304. https://doi.org/10.1016/j.biomaterials.2009.06.059

Gnanaprakasam, F., Muthu, J., Sankar, V., & Gopal, R. K. (2013). Growth and survival of cells in biosynthetic poly vinyl alcohol – alginate IPN hydrogels for cardiac applications. *Colloids and Surfaces B: Biointerfaces*, *107*, 137–145.

Goswami, P., & O'Haire, T. (2016). Developments in the use of green (biodegradable), recycled and biopolymer materials in technical nonwovens. In *Advances in Technical Nonwovens* (pp. 97–114). https://doi.org/doi.org/10.1016/B978-0-08-100575-0.00003-6

Guo, Baolin, Qu, J., Zhao, X., & Zhang, M. (2019). Degradable conductive self-healing hydrogels based on dextran-graft-tetraaniline and N-carboxyethyl chitosan as injectable carriers for myoblast cell therapy and muscle regeneration. *Acta Biomaterialia*, *84*, 180–193. https://doi.org/10.1016/j.actbio.2018.12.008

Gvozdenović, M. M., Jugović, B. Z., Stevanović, J. S., & Grgur, B. N. (2014). Electrochemical synthesis of electroconducting polymers. *Hemijska Industrija*, *68*(6), 673–684. https://doi.org/10.2298/hemind131122008g

Hernández-Ochoa, E. O., & Schneider, M. F. (2018). Voltage sensing mechanism in skeletal muscle excitation-contraction coupling: Coming of age or midlife crisis? *Skeletal Muscle*, *8*(1), 1–20. https://doi.org/10.1186/s13395-018-0167-9

Higuchi-Takeuchi, M., Morisaki, K., Toyooka, K., & Numata, K. (2016). Synthesis of high-molecular-weight polyhydroxyalkanoates by marine photosynthetic purple bacteria. *PLoS ONE*, *11*(8). https://doi.org/10.1371/journal.pone.0160981

Hodking, A. L., & Huxley, A. F. (1952). A Quantitative Description of Membrane Current and its Application to Conduction and Excitation in Nerve. *The Journal of Physiology*, *117*. https://doi.org/10.1113/jphysiol.1952.sp004764

Hopkins, P. M. (2006). Skeletal muscle physiology. *Continuing Education in Anaesthesia, Critical Care and Pain*, *6*(1), 1–6. https://doi.org/10.1093/bjaceaccp/mki062

Huang, B. (2020). Carbon nanotubes and their polymeric composites: the applications in tissue engineering. *Biomanufacturing Reviews*, *5*(1), 1–26. https://doi.org/10.1007/s40898-020-00009-x

Huang, Z., Ma, Y., Jing, W., Zhang, Y., Jia, X., Cai, Q., Ao, Q., & Yang, X. (2020). Tracing Carbon Nanotubes (CNTs) in Rat Peripheral Nerve Regenerated with Conductive Conduits Composed of Poly(lactide-co-glycolide) and Fluorescent CNTs. *ACS Biomaterials Science and Engineering*, *6*(11), 6344–6355. https://doi.org/10.1021/acsbiomaterials.0c01065

Hurtado, A., Cano-Vicent, A., Tuñón-Molina, A., Aparicio-Collado, J. L., Salesa, B., i Serra, R. S., & Serrano-Aroca, Á. (2022). Engineering alginate hydrogel films with poly(3-hydroxybutyrate-co-3-valerate) and graphene nanoplatelets: Enhancement of antiviral activity, cell adhesion and electroactive properties. *International Journal of Biological Macromolecules*, *219*(July), 694–708. https://doi.org/10.1016/j.ijbiomac.2022.08.039

Huxley, H. E. (1969). The Mechanism of Muscular Contraction. *Science*, *164*(3886), 1356–1366. https://doi.org/10.1126/science.164.3886.1356

Inoue, H., Kunida, K., Matsuda, N., Hoshino, D., Wada, T., Imamura, H., Noji, H., & Kuroda, S. (2018). Automatic quantitative segmentation of myotubes reveals single-cell dynamics of S6 kinase activation. *Cell Structure and Function*, *43*(2), 153–169. https://doi.org/10.1247/csf.18012

Joe, A. W. B., Yi, L., Natarajan, A., Le Grand, F., So, L., Wang, J., Rudnicki, M. A., & Rossi, F. M. V. (2010). Muscle injury activates resident fibro/adipogenic progenitors that facilitate myogenesis. *Nature Cell Biology*, *12*(2), 153–163. https://doi.org/10.1038/ncb2015

Jurkat-Rott, K., & Lehmann-Horn, F. (2004). Ion Channels and Electrical Properties of Skeletal Muscle. *Myology, 3rd Edition*, *January 2004*, 203–231. ISBN 0-07-137180-x

Kaniuk, Ł., & Stachewicz, U. (2021). Development and Advantages of Biodegradable PHA Polymers Based on Electrospun PHBV Fibers for Tissue Engineering and Other Biomedical Applications. *ACS Biomaterials Science and Engineering*, *7*(12), 5339–5362. https://doi.org/10.1021/acsbiomaterials.1c00757

Kaur, G., Adhikari, R., Cass, P., Bown, M., & Gunatillake, P. (2015). Electrically conductive polymers and composites for biomedical applications. *Royal Society of Chemistry Advances*, *5*(47). https://doi.org/10.1039/c5ra01851j

Kim, J., Leem, J., Kim, H. N., Kang, P., Choi, J., Haque, M. F., Kang, D., & Nam, S. W. (2019). Uniaxially crumpled graphene as a platform for guided myotube formation. *Microsystems and Nanoengineering*, *5*(1). https://doi.org/10.1038/s41378-019-0098-6

Kim, T. H., An, D. B., Oh, S. H., Kang, M. K., Song, H. H., & Lee, J. H. (2015). Creating stiffness gradient polyvinyl alcohol hydrogel using a simple gradual freezing-thawing method to investigate stem cell differentiation behaviors. *Biomaterials*, *40*, 51–60. https://doi.org/10.1016/j.biomaterials.2014.11.017

Kin, S., Hagiwara, A., Nakase, Y., Kuriu, Y., Nakashima, S., Yoshikawa, T., Sakakura, C., Otsuji, E., Nakamura, T., & Yamagishi, H. (2007). Regeneration of skeletal muscle using in situ tissue engineering on an acellular collagen sponge scaffold in a rabbit model. *ASAIO Journal*, *53*(4), 506–513. https://doi.org/10.1097/MAT.0b013e3180d09d81

Ko, I. K., Lee, B. K., Lee, S. J., Andersson, K. E., Atala, A., & Yoo, J. J. (2013). The effect of in vitro formation of acetylcholine receptor (AChR) clusters in engineered muscle fibers on subsequent innervation of constructs in vivo. *Biomaterials*, *34*(13), 3246–3255. https://doi.org/10.1016/j.biomaterials.2013.01.029

Kratofil, R. M., Kubes, P., & Deniset, J. F. (2017). Monocyte conversion during inflammation and injury. *Arteriosclerosis, Thrombosis, and Vascular Biology*, *37*(1), 35–42. https://doi.org/10.1161/ATVBAHA.116.308198

Kroehne, V., Heschel, I., Schügner, F., Lasrich, D., Bartsch, J. W., & Jockusch, H. (2008). Use of a novel collagen matrix with oriented pore structure for muscle cell differentiation in cell culture and in grafts. *Journal of Cellular and Molecular Medicine*, *12*(5A), 1640–1648. https://doi.org/10.1111/j.1582-4934.2008.00238.x

Kulinets, I. (2015). Biomaterials and their applications in medicine. In *Regulatory Affairs of Biomaterials and Medical Devices* (pp. 1–10). Woodhead Publishing Series in

Biomaterials. https://doi.org/https://doi.org/10.1533/9780857099204.1

Kumar, Anuj, & Han, S. S. (2017). PVA-based hydrogels for tissue engineering: A review. *International Journal of Polymeric Materials and Polymeric Biomaterials*, *66*(4), 159–182. https://doi.org/10.1080/00914037.2016.1190930

Kumar, Ashok, Chaudhry, I., Reid, M. B., & Boriek, A. M. (2002). Distinct signalling pathways are activated in response to mechanical stress applied axially and transversely to skeletal muscle fibers. *The Journal of Biological Chemistry*, *277*(48), 46493–46503. https://doi.org/10.1074/jbc.M203654200

Kuo, I. Y., & Ehrlich, B. E. (2015). Signalling in muscle contraction. *Cold Spring Harbor Perspectives in Biology*, *7*(2). https://doi.org/10.1101/cshperspect.a006023

Labet, M., & Thielemans, W. (2009). Synthesis of polycaprolactone: A review. *Chemical Society Reviews*, *38*(12), 3484–3504. https://doi.org/10.1039/b820162p

Le Moal, E., Juban, G., Bernard, A. S., Varga, T., Policar, C., Chazaud, B., & Mounier, R. (2018). Macrophage-derived superoxide production and antioxidant response following skeletal muscle injury. *Free Radical Biology and Medicine*, *120*(July 2017), 33–40. https://doi.org/10.1016/j.freeradbiomed.2018.02.024

Lee, E. A., Kwak, S. Y., Yang, J. K., Lee, Y. S., Kim, J. H., Kim, H. D., & Hwang, N. S. (2021). Graphene oxide film guided skeletal muscle differentiation. *Materials Science and Engineering C*, *126*(February). https://doi.org/10.1016/j.msec.2021.112174

Li, S., Fu, Y., Pang, Y., Tong, H., Li, S., & Yan, Y. (2019). GRP94 promotes muscle differentiation by inhibiting the PI3K/AKT/mTOR signalling pathway. *Journal of Cellular Physiology*, *234*(11), 21211–21223. https://doi.org/10.1002/jcp.28727

Li, W., Nooeaid, P., Roether, J. A., Schubert, D. W., & Boccaccini, A. R. (2014). Preparation and characterization of vancomycin releasing PHBV coated 45S5 Bioglass®-based glass-ceramic scaffolds for bone tissue engineering. *Journal of the European Ceramic Society*, *34*(2), 505–514. https://doi.org/10.1016/j.jeurceramsoc.2013.08.032

Liang, Y., & Goh, J. C. H. (2020). Polypyrrole-Incorporated Conducting Constructs for Tissue Engineering Applications: A Review. *Bioelectricity*, *2*(2), 101–119. https://doi.org/10.1089/bioe.2020.0010

Liu, Y. xiao, Wu, B. bing, Gong, L., An, C. rui, Lin, J. xin, Li, Q. kai, Jiang, D. ming, Jin, K. xiu, Mechakra, A., Bunpetch, V., Li, Y., Zou, Y. wei, Ouyang, H. W., & Zou, X. H. (2019). Dissecting cell diversity and connectivity in skeletal muscle for myogenesis. *Cell Death and Disease*, *10*(6). https://doi.org/10.1038/s41419-019-1647-5

Lu, T., Yang, B., Wang, R., & Qin, C. (2020). Xenotransplantation: Current Status in Preclinical Research. *Frontiers in Immunology*, *10*(January). https://doi.org/10.3389/fimmu.2019.03060

Maharjan, B., Kaliannagounder, V. K., Jang, S. R., Awasthi, G. P., Bhattarai, D. P., Choukrani, G., Park, C. H., & Kim, C. S. (2020). In-situ polymerized polypyrrole nanoparticles immobilized poly(ε-caprolactone) electrospun conductive scaffolds for bone tissue engineering. *Materials Science and Engineering C*, *114*(September 2019). https://doi.org/10.1016/j.msec.2020.111056

Mahdy, M. A. A. (2019). Skeletal muscle fibrosis: an overview. *Cell and Tissue Research*, *375*(3), 575–588. https://doi.org/10.1007/s00441-018-2955-2

Mansouri, N., Al-Sarawi, S. F., Mazumdar, J., & Losic, D. (2019). Advancing fabrication and properties of three-dimensional graphene-alginate scaffolds for application in neural tissue engineering. *RSC Advances*, *9*(63), 36838–36848. https://doi.org/10.1039/c9ra07481c

McCullen, S. D., Chow, A. G. Y., & Stevens, M. M. (2011). In vivo tissue engineering of musculoskeletal tissues. *Current Opinion in Biotechnology*, *22*(5), 715–720. https://doi.org/10.1016/j.copbio.2011.05.001

Meng, J., Chun, S., Asfahani, R., Lochmüller, H., Muntoni, F., & Morgan, J. (2014). Human skeletal muscle-derived CD133+ Cells form functional satellite cells after intramuscular transplantation in immunodeficient host mice. *The American Society of Gene & Cell Therapy*, *22*(5), 1008–1017. https://doi.org/10.1038/mt.2014.26

Mnatsakanyan, H., Serra, R. S. i., Rico, P., & Salmerón-Sánchez, M. (2018). Zinc uptake promotes myoblast differentiation via Zip7 transporter and activation of Akt signalling transduction pathway. *Scientific Reports*, *8*(1), 1–14. https://doi.org/10.1038/s41598-018-32067-0

Mondal, D., Griffith, M., & Venkatraman, S. S. (2016). Polycaprolactone-based biomaterials for tissue engineering and drug delivery: Current scenario and challenges. *International Journal of Polymeric Materials and Polymeric Biomaterials*, *65*(5), 255–265. https://doi.org/10.1080/00914037.2015.1103241

Mukund, K., & Subramaniam, S. (2020). Skeletal muscle: A review of molecular structure and function, in health and disease. *Wiley Interdisciplinary Reviews: Systems Biology and Medicine*, *12*(1), 1–46. https://doi.org/10.1002/wsbm.1462

Ngandu Mpoyi, E., Cantini, M., Reynolds, P. M., Gadegaard, N., Dalby, M. J., & Salmerón-Sánchez, M. (2016). Protein Adsorption as a Key Mediator in the Nanotopographical Control of Cell Behavior. *ACS Nano*, *10*(7), 6638–6647. https://doi.org/10.1021/acsnano.6b01649

Ohashi, K., Nagata, Y., Wada, E., Zammit, P. S., Shiozuka, M., & Matsuda, R. (2015). Zinc promotes proliferation and activation of myogenic cells via the PI3K/Akt and ERK signalling cascade. *Experimental Cell Research*, *333*(2), 228–237. https://doi.org/10.1016/j.yexcr.2015.03.003

Orekhov, A. N., Orekhova, V. A., Nikiforov, N. G., Myasoedova, V. A., Grechko, A. V., Romanenko, E. B., Zhang, D., & Chistiakov, D. A. (2019). Monocyte differentiation and macrophage polarization. *Vessel Plus*, *3*. https://doi.org/10.20517/2574-1209.2019.04

Patel, M., Min, J. H., Hong, M. H., Lee, H. J., Kang, S., Yi, S., & Koh, W. G. (2020). Culture of neural stem cells on conductive and microgrooved polymeric scaffolds fabricated via electrospun fiberlate lithography. *Biomedical Materials*, *15*(4). https://doi.org/10.1088/1748-605X/ab763b

Pawlikowski, B., Vogler, T. O., Gadek, K., & Olwin, B. B. (2017). Regulation of skeletal muscle stem cells by fibroblast growth factors. *Developmental Dynamics*, *246*(5), 359–367. https://doi.org/10.1002/dvdy.24495

Perez-Puyana, V., Wieringa, P., Yuste, Y., de la Portilla, F., Guererro, A., Romero, A., & Moroni, L. (2021). Fabrication of hybrid scaffolds obtained from combinations of PCL with gelatin or collagen via electrospinning for skeletal muscle tissue engineering. *Journal of Biomedical Materials Research - Part A*, *109*(9), 1600–1612. https://doi.org/10.1002/jbm.a.37156

Pinho, T. S., Cunha, C. B., Lanceros-Méndez, S., & Salgado, A. J. (2021). Electroactive Smart Materials for Neural Tissue Regeneration. *ACS Applied Bio Materials*. https://doi.org/10.1021/acsabm.1c00567

Pryadko, A., Surmeneva, M. A., & Surmenev, R. A. (2021). Review of hybrid materials based on polyhydroxyalkanoates for tissue engineering applications. *Polymers*, *13*(11). https://doi.org/10.3390/polym13111738

Qazi, T. H., Mooney, D. J., Pumberger, M., Geißler, S., & Duda, G. N. (2015). Biomaterials based strategies for skeletal muscle tissue engineering: Existing technologies and future trends. *Biomaterials*, *53*, 502–521. https://doi.org/10.1016/j.biomaterials.2015.02.110

Rao, L., Qian, Y., Khodabukus, A., Ribar, T., & Bursac, N. (2018). Engineering human pluripotent stem cells into a functional skeletal muscle tissue. *Nature Communications*, *9*(1), 1–12. https://doi.org/10.1038/s41467-017-02636-4

Rebbeck, R. T., Karunasekara, Y., Board, P. G., Beard, N. A., Casarotto, M. G., & Dulhunty, A. F. (2014). Skeletal muscle excitation-contraction coupling: Who are the dancing partners? *The Nternational Journal of Biochemistry and Cell Biology*, *48*(1), 28–38. https://doi.org/10.1016/j.biocel.2013.12.001

Rico, P., Rodrigo-Navarro, A., & Salmerón-Sánchez, M. (2015). Borax-Loaded PLLA for Promotion of Myogenic Differentiation. *Tissue Engineering - Part A*, *21*(21–22), 2662–2672. https://doi.org/10.1089/ten.tea.2015.0044

Rivera-briso, A. L., Aparicio-Collado, J. L., & Sabater, R. (2022). *Graphene Oxide versus Carbon Nanofibers in Simulated Intestinal Environments*. *14*. https://doi.org/https://doi.org/10.3390/polym14020348

Roh, J. S., & Sohn, D. H. (2018). Damage-Associated Molecular Patterns in Inflammatory Diseases. *Immune Network*, *18*(4). https://doi.org/https://doi.org/10.4110/in.2018.18.e27

Rossi, C. A., Flaibani, M., Blaauw, B., Pozzobon, M., Figallo, E., Reggiani, C., Vitiello, L., Elvassore, N., & De Coppi, P. (2011). In vivo tissue engineering of functional skeletal muscle by freshly isolated satellite cells embedded in a photopolymerizable hydrogel . *The FASEB Journal*, *25*(7), 2296–2304. https://doi.org/10.1096/fj.10-174755

Rotini, A., Martínez-Sarrà, E., Duelen, R., Costamagna, D., Di Filippo, E. S., Giacomazzi, G., Grosemans, H., Fulle, S., & Sampaolesi, M. (2018). Aging affects the in vivo regenerative potential of human mesoangioblasts. *Aging Cell*, *17*(2), 1–14. https://doi.org/10.1111/acel.12714

Sacchetti, B., Funari, A., Remoli, C., Giannicola, G., Kogler, G., Liedtke, S., Cossu, G., Serafini, M., Sampaolesi, M., Tagliafico, E., Tenedini, E., Saggio, I., Robey, P. G., Riminucci, M., & Bianco, P. (2016). No identical “mesenchymal stem cells” at different times and sites: Human committed progenitors of distinct origin and

differentiation potential are incorporated as adventitial cells in microvessels. *Stem Cell Reports*, *6*(6), 897–913. https://doi.org/10.1016/j.stemcr.2016.05.011

Sajesh, K. M., Jayakumar, R., Nair, S. V., & Chennazhi, K. P. (2013). Biocompatible conducting chitosan/polypyrrole-alginate composite scaffold for bone tissue engineering. *International Journal of Biological Macromolecules*, *62*, 465–471. https://doi.org/10.1016/j.ijbiomac.2013.09.028

Salem, D. M. S. A., Sallam, M. A. E., & Youssef, T. N. M. A. (2019). Synthesis of compounds having antimicrobial activity from alginate. *Bioorganic Chemistry*, *87*, 103–111. https://doi.org/10.1016/j.bioorg.2019.03.013

Samadian, H., Mobasheri, H., Azami, M., & Faridi-Majidi, R. (2020). Osteoconductive and electroactive carbon nanofibers/hydroxyapatite nanocomposite tailored for bone tissue engineering: in vitro and in vivo studies. *Scientific Reports*, *10*(1), 1–14. https://doi.org/10.1038/s41598-020-71455-3

Scharner, J., & Zammit, P. S. (2011). The muscle satellite cell at 50: The formative years. *Skeletal Muscle*, *1*(1), 1–13. https://doi.org/10.1186/2044-5040-1-28

Sengupta, D., Waldman, S. D., & Li, S. (2014). From in vitro to in situ tissue engineering. *Annals of Biomedical Engineering*, *42*(7), 1537–1545. https://doi.org/10.1007/s10439-014-1022-8

Serrano-Aroca, Á., Ferrandis-Montesinos, M., & Wang, R. (2021). Antiviral Properties of Alginate-Based Biomaterials: Promising Antiviral Agents against SARS-CoV-2. *ACS Applied Bio Materials*, *4*(8), 5897–5907. https://doi.org/10.1021/acsabm.1c00523

Shandalov, Y., Egozi, D., Koffler, J., Dado-Rosenfeld, D., Ben-Shimol, D., Freiman, A., Shor, E., Kabala, A., & Levenberg, S. (2014). An engineered muscle flap for reconstruction of large soft tissue defects. *Proceedings of the National Academy of Sciences of the United States of America*, *111*(16), 6010–6015. https://doi.org/10.1073/pnas.1402679111

Siddiqui, N., Asawa, S., Birru, B., Baadhe, R., & Rao, S. (2018). PCL-Based Composite Scaffold Matrices for Tissue Engineering Applications. *Molecular Biotechnology*, *60*(7), 506–532. https://doi.org/10.1007/s12033-018-0084-5

Simón-Yarza, T., Formiga, F. R., Tamayo, E., Pelacho, B., Prosper, F., & Blanco-Prieto, M. J. (2012). Vascular endothelial growth factor-delivery systems for cardiac repair: An overview. *Theranostics*, *2*(6), 541–552. https://doi.org/10.7150/thno.3682

Smith, A. T., LaChance, A. M., Zeng, S., Liu, B., & Sun, L. (2019). Synthesis, properties, and applications of graphene oxide/reduced graphene oxide and their nanocomposites. *Nano Materials Science*, *1*(1), 31–47. https://doi.org/10.1016/j.nanoms.2019.02.004

Speranza, G. (2021). Carbon nanomaterials: Synthesis, functionalization and sensing applications. *Nanomaterials*, *11*(4). https://doi.org/10.3390/nano11040967

Stout, R. D., & Suttles, J. (2004). Functional plasticity of macrophages: reversible adaptation to changing microenvironments. *Journal of Leukocyte Biology*, *76*(3), 509–513. https://doi.org/10.1189/jlb.0504272

Sun, L., Liu, L., Yang, X. J., & Wu, Z. (2004). Akt binds prohibitin 2 and relieves its repression of MyoD and muscle differentiation. *Journal of Cell Science*, *117*(14), 3021–3029. https://doi.org/10.1242/jcs.01142

Tedesco, F. S., Moyle, L. A., & Perdiguero, E. (2017). Muscle Intersitial Cells: A Brief Guide to Non-satellite Cell Populations in Skeletal Muscle. In *Muscle Stem Cells. Methods in Molecular Biology* (pp. 129–147). https://doi.org/10.1007/978-1-4939-6771-1_7

Ten Broek, R. W., Grefte, S., & Von Den Hoff, J. W. (2010). Regulatory factors and cell populations involved in skeletal muscle regeneration. *Journal of Cellular Physiology*, *224*(1), 7–16. https://doi.org/10.1002/jcp.22127

Thong, C. C., Teo, D. C. L., & Ng, C. K. (2016). Application of polyvinyl alcohol (PVA) in cement-based composite materials: A review of its engineering properties and microstructure behavior. *Construction and Building Materials*, *107*, 172–180. https://doi.org/10.1016/j.conbuildmat.2015.12.188

Tian, P., Tang, L., Teng, K. S., & Lau, S. P. (2018). Graphene quantum dots from chemistry to applications. *Materials Today Chemistry*, *10*, 221–258. https://doi.org/10.1016/j.mtchem.2018.09.007

Tidball, J. G. (2005). Inflammatory processes in muscle injury and repair. *American Journal of Physiology - Regulatory Integrative and Comparative Physiology*, *288*(2 57-2), 345–353. https://doi.org/10.1152/ajpregu.00454.2004

Ullah, S., & Chen, X. (2020). Fabrication, applications and challenges of natural biomaterials in tissue engineering. *Applied Materials Today*, *20*. https://doi.org/10.1016/j.apmt.2020.100656

Urciuolo, A., Quarta, M., Morbidoni, V., Gattazzo, F., Molon, S., Grumati, P., Montemurro, F., Tedesco, F. S., Blaauw, B., Cossu, G., Vozzi, G., Rando, T. A., & Bonaldo, P. (2013). Collagen VI regulates satellite cell self-renewal and muscle regeneration. *Nature Communications*, *4*(May). https://doi.org/10.1038/ncomms2964

van der Wal, E., Herrero-Hernandez, P., Wan, R., Broeders, M., in 't Groen, S. L. M., van Gestel, T. J. M., van IJcken, W. F. J., Cheung, T. H., van der Ploeg, A. T., Schaaf, G. J., & Pijnappel, W. W. M. P. (2018). Large-Scale Expansion of Human iPSC-Derived Skeletal Muscle Cells for Disease Modeling and Cell-Based Therapeutic Strategies. *Stem Cell Reports*, *10*(6), 1975–1990. https://doi.org/10.1016/j.stemcr.2018.04.002

Velasco-Mallorquí, F., Fernández-Costa, J. M., Neves, L., & Ramón-Azcón, J. (2020). New volumetric CNT-doped gelatin-cellulose scaffolds for skeletal muscle tissue engineering. *Nanoscale Advances*, *2*(7), 2885–2896. https://doi.org/10.1039/d0na00268b

Vijayavenkataraman, S., Kannan, S., Cao, T., Fuh, J. Y. H., Sriram, G., & Lu, W. F. (2019). 3D-Printed PCL/PPy Conductive Scaffolds as Three-Dimensional Porous Nerve Guide Conduits (NGCs) for Peripheral Nerve Injury Repair. *Frontiers in Bioengineering and Biotechnology*, *7*(October). https://doi.org/10.3389/fbioe.2019.00266

Yang, H. S., Lee, B., Tsui, J. H., Macadangdang, J., Jang, S. Y., Im, S. G., & Kim, D. H. (2016). Electroconductive Nanopatterned Substrates for Enhanced Myogenic

Differentiation and Maturation. *Advanced Healthcare Materials*, *5*(1), 137–145. https://doi.org/10.1002/adhm.201500003

Yang, J. S., Xie, Y. J., & He, W. (2011). Research progress on chemical modification of alginate: A review. *Carbohydrate Polymers*, *84*(1), 33–39. https://doi.org/10.1016/j.carbpol.2010.11.048

Yang, W., & Hu, P. (2018). Skeletal muscle regeneration is modulated by inflammation. *Journal of Orthopaedic Translation*, *13*, 25–32. https://doi.org/10.1016/j.jot.2018.01.002

Yi, H., Forsythe, S., He, Y., Liu, Q., Xiong, G., Wei, S., Li, G., Atala, A., Skardal, A., & Zhang, Y. (2017). Tissue-specific extracellular matrix promotes myogenic differentiation of human muscle progenitor cells on gelatin and heparin conjugated alginate hydrogels. *Acta Biomaterialia*, *62*, 222–233. https://doi.org/10.1016/j.actbio.2017.08.022

Yu, C., Yao, F., & Li, J. (2022). Rational design of injectable conducting polymer-based hydrogels for. *Acta Biomaterialia*, *139*, 4–21. https://doi.org/10.1016/j.actbio.2021.04.027

Zhang, W., Liu, Y., & Zhang, H. (2021). Extracellular matrix: an important regulator of cell functions and skeletal muscle development. *Cell and Bioscience*, *11*(1), 1–13. https://doi.org/10.1186/s13578-021-00579-4

Zou, X., Zhang, L., Wang, Z., & Luo, Y. (2016). Mechanisms of the antimicrobial activities of graphene materials. *Journal of the American Chemical Society*, *138*(7). https://doi.org/10.1021/jacs.5b11411